

**Conformational Dynamics of Calmodulin and  
Ribosome-Nascent Chain Complexes Studied  
by Time-Resolved Fluorescence Anisotropy**

Inaugural-Dissertation

zur Erlangung des Doktorgrades  
der Mathematisch-Naturwissenschaftlichen Fakultät  
der Heinrich-Heine-Universität Düsseldorf

vorgelegt von

**Paraskevas Lamprou**  
aus Thessaloniki (Griechenland)

Jülich, Juni 2013

aus dem Institut für komplexe Systeme 5  
des Forschungszentrums Jülich GmbH

Gedruckt mit der Genehmigung der  
Mathematisch-Naturwissenschaftlichen Fakultät der  
Heinrich-Heine-Universität Düsseldorf

Referent: Prof. Dr. Jörg Fitter

Koreferent: Prof. Dr. Dieter Willbold

Tag der mündlichen Prüfung: 15.10.2013

To my mother, Anastasia

To my brother, Dimitrios

Στή λατρευτή μου μητέρα, Άννασταςία

Στόν πολυαγαπημένο μου άδερφό, Δημήτρη

# *Preface*

Now that I recall my work for my PhD and the route I had to take till its fulfillment, the story of Odysseus, who had to go through a lot to achieve his goal, comes to my mind again and again. Indeed, the way to my Ithaki was long, but not always endurable; however, I had to confront all the difficulties that showed up. During this journey, I had the opportunity to meet and collaborate with many interesting people, and I gained a lot from their experience and knowledge, that definitely contributed to the development of my own scientific judgement.

My adventure began in October 2009, almost three and half years ago, when I travelled abroad for the first time in my life, to explore the possibility to become a PhD student at Forschungszentrum Jülich in Germany, and a fellow in International School for Biophysics and Soft matter (BioSoft), branch of Helmholtz Association. I really cannot find words to express my gratitude to Emeritus Prof. Dr. Georg Büldt, retired director of the department of Molecular Biophysics, ICS-5, of the Institute of Complex Systems, who admitted me to his group at Forschungszentrum Jülich. I thank him from the bottom of my heart for the opportunity he offered me to work in a fully organized laboratory as well as for the scientific guidance and the financial support.

I also thank BioSoft and its coordinator, Dr. Thorsten Auth, for the chance they offer fellows and other students to attend lectures from many disciplines, including cellular biophysics, theoretical physics, etc. Additionally, I thank BioSoft for the opportunity they gave us to attend skills courses in time management, presentation skills, and developing career.

I owe many thanks to Prof. Dr. Jörg Fitter, temporary director of ICS-5, who accepted to be my official supervisor, since Prof. Büldt is already retired. I also thank him and Dr. Alexandros Katranidis for the endless discussions on topics that concerned my PhD work, their precious help and guidance, their felicitous remarks, and the patience they showed when I was making a lot and bothersome questions. I also thank both of them for their willingness to read through my PhD dissertation and to correct my mistakes. I also owe many thanks to Prof. Dr. Dieter Willbold who accepted to be the second reviewer of

my dissertation since we needed a professor in the commission who is still a professor at University of Düsseldorf.

I also thank Prof. Dr. Arnd Baumann (ICS-4, Cellular Biophysics, Forschungszentrum Jülich) for providing us with the plasmid carrying the gene of wild-type Calmodulin bovine.

Many thanks especially to Daryan Kempe, PhD student in our group, for the Matlab scripts he gave me to analyze the time-resolved fluorescence anisotropy data. Many thanks also to Henning Höfig, master student at I. Physikalisches Institut (IA) in RWTH Aachen, for the pdb files with FIAsh bound to Calmodulin. I thank the technicians, Ms. Ramona Justinger and Ms. Ilona Ritter, for helping me with the sequencing of my DNA constructs. I also thank the other members of ICS-5, Dr. Tina Züchner, Ms. Birgit Gehrman, Dr. Renu Batra-Safferling, Ms. Anne Cousin, Dr. Ramona Schlesinger, Matteo Gabba, Axel Baumann, Sascha Lehmann, Dr. Jaydeep Bhattacharya, Dr. Diaa Atta, Dr. Tobias Rosenkranz, and the new PhD students of our group, Ms. Cristina Remeş and Ms. Antonie Schöne, for the friendly working environment.

I owe a lot of thanks to my family, my mother, Anastasia, and my older brother, Dimitrios, for their support and understanding, the encouragement and love they gave me all these years, that helped me to come to this point.

And finally, I dedicate all my honour and glory to our Lord, Jesus Christ (*in Greek: Δόξα σοι ὁ Θεός, ἡ μόνη ἐλπίς ἡμῶν, δόξα σοι!*).

Paraskevas Lamprou



|   |    |
|---|----|
| 2.3-2 Labelling of CaM with FIAsH (Fluorescein Arsenical Helix Binder)  | 45 |
| 2.4 Spectroscopic techniques  | 46 |
| 2.4-1 Absorption spectroscopy   | 46 |
| 2.4-2 Circular dichroism spectroscopy (CD)  | 46 |
| 2.4-3 Principles of fluorescence  | 49 |
| 2.4-3.1 Steady-state fluorescence spectroscopy  | 52 |
| 2.4-3.2 Time-resolved fluorescence spectroscopy   | 54 |
| 2.4-4 Functionality tests with calcium (Ca <sup>2+</sup> )  | 56 |
| 2.4-5 Fluorescence correlation spectroscopy (FCS)   | 57 |
| 2.4-6 Fluorescence anisotropy   | 60 |
| 2.4-6.1 Definition of fluorescence anisotropy   | 61 |
| 2.4-6.2 Theory for fluorescence anisotropy  | 62 |
| 2.4-6.3 Measurement of steady-state anisotropies  | 65 |
| 2.4-6.4 The Perrin's equation   | 66 |
| 2.4-6.5 Time-resolved fluorescence anisotropy analysis  | 67 |
| 3. Results  | 75 |
| 3.1 Preparation and purification of CaM containing the tetra-Cys motif near the N-terminus  | 75 |
| 3.1-1 Isolation of the mutated gene of CaM containing the tetra-Cys motif near the N-terminus and a His <sub>6</sub> -tag at the C-terminus | 75 |
| 3.1-2 Cloning of the gene of CaMmut(4Cys)-6His into pCR-Blunt, and subsequently into pET27b   | 77 |
| 3.1-3 Purification of CaMmut(4Cys)-6His by Ni-NTA column and size-exclusion chromatography  | 77 |
| 3.2 Characterization of CaM with the tetra-Cys motif  | 80 |
| 3.2-1 Functionality tests with Ca <sup>2+</sup>   | 80 |
| 3.2-2 Circular dichroism (CD) measurements on CaMmut(4Cys) and CaMwt, both in apo-buffer and upon Ca <sup>2+</sup> binding                  | 83 |
| 3.2-3 Labelling of CaMmut(4Cys) with FIAsH  | 85 |
| 3.2-4 Characterization of the CaM-FIAsH complex   | 87 |

|  |     |
|--|-----|
| 3.3 Time-resolved fluorescence anisotropy of free diffusing CaM-FIAsH complex in solution  | 92  |
| 3.3-1 Time-resolved fluorescence anisotropy of apo-CaM-FIAsH complex   | 96  |
| 3.3-2 Time-resolved fluorescence anisotropy of CaM-FIAsH complex in the presence of Ca <sup>2+</sup>   | 104 |
| 3.4 Preparation and characterization of ribosome-nascent chain complexes (RNCs)  | 105 |
| 3.4-1 Isolation of the mutated gene of CaM containing the tetra-Cys motif near the N-terminus, without stop codon                            | 105 |
| 3.4-2 Creating the construct of CaMmut(4Cys) fused with Ser/Gly linker and SecM without stop codon, and cloning in pRSET                     | 106 |
| 3.4-3 Isolation of the mutated gene of the 1 <sup>st</sup> EF-hand of CaM and half CaM, and cloning in pRSET with Ser/Gly linker and SecM    | 108 |
| 3.4-4 Isolation of the mutated gene of the 1 <sup>st</sup> EF-hand of CaM and half CaM, and cloning in pET27b                                | 109 |
| 3.4-5 Purification of 1 <sup>st</sup> EF-hand of CaM and half CaM by Ni-NTA column and size-exclusion chromatography                         | 110 |
| 3.4-6 Circular dichroism (CD) measurements on truncated and full length CaM, both in apo-buffer and upon Ca <sup>2+</sup> binding            | 111 |
| 3.4-7 <i>In vitro</i> transcription-translation reactions, labelling with FIAsH, and purification of ribosome-nascent chain complexes (RNCs) | 113 |
| 3.4-8 Isolation of ribosome-nascent chain complexes (RNCs) by ultracentrifugation: control experiments                                       | 121 |
| 3.5 Time-resolved fluorescence anisotropy of free diffusing ribosome-nascent chain complexes (RNCs) and released polypeptides in solution    | 124 |
| 3.5-1 Time-resolved fluorescence anisotropy of Ribos-(1 <sup>st</sup> EF-hand) and released EF-hand  | 127 |

|   |     |
|---|-----|
| 3.5-2 Time-resolved fluorescence anisotropy of Ribos-(half CaM / N-term.) and released polypeptide                                  | 128 |
| 3.5-3 Time-resolved fluorescence anisotropy of Ribos-(CaM full length) and released CaM   | 130 |
| 3.5-4 Time-resolved fluorescence anisotropy of Ribos-(CaM full length) and released CaM using the control construct with STOP codon | 132 |
| 4. Discussion and Conclusion  | 134 |
| Summary   | 143 |
| Zusammenfassung   | 144 |
| Bibliography  | 146 |
| Erklärung   | 155 |
| Appendix A  | 156 |
| Appendix B  | 158 |

## 1. Introduction

### 1.1 Protein folding

Proteins are required to perform several biochemical functions, ranging from modules of the overall cellular architecture, like tubulin and actin, up to complex molecular machines, such as ribosomes and DNA polymerases. In all cases, it is essential the proteins to adopt a proper structure to carry out their function. Failing to do so may lead to perturbation of the cellular homeostasis [1][2]. Protein misfolding and aggregation is related to several neurodegenerative and brain disorders, such as Alzheimer's, Creutzfeld-Jacob, Parkinson's disease, and Huntington's chorea. A deep insight into the protein folding problem is a holy grail of molecular biology. Therefore, understanding the principles of this basic biological phenomenon will likely lead to long-term benefits to human health, as it would allow structure-based design of novel drugs. It could also facilitate the specific design and engineering of enzymes necessary in biotechnological applications [3][4][5].

Inside a cell, proteins fold during, or immediately after, their synthesis in the ribosomes with the support of auxiliary proteins, called molecular chaperones [6][7]. Nevertheless, the information required the proteins to adopt their native conformation appears to be wholly encoded in the amino acid sequence, since polypeptide chains fold *in vitro* in the absence of any auxiliary factors. Indeed, the capability of self-assembly of proteins has allowed the early biologically-driven chemical processes, and it is believed that the stability of such biological catalysts is crucial for evolution of life [8]. An unbiased search for the most stable conformation would demand a population of all possible conformations a polypeptide chain could adopt, until the state with the lowest energy is attained. As the average size of a protein is 100-300 amino acids, it would need an astronomical amount of time ( $10^{73}$  years) to fold via a random walk through all the possible conformations. This amount of time is much bigger than the biological relevant timescale, known as the Levinthal paradox. However, protein folding lasts only a few microseconds up to seconds, suggesting that there is a pathway of preferential folding events ultimately

leading to the native conformation, which would significantly speed up the whole process [9].

## 1.2 The energy landscape of protein folding

Several models have emerged to explain the existence of folding pathways (Fig. 1.2.1). Let us first go over the case of a polypeptide chain in the unfolded state, where structural elements are completely absent. In this state, there is an ensemble of different conformations characterized by few stabilizing interactions, and thus high conformational entropy and high free energy. Therefore, protein folding involves the reduction of conformational entropy through many weak interactions, like hydrogen bonds, electrostatic or hydrophobic interactions [10][11].

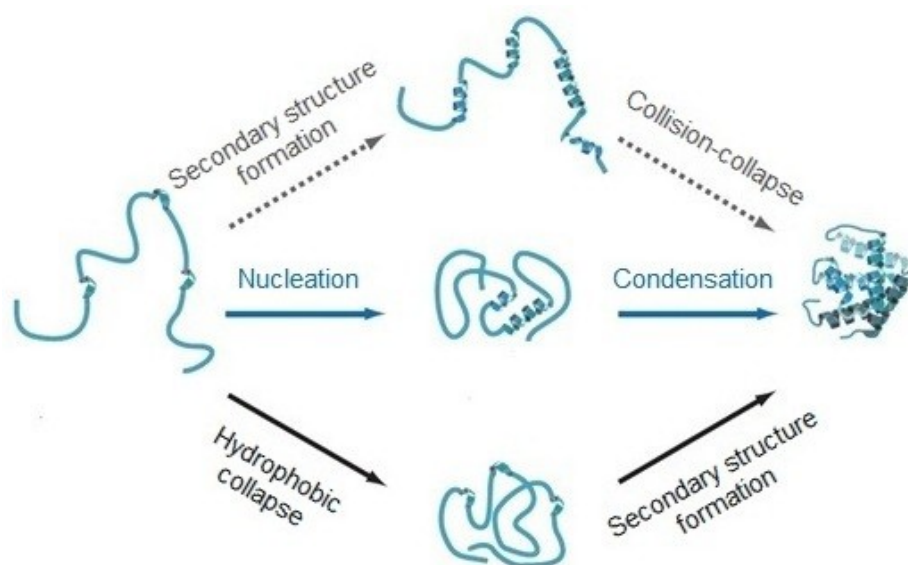


**Fig. 1.2.1.** Different models for protein folding; collision-collapse, nucleation-condensation, and the hydrophobic collapse model [12].

In the nucleation-condensation model, folding initiates locally from several stable nuclei. These nuclei serve as scaffolds that assist the polypeptide in adopting its native conformation, by formation and rearrangement of structural elements [13]. In the collision-collapse model, folding starts with the formation

of secondary structure elements leading to more compact states from which the tertiary structure evolves [10]. A third model, the hydrophobic collapse model, hypothesizes that the polypeptide collapses rapidly around an inner core of hydrophobic side chains and then rearranges to form a globule [11]. A single generic mechanism might not exist in nature, and a polypeptide chain may fold via several pathways [14].

A conceptual mechanism to understand how a protein folds avoiding the Levinthal paradox is the folding funnel, which describes all the possible pathways that lead to the native structure [15][16][17]. In a folding funnel, as shown in Fig. 1.2.2, the unfolded state is the state with the highest free energy and it comprises a heterogeneous ensemble of conformations, representing the starting point of the folding pathway. The fast dynamics and the low conformational restriction that occur allow interactions between different parts of the chain, and energetically favoured native-like contacts can appear. This may cause the formation of hydrophobic clusters which decrease the free energy of the system. Hence, proteins may fold by collapsing and rearranging. From these states, more and more native-like interactions are formed and, finally, the protein folds to its native structure.

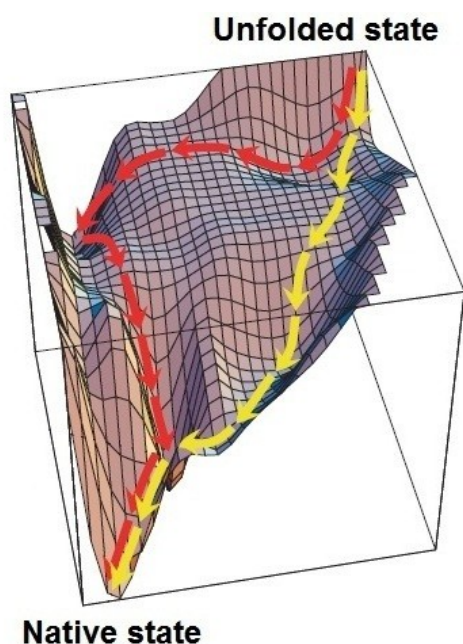


**Fig. 1.2.2.** Energy landscape for protein folding illustrated as a funnel. Proteins fold by collapsing and reconfiguring. Native-like contacts involving neighbouring residues, which lead to the adoption of intermediate conformations, can appear, and different pathways may be followed. After the saddle point is reached, folding quickly occurs downhill [17].

Conformations with increasing amount of stable secondary structure, with turns and helices forming more rapidly than  $\beta$ -sheets, arise. This also requires neighbouring residues to adopt concerted backbone conformations capable of forming hydrogen bonds between the amide and carbonyl groups of the backbone chain [18][19][20]. There can also be stable conformations which adopt an overall three-dimensional shape that closely resembles that one of the native state of the protein [21]. A merely collapsed state with very weak secondary structure, known as “molten globule” might also be observed. On the way to the free energy minimum, intermediate states can also occur. In this case, some interactions have to be broken, which is, in general, a relatively slow step before the protein adopts its native conformation [11]. According to the transition state theory, for a protein to transit from the unfolded state to intermediate states and finally to its native state, an energy barrier,  $\Delta G_F$ , has to be overcome (Fig. 1.2.3) [22].

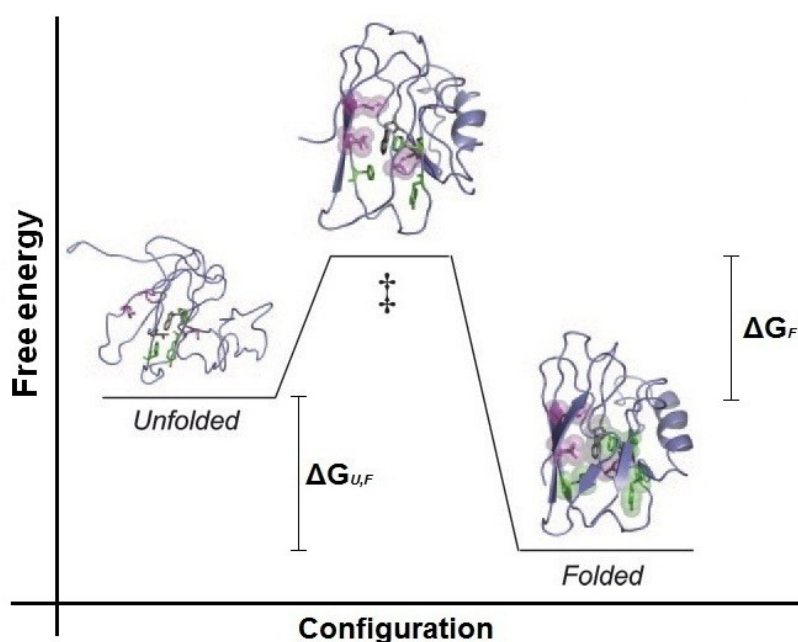


**Fig. 1.2.3.** Transition state theory applied to protein folding. An energy barrier,  $\Delta G_F$ , which represents the kinetic stabilization of the unfolded state, has to be overcome. On the way to the native state, the protein may transit to intermediate states that contain few secondary structure elements [22].

### 1.3 Ribosomes

Ribosomes are cellular particles that catalyze the polymerization of amino acids according to the genetic information encoded in messenger RNA (mRNA), so that proteins are synthesized. Their main function is to ensure the correct decryption of the genetic information as well as the formation of the peptide bond between amino acids. It is also probable that ribosomes are involved in the correct folding of the nascent polypeptide chains. It is constructive to mention what ribosomes are, and to explain how they function, as well.

Ribosomes are RiboNucleoProtein (RNP) complexes, where two-third is ribosomal RNA (rRNA) and one-third are proteins [23]. RNPs comprise two subunits of unequal size, the small and the large subunit. Both subunits are involved in translation of genetic information by stabilizing the interactions between mRNA and tRNA. The large subunit contains the peptidyl-transferase center, which catalyzes the formation of the peptide bond [24]. In prokaryotic cells, the small subunit (30S) consists of one rRNA molecule (16S rRNA) and 21 ribosomal proteins, while the large subunit (50S) consists of two rRNA molecules (23S rRNA and 5S rRNA) and 34 ribosomal proteins [25]. The association of the small with the large subunit leads to the formation of the 70S ribosomal particle (S is equivalent to  $10^{-13}$  sec and it denotes the Svedberg constant, which is the rate of sedimentation during centrifugation). The 50S subunit is almost spherical with a diameter of 200-250 Å (Fig 1.3.1). There are three protuberances located at the area which is involved in the association with the small subunit (Fig 1.3.2, A). The 'Central protuberance' is the head of the 50S subunit, while the shape of the lateral ones is less wide. One of them is called 'L7/L12 stalk', because it contains the L7/L12 complex; L7 and L12 are identical with the exception of the N-terminal serine in L7 which is acetylated. The other protuberance is called 'L1 stalk' because it contains the L1 ribosomal protein [26]. The 30S subunit is an asymmetric particle with a diameter of 230 Å. It consists of two major areas, the 'Head' which is  $\frac{1}{3}$  of the subunit, and the 'Body' which is connected to the head by the so-called 'Neck'. The body comprises some additional structural motifs.

These are the protruding 'Platform', the 'Shoulder' and the 'Bottom or Spur' (Fig 1.3.2, B) [27].

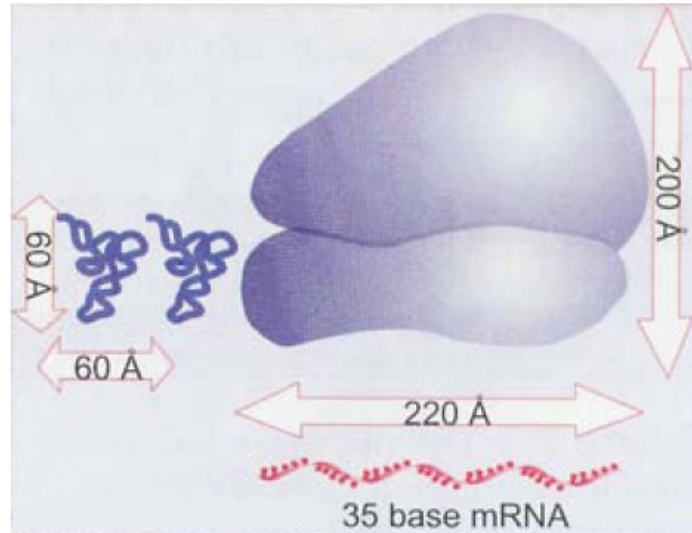


**Fig. 1.3.1.** Size comparisons show that the ribosome is large enough to bind tRNAs and mRNA [25].

Most of the ribosomal proteins comprise a lot of lysines and arginines, and for that reason they are basic proteins with an isoelectric point between 8.5 and 10. Another important feature is that the ribosomal proteins contribute to the stabilization of the structure of the ribosome by electrostatic interactions between the positively charged basic proteins and the negative charge of the phosphate groups of the rRNA [28]. The secondary structure of the ribosomal rRNA is also stabilized by the presence of  $Mg^{2+}$  as well as by hydrogen bonds between bases of the rRNA [29]. In addition, most of the proteins are located at the periphery of the ribosome with some of their side chains orientated outwards, so that other non-ribosomal factors, which are necessary for the translation, can be effectively attached to the ribosome [25].

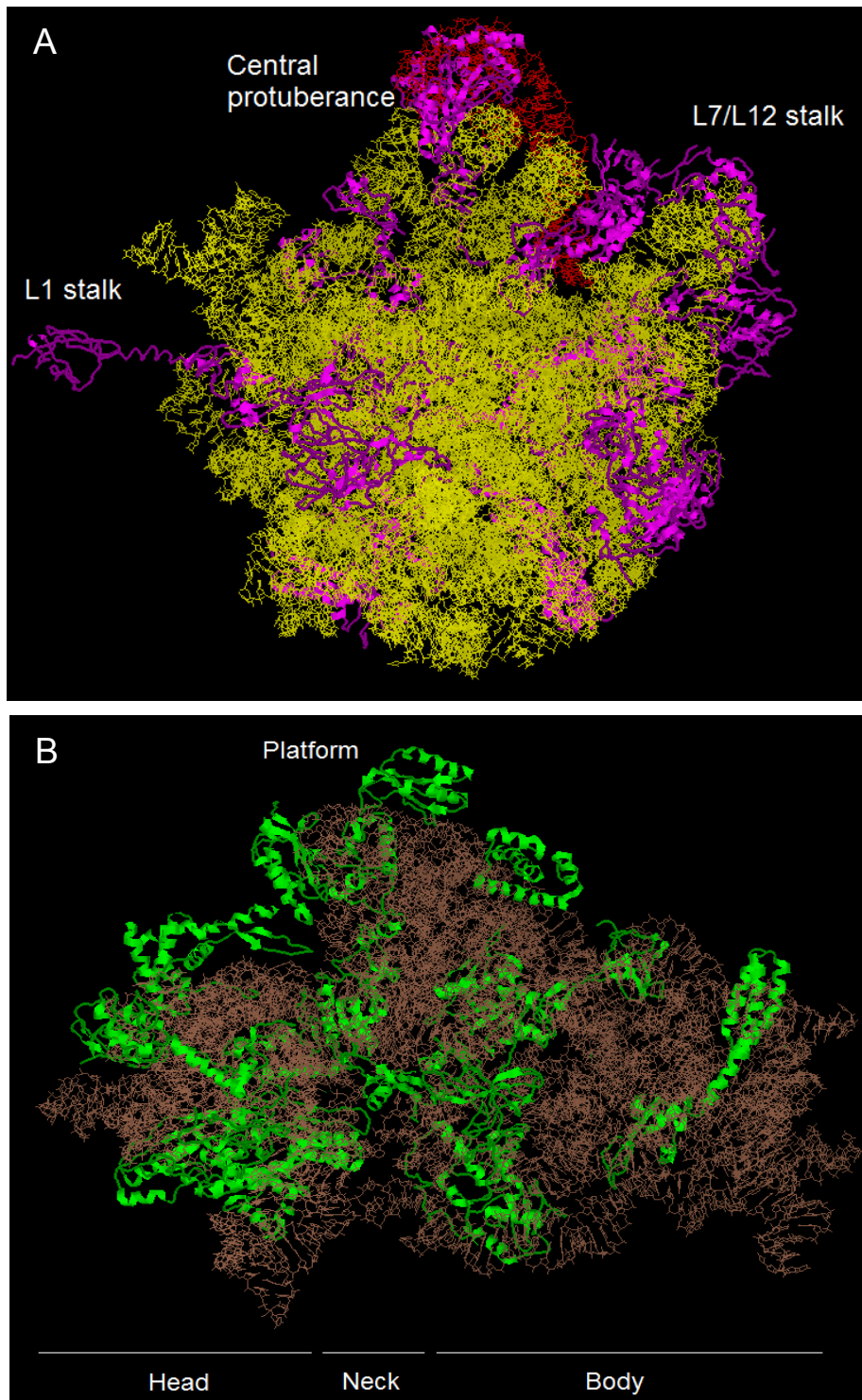


**Fig. 1.3.2.** (A) The 50S subunit has a central protuberance, where 5S rRNA (in red) is located, separated by a notch from a stalk of L7 copies. The 23S rRNA is shown in yellow and the ribosomal proteins in magenta. (B) The 30S subunit has a head separated from the body by a neck. The 16S rRNA is shown in brown and the ribosomal proteins in green [25].

### 1.3-1 Ribosomal function

The ribosome reads triplets of ribonucleotides in mRNA and translates them to the corresponding amino acids comprising a protein. In prokaryotic ribosomes, there are three tRNA-binding sites necessary for translation. These are the A-site, where the aminoacyl-tRNA is attached, the P-site, where the peptidyl-tRNA with the nascent chain is transferred during the elongation, and finally the E-site, which is the exit of the tRNA that does not carry any amino acid (Fig. 1.3-1.1) [30]. During translation, three stages can be distinguished, the initiation, elongation and termination.

Herein, it should be mentioned that mRNA molecules in prokaryotic cells are usually polycistronic, where a single mRNA molecule might carry more than two transcribed genes. One or more different genes in the same mRNA might be translated by different ribosomes at the same time. The complex that is formed is called polysome. But there is also the possibility that the same ribosome initiates the translation of the gene downstream. Ribosomes in prokaryotes may also start the translation before a gene or an operon in DNA is fully transcribed to mRNA [25].

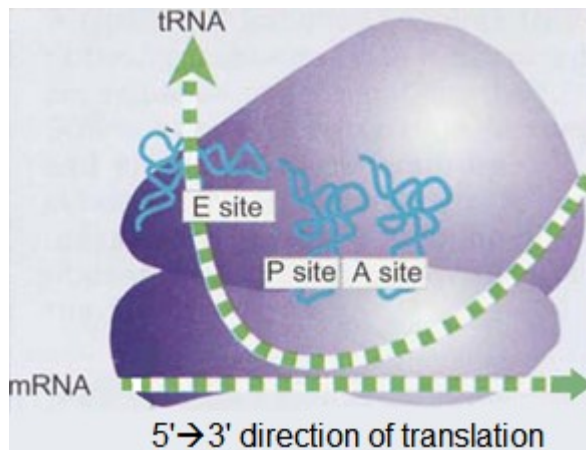


**Fig. 1.3-1.1.** tRNA molecules move through the ribosome during translation from A-site to E-site [25].

### Initiation

Protein synthesis usually starts after recognition of the first AUG codon (initiation codon), which corresponds to the amino acid methionine. In prokaryotic cells, there is a purine-rich sequence (6-10 nucleotides) upstream

the coding region, called Shine-Dalgarno (SD) sequence. The SD sequence is complementary to a region near the 3'-end of the 16S rRNA of the small subunit and it contributes to the stabilization of the initiation complex [31]. The initiation complex consists of the mRNA, the small subunit (30S), the initiator tRNA and the initiation factors (IF). There are three initiation factors in bacteria, IF1, IF2 and IF3 [32].

In the beginning, IF1 binds to the A-site of the 30S subunit, and it also induces the binding of IF3 to the E-site of the 30S subunit. In this way the association of the two subunits is hindered [33][34]. Then, mRNA is bound through interactions between SD sequence and its complementary in 16S rRNA, so that the initiation codon is in the P-site. The attachment of mRNA is also assisted by IF3. Subsequently, IF2 recognizes and brings the tRNA, which carries the formylated form of methionine (fMet-tRNA<sup>Met</sup>), to the P-site. IF2 together with IF3 stabilize the binding of the tRNA to the AUG codon in the P-site by codon-anticodon interactions [35]. After that, IF1 and IF3 dissociate from the 30S subunit, and IF2 induces the association of 50S subunit with the 30S. IF2 is a monomeric G-protein, which is dissociated from the ribosome by hydrolysis of its GTP to GDP and Pi after the attachment of the 50S subunit [36]. At the end of this stage, a complex comprising the 70S ribosome, the fMet-tRNA<sup>Met</sup> and the mRNA is formed (Fig. 1.3-1.2).

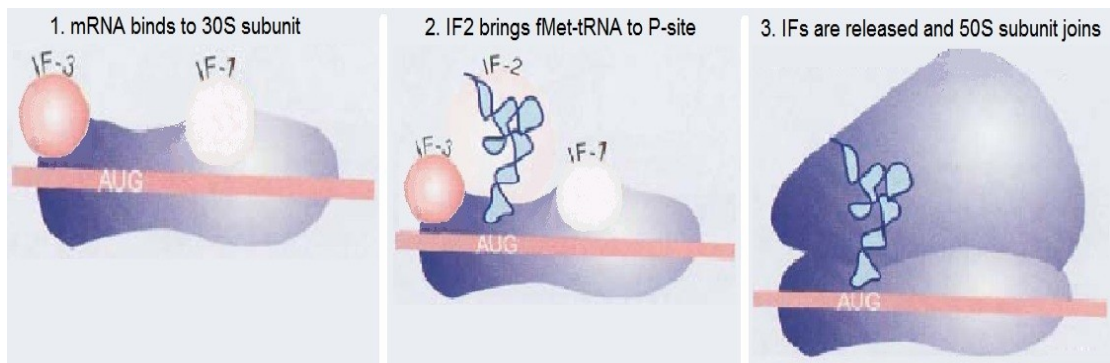


**Fig. 1.3-1.2.** Initiation factors bind to free 30S subunits and bring initiator tRNA to the 30S-mRNA complex [25].

### Elongation

The elongation is the process where each time a new amino acid is added to the nascent chain. In prokaryotic cells, there are two monomeric G-proteins called elongation factors (EF), these are the EF-Tu and EF-G. Three steps can be distinguished (Fig. 1.3-1.3).

The first step begins with the entry of an aminoacyl-tRNA (aa-tRNA) in A-site. To be accomplished, a complex between the GTP-form of EF-Tu and one aa-tRNA is formed, which enters the A-site. In this way, EF-Tu brings one amino acid to the A-site. Only if the correct aa-tRNA has been inserted into the A-site, the affinity for that tRNA increases and EF-Tu can hydrolyze its GTP to GDP and Pi [37]. The GDP-form of EF-Tu has low affinity for the ribosome and it is dissociated. There is another factor, called EF-Ts, which changes the GDP on EF-Tu with another GTP, and now EF-Tu is able to bind another aa-tRNA [25].

The second step involves the peptide bond formation, which is catalyzed at the peptidyl-transferase center (PTC) of 50S subunit. The amino group (-NH<sub>2</sub>) of the amino acid on aa-tRNA in A-site reacts with the carbonyl group (-C=O) of the peptide on peptidyl-tRNA in P-site, leading to peptide bond formation. The peptide chain is transferred to the tRNA in A-site. In the end, there is a peptidyl-tRNA elongated by one amino acid in A-site and one deacylated-tRNA in P-site [25]. After peptide bond formation between initiator methionine and second amino acid, the interactions between SD sequence and 16S rRNA become weaker. Probably, this is absolutely necessary for ribosome movement along the mRNA [38].

In the third step, the translocation occurs where the ribosome moves one codon. This process is catalyzed by elongation factor EF-G. The GTP-form of EF-G binds to A-site and moves mRNA and the two tRNAs in A- and P-site three nucleotides ahead [39]. Therefore, the peptidyl-tRNA is now in P-site, the deacylated-tRNA leaves via E-site and A-site is empty, so that a new elongation cycle can start. Then, EF-G hydrolyzes the GTP to GDP and Pi, and it is dissociated from the ribosome [25].

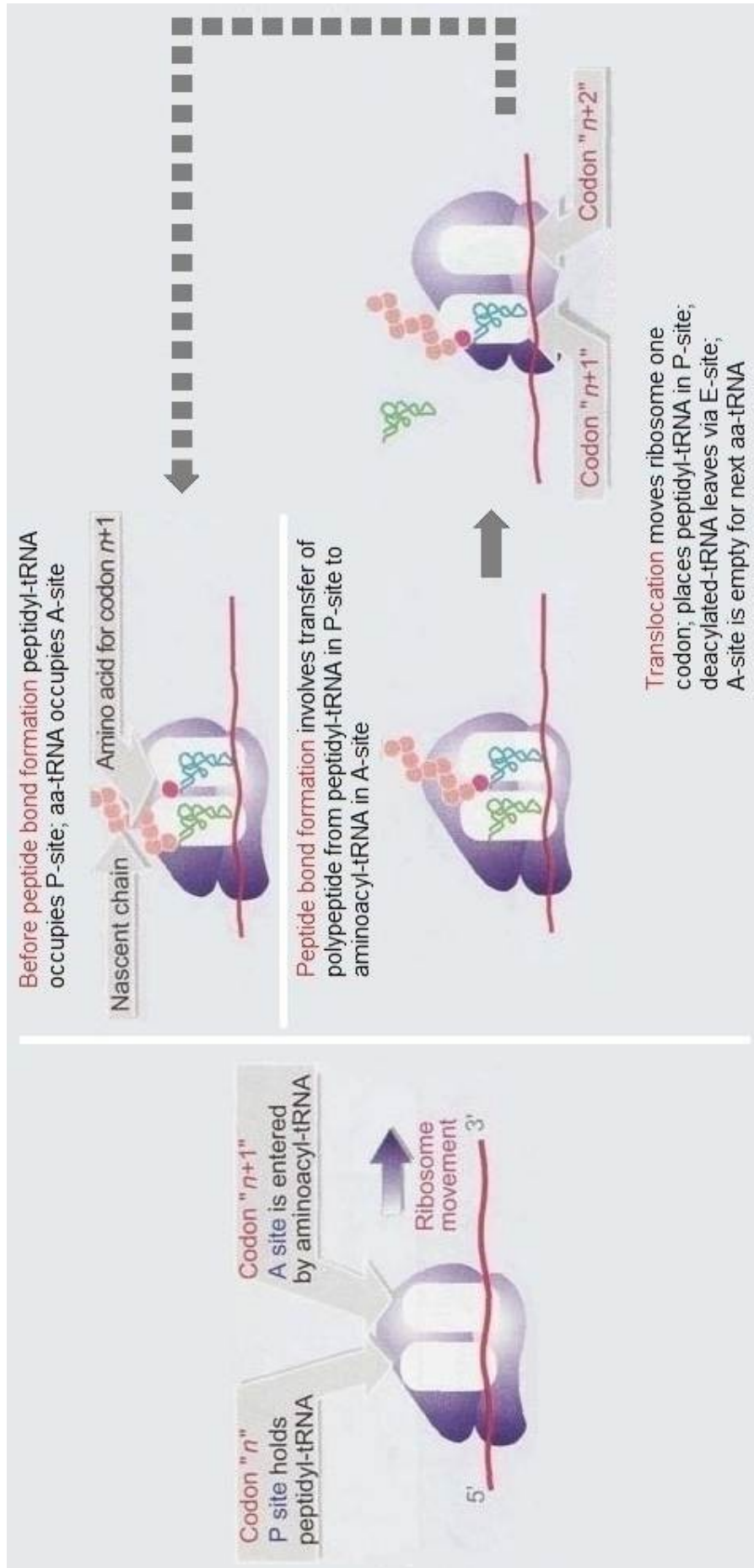


Fig. 1.3-1.3. The ribosome has two sites for binding charged tRNAs [25].

An allosteric A-E-site model has been proposed. The most important characteristic of this model is that A-site and E-site influence each other through 'negative allostery' [40]. This means that attachment of a trimeric complex in A-site decreases the affinity of E-site for deacylated-tRNAs, and vice versa [41]. In the beginning, the A-site has low affinity for trimeric complex because E-site is occupied. First, it is confirmed that the correct aa-tRNA has entered the A-site. After that, the affinity of A-site for aa-tRNA increases resulting to a reduction in the affinity of E-site for deacylated-tRNA. Finally, the deacylated-tRNA is released from the ribosome [42].

## Termination

The elongation of the polypeptide chain usually stops when a stop codon (UGA, UAA, or UAG) appears in A-site. These triplets are recognized not by tRNAs, but by proteins called release factors (RF). There are two types of release factors. In prokaryotic cells, RF1 and RF2 belong to type I, and RF3 belongs to type II. They recognize the stop codons and catalyze the hydrolysis of the ester bond between polypeptide chain and tRNA. The UAA and UAG codons are recognized by RF1, while UAA and UGA are recognized by RF2. The release factor RF3 hydrolyzes GTP and dissociates RF1 and RF2 from the ribosome [25][43].

The nascent chain exits the ribosome through an exit tunnel that occurs in the large subunit. After termination and release of nascent chain, there is still a deacylated-tRNA in P-site, and the mRNA is still attached to the ribosome. The ribosome recycling factor (RRF) enters A-site and EF-G moves RRF from A-site to P-site and deacylated-tRNA from P-site to E-site. It seems that the role of RRF and EF-G in this stage is to move deacylated-tRNA from P-site to E-site [44][45]. It is the initiation factor IF3 that dissociates the two ribosomal subunits and it does not allow them to reassociate till another SD sequence is recognized by 30S subunit, and a new initiation complex is formed [25][46].

## 1.4 Protein folding in the cell

In the cellular environment, protein folding starts co-translationally, mainly due to the slow rate of protein synthesis (~20 amino acids per second in bacteria). Molecular chaperones (Fig. 1.4.1) are those auxiliary proteins that bind to hydrophobic areas of newly synthesized polypeptides, preventing them from being exposed and interacting non-specifically with other proteins of the cytosol. In this way, protein aggregation due to macromolecular crowding is avoided [47]. Many cytosolic chaperones belong to the family of heat-shock proteins (HSPs), like HSP60s (GroEL-GroES), HSP70s, HSP90s. Another important family is the foldases, e.g. peptidyl-prolyl *cis-trans* isomerases [48].

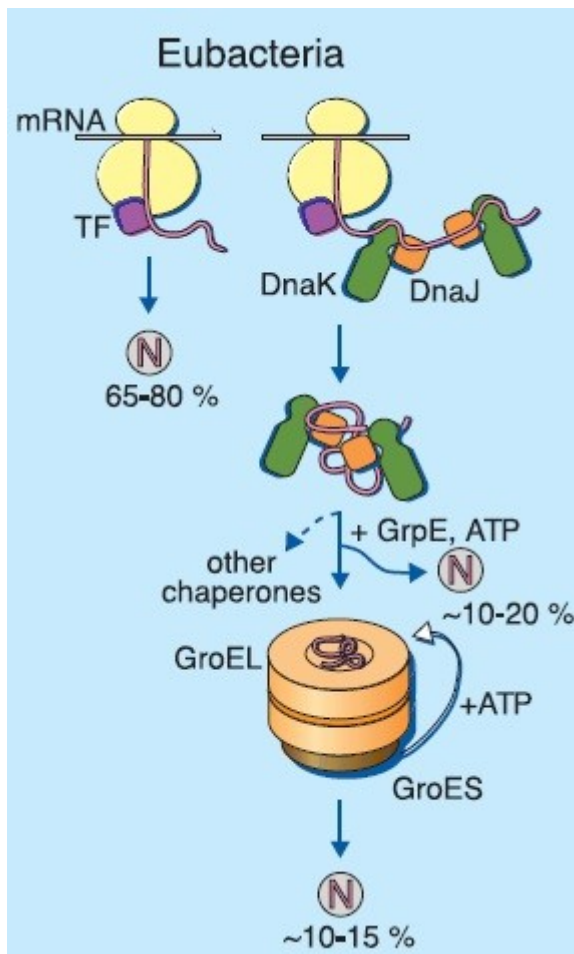


**Fig. 1.4.1.** Protein folding in bacteria is assisted by molecular chaperones. Emerging nascent chains associate with trigger factor (TF). Larger proteins interact with DnaK-DnaJ system subsequently to TF, or with GroEL-GroES chaperonins after they have been released from the ribosome. N: native conformation [47].

High resolution structural studies on bacterial chaperones provided valuable information about the mechanism of protein folding *in vivo*, but mammalian systems are homologous and very likely to behave in a similar way [48]. As mentioned, the speed of protein synthesis in bacteria is 20 amino acids per second, and the nascent polypeptide chain leaves the ribosome through an 80-100 Å exit tunnel located in the large subunit. This hollow cage can accommodate up to 35 amino acids, but its narrow diameter of 10-20 Å impedes folding. The ribosome-associated chaperone trigger factor (TF) is recruited at the end of the ribosomal tunnel (Fig. 1.4.2). TF is a 48 kDa protein which binds to emerging hydrophobic stretches providing a molecular cradle for nascent chains, so that non-specific hydrophobic interactions are not allowed. The affinity of TF for hydrophobic residues becomes weak as nascent chains fold and such residues are buried, leading to its dissociation from the polypeptide chain [49][50].

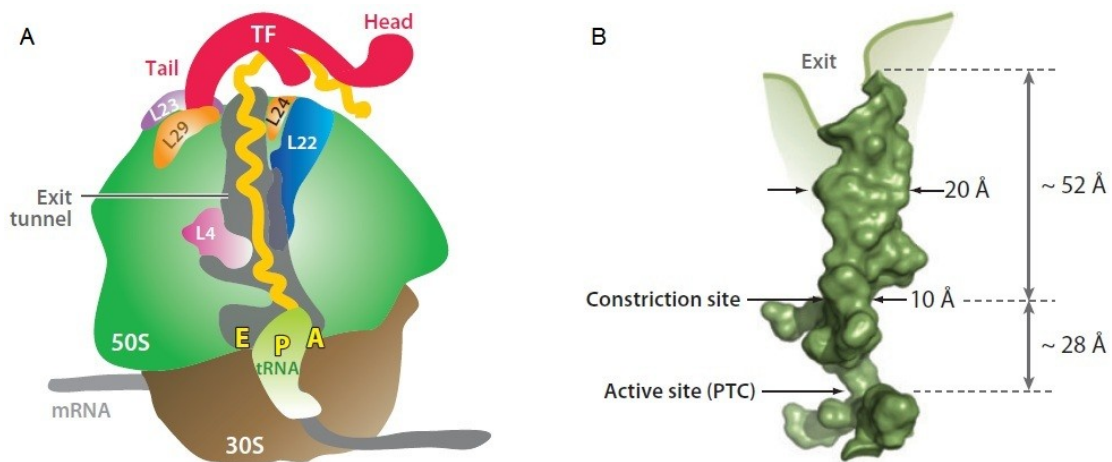


**Fig. 1.4.2.** (A) Schematic representation of a vertical section of the 70S prokaryotic ribosome highlighting the ribosomal proteins facing or near the exit tunnel and the ribosome-associated TF chaperone. A hypothetical nascent polypeptide chain is drawn in yellow. (B) Structure of the ribosomal exit tunnel. Abbreviations: PTC, peptidyl transferase centre, TF, trigger factor [12].

Two other systems also assist folding process, the DnaK-DnaJ chaperone complex (HSP70 family) and GroEL-GroES chaperonins (HSP60 family). Contrary to TF, these two systems require ATP and co-chaperones. DnaK preferentially associates with nascent chains larger than 20-30 kDa, and thus it acts subsequently to TF. It has been suggested that DnaK also facilitates the post-translational folding of multi-domain proteins through binding and release cycles [51]. Polypeptides up to 60 kDa with non-native structure can be encapsulated and are free to fold in the GroEL-GroES cage (also termed 'Anfinsen cage') [47].

In a living cell, a nascent polypeptide chain can fold co-translationally on the ribosome, domain by domain. Attempts to refold proteins *in vitro* seems to be successful only for small to medium-size proteins, while large multi-domain proteins often aggregate, mainly due to intra- and inter-molecular interactions [52]. Co-translational and sequential folding, i.e. the folding of one domain well-before another one is synthesized, avoids this problem [53]. In some cases, pausing during mRNA translation plays some role in ensuring proper folding of newly synthesized sections of a polypeptide chain. Such pausing occurs when rare triplets are encountered, as it takes additional time for the corresponding rare species of tRNA to be delivered [54]. It is believed that some amino acids and the residues downstream to them can determine which conformation will be adopted, which points out that *in vivo* the folding of a protein is exclusively dictated by the amino acid code of the polypeptide chain [55]. It is also shown that misfolding and aggregation of large multi-domain proteins in the cell decreases with markedly decreasing sequence identity [56]. The presence of additional domains can have significant impact on the folding of the protein. First, it is probable that each domain folds independent of the other ones. Second, the native conformation can be stabilized through inter-domain interactions. Third, the folding of one domain may precipitate the folding of an adjacent one. A 'hinge' region between two adjacent domains undertakes a key role. Large flexible linkers allow for independent domain folding, while small ones can result to many inter-domain interactions at the interface between those domains through a sequential folding mechanism [57][58]. All in all, chaperones foster the overall efficiency of the process by reducing the probability of competing reactions, particularly aggregation [59].

In addition, confinement in the chaperone cage may smooth the energy landscape of folding, either by preventing the formation of kinetically trapped intermediates or by facilitating their progression towards the native state (Fig. 1.4.3) [47].

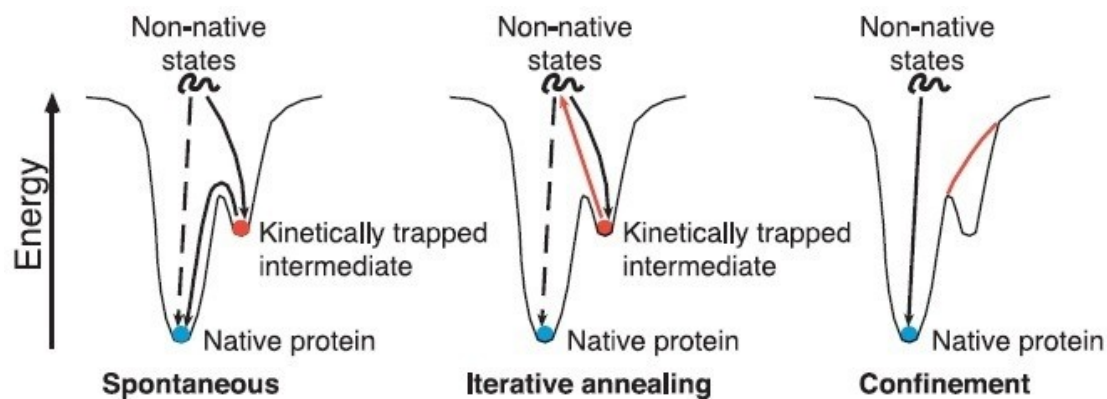


**Fig. 1.4.3.** Mechanisms of accelerated folding. Left: A protein that forms a kinetically trapped intermediate during spontaneous folding. Middle: In the iterative annealing model, this intermediate is thought to be actively unfolded by GroEL-GroES and allowed to reconfigure. Right: Confinement of non-native protein in the narrow, hydrophilic environment of the GroEL-GroES cage is suggested to result in a smoothing of the energy landscape, so that the formation of certain trapped intermediates is avoided [47].

## 1.5 Calmodulin (CaM): a pivotal calcium sensor in eukaryotes

The complexity of intermolecular communication increases with the complexity of the organism, however, it does not seem that there is a parallel increase in the number of the cellular regulators. Hormones, cyclic nucleotides, and calcium ions are the three most important groups of regulators or messengers in mammalian cells. Their activities are inter-related, that means the metabolism of one can influence the biochemical effect of the others. Calcium ions influence many biological processes, such as cell motility, muscle contraction, chromosome movement, neurotransmitter

release, endocytosis, and exocytosis. The relation between metabolism and function of cyclic nucleotides and  $\text{Ca}^{2+}$  is widely recognized. Evidence acquired suggests that Calmodulin (CaM), a multifunctional  $\text{Ca}^{2+}$ -dependent modulator protein, is a primary receptor of this important bivalent cation. The viewpoint that CaM is both a mediator of  $\text{Ca}^{2+}$  functions and a regulator of  $\text{Ca}^{2+}$ -dependent adenylate cyclase and phosphodiesterase provides a link between these two classes of regulators [60].

Transient  $\text{Ca}^{2+}$  elevations are sensed by several  $\text{Ca}^{2+}$ -binding proteins, which usually contain the 'EF-hand' motif(s), a helix-loop-helix structure. There are three major classes of EF-hand  $\text{Ca}^{2+}$  sensors; these are Calmodulin (CaM), Calcium-dependent protein kinase (CDPK), and Calcineurin B-like protein (CBL) [61]. In this study, we exploited CaM bovine as a protein model to achieve our objectives because it is a water-soluble small protein (17 kDa) comprising two globules linked by a 'hinge' region, and it can be overexpressed in bacteria, as well. Therefore, this section will focus on the characterization of CaM.

CaM is a small acidic protein present in all eukaryotes, containing around 150 amino acids, with isoelectric point (pI) around 4. It participates in signaling pathways that regulate many crucial processes such as growth, proliferation and movement (Fig. 1.5.1). Recent studies of CaM showed that it is found throughout the cytosol and nucleus in HeLa cells, while it is concentrated around the mitotic apparatus in cells during mitosis. Other studies on unstimulated smooth-muscle cells showed that most CaM molecules are bound, probably to  $\text{Ca}^{2+}$ -independent binding proteins, at resting concentrations of free  $\text{Ca}^{2+}$ . The synchronization between CaM function and  $\text{Ca}^{2+}$  signals is also being explored. A direct relationship between the increase in the levels of intracellular free  $\text{Ca}^{2+}$  and the  $\text{Ca}^{2+}$ -dependent activation of CaM was first observed during a response to wound healing in fibroblasts. It has been found that the  $\text{Ca}^{2+}$ -dependent activation of CaM exhibits a heterogenous distribution pattern in the cells, indicating the presence of distinct populations of CaM. Some classes of proteins might anchor CaM to specific cellular locations, depending on the stability of particular CaM-effector complex in the absence or presence of a  $\text{Ca}^{2+}$  signal. These studies point out

how important the temporal and spatial relation between  $\text{Ca}^{2+}$  signals and CaM function is [61][62].

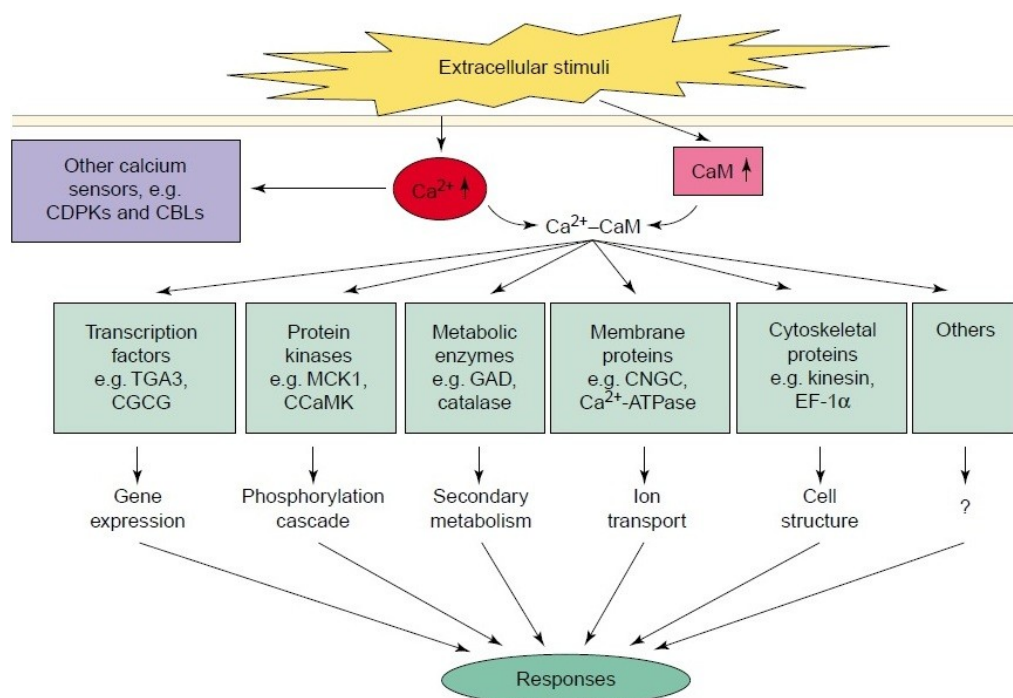


**Fig. 1.5.1.** Model of  $\text{Ca}^{2+}$ /CaM mediated signaling network [61].

The four EF-hand  $\text{Ca}^{2+}$ -binding domains occur in pairs embedded within two adjacent globular regions, noted as N-terminal and the C-terminal regions separated by a flexible linker forming a dumbbell-like structure. It seems that the hydrophobic regions of CaM that are exposed due to the conformational change upon  $\text{Ca}^{2+}$  binding are responsible for its ability to regulate the target enzyme activity. However, electrostatic interactions may also play a role [61]. In the absence of  $\text{Ca}^{2+}$ , CaM adopts a 'semiopen' conformation in which a partially exposed hydrophobic area is accessible to solvent. This might allow CaM to interact with some target proteins at resting levels of intracellular free  $\text{Ca}^{2+}$ . Once there is transient rise in  $\text{Ca}^{2+}$ , the  $\text{Ca}^{2+}$  ion is coordinated in each  $\text{Ca}^{2+}$ -binding loop of CaM by the electronegative charge of, primarily, carboxylate ligands. The binding of  $\text{Ca}^{2+}$  leads to substantial alterations in the inter-helical angles within the EF hands in each globular region resulting in production of more 'open' conformations. These structural rearrangements in CaM result in the concerted exposure of hydrophobic groups in a methionine-

rich cleft of each globule that is distinct from the  $\text{Ca}^{2+}$ -binding loops (Fig. 1.5.2). The  $\text{Ca}^{2+}$ -controlled exposure of hydrophobic groups in the two globules of CaM releases a considerable amount of biochemical energy, which is transduced into two separable effects: a change in the affinity of CaM for the effector and/or an alteration in the effector's function.  $\text{Ca}^{2+}$ -sensor proteins are characterized by their capacity to convert the  $\text{Ca}^{2+}$ -binding event into biochemical energy. This is also the basis of their ability to transduce  $\text{Ca}^{2+}$  signals [62].

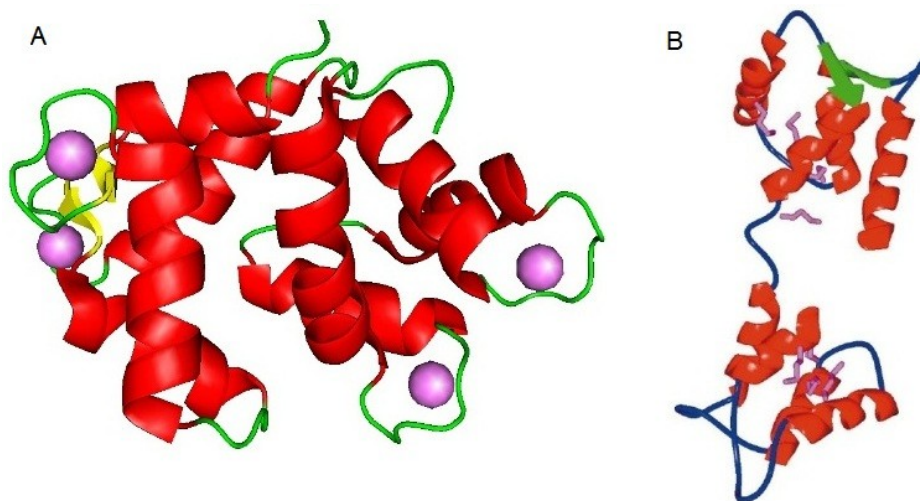


**Fig 1.5.2.** (A) Crystal structure of CaM bovine (PDB: 1PRW) with  $\text{Ca}^{2+}$  (in violet) bound to the loops of the EF-hands. (B) Methionine side chains are shown in purple to denote the location of potential hydrophobic pockets.  $\text{Ca}^{2+}$  binding produces large conformational changes in the helices, resulting in the exposure of several hydrophobic residues [62].

In contrast to CaM, whose amino acid sequence shows remarkable conservation, CaM-binding domains in target proteins exhibit sequence variability reflecting the flexibility of CaM regulation. CaM-binding domains are usually stretches of 16-35 residues forming basic amphiphilic helices. One activation mechanism is relieving autoinhibition. Upon  $\text{Ca}^{2+}$  binding, CaM exposes its hydrophobic regions that are able to accommodate the amphiphilic helix and to displace it from the active site of the target enzyme allowing full enzymatic activity. Another possible mechanism is active site remodeling,

where the rotation of a helical domain away from the catalytic core leads to enzyme activation (Fig 1.5.3) [61].

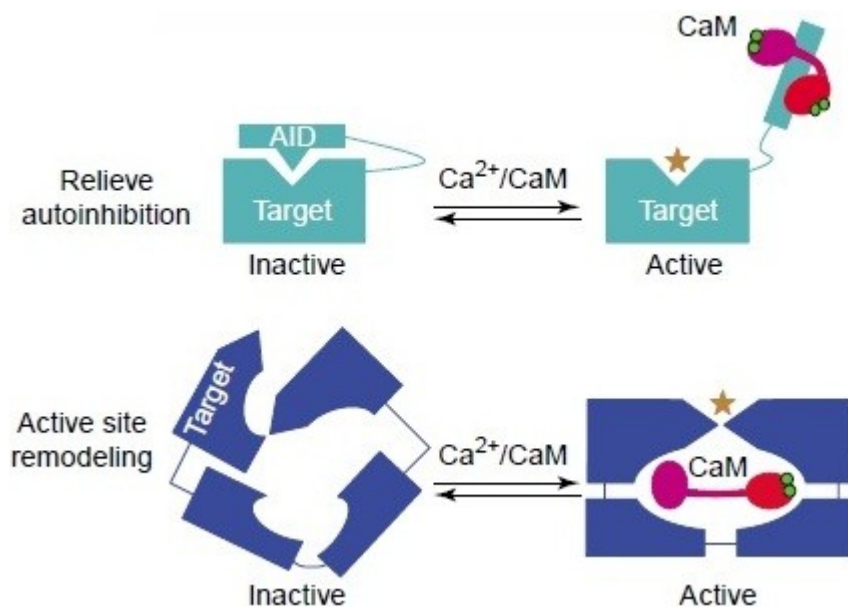


**Fig. 1.5.3.** Probable activation mechanisms of CaM [61].

Till now it was alleged that CaM functions as a  $\text{Ca}^{2+}$  sensor; it binds  $\text{Ca}^{2+}$  and activates other protein targets. An investigation on CaM showed that CaM can also work in a  $\text{Ca}^{2+}$ -independent manner. The function that is required for growth and division of yeast cells apparently does not require the ability to bind  $\text{Ca}^{2+}$ . So, the essential role of CaM is not to act as a  $\text{Ca}^{2+}$  receptor, but rather to perform a  $\text{Ca}^{2+}$ -independent function. It has been demonstrated that the ability of CaM to bind to the mitotic apparatus is not dependent on the presence of  $\text{Ca}^{2+}$ , which might suggest that CaM is an essential component of the mitotic apparatus. Whether or not CaM performs the same  $\text{Ca}^{2+}$ -independent function in higher eukaryotes is unknown. Nevertheless, it is known that in higher eukaryotes, in the absence of  $\text{Ca}^{2+}$ , CaM binds to neuromodulin, an abundant neuronal protein associated with neuronal growth and neurite extension [63].

## 1.6 Aim of the PhD dissertation

In this study, we took advantage of the ability of the biarsenical ligand FIAsh (Fluorescein Arsenical Helix Binder) to be rigidly attached to tetra-Cys motifs within a larger segment of a protein. For this reason, the orientation of the fluorophore is expected to follow the overall rotation of the protein or the segmental motion. If a dye (FIAsh) is rigidly bound to its target, this will have an impact on the anisotropy of the fluorescence of the measured dye, since the average angular displacement of a dye, which occurs between absorption and fluorescence emission, reflects the mobility of the fluorophore as well as that one of the protein molecule. To be more specific, we explored the possibility to use FIAsh as a dye probe to follow the folding of a protein. One of the questions was whether rigid attachment provides an advantage over single covalent bond attachment. First, we wanted to measure the rotational correlation time of overall tumbling motion of CaM as well as to detect conformational dynamics by time-resolved fluorescence anisotropy measurements. Second, we attempted to detect changes in the size of CaM when it is unfolded, and when  $\text{Ca}^{2+}$  is bound, as well. Third, there is the question whether a nascent chain that emerges from the ribosome can fold during its synthesis, or whether folding occurs only after release from the ribosome. Therefore, our major objective was to study folding of nascent chains, and released polypeptides, as well. We wanted to detect the increase in the size of a nascent chain of different lengths emerging from the ribosomal tunnel as well as changes in the anisotropy of the fluorescence when the nascent chain is released. Mathematical models were applied to describe the structural properties of the polypeptides. Our ultimate goal is to study folding of a nascent chain while it is synthesized by the ribosome. By measuring changes in the anisotropy, one should be able to detect folding/unfolding transitions of the protein.

## 2. Materials and Methods

### 2.1 Materials

#### 2.1-1 Instruments

##### **Confocal setup**

Microtime 200 (Picoquant, Berlin, Germany)

- Inverted microscope Olympus IX-81 (Olympus, Hamburg, Germany)
- Objective: UPLSAPO 60x PlanApochromat, NA 1.2, water immersion (Olympus, Hamburg, Germany)
- Multichannel Picosecond Laser Diode Driver "Sepia II" (Picoquant, Berlin, Germany)
- Picosecond Laser Diode Heads: LDH-P-C-470B (470nm), LDH-P-C-640B (640nm) (PicoQuant, Berlin, Germany)
- Major Dichroic: Fitc/Cy5 dual band (AHF, Tübingen, Germany)
- Polarizing Beam Splitter cube (Linos Photonics, Göttingen, Germany)
- 50/50 beam-splitter (Linos Photonics, Göttingen, Germany)
- Pinhole: 100  $\mu\text{m}$ ; Dichroic mirror: 600dcr (Chroma Technology, Bellows Falls, VT, USA)
- Emission Filters: FF01-520/35, (AHF, Tübingen, Germany); HQ690/70M, (Chroma Technology, Bellows Falls, VT, USA)
- Photon Counting Module  $\tau$ -SPAD: VLoK silicon avalanche photodiode (Laser Components, Olching, Germany) with quenching electronics (Picoquant, Berlin, Germany)  
Avalanche Photon Diodes SPCM-AQR-14, SPDM CD337H (Perkin Elmer, Woodbridge, Ontario, Canada)
- Time-Correlated Single-Photon Counting card: HydraHarp 400 (Picoquant, Berlin, Germany)

The hardware was operated with software Symphotime 5.2 (Picoquant, Berlin, Germany).

**Absorption spectrometer**

UV 2101 PC Spectrophotometer (Shimadzu, Duisburg, Germany)

**Fluorescence spectrometer**

Spectrofluorometer QM-7 (Photon Technology International, NJ, USA)

**Circular dichroism spectrometer**

Spectropolarimeter J-810 (Jasco, Gross Umstadt, Germany)

**PCR thermocycler**

PTC-200 Peltier Thermal Cycler (MJ Research, MA, USA)

**DNA-sequencer**

Long Read/IR 4200 (MWG Biotech, Ebersberg, Germany)

**Plasma cleaner**

Electronic Diener ZEPTO (Diener Electronic GmbH, Ebhausen, Germany)

2.1-2 Competent cells

The following *Escherichia coli* strains were used in the present work.

- BL21 DE3 (Invitrogen, Carlsbad, California, USA)  
(courtesy by Dr. Filippos Peidis, Laboratory of Biochemistry, Aristotle University of Thessaloniki, Greece)
- Top10 (Invitrogen, Carlsbad, California, USA)  
F- *mcrA*  $\Delta(mrr-hsdRMS-mcrBC)$   $\phi80/lacZ\Delta M15$   $\Delta lacX74$  *recA1*  
*araD139*  $\Delta(araleu)$  7697 *galU galK rpsL endA1 nupG*, AmpR, TetR

2.1-3 Vectors and oligonucleotides

The following plasmids were used in the present work:

- pET11a carrying the gene of Calmodulin bovine wild-type

(courtesy by Prof. Dr. Arnd Baumann, ICS-4: Cellular Biophysics, Forschungszentrum Jülich, Germany)

- pET27b (Novagen, Merck, Darmstadt, Germany)
- pBLUNT (Invitrogen, Carlsbad, California, USA)
- pRSET (Invitrogen, Carlsbad, California, USA)

Oligonucleotides were purchased from Eurofins MWG, Ebersberg, Germany.

### 2.1-4 Kits and enzymes

- Zero Blunt Cloning Kit (Invitrogen, Carlsbad, CA, USA)
- Rapid Ligation Kit containing T4-Ligase (Fermentas, St. Leon-Rot, Germany)
- Nucleospin Plasmid (Macherey-Nagel, Düren, Germany)
- QIAprep Spin Miniprep Kit (Qiagen, Hilden Germany)
- PURE *in vitro* transcription-translation system (New England Biolabs, Ipswich, MA, USA)
- Restriction Enzymes were purchased as “Fast Digest” from Fermentas, St. Leon-Rot, Germany
  - NdeI, XhoI, HindIII
- Antarctic Phosphatase and the corresponding buffer were purchased from New England Biolabs, Ipswich, MA, USA.
- Phusion Hot Start DNA-polymerase (New England Biolabs, Ipswich, MA, USA)

### 2.1-5 Chemicals and other consumables

If not stated otherwise, all chemicals used in the present work were of the analytical grade and purchased from Sigma-Aldrich, St. Louis, Missouri, USA:

Alexa488-maleimide, FIAsh-EDT<sub>2</sub> (Invitrogen, Carlsbad, CA, USA)

Ammonium acetate

Ampicillin (Roth, Karlsruhe, Germany)  
Calcium chloride  
Calmodulin, Bovine Brain, High Purity, 1 mg (EMD Biosciences, CA, USA)  
Coomassie Brilliant Blue (Serva, Heidelberg, Germany)  
Ethanol, HPLC grade (Applichem, Darmstadt, Germany)  
Ethylene-diamine-tetra-acetic acid (EDTA), disodium salt  
EGTA, disodium salt  
Guanidine hydrochloride 99.9%  
Imidazole  
Isopropyl  $\beta$ -D-1-thiogalactopyranoside (IPTG)  
Kanamycin (Applichem, Darmstadt, Germany)  
Magnesium acetate  
3-N-[Morpholino]-propansulfonic acid (Applichem, Darmstadt, Germany)  
Sephadex G 25, PD-10 Columns (GE-Healthcare, Upsala, Sweden)  
Sephadex G 25, Column Material (GE Healthcare, Upsala, Sweden)  
Sephadex G 75, Column Material (GE Healthcare, Upsala, Sweden)  
Sodium chloride (Fluka Chemie GmbH, Oberhaching, Germany)  
Tris(2-chlorethyl)phosphine (TCEP)  
Trizma-BASE, 99.9%  
Trypton (Applichem GmbH, Darmstadt, Germany)  
Tween 20 (Applichem GmbH, Darmstadt, Germany)  
Yeast cell extract (Applichem, Darmstadt, Germany)

### 2.1-6 Medium

DYT: 1.6% w/v Trypton, 1% w/v yeast cell extract, 0.5% w/v NaCl  
Antibiotics: Ampicillin 200  $\mu$ g/ml culture,  
Kanamycin 50  $\mu$ g/ml culture

## 2.2 Molecular Biology methods

### 2.2-1 Polymerase Chain Reaction (PCR)

The polymerase chain reaction (PCR) is a simple and straightforward method to amplify DNA, with many applications in molecular biology. It can be a reliable tool for diagnostics, genome analysis, DNA-sequencing or mutagenesis. The polymerase chain reaction was used in the present work to generate mutants of Calmodulin bovine, and as a tool for DNA sequencing. This method takes advantage of the high thermostability of several DNA-polymerases. In our case Finnzymes Phusion Hot-start DNA-polymerase was used. By heating a reaction mixture containing a template, primers as well as nucleotides, the template DNA can be denatured into single strands, while the polymerase remains intact.

Typically, a PCR is divided into three steps: denaturation, annealing and polymerization. In order to denature the DNA into single strands, the reaction mix is heated up to 98 °C. During the initial denaturation step the complete template has to be denatured. Therefore, the first melting step can take up to 3 minutes. Later on, when mainly shorter fragments have to be denatured, this step can be shortened down to ten seconds. It should be noted, that high temperatures are harmful to all involved reactants. Thus, the denaturation step should be kept as short as possible. The DNA polymerase also requires a primer to initiate the DNA polymerization. To amplify a piece of DNA, two primers are used, facing in opposite direction. One speaks of forward and reverse primers. These two pieces of DNA flank the region to be amplified. To hybridize the primers with the template DNA, the reaction mixture is annealed to a temperature within 5 °C and 10 °C below the theoretical melting point of the primers. The polymerization step is carried out at the optimum temperature, which is in our case 72 °C [64].

The PCR conditions used for amplification were the following:

1. 98 °C, 30 sec
2. 98 °C, 10 sec
3. 72 °C, 15 sec

4. 72 °C, 15 sec
5. Repeat steps 2-4 45 times
6. 72 °C, 5 min
7. 4 °C, ∞

### 2.2-2 Site-directed mutagenesis

Primers used in PCR may carry the mutations to be inserted. In order to prepare a tetra-cysteine mutant two primers were required: one forward primer which introduces both a restriction site at the 5'-end of the gene and the sequence codifying for the tetra-cysteine motif, and one reverse primer bearing another restriction site, different from the one in the forward primer. The mutagenesis is then carried out in only one step.

In case it is necessary to incorporate point mutations, or insert a DNA sequence, or maybe delete a part of the sequence within the gene and away from the two termini, one can utilize the mega-primer technique. A primer which carries the mutation and hybridizes with an internal sequence of the gene is used together with the forward or the reverse primer to amplify a part of the gene by PCR. It is recommended to design the internal primer in such a way so that the larger part of the gene is amplified during this PCR. Then, the PCR product, which is a large DNA fragment, is utilized in a second PCR as a mega-primer together with the forward or the reverse primer to amplify the whole sequence of the gene.

### 2.2-3 DNA-sequencing

In order to confirm that the desired mutations are introduced into the DNA sequence of the gene, all clones were sequenced using the Sanger sequencing method. The basic principle of this method is the termination of the DNA replication at a specific nucleotide by dideoxynucleotide phosphates (ddNTPs) which lack the 3'-hydroxyl group. Since the latter is required to bind a new dNTP to the DNA chain via a phosphate group, the DNA replication is

terminated at that position. In a typical sequencing procedure, this is combined with a PCR. For each nucleotide a separate reaction is necessary. Each reaction mixture consists of the respective ddNTP, a vector-specific fluorescent labelled primer and all four dNTPs. Since only small concentrations of ddNTPs are used, the DNA replication is terminated occasionally at the respective nucleotide. By separating the different DNA fragments according to their size, a sequence can be read. The samples are electrophorized in a polyacrylamide gel with one nucleotide resolution on an automated infrared DNA-sequencer which detects the fluorescent labelled DNA. With this method 500-1000 nucleotides can be sequenced [64]. In all cases two different primers were used and the gene was sequenced starting upstream and downstream. After data analysis, a clone can either be regarded as verified or rejected.

#### 2.2-4 Cloning

Cloning is defined as the insertion of a DNA fragment into a vector, a plasmid for instance. PCR products as well as fragments after digestion with restriction endonucleases can be used as an insert. However, there is one important difference between those two types of insert. By amplification using a Phusion polymerase, PCR-products with blunt ends are produced, while restriction fragments are usually characterized by overhangs of one of the two DNA strands, which are termed sticky ends. These two features have an influence on the cloning strategy.

The cloning procedure comprises four steps, which are digestion of DNA, ligation of DNA fragments, transformation in competent *E. coli* cells, and finally screening. In the beginning both the vector and the insert have to be digested with the same set of restriction enzymes. The use of two different restriction sites upstream and downstream allows for controlling the orientation of a fragment in the new vector. This can be of particular importance when the gene is modified in a cloning step. Examples for this kind of modifications could be an addition of a tag to one terminus of the

protein or the removal or recombination of mutations which are available in other constructs.

After digestion, the vector and the insert could in principle be ligated together without further preparation. The enzyme used for this purpose is DNA ligase from the T4 phage. Energy for the DNA ligation is provided by cleaving a phosphate bond at the 5'-end of the DNA. Since both the vector and the insert carry these phosphates two reactions would be in competition to each other: the ligation of the insert to the vector and the auto-ligation of the vector. Therefore the vector is dephosphorylated at the 5'-end using an alkaline phosphatase from shrimp. It is essential for further steps to completely purify the vector from the phosphatase. A contaminated with phosphatase vector solution would decrease the ligation reaction yield, since the enzyme would dephosphorylate the 5'-end of the insert, as well. Now the insert and the vector can be mixed together, and the ligase will connect their ends. The incubation time is usually ten minutes. When cloning into large vectors, heating up the insert-vector mixture at 70 °C and then cooling down on ice prior to the ligation reaction eliminates probable secondary structure.

Then, *E. coli* TOP10 cells are transformed with the ligation reaction, and subsequently streaked on an agar plate, which contains an antibiotic to select for the right clones. The plasmid-vector carries a resistance gene for the specific antibiotic, therefore, only the cells carrying the plasmid can grow under these conditions. Single colonies are then inoculated into five milliliters of DYT medium with the same antibiotic, and incubated overnight.

Finally, by plasmid isolation and digestion with the same set of restriction endonucleases, the incorporation of the insert into the vector can be verified.

## 2.2-5 Transformation

The intake of a free DNA molecule from the environment by a bacterial cell is called transformation [64]. The ability of a cell to take in a plasmid can be enhanced by several methods leading to competent cells. After adding the desired DNA to an aliquot of these cells the mixture is incubated for 20

minutes. To facilitate the DNA intake this incubation is followed by a heat shock: The mixture is heated to 42°C for two minutes and then cooled on ice for another minute. After adding 800 µl of medium to the mixture, the cells are incubated at 37°C for 55 minutes. Finally the cells are streaked on selective agar plates and incubated at 37°C overnight.

## 2.2-6 Plasmid isolation (minipreps/midipreps)

Plasmids were isolated using the kits purchased from Macherey-Nagel (Düren, Germany) or Qiagen (Hilden, Germany) according to the protocol provided by the manufacturer. The protocol requires 3 ml of an *E. coli* TOP10 cell culture grown over night for minipreps, and 400 ml of culture for midipreps.

### 2.2-6.1 Minipreps

- 1) 3 ml culture was centrifuged at maximum speed (20000 x g) for 1 min.
- 2) The pellet was resuspended with 250 µl RESUSPENSION BUFFER (25 mM Tris-HCl, 50 mM glucose, 10 mM EDTA, pH 8).
- 3) Cells were lysed with 250 µl LYSIS BUFFER (1% SDS, 0.2 N NaOH), they were mixed gently with the lysis buffer and incubation at room temperature for 5 min followed.
- 4) Neutralization with 300 µl cold NEUTRALIZATION BUFFER (potassium acetate for alkaline lysis) and gentle mixing followed. Small sediments of CH<sub>3</sub>COOK can be formed, which may degrade the DNA; therefore, next step should take place immediately.
- 5) Centrifugation at maximum speed (20000 x g) for 10 min.
- 6) The supernatant was loaded onto an anion-exchange column and centrifugation at maximum speed (20000 x g) for 1 min followed.
- 7) The flow-through was discarded and column was washed with 700 µl WASH BUFFER (0.3 M CH<sub>3</sub>COONa pH 5.2, more than 2.5 volumes cold absolute ethanol).

- 8) Flow-through was discarded and column was dried by centrifugation for 2 min, since traces of ethanol in DNA solutions can inhibit enzymatic reactions and transformation.
- 9) DNA was eluted with 100  $\mu$ l ELUTION BUFFER (10 mM Tris-HCl, pH 8.5). The elution buffer was loaded onto the column, incubation for 1 min, and centrifugation for 1 min followed. After that, the collected elution could be stored at 4 °C or -20 °C.

### 2.2-6.2 Midipreps

- 1) Cells were harvested by centrifugation at 4700 rpm for 20 min and resuspended with 8 ml RESUSPENSION BUFFER.
- 2) The column was equilibrated with 12 ml EQUILIBRATION BUFFER.
- 3) Cells were lysed by addition of 8 ml LYSIS BUFFER to the resuspension, they were mixed gently with the lysis buffer, and incubation at room temperature for 5 min followed.
- 4) Neutralization by addition of 8 ml NEUTRALIZATION BUFFER to the lysate, gentle mixing and centrifugation at 4700 rpm for 20 min followed.
- 5) The supernatant was loaded and passed through the column by gravity flow.
- 6) The column was washed once again with 5 ml EQUILIBRATION BUFFER.
- 7) One wash with 8 ml WASH BUFFER followed.
- 8) DNA was eluted with 5 ml ELUTION BUFFER, and the concentration was calculated by measuring the absorbance at 260 nm.
- 9) DNA was precipitated by addition of 0.7 volumes cold isopropanol, it was gently mixed, and incubation for 2 min at room temperature followed.
- 10) The mixture was injected through a finalizer, which binds the DNA (the finalizer is provided with the kit).
- 11) The finalizer was washed with 2 ml of cold 70% ethanol, and dried 20 times.

- 12) Two elutions were collected by injecting through the finalizer 200  $\mu$ l ELUTION BUFFER (5 mM Tris-HCl, pH 8.5), the absorbance at 260 nm was measured again, and the concentration as well as the recovery ratio was calculated. After that, the collected elutions could then be stored at 4 °C or -20 °C.

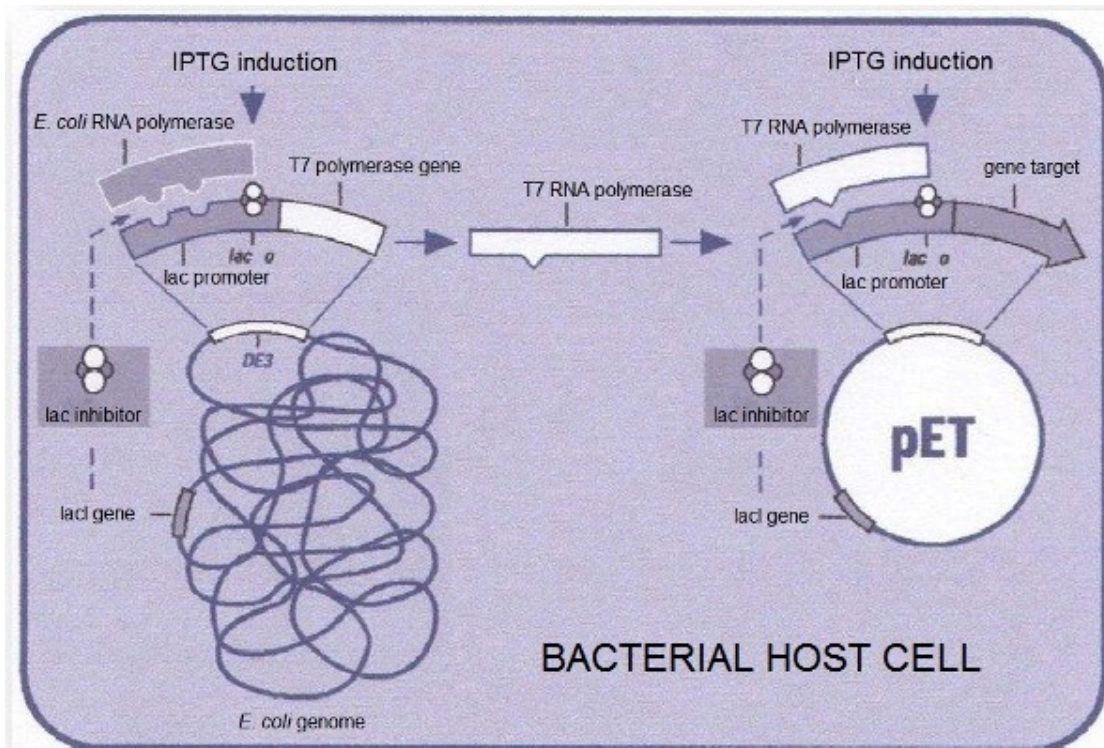
### 2.2-7 DNA electrophoresis

Electrophoresis can be defined as the mobility of a molecule in an electrical field. Thus, a molecule can be accelerated through a mesh which acts as a molecular sieve. The material used for DNA electrophoresis is chosen according to the desired resolution. Agarose gels can be used when the analyte is large. Gels containing 1% low-melting agarose in TAE buffer (40 mM Tris, 2.5 mM EDTA, pH 8), as used here, are preferred for the separation of DNA fragments between 0.4 and 6 kB. Larger fragments tend to align in the electric field in a way that their mobility through the mesh is independent of their size. They will form a large band in a region of high molecular DNA fragments but remain unresolved. To make the DNA visible within the gel, an intercalating fluorescent dye, GelRed, is added in a 1:10000 dilution. Under illumination with UV light the DNA can be analyzed or, if required, exported. To do so, the band of interest is cut out with a scalpel, and the agarose is dissolved in QX buffer at 50 °C. The solution can then be applied to an anion-exchange column and the DNA can be purified. Gels with a smaller pore size can be prepared using acrylamide and bis-acrylamide. The pore size depends on both the acrylamide and the bis-acrylamide concentration. DNA sequencing gels were prepared in a way that a resolution of one base pair was achieved. To obtain the desired resolution, a large gel (66 cm) containing 4.8% acrylamide was cast. By adding urea, DNA secondary structure, like hairpins, which affects the electrophoretic mobility, can be minimized [64]. The gel was run on an automated infrared DNA-sequencer as mentioned in Section 2.2-3.

## 2.3 Biochemistry methods

### 2.3-1 Protein overexpression and purification

To express the gene of Calmodulin (CaM), the vector pET27b was used. This vector is using the T7 promoter and the lacO operator to control the expression of a protein target. This promoter is originally part of the genome of the T7 phage and serves as a binding site for a specific RNA-polymerase of T7 phage, which therefore has to be co-expressed. The gene coding for this polymerase is inserted into the chromosome of the *E. coli* strain BL21 (DE3) that was used for all expressions performed in the present work. To regulate the expression of the polymerase the lacO operator is used. It suppresses the expression of T7 RNA polymerase in absence of an inducer. In nature the inducer would normally be lactose. In order to maintain a constant inducer concentration in the medium, a non-digestible analog was employed - isopropyl  $\beta$ -D-1-thiogalactopyranoside (IPTG). After the addition of the inducer, T7 RNA polymerase is produced, which then transcribes the gene of the protein target.



### 2.3-1.1 Protein purification with Ni-NTA column

Mutated CaM tagged with 6 histidines was overexpressed in *E. coli* BL21 (DE3) cells and purified according to the following batch-purification protocol [65]:

- 1) Cells were grown in 100 ml selective DYT (1.6% tryptone, 1% yeast extract, 0.5% NaCl, 50 µg/ml kanamycin).
- 2) CaM was overexpressed for 45 min after induction with 1 mM IPTG when the culture had grown to an OD<sub>600</sub> equal to 0.5.
- 3) Cells were centrifuged and the pellet was dissolved in lysis buffer (10 mM MOPS, 500 mM NaCl, 6 M GndHCl, 1 mM TCEP, pH 7.4).
- 4) Lysis by sonication followed.
- 5) Ni-NTA agarose beads were washed 3 times with the same buffer
- 6) The lysate was centrifuged and the supernatant was mixed with the beads for 3 h at 4 °C.
- 7) The beads were washed with lysis buffer, and the concentration of GndHCl was decreased by sequential washing steps with buffers containing 5 M, 4 M, 3 M, 2 M, and 1 M GndHCl.
- 8) Another wash with buffer without GndHCl followed.
- 9) The beads were washed 3 times with wash buffer (10 mM MOPS, 500 mM NaCl, 5 mM imidazole, 1 mM TCEP, pH 7.4).
- 10) Three elution steps at room temperature with elution buffer (10 mM MOPS, 500 mM NaCl, 250 mM imidazole, 1 mM TCEP, pH 7.4) followed. Washes and elutions were collected and stored at 4 °C. To remove the excess of imidazole, two approaches are possible, either dialysis or size-exclusion chromatography.

Size-exclusion chromatography was applied in the present work for buffer exchanges as well as for separation of fluorescently labelled protein molecules from free diffusing dye in the solution. In size-exclusion chromatography a porous gel matrix (Sephadex beads) is used to separate molecules according to their size. Depending on the purity requirements, column materials with a different molecular weight cut-off (with large or smaller pores) are available. Molecules that are larger than the respective molecular weight cut-off cannot diffuse through the pores of the beads. The

total accessible space is smaller, therefore, large molecules diffuse faster, and are typically eluted in the first fractions. Smaller molecules (below the molecular weight cut-off) follow a much longer route through the beads. Hence, they are eluted in later fractions. The buffer does not play any important role here, but should nevertheless contain 50-100 mM NaCl to prevent non-specific interactions between the molecules and the beads.

### 2.3-1.2 SDS-polyacrylamide gel electrophoresis (SDS-PAGE)

The mobility of proteins strongly depends on their charge and on their shape. To analyze proteins irrespective of these parameters and only with respect to their molecular weight, a denaturing gel is required. The proteins are unfolded by the addition of sodium dodecyl sulfate (SDS), which also covers the individual charges of the protein. By adding  $\beta$ -mercaptoethanol, inter- and intra-molecular disulfate bonds are reduced. Under these conditions, the mobility of the protein depends only on the mass of the protein-SDS micelle. To further improve the separation, discontinuous electrophoresis was performed. The acrylamide gel itself consists of two parts: First the protein solution passes through the stacking gel containing only a small amount of acrylamide. All proteins can pass through this gel without any extensive major separation in the mesh. Between the leading and terminating ions however an electrostatic gradient is formed, which concentrates the protein solution into a thin layer. The separation gel which follows, where (as the name suggests) the actual separation takes place, contains 15% acrylamide. After the front has passed through both gels, proteins can be stained with a solution containing 0.1% Coomassie Brilliant Blue R-250 and the gel can then be destained by washing with 10% acetic acid.

### 2.3-2 Labelling of CaM with FIAsh (Fluorescein Arsenical Helix Binder)

The labelling of tetra-Cys-CaM with a fluorescent dye (FIAsh) was accomplished as follows: protein was dissolved in labelling buffer (10 mM MOPS, 500 mM NaCl, 1 mM TCEP, pH 7.4) to final concentration 20  $\mu$ M in a low-adhesion eppendorf tube, the mixture was degassed for 30 min under 250 mbar vacuum, and it was left at room temperature for 2.5 h, so that the disulphide bonds are reduced. Then FIAsh was added to final concentration 4  $\mu$ M in the presence of nitrogen gas. The concentration ratio between protein and FIAsh was 5:1. This was necessary so that most of the dye molecules (90-100 %) were attached to the tetra-Cys motif (Fig. 2.3-2). Nevertheless, the label ratio that could be achieved, which is defined as the percentage of the labelled protein molecules, was low, around 20%. The labelling reaction took place at 37 °C in complete darkness for 3 h. Finally, the eppendorf tube was stored at 4 °C, again in complete darkness, for 2 days [66].

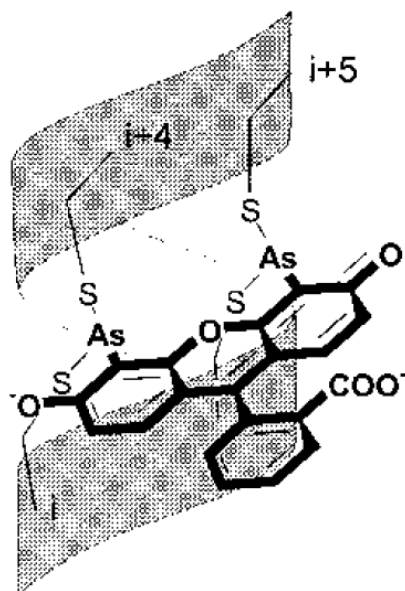


**Fig. 2.3-2.** Fluorescent complex of FIAsh attached to a tetra-Cys motif [67].

## 2.4 Spectroscopic techniques

### 2.4-1 Absorption spectroscopy

The property of a molecule to absorb light of a given wavelength, and thus transiting to an excited state, may have a lot of applications in spectroscopy studies. On the molecular level, absorption can be described as a dipole interaction between the incident light and a molecule, where upon absorption, the molecule is excited. Light emission from the excited state opens a wide range of fluorescence spectroscopy techniques. The most straightforward application of absorption spectroscopy is the concentration determination. Non-polarized light of a given wavelength illuminates the sample and a reference solution, and the intensity of the transmitted light is recorded. By the usage of the Lambert-Beer law, the concentration of the sample can be calculated [68].

$$A = \log \frac{I_0}{I} = \epsilon * c * d \quad [\text{Eq. 2.4 - 1}]$$

where A is the absorbance,  $I_0$  and I are the intensities of the incident and transmitted light, respectively, c refers to the molar concentration, M, of the sample,  $\epsilon$  is the molar absorption coefficient in  $M^{-1}\text{cm}^{-1}$ , and d is the path length of the cell in cm.

### 2.4-2 Circular dichroism spectroscopy (CD)

Circular dichroism (CD) is being increasingly recognized as a valuable technique for examining the structure of proteins in solution. Linear polarized light can be viewed as being made up of two circularly polarized components, one rotating clockwise (left-handed, L) and the other one counter-clockwise (right-handed, R). Circular dichroism (CD) refers to the differential absorption of these two components ( $\Delta A = A_L - A_R$ ). If L and R components are absorbed to different extents, the transmitted signal would be said to possess elliptical polarization. A CD signal would be observed if a chromophore is

chiral (optically active) for one of the following reasons: 1) it is intrinsically chiral, for example a C atom with four different substituents, 2) it is covalently linked to a chiral centre, or 3) it is accommodated in an asymmetric environment by virtue of the 3-dimensional structure adopted by the molecule [69].

In proteins, the chromophores of interest include the peptide bond (absorption below 240 nm), aromatic aminoacids' side chains (absorption in the range 260 to 320 nm), and disulphide bonds (weak broad bands centred at 260 nm). Absorption in the region below 240 nm is in principle due to peptide bonds; there is a weak but broad  $n \rightarrow \pi^*$  transition centred at around 220 nm and a more intense  $\pi \rightarrow \pi^*$  transition centred at 190 nm. The different types of secondary structure give rise to characteristic CD spectra in the far UV (Fig 2.4-2). As it can be observed in Fig. 2.4-2 the most significant differences between  $\alpha$ -helix,  $\beta$ -sheet and random coil lie below 200 nm, but this region is often not accessible. At longer wavelengths, the spectrum of  $\alpha$ -helical structure is characterized by two negative local minima, one at 208 nm and another one at 222 nm, which are clearly distinguishable from  $\beta$ -sheets, which are characterized by a negative minimum at 218 nm. Random coils present weaker CD signals which are noisy in the near UV and start increasing at around 210 nm [69].

It should be noted that chemical substances in protein buffer solutions can also contribute to the CD signal. For this reason, it is important that chemicals, which absorb in the desired region, are not added in high concentration, or they should be simply avoided, if applicable. These could be NaCl, MOPS, GndHCl, HEPES, etc. Since absorbance and, thus, the CD signal is dependent on the concentration of the peptide bonds in the solution, the protein concentration should be as high as the experiment permits. Additionally, it is useful the obtained CD spectrum to be normalized to the Mean Residue Ellipticity (MRE)  $[\theta]_{MRW,\lambda}$  in order to be comparable with other spectra.

$$[\theta]_{MRW,\lambda} = \frac{MRW * \theta_{\lambda}}{10 * d * c} \quad [\text{Eq. 2.4 - 2}]$$

where  $\theta_\lambda$  is the observed ellipticity (degrees) at wavelength  $\lambda$ ,  $d$  is the path length (cm) of the cell,  $c$  is the concentration (g/ml), and MRW is the mean residue weight which can be calculated by dividing the molecular weight of the protein by the number of the peptide bonds. The mean residue ellipticity is expressed in  $\text{deg cm}^2 \text{dmol}^{-1}$ . Nevertheless, comparisons between CD spectra can also be made using the ellipticities expressed in mdeg if the same concentration of one and the same protein is measured each time.

In this study, CaM was measured. The concentration of the measured protein was adjusted to around 0.2 mg/ml to acquire a reliable CD signal. The pathlength of the cell was 1 mm. Each time a sample was measured, the scan rate was adjusted to 50 nm/min, the temperature to 20 °C, and two scans were acquired each time. The buffer was also measured, and subsequently, subtracted from the raw data.

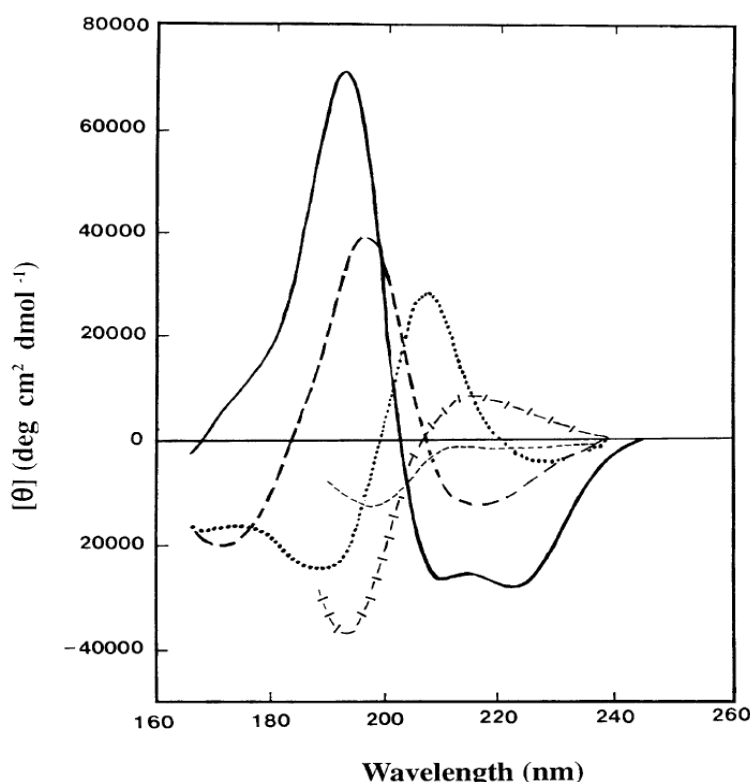


**Fig. 2.4-2.** Far UV spectra associated with various types of secondary structure. Solid line,  $\alpha$ -helix; long dashed line, anti-parallel  $\beta$ -sheet; dotted line, type I  $\beta$ -turn; cross dashed line, extended 3(10)-helix or poly-Pro II helix; short dashed line, random coil [69].

It is known that CaM comprises  $\alpha$ -helices. It is useful to mention what are these two local minima that are usually observed in the CD spectra of  $\alpha$ -helices. The most abundant chromophore in peptides and proteins is the amide group. According to G.D. Fasman, *et al* (1996), the long-wavelength negative band with a maximum at around 222 nm has been assigned to the  $n\pi^*$  transition. This transition occurs due to energy absorption by the  $\sigma$  electrons of the oxygen of the carbonyl group, with a transition moment along the carbonyl bond. Despite that this transition is electrically forbidden ( $\epsilon_{\max} \sim 100 \text{ M}^{-1}\text{cm}^{-1}$ ), the dominant mechanism by which the  $n\pi^*$  transition acquires its rotational strength is that it borrows energy from the electrically allowed ( $\epsilon_{\max} \sim 10000 \text{ M}^{-1}\text{cm}^{-1}$ ) amide  $\pi\pi^*$  transition, with a transition moment approximately oriented along the NO direction. One well-known  $\pi\pi^*$  transition is usually recorded as a positive band at 190 nm. The 208 nm negative band and the 190 nm positive band result from exciton splitting of the  $\pi\pi^*$  transition into a long-wavelength component polarized along the helix axis (208 nm) and a short-wavelength degenerate pair of bands polarized perpendicular to the helix axis (190 nm) [70]. Measurements at shorter wavelengths (shorter than 200 nm) were not performed because both MOPS and NaCl also absorb at around 195 nm. Nevertheless, the helical content can still be judged by a closer observation at both of these two local minima.

### 2.4-3 Principles of fluorescence

During the last 20 years there has been considerable progress in the development of fluorescence spectroscopy techniques as research tools in biochemistry and nanotechnology. Fluorescence spectroscopy can be applied to obtain information about many molecular processes, including diffusion of molecules in solutions, rotational freedom, conformational changes, and interactions with other molecules [68].

The processes that occur between the absorption and emission of light are often depicted in a Jablonski diagram (Fig. 2.4-3.1) [68][71].

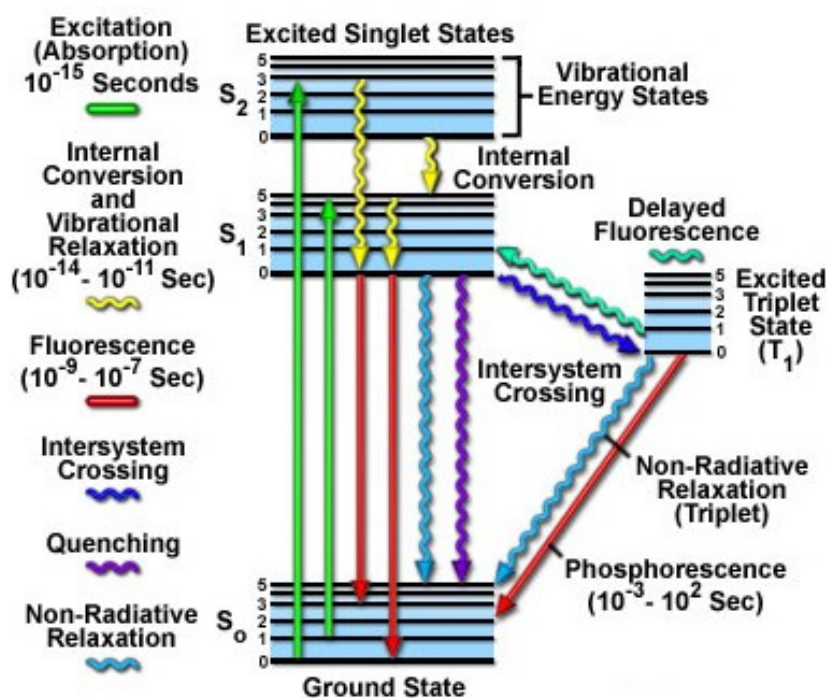


Fig. 2.4-3.1. The Jablonski energy diagram.

When a photon is absorbed, an electron transits to a singlet excited state, which is a higher energy state. Consequently, the electron is likely to return to the ground state (lower energy state) by emission of a photon. Speaking of fluorescence, the transition to the ground state occurs in the nanosecond timescale. A typical fluorescence lifetime is only a few nanoseconds (1-5 ns). A fluorophore is usually excited to some higher vibrational level of either  $S_1$  or  $S_2$ , and then molecules rapidly relax to the lowest vibrational level of  $S_1$ . This process is called internal conversion and occurs within a few picoseconds. Since lifetime is usually a few nanoseconds, internal conversion is usually completed before emission. Thus, fluorescence emission generally results from the excited state with the lowest energy. Through internal conversions a fraction of the energy is dissipated, and due to energy dissipation, the Stokes shift phenomenon is observed. This phenomenon is a shift of the emission spectrum to longer wavelengths compared to the absorption spectrum (red shift). Another important feature is that the emission spectrum is, in general, independent of the excitation wavelength within the absorption band. By excitation at absorption maximum, only the probability of excitation becomes

larger, leading to an increase in the emission intensity. Molecules in the  $S_1$  state may also undergo a spin conversion to the first triplet state  $T_1$ . Emission from  $T_1$  is called phosphorescence, and is generally shifted to longer wavelengths (lower energy) relative to the fluorescence. Conversion from  $S_1$  to  $T_1$  is called intersystem crossing. Various quenching processes or reduction-oxidation reactions usually lead to a non-radiative depopulation of the triplet state so that no phosphorescence can be observed. Heavy atoms in molecules facilitate intersystem crossing, and thus lower fluorescence quantum yields [68].

The quantum yield and the lifetime are perhaps the most important characteristics of a fluorophore. The quantum yield,  $Q$ , is defined as the ratio of the number of emitted photons ( $\Phi_{em}$ ) to the number of absorbed photons ( $\Phi_{abs}$ ). Substances, e.g. rhodamine, with the largest quantum yields display the brightest emissions.

$$Q = \frac{\Phi_{em}}{\Phi_{abs}}, \quad Q = \frac{\Gamma}{\Gamma + k_{nr}} \quad [\text{Eq. 2.4 - 3.1}]$$

where  $\Gamma$  denotes the emissive rate, and  $k_{nr}$  the non-radiative transition rate to the ground state.

The lifetime is also important, as it determines the time available to detect interactions of the fluorophore with its environment as well as diffusion times and diffusion coefficients; hence, the information available from fluorophore's emission. The average lifetime,  $\bar{\tau}$ , is the average amount of time a fluorophore remains in the excited state (see also Fig. 2.4-6.5.1, TCSPC histograms, later on).

$$\bar{\tau} = \frac{1}{\Gamma + k_{nr}}, \quad \text{and} \quad \bar{\tau} = \langle t \rangle = \frac{\int_0^T t I(t) dt}{\int_0^T I(t) dt} \quad [\text{Eq. 2.4 - 3.2}]$$

The intensity of fluorescence can be decreased by a wide variety of processes, e.g. photon-induced electron transfer (PET) and Förster resonance energy transfer (FRET), which can be used to monitor folding and dynamics of proteins. Such decreases in the intensity are called quenching. Quenching can occur by different mechanisms. Collisional quenching occurs when the excited-state fluorophore is deactivated upon contact with some

other molecule in solution, which is called quencher. In this case the fluorophore is returned to the ground state during a diffusive encounter with the quencher. The molecules are not chemically altered in the process. Except from collisional quenching, fluorescence quenching may occur by a variety of other processes. Fluorophores can form non-fluorescent complexes with quenchers. This process is called static quenching. It occurs in the ground state and is, typically, independent of the collision rate. The mechanism of quenching varies with the fluorophore-quencher pair, e.g. quenching by halogen and heavy atoms occurs due to spin-orbit coupling and intersystem crossing to the triplet state [68].

There are two major categories of fluorescence measurements: steady-state and time-resolved. Steady-state measurements, the most common type, are those performed with constant illumination and observation. The sample is exposed to a continuous light beam and the emission spectrum is recorded. The second type of measurement is time-resolved, which is used for measuring intensity decays or anisotropy decays. In this case the fluorophore is excited by a pulse of light, where the pulse width is typically much shorter than the fluorescence lifetime. This intensity decay is recorded with a high-speed detection system that allows the intensity or anisotropy to be measured on a timescale of hundreds of picoseconds, at least.

### 2.4-3.1 Steady-state fluorescence spectroscopy

Fluorescence emission spectra are acquired using a spectrofluorometer (Fig. 2.4-3.1.1). Two different types of spectra can be recorded. The emission spectrum is recorded using a monochromator, holding the excitation light at a constant wavelength. An excitation spectrum is obtained when the emission light is held at a constant wavelength, and the excitation light is varied by scanning through many different wavelengths via a monochromator. It is instructive to mention what monochromators are. Monochromators disperse polychromatic light into several wavelengths. The stray light level of a monochromator is a critical parameter. Stray light is any light that is transmitted by the monochromator besides the desired wavelength.

Therefore, monochromators should exhibit low levels of stray light. The fluorescence light was measured at a  $90^\circ$  angle relative to the excitation light. This geometry is used instead of placing the emission monochromator at the line of the excitation light at a  $180^\circ$  angle in order to avoid interference of the transmitted excitation light. This results in a better signal-to-noise ratio as compared to the  $180^\circ$  geometry. The intensity of light that is transmitted by the monochromator is approximately proportional to the square of the entrance and exit slit width. Larger slit widths yield increased signal levels, and thus higher signal-to-noise ratios, while smaller slit widths provide higher resolution, but lower intensity. Monochromators might have planar or concave gratings. Stray light transmission can be caused by imperfect gratings. Less stray light can be transmitted by concave gratings because they have fewer imperfections. Moreover, monochromators with concave gratings have fewer reflecting surfaces resulting in decreased probability of occurrence of stray light. Monochromators also exhibit different transmission efficiencies for different polarizations of the light. This can result in spectral shift as well as different shape of the emission spectrum, depending on the polarization conditions chosen to record the emission spectrum. Therefore, a correction factor,  $G_r$ , is needed to correct for different transmission efficiencies, which will be described in a later section [68]. Each time a sample was measured, the slit widths were adjusted to 1 mm, and the temperature to  $20^\circ\text{C}$ . Whenever steady-state anisotropy was measured, excitation and emission polarizers were utilized as well as the slit widths were adjusted to 2 mm.

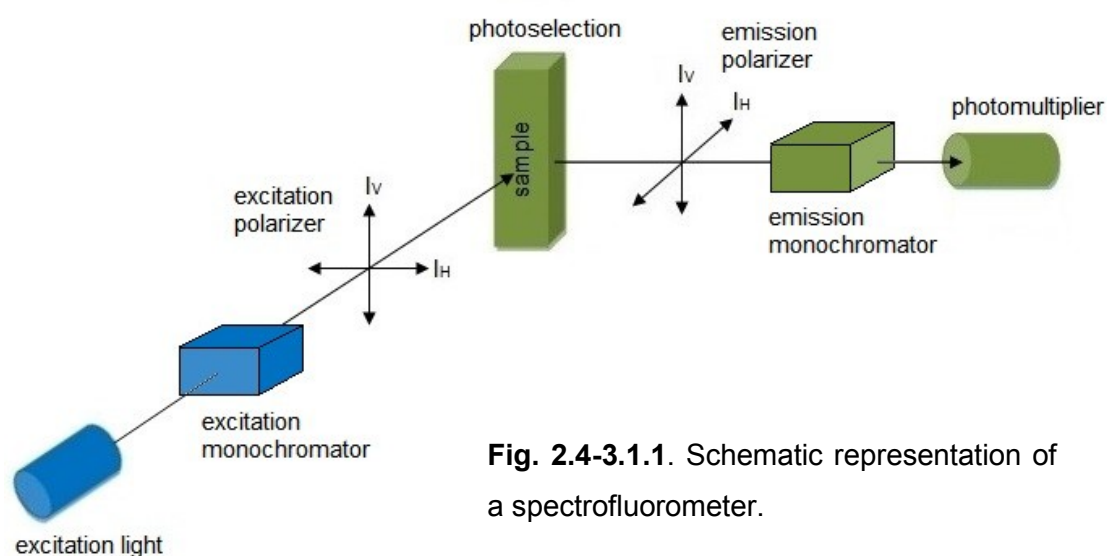


**Fig. 2.4-3.1.1.** Schematic representation of a spectrofluorometer.

### 2.4-3.2 Time-resolved fluorescence spectroscopy

Given that it is easy to perform steady-state measurements and there is no need for complex and expensive instrumentation (Fig. 2.4-3.2.1), what is the value of more complicated techniques? It is important to understand the relation between steady-state and time-resolved measurements. A steady-state observation is an average of the time-resolved phenomena over the intensity decay of the sample. It turns out that most of the molecular information available is lost during the averaging process. Let us assume we have macromolecules labelled with a fluorescent dye. The anisotropy decays of fluorescent macromolecules are frequently more complex than a single exponential. The anisotropy decay formula contains information about the depolarization caused by segmental motion and overall tumbling motion. It also contains information about the flexibility of the labelled branches of the macromolecule. Unfortunately, this information is lost when the anisotropy is averaged over the decay time (see also Section 2.4-6.4, Perrin's equation, later on) [68]. To be precise, steady-state anisotropy can still give evidence whether the fluorophore is able to change its orientation and to what extent, but nothing more than that.

The required instrumentation for time-resolved measurements will be briefly described. For imaging purposes, but also for measurements on free diffusing molecules in solution, a confocal microscope can be utilized (Fig. 2.4-3.2.1). In such a setup the excitation light emitted from pulsed-laser diodes is focused on a diffraction limited spot into the sample. The emission is focused through a confocal pinhole with a diameter 50  $\mu\text{m}$  - 100  $\mu\text{m}$  to discard the out of focus light. The detectors used in the present work are single-photon avalanche diodes (SPADs). These highly sensitive detectors offer a high time resolution (FWHM: 400 ps), so that it is possible to resolve processes in the nanosecond timescale.



#### 2.4-4 Functionality tests with calcium ( $\text{Ca}^{2+}$ )

CaM comprises four  $\text{Ca}^{2+}$ -binding domains (EF-hands) and a 'hinge' region between the two N-terminal EF-hands and the two C-terminal ones. The structure of each one of these EF-hands is helix-loop-helix, and one  $\text{Ca}^{2+}$  cation binds to each one of these electronegative loops. The two N-terminal loops are called I and II sites, and the C-terminal loops are called III and IV sites. The C-terminal sites have a 20-fold higher affinity for  $\text{Ca}^{2+}$  ( $K_d = 80 \text{ nM}$ ) than the N-terminal ones ( $K_d = 2 \text{ }\mu\text{M}$ ) [72]. Therefore, sites III and IV are filled almost completely before I and II sites begin to be occupied.

It has been shown by steady-state and time-resolved fluorescence studies that phenylalanine fluorescence ( $\lambda_{\text{exc}} = 250 \text{ nm}$ ,  $\lambda_{\text{em}} = 280 \text{ nm}$ ) can be used selectively to detect  $\text{Ca}^{2+}$ -binding to sites I and II, and tyrosine fluorescence ( $\lambda_{\text{exc}} = 277 \text{ nm}$ ,  $\lambda_{\text{em}} = 320 \text{ nm}$ ) for  $\text{Ca}^{2+}$ -binding to III and IV sites. Emission and excitation spectra of samples (6  $\mu\text{M}$ ) in apo-buffer (10 mM MOPS, 500 mM NaCl, 0.05 mM EGTA, and 5 mM nitrilotriacetic acid (NTA), pH 7.4) and  $\text{Ca}^{2+}$ -saturated buffer (apo-buffer with 10 mM  $\text{CaCl}_2$ ) were collected in 1 nm increments [73]. The slit widths were adjusted to 1 mm and the temperature to 20 °C. A buffer scan was also subtracted from each spectrum. The experimental procedure is the following:

- 1) An excitation spectrum from 240 nm to 265 nm monitored at 280 nm is acquired. If  $\text{Ca}^{2+}$  is bound to N-terminal loops, a decrease in the intensity at a wavelength of 250 nm will be observed.
- 2) An emission spectrum from 270 nm to 380 nm at an excitation wavelength 250 nm is acquired. If  $\text{Ca}^{2+}$  is bound to N-terminal loops, a decrease in the intensity at a wavelength of 280 nm will be observed.
- 3) An excitation spectrum from 240 nm to 300 nm monitored at 320 nm is acquired. If  $\text{Ca}^{2+}$  is bound to C-terminal loops, an increase in the intensity at a wavelength of 277 nm will be observed.
- 4) An emission spectrum from 290 nm to 380 nm at an excitation wavelength 277 nm is acquired. If  $\text{Ca}^{2+}$  is bound to C-terminal loops, an increase in the intensity at a wavelength of 320 nm will be observed.

## 2.4-5 Fluorescence correlation spectroscopy (FCS)

To study translational diffusion of molecules diluted in solution, one can utilize fluorescence correlation spectroscopy (FCS). FCS measures the fluctuations of fluorescence intensity over time, which is based on the fact that molecules at moderate temperatures are subject to Brownian motion. These fluctuations can be analyzed and diffusion coefficients as well as diffusion times through the focal volume can be obtained [68]. The time trace of a pM dilution of Alexa488 with a bin width of 1 ms is depicted in Fig. 2.4-5.1.

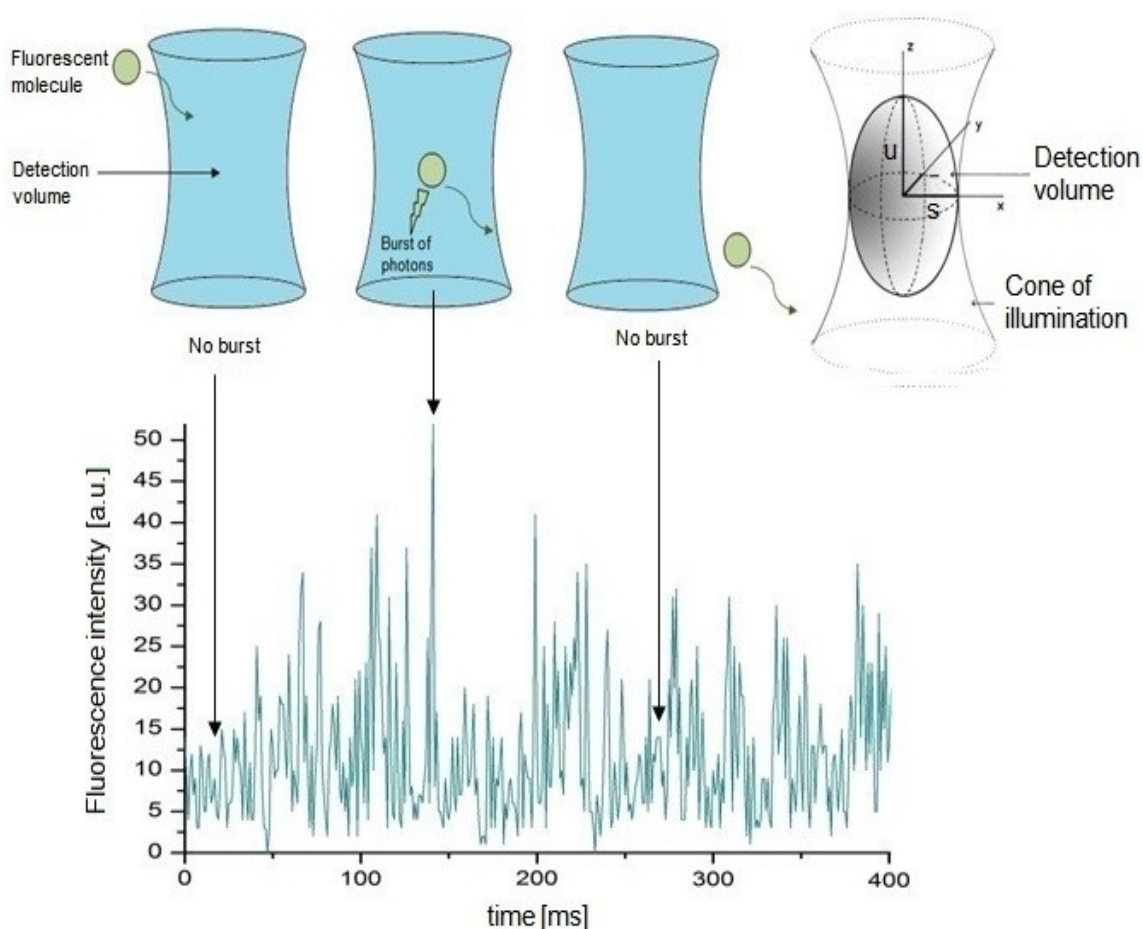


**Fig. 2.4-5.1.** Time trace of a pM dilution of Alexa488. The ellipsoidal detection volume is shown on the right in grey, where  $s$  denotes the radius and  $u$  the half-length axis.

Calculation of the autocorrelation function of these fluctuations and fitting a model to it, yields estimates of the diffusion time of the molecules and their average number in the detection volume. This can be used to obtain the diffusion coefficient and the sample concentration, respectively. One should not measure samples with high concentration of fluorescent molecules because fluctuations in the intensity become too small.

Another feature that should also be taken into consideration is the afterpulsing of the detectors, which means that each real signal pulse can be followed by an artificial afterpulse at a later time, causing a virtual fast component in the autocorrelation function. A common approach to avoid such effects is calculating the cross-correlation function of a split signal that arrives at two detectors. So, the calculated function is still the autocorrelation function of the detected signal. Cross-correlation is performed only for technical reasons. As afterpulsing occurs independently and randomly in two different detection channels, it will not be correlated, and thus canceled out. Therefore, the emission light was split by a 50/50 beam-splitter, and detected by two SPADs (Single-Photon Avalanche Diodes) instead of one.

The cross-correlation function is defined as:

$$G(\tau) = \frac{\sum_{i=0}^{M-m} I_1(i\tau) I_2(i\tau + m\tau)}{\langle I_1 \rangle \langle I_2 \rangle (M - m)} \quad [\text{Eq. 2.4 - 5.1}]$$

where  $m$  is an integer multiple of a time interval,  $\tau$ , such that  $\Delta t = m\tau$  (where  $0 \leq m < M$ ).  $M$  denotes the number of the observations,  $I_1(t)$  and  $I_2(t)$  the time traces from the two detection channels, and  $\langle I_1 \rangle$  and  $\langle I_2 \rangle$  the mean intensities of the signals. Considering only free diffusion in three dimensions, the autocorrelation function can be written as:

$$G_{3D}(\tau) = \frac{1}{V_{\text{eff}} \langle c \rangle N_A} \frac{1}{1 + \frac{\tau}{\tau_D}} \frac{1}{\sqrt{1 + \frac{s^2}{u^2} \frac{\tau}{\tau_D}}} \quad [\text{Eq. 2.4 - 5.2}]$$

$$\langle N \rangle = V_{\text{eff}} \langle c \rangle N_A, \quad \text{and} \quad G(0) = \frac{1}{\langle N \rangle} \quad [\text{Eq. 2.4 - 5.3}]$$

where  $V_{\text{eff}}$  denotes the effective detection volume,  $\langle c \rangle$  the mean concentration,  $N_A$  the Avogadro's constant,  $\langle N \rangle$  the average number of

molecules which are present in the focal volume at any time,  $\tau$  the time lag,  $\tau_D$  the diffusion time,  $s$  the radius of the ellipsoidal detection volume, and  $u$  the half-length axis [68].

The estimated value for diffusion time can be used to calculate the translational diffusion coefficient ( $D$ ):

$$\tau_D = \frac{s^2}{4D} \quad [\text{Eq. 2.4 - 5.4}]$$

It becomes apparent that the spatial extension of the detection volume has to be known to calculate diffusion coefficients accurately. Therefore, a calibration measurement using a fluorescent dye with the same spectral characteristics and a known diffusion coefficient is performed before each series of measurements [68].

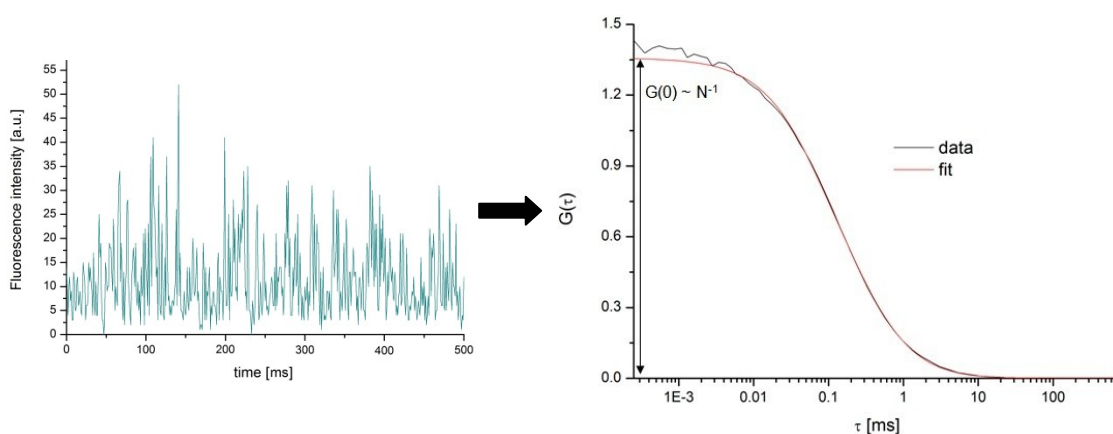


**Fig. 2.4-5.2.** Example of time trace and autocorrelation curve.

Assuming that the fluorescent molecule is a sphere, or it behaves like a spherical particle, the Stokes-Einstein equation can be utilized to determine the hydrodynamic radius of the molecule:

$$D = \frac{k_B T}{6 \pi \eta r_h} \quad [\text{Eq. 2.4 - 5.5}]$$

where  $k_B$  denotes the Boltzmann constant,  $T$  the absolute temperature,  $\eta$  the viscosity of the buffer, and  $r_h$  the hydrodynamic radius.

## 2.4-6 Fluorescence anisotropy

Fluorescence anisotropy is a powerful tool in biochemical research. It can be used to study protein denaturation, which usually results in increased flexibility of the peptide backbone, and protein association with other macromolecules, which changes the overall rate of rotation. Anisotropy measurements can also be used to detect dynamics of proteins. Upon excitation with linear polarized light, the emission light from many samples can also be polarized. The extent of polarization of the emission is described in terms of the anisotropy ( $r$ ). Samples exhibiting nonzero anisotropies are said to display polarized emission, except if there are lifetime effects, but these are going to be explained later on. The origin of anisotropy is the existence of transition dipole moments for absorption and for emission that lie along specific directions within the fluorophore structure. In homogeneous solution the ground-state fluorophores are all randomly oriented. When exposed to linear polarized light, those fluorophores that have their absorption transition moments oriented parallel to the electric vector of the incident light are preferentially excited (photoselection).

The emission can become depolarized by a number of processes. All chromophores have transition moments that occur along a specific direction in the molecular axis. Rotational diffusion of the molecule is one common cause of depolarization, as it changes the direction of the transition moments. Anisotropy reveals the average angular displacement of the fluorophore that occurs between absorption and emission. This angular displacement is dependent of the rotational rate and the extent of rotational diffusion during the lifetime of the excited state. The rate of rotational diffusion depends on the viscosity of the solvent as well as the size and shape of the rotating unit. For small fluorophores in low-viscosity solutions, the rate of rotational diffusion is typically faster than the rate of emission. On that occasion, the emission is depolarized and the anisotropy is close to zero [68]. In this chapter, the theory for steady-state and time-resolved anisotropy measurements will be described, but firstly, how fluorescence anisotropy is defined will be mentioned.

## 2.4-6.1 Definition of fluorescence anisotropy

The measurement of fluorescence anisotropy is illustrated in Fig. 2.4-6.1. Let us assume the sample is excited with horizontal polarized light; the electric vector of the excitation light is oriented parallel to the x-axis. The intensity of the emission is measured through a polarizer. When the polarizer is oriented parallel ( $\parallel$ ) to the polarization of the excitation light, the observed intensity is called  $I_{\parallel}$  or  $I_{HH}$ . Similarly, when the polarizer is oriented perpendicularly ( $\perp$ ) to the polarization of the excitation light, the observed intensity is called  $I_{\perp}$  or  $I_{HV}$ . These intensity values are used to calculate the anisotropy,  $r$ , which is defined as the ratio of the polarized component to the total intensity,  $I_T$  [68].

$$r = \frac{I_{\parallel} - I_{\perp}}{I_{\parallel} + 2I_{\perp}} \quad [\text{Eq. 2.4 - 6.1}]$$

It is obvious that the anisotropy is a dimensionless quantity that is independent of the total intensity of the sample. This is because the difference  $I_{\parallel} - I_{\perp}$  is normalized by the total intensity, which is equal to  $I_{\parallel} + 2I_{\perp}$ .

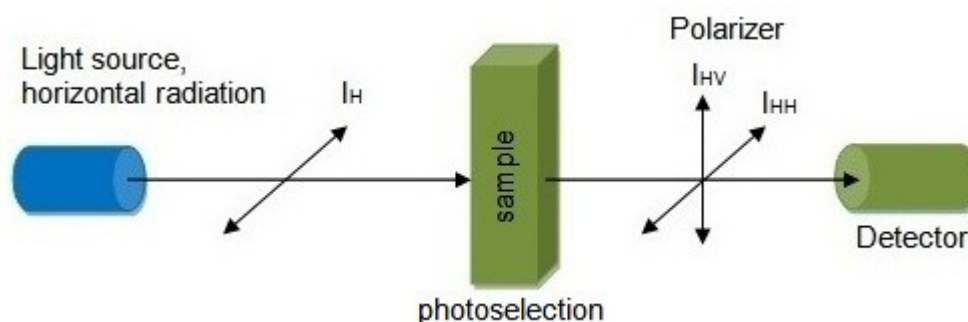


**Fig. 2.4-6.1.** Schematic diagram for measurement of fluorescence anisotropy regardless of the geometry of the setup.

Now, why the total intensity is equal to  $I_{\parallel} + 2I_{\perp}$  will be explained. Suppose that  $I_x$  is the parallel component and  $I_z$  the perpendicular, and  $x, y, z$  the three dimensions. When the excitation is polarized along the  $x$ -axis, the emission is symmetrical around the  $x$ -axis (see Fig. 2.4-6.2). Hence  $I_y = I_z$ . Recalling  $I_x = I_{\parallel}$  and  $I_z = I_{\perp}$ , one obtains Eq. 2.4-6.1:  $r = \frac{I_x - I_z}{I_x + I_y + I_z} \Rightarrow r = \frac{I_x - I_z}{I_x + 2I_z} \Rightarrow r = \frac{I_{\parallel} - I_{\perp}}{I_{\parallel} + 2I_{\perp}}$

### 2.4-6.2 Theory for fluorescence anisotropy

The theory for fluorescence anisotropy can be derived by consideration of a population of randomly distributed single molecules. As already mentioned, when a sample is illuminated with polarized light, those molecules with absorption transitions aligned parallel to the electric vector of the polarized excitation have the highest probability of excitation. Let us assume again the polarization of the excitation is parallel to the x-axis. The electric dipole of a fluorophore need not be precisely aligned with the x-axis to absorb light polarized along this axis. The probability of absorption is proportional to the  $\cos^2\theta$ , where  $\theta$  denotes the angle the absorption dipole makes with the x-axis. Thus, excitation with polarized light results in a population of excited fluorophores that are partially oriented along the x-axis (Fig. 2.4-6.2). This phenomenon is called photoselection [68]. The excited-state population is symmetrical around the x-axis, where most of the excited fluorophores are aligned close to the x-axis.

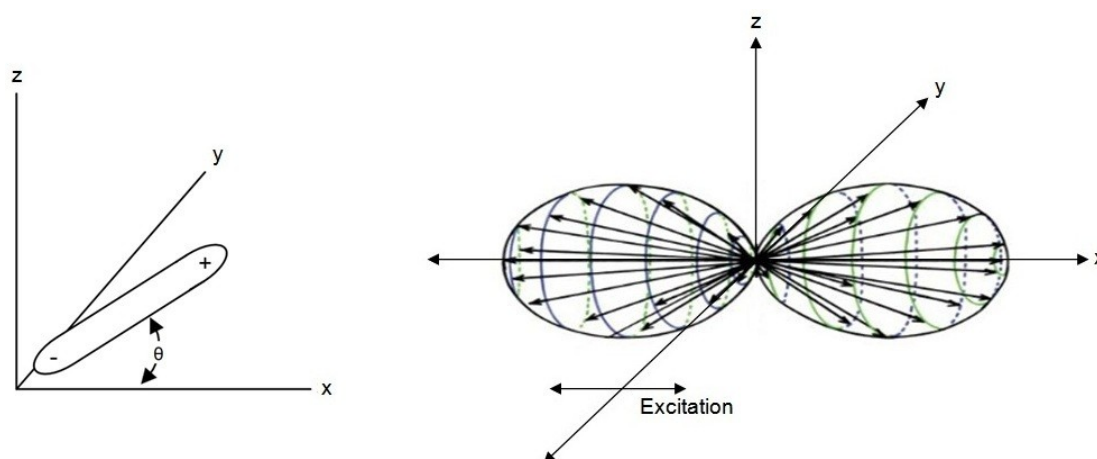


**Fig. 2.4-6.2.** Left: Dipole in a coordinate system, where  $\theta$  denotes the angle between the absorption dipole and the x-axis. Right: Excited-state distribution for immobile fluorophores.

It can be proved for anisotropy,  $r$ , that:

$$r = \frac{3\langle \cos^2\theta \rangle - 1}{2} \quad [\text{Eq. 2.4 - 6.2}]$$

It is important to consider the relationship between  $r$  and  $\theta$ . For a single fluorophore oriented along the x-axis, where  $\theta=0^\circ$ , then Eq. 2.4-6.2 shows that  $r=1$ . Nevertheless, it is not possible to obtain a perfectly oriented population of fluorophores in solution. Consequently, the anisotropy is always less than unity. The anisotropy is a function of  $\langle \cos^2\theta \rangle$ . It can be proved for randomly distributed fluorophores with absorption dipole partially oriented parallel to the electrical vector of the excitation light that  $\langle \cos^2\theta \rangle$  is equal to  $3/5$ , and thus  $r=0.4$ . This is called loss of anisotropy due to photoselection. It should be noted that these values are not valid for fluorophores in ordered systems, e.g. crystals, because the  $\langle \cos^2\theta \rangle$  can be different from  $3/5$  [68].

Till now, it was assumed that the absorption and emission moments are perfectly collinear, but in fact this occurs in few fluorophores. This can be explained by the displacement of the transition moments by an angle  $\beta$  relative to each other, which is called angular displacement, and since the orientation of the absorption dipole differs for each absorption band, the angle  $\beta$  varies with excitation wavelength. It was mentioned that an angle  $\theta$  between the absorption dipole and the electric vector of the excitation light can cause a decrease in the anisotropy by a factor  $(3\langle \cos^2\theta \rangle - 1)/2$ . Similarly, the displacement of the absorption and emission dipoles by an angle  $\beta$  may result in a further loss of anisotropy. The anisotropy of the fluorescence in a vitrified dilute solution of fluorophores is a product of the loss of anisotropy due to photoselection ( $2/5$ ), and that due to angular displacement of the dipoles. The fundamental anisotropy ( $r_0$ ), which is the value of the anisotropy at time zero (see Table 2.4-6.1), is given by [68]:

$$r_0 = \frac{2}{5} \left( \frac{3\cos^2\beta - 1}{2} \right) \quad [\text{Eq. 2.4 - 6.3}]$$

**Table 2.4-6.1.** Relationship between the Angular Displacement ( $\beta$ ) and the Fundamental Anisotropy ( $r_0$ ).

| $\beta$ (deg) | $r_0$ |
|---------------|-------|
| 0             | 0.4   |
| 45            | 0.1   |
| 54.7          | 0     |
| 90            | -0.2  |

It becomes apparent that for any fluorophore randomly distributed in solution the value for fundamental anisotropy,  $r_0$ , lies between -0.2 and 0.4. The largest  $r_0$  values are usually observed for the longest wavelength absorption band. This occurs because the lowest excited singlet state ( $S_1$ ) is generally responsible for the observed fluorescence. Absorption and emission involving the same electronic transition have nearly collinear moments (Kasha's rule). Larger  $\beta$  values (lower  $r_0$ ) are observed after excitation into higher electronic states, which are usually not the states responsible for fluorescence. Rather, the electrons rapidly transit to the lowest singlet state or to a triplet state. The angular displacement,  $\beta$ , may be revealed. However, the orientation of these moments within the molecule itself is not revealed [68].

The fundamental anisotropy,  $r_0$ , can be obtained by measuring a vitrified dilute solution of the fluorophore in propylene glycol or glycerol at  $-70$  °C, though some groups measure at  $-10$  °C [68]. Under these conditions the fluorophores remain immobile during the lifetime of the excited state. Glycerol also forms a rigid glass at low temperature. However, glycerol typically displays more autofluorescence than propylene glycol. Nevertheless, the signal-to-noise ratio can be measured and if it's still satisfactory, then both can be used. In these rigid solutions, the anisotropy values,  $r_0$ , provide a measure of the angle between the absorption and emission dipoles. Generally, in all cases, either the  $r_0$  is measured or not, the solutions should be optically dilute to avoid depolarization due to emission and reabsorption, or due to resonance energy transfer. In these cases the lifetime becomes

smaller and this might cause problems to the anisotropy analysis, as will be explained in Section 2.4-6.4 (Perrin's equation), later on [68].

### 2.4-6.3 Measurement of steady-state anisotropies

There are two methods commonly used. These are the L-format, where a single emission channel is used, and the T-format, where the parallel and the perpendicular component are measured simultaneously through separate detection channels. The L-format method was utilized in this work. The procedure requires continuous illumination and four individual measurements,  $I_{HH}$ ,  $I_{HV}$ ,  $I_{VV}$  and  $I_{VH}$ , an excitation polarizer and an emission polarizer. The steady-state anisotropy was measured with vertical excitation, but the use of horizontal excitation would lead to the same result.

The emitted photons were detected by using a monochromator. Monochromators usually have different transmission efficiencies for different polarizations. Thus, rotation of the emission polarizer changes the measured intensities even if the emission is rapidly depolarized, where the intensities for parallel and perpendicular component are expected to be equal. Therefore, the task is to correct for these differences in the transmission efficiencies, and the related correction factor is called G-factor. Given that a small fluorophore is expected to rotate freely in solution, and thus the emission will be rapidly depolarized, the G-factor can be easily measured with freely diffusing fluorophores [68]. Let  $S_V$  and  $S_H$  be the sensitivities for vertical and horizontal polarization, respectively. Any measured difference in the intensities of the vertical and horizontal component must be due to the detection system. So,

$$\frac{I_{VV}}{I_{VH}} = \frac{S_V}{S_H} \frac{I_{\parallel}}{I_{\perp}} = G \frac{I_{\parallel}}{I_{\perp}} \Rightarrow \frac{I_{VV}}{I_{VH}} \frac{1}{G} = \frac{I_{\parallel}}{I_{\perp}} \quad [\text{Eq. 2.4 - 6.4}]$$

and from Eq. 2.4-6.1 and Eq. 2.4-6.4 we have:

$$r = \frac{I_{\parallel} - I_{\perp}}{I_{\parallel} + 2I_{\perp}} = \frac{\frac{I_{\parallel}}{I_{\perp}} - 1}{\frac{I_{\parallel}}{I_{\perp}} + 2} \Rightarrow r = \frac{I_{VV} - G I_{VH}}{I_{VV} + 2 G I_{VH}} \quad [\text{Eq. 2.4 - 6.5}]$$

$$\text{where } G = \frac{S_V}{S_H} = \frac{I_{VV}}{I_{VH}} = \frac{I_{HV}}{I_{HH}} \quad [\text{Eq. 2.4 - 6.6}]$$

The steady-state anisotropy can also be calculated by averaging the anisotropy decay,  $r(t)$ , over the intensity decay,  $I(t)$ :

$$r = \frac{\int_0^T r(t) I(t) dt}{\int_0^T I(t) dt} \quad [\text{Eq. 2.4 - 6.7}]$$

It becomes apparent from Eq. 2.4-6.7 that if the emission becomes rapidly depolarized, so  $r(t)$  tends to zero, then  $r$  also tends to zero, and this usually occurs with small fluorophores that diffuse freely in solution.

#### 2.4-6.4 The Perrin's equation

Rotational diffusion of fluorophores is a dominant cause of fluorescence depolarization, and most applications depend on the rate of rotation. For spherical rotors this is described by Perrin's equation [68]. As known, during the averaging process both the intensity decay and the anisotropy decay become single-exponentials. By solving Eq. 2.4-6.7 the result is Perrin's equation:

$$r = \frac{r_0}{1 + \frac{\tau}{\theta}} \quad [\text{Eq. 2.4 - 6.8}]$$

$$\text{where } \theta = \frac{\eta V}{RT} = \frac{\eta MW (h + \bar{v})}{RT} \quad [\text{Eq. 2.4 - 6.9}]$$

In the above-mentioned equations,  $r$  is the steady-state anisotropy,  $r_0$  the fundamental anisotropy,  $\tau$  the average lifetime,  $\theta$  the rotational correlation time, which is the rate of depolarization,  $\eta$  the viscosity of the buffer in Poise,  $V$  the volume of the rotating unit,  $T$  the absolute temperature,  $R$  the ideal gas constant ( $R \sim 8.31 \text{ J mol}^{-1} \text{ K}^{-1}$ ),  $h$  the hydration, and  $\bar{v}$  the specific volume of the protein. Values of  $\bar{v}$  for proteins are typically near  $0.73 \text{ ml/g}$ , and the hydration is near  $0.23 \text{ ml H}_2\text{O per g of protein}$ . Once the volume of the rotating unit is calculated, the hydrodynamic radius,  $r_h$ , can also be obtained.

Assuming that the fluorophore behaves like a spherical particle, the  $r_h$  can be calculated as follows:

$$r_h = \left( \frac{3V}{4\pi} \right)^{\frac{1}{3}} \quad [\text{Eq. 2.4 – 6.10}]$$

Perrin's equation displays an important feature. If the rotational correlation time is similar or much larger than the fluorescence lifetime,  $\theta$  cannot be detected because the time window, which is the fluorescence decay, would be too short and essentially, there would not be enough emitted photons.

#### 2.4-6.5 Time-resolved fluorescence anisotropy analysis

In a previous section, the measurement and interpretation of steady-state fluorescence anisotropies were described. These values are measured using continuous illumination, and represent an average of the anisotropy decay. However, additional information is available from measurements of the time-domain anisotropy, that is, the values of  $r(t)$  following pulsed excitation. The form of the anisotropy decay depends on the size, shape, and flexibility of the labelled molecule; it is usually multi-exponential. In this study, only time-domain anisotropy analysis was utilized.

Let us assume a fluorophore is excited with pulsed horizontal polarized light; the anisotropy decay is determined by measuring the decays of the horizontal ( $I_{\parallel}$ ) and the vertical ( $I_{\perp}$ ) polarized emission simultaneously. Initially, the excitation with pulsed light results in a population of fluorophores which is enriched in the parallel orientation. Generally, it is expected that the parallel component decays more rapidly than the perpendicular one. This occurs because the parallel component decays with a rate  $\tau$ , and rotation out of the horizontal orientation with a correlation time  $\theta$ . Even if the sample displays a single lifetime and a single correlation time, the intensity decays of the two different polarized components are multi-exponential:

$$I_{\parallel}(t) = \frac{1}{3} I(t) [1 + 2 r(t)] \quad [\text{Eq. 2.4 – 6.11}]$$

$$I_{\perp}(t) = \frac{1}{3} I(t) [1 - r(t)] \quad [\text{Eq. 2.4 - 6.12}]$$

As shown in a Section 2.4-6.1 the total intensity is equal to  $I_{\parallel} + 2GI_{\perp}$ , where  $G$  denotes the G-factor. Similarly, the total intensity decay is given by:

$$I_T(t) = I_{\parallel}(t) + 2 G I_{\perp}(t) \quad [\text{Eq. 2.4 - 6.13}]$$

The intensity decays of the two components can be used to calculate the time-domain anisotropy decay,  $r(t)$ :

$$r(t) = \frac{I_{\parallel}(t) - G I_{\perp}(t)}{I_{\parallel}(t) + 2 G I_{\perp}(t)} \quad [\text{Eq. 2.4 - 6.14}]$$

However, it is preferable to directly analyze the intensity decays of the polarized components rather than calculating the anisotropy values as mentioned above [68].

To obtain these observations on both the single-molecule and the ensemble level, a well-defined illumination and detection volume are needed, which can be achieved by a confocal microscope setup. The main feature of such a setup is a pinhole acting as a spatial filter.

The optical setup used in this work is depicted in Fig. 2.4-3.2.1. The typical sample volume placed on a clean cover-glass slide lie between 50 and 100  $\mu\text{l}$ . The concentration typically lies in the picomolar range or a few nM for ensemble measurements. In addition, each sample solution contained 0.001% of Tween-20 to minimize non-specific binding of labelled species to the surface. The setup used here offered the possibility of two-colour excitation, employing linearly polarized, pulsed laser beams of wavelengths  $\lambda_{\text{blue}}=470$  nm and  $\lambda_{\text{red}}=640$  nm. It is important to mention that the pulsed-laser diodes emit vertical polarized light, but due to a change in the orientation of the optical fibre, which couples the lasers with the microscope, the polarization of the emitted light also changes, from vertical to horizontal. Therefore, we have horizontal excitation. The pulsed beams were reflected by a dual-band dichroic mirror into a high numerical aperture water-immersion objective. To ensure that the diffraction-limited focal spot was placed in the solution, the focus was first set on the cover-glass surface (using the second back-reflection) and then placed well-above this reference ( $\sim 30$   $\mu\text{m}$ ). Every

time a fluorophore diffused through the focal volume, a burst of photons was observed. The emitted fluorescence was focused on a 50  $\mu\text{m}$  or 100  $\mu\text{m}$  pinhole, resulting in detection volumes of 1-3 fl. Depending on the required measurement, the fluorescence light passed through a second dichroic mirror (DM), and it was either split to two beams of almost equal intensity by a 50/50 beam-splitter or separated to its polarization components by a polarizing beam-splitter (PBS). Then the light was detected simultaneously by two/four highly sensitive detectors called Single Photon Avalanche Diodes (SPADs).

The output was transferred to a Time-Correlated Single-Photon Counting (TCSPC) module, saving the data in the Time-Tagged Time-Resolved (TTTR) mode. This means that each detected photon is registered with three tags [74]:

- the channel detecting the photon event, in our case 1, 2, 3 or 4; this also yields information about the spectral region and polarization of each photon,
- the arrival time of the photon with respect to the laser-pulse, called microtime, typically located in the picosecond to nanosecond regime; this is crucial for building up the TCSPC histograms (Fig. 2.4-6.5.1)
- the arrival time of the photon with respect to the beginning of the measurement, called macrotime.

For TCSPC measurements it is necessary to use pulsed lasers, otherwise a suitable reference point for microtime data would be missing [74].

It becomes apparent from Eq. 2.4-6.11 and 2.4-6.12 that the formula of the intensity decay must be known beforehand. The intensity decay is usually a multi-exponential function, depending on the geometry of the measured fluorophore as well as on photophysical phenomena (transition to triplet states, quenching, etc.). The most convenient way is to measure a sample without a polarizing beam-splitter. This means that the photons will arrive only at SPAD3, if the sample is excited with blue colour (also see Fig. 2.4-3.2.1). Then, we would have to find the best fit of the measured data. But it is not so straightforward. It should be noted that the raw data,  $N(t)$ , is a convolution between the excitation pulse,  $P(t)$ , the detectors' response,  $R(t)$ , and the

intensity decay,  $I(t)$ . The convolution between the excitation pulse and the detectors' response is called instrument response function (IRF).

$$N(t) = P(t) \otimes R(t) \otimes I(t) \quad [\text{Eq. 2.4 - 6.15}]$$

Similarly, for both polarizations we have (Fig. 2.4-6.5.1):

$$N_{\parallel}(t) = \text{IRF}_{\parallel} \otimes I_{\parallel}(t) \quad \text{and} \quad N_{\perp}(t) = \text{IRF}_{\perp} \otimes I_{\perp}(t) \quad [\text{Eq. 2.4 - 6.16}]$$

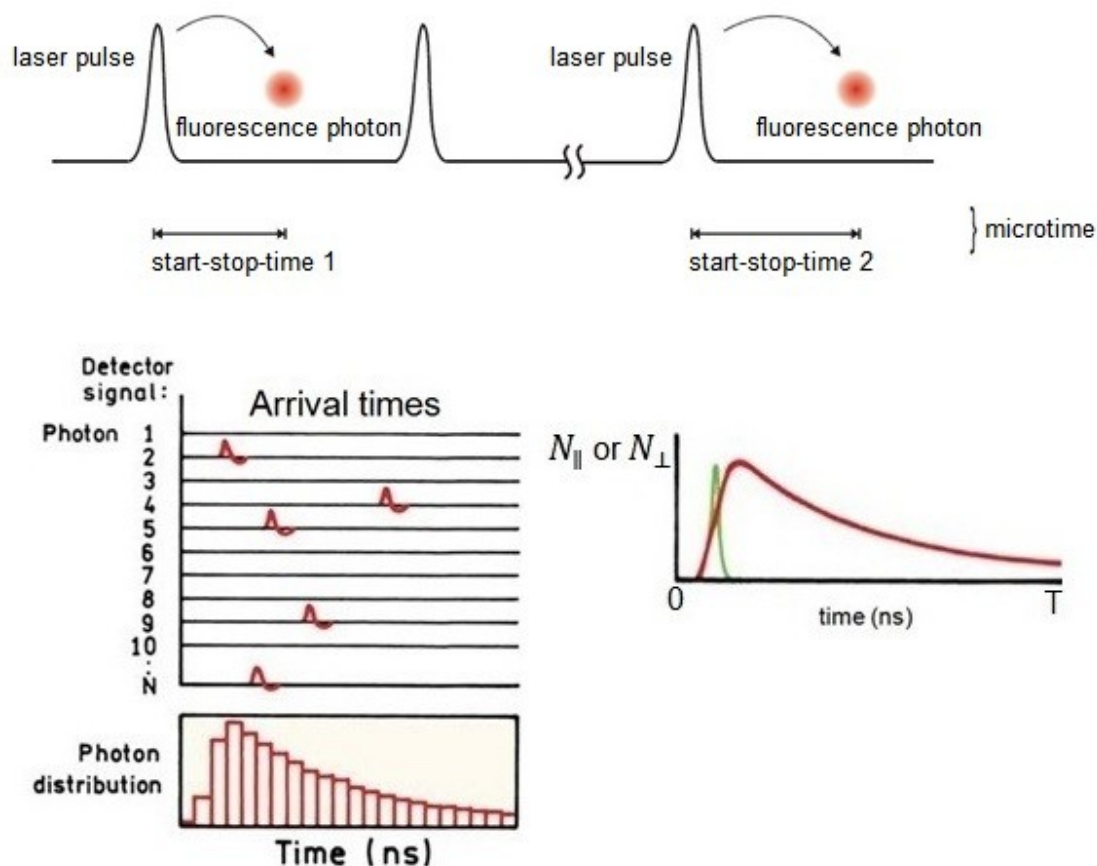


**Fig. 2.4-6.5.1.** Example of a TCSPC histogram, the instrument response function (IRF) is shown in green,  $N_{\parallel}$  and  $N_{\perp}$  denote the raw data, and  $T$  the period [68, 74].

The IRF can be obtained by focusing the beam on the upper surface of a glass slide and measuring the backscattered light. But this method is not totally correct because it can introduce systematic errors to the data analysis, called colour-effects of the IRF. It should be taken into consideration that a percentage of the energy of the photons can be dissipated due to the inelastic collisions that occur with the molecules of the glass slide. Therefore, the

outcome is a bundle of photons of several wavelengths, and because of the major dual-band dichroic mirror, a big number of photons is not detected. Consequently, the measured shape of the IRF is not exactly the real one. Rather, a fluorophore which exhibits the same emission spectrum as the dye of our interest, but with very short lifetime, a few hundred picoseconds, should be measured [68].

The mathematical method used for analysis of intensity and anisotropy decay laws is called iterative 'reconvolution'. The concept is to find a formula that if one convolutes with the instrument response function (IRF), the result best matches the measured data [68]. To perform such analysis, this algorithm was written in Matlab code by Daryan Kempe (ICS-5: Molecular Biophysics, Forschungszentrum Jülich). Concerning intensity decays of polarized components, global fitting was implemented, where one seeks to find simultaneously the best fit for both components, in order to analyze rotational correlation times.

A correction factor,  $G$ , for different detection efficiencies of the SPADs is also taken into consideration. In this work, the  $G$ -factor was obtained using the tail matching method. In principle, it is based on the fact that after the emission is depolarized, the intensity decay curves of the parallel and perpendicular components should not show any difference. In case there is a difference, the  $G$ -factor is the multiplicative factor that corrects for that deviation. Taking advantage of that, aqueous solutions containing free dye holding the same spectral characteristics and about the same concentration as the specimen, and with a depolarization time substantially shorter than the fluorescence lifetime, e.g. Alexa488, were measured.

Another feature that was taken into consideration was the depolarization that can be caused by objectives of high numerical aperture. This can be corrected by inserting two correction factors in Eq. 2.4-6.11 and 2.4-6.12,  $k_1$  and  $k_2$ , respectively. So, these equations will become [75]:

$$I_{\parallel}(t) = \frac{1}{3} I(t) [1 + (2 - 3 k_1) r(t)] \quad [\text{Eq. 2.4 - 6.17}]$$

$$I_{\perp}(t) = \frac{1}{3} I(t) [1 - (1 - 3 k_2) r(t)] \quad [\text{Eq. 2.4 - 6.18}]$$

Regarding the objective of the confocal setup in our lab it was found that  $k_1$  equals 0.33, and  $k_2$  equals zero (private communication from Daryan Kempe, ICS-5: Molecular Biophysics, Forschungszentrum Jülich).

Another prerequisite for Time-Correlated Single-Photon Counting is to register only one photon per excitation/emission cycle. Due to the active quenching electronics of the SPADs, which is to some extent time-consuming, after a photon is detected, a dead time (~60 ns) occurs in which no photons can be registered anymore. If the number of photons occurring in one excitation cycle was typically bigger than one, the system would very often register the first photon, but miss the following ones. This would lead to an overrepresentation of the photons arriving first. In lifetime histograms, where the microtime is binned according to the available time-channels, this is called pile-up effect [68]. For that reason, it is crucial to keep the probability of cycles with more than one photon low. To quantify this demand, it is recommended to detect one photon in 20-100 excitation pulses. Thus, the count-rate at the detector should be less than 1% of the excitation rate. An excitation frequency of 20 MHz was used here; therefore, the count-rates had to be kept below 200 kHz. However, it is recommended by Picoquant to keep the count-rate below the 1/10 of that threshold. To achieve this, concentrations of fluorophores should typically not exceed 5 nM (depending on the dye used). Accordingly, the same apply to measurements of IRF, the count-rate was kept at around 1200 Hz.

In the last part of this section, the utilized anisotropy decay laws will be described. Depending upon the size and shape of the fluorophore, and its local environment, a wide variety of anisotropy decay laws are possible. A spherical molecule displays a single rotational correlation time. Anisotropy decays can be more complex if the fluorophore is non-spherical. Another origin of complex anisotropy decays is the flexibility of protein segments (e.g.  $\alpha$ -helix) with a fluorophore attached, within a larger macromolecule [68]. In this study, we used the biarsenical ligand FIAsh because it binds rigidly to a tetra-Cys motif in a larger  $\alpha$ -helix, and thus the movement of the fluorophore will follow the movement of the protein, or of the  $\alpha$ -helix, at least. Taking advantage of that, we explored the possibility to use this fluorophore as a

probe to detect the increase in the size of a nascent polypeptide chain, i.e. while it emerges from the ribosomal tunnel.

If a molecule is non-spherical, there are different rotational rates around each axis. The theory for rotational diffusion of anisotropic rotors is complex. It is now agreed that the anisotropy is expected to decay as a sum of exponentials:

$$r(t) = \sum_{j=1}^5 r_{0,j} e^{-\frac{t}{\theta_j}} \quad [\text{Eq. 2.4 - 6.19}]$$

There may be as many as five exponential terms for an asymmetric body, but in practice only two correlation times are expected to be distinguishable. The values of  $r_{0,j}$  and  $\theta_j$  are complex functions of the rates of rotation around the molecular axes of the non-symmetric body and the orientation of the absorption and the emission dipoles relative to these axes. Moreover, it is important to remember that the theory for rotation of non-spherical molecules assumes hydrodynamic behaviour, in which the rates of rotation are determined by the viscous drag of the solvent. This theory fails with many small molecules in solution. This failure occurs when the molecule slips within the solvent or the molecule is not hydrogen bonded to the solvent. A multi-exponential anisotropy decay can be recovered, but the values of  $r_{0,j}$ , and rotational correlation times,  $\theta_j$ , might not be reasonable [68].

Decays of fluorescence anisotropy can be more complex even for isotropic rotors, if these molecules are contained in an anisotropic environment, where rotational diffusion can be hindered. By 'hindered' we mean that the angular range of the rotational motion is limited. In such cases a limiting anisotropy,  $r_\infty$ , is observed at times which are long compared to the fluorescence lifetime. The anisotropy decay for the simplest case is described by [68][76]:

$$r(t) = (r_0 - r_\infty) e^{-\frac{t}{\theta}} + r_\infty \quad [\text{Eq. 2.4 - 6.20}]$$

This formula is also called 'hindered rotor' model. The constant term  $r_\infty$  has been interpreted as resulting from an energy barrier that prevents rotational diffusion of the fluorophore beyond a certain angle  $\varphi_{\max}$ .

$$A_\infty = \frac{r_\infty}{r_0} = \left[ \frac{1}{2} (1 + \cos \varphi_{\max}) \cos \varphi_{\max} \right]^2 \quad [\text{Eq. 2.4 - 6.21}]$$

Additionally, considering an isotropic overall tumbling motion of the dye-protein complex as a whole, described by a rotational correlation time  $\theta_G$  the anisotropy of the fluorescence of the protein-attached dye is given by:

$$r(t) = r_0 \left[ (1 - A_\infty) e^{-\frac{t}{\theta}} + A_\infty \right] e^{-\frac{t}{\theta_G}} \quad [\text{Eq. 2.4 - 6.22}]$$

These formulas are known as 'wobbling-in-a-cone' models (Fig. 2.4-6.5.2 A). The orientation of the dye is also affected by the local flexibility of the protein, which may be of particular interest. The resulting surface changes affect cone orientation and possibly, also cone angle (Fig. 2.4-6.5.2 B, top). In a simple model, these protein-related conformational changes may also be described by a restricted motion of the dye cone within a (second) cone (Fig. 2.4-6.5.2 B, bottom), and this effect gives rise to a second decay factor:

$$r(t) = r_0 \left[ (1 - A_1) e^{-\frac{t}{\theta_1}} + A_1 \right] \left[ (1 - A_2) e^{-\frac{t}{\theta_2}} + A_2 \right] e^{-\frac{t}{\theta_G}} \quad [\text{Eq. 2.4 - 6.23}]$$

This is also known as 'cone-in-a-cone' model [76].

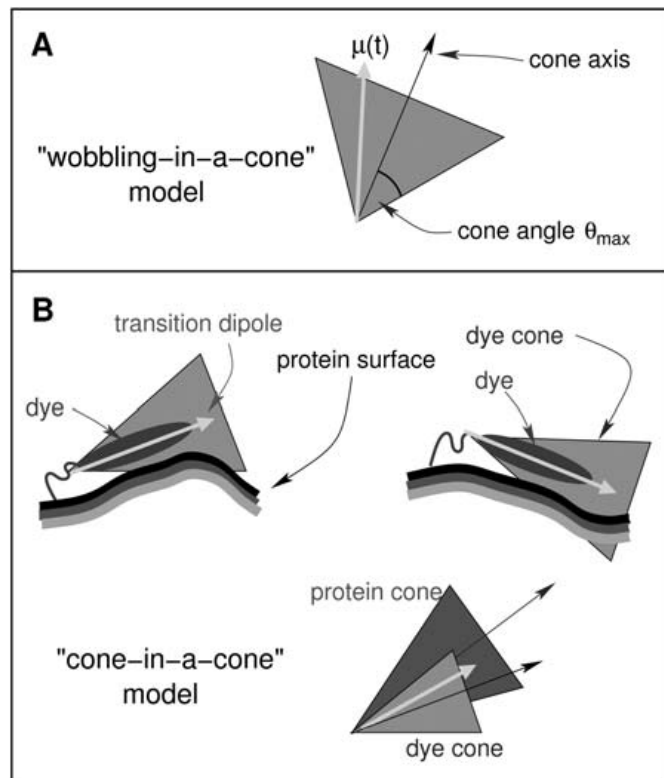


**Fig. 2.4-6.5.2.**

(A) *Wobbling-in-a-cone model.*

The transition dipole moment  $\hat{\mu}$  is assumed to freely diffuse inside a cone with a semicone angle  $\phi_{max}$ .

(B) *Cone-in-a-cone model.*

The two top figures indicate a motion, which is due to the protein flexibility. The bottom figure shows how the protein flexibility is described in the cone-in-a-cone model by the protein cone, within which the dye cone freely diffuses [76].

### 3. Results

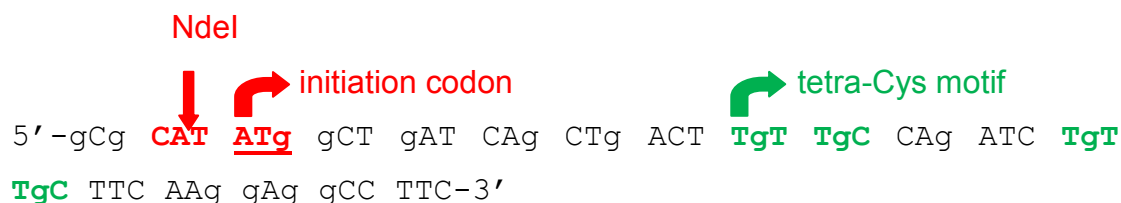
#### 3.1 Preparation and purification of CaM containing the tetra-Cys motif near the N-terminus

One of our major objectives was to study the folding of CaM while it is synthesized on the ribosome using a dye (FIAsH) that can be rigidly attached to a tetra-Cys motif. What was necessary at the beginning was to check whether we are able to study the mutated full length CaM itself, and to use the final result as a control. Therefore, we prepared first the plasmid that carried the mutated CaM fused with a His<sub>6</sub>-tag, the protein was subsequently overexpressed in bacteria, and was finally purified.

##### 3.1-1 Isolation of the mutated gene of CaM containing the tetra-Cys motif near the N-terminus and a His<sub>6</sub>-tag at the C-terminus

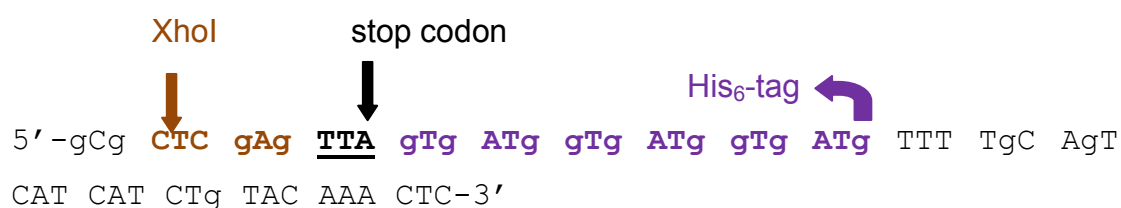
Polymerase Chain Reaction (PCR) was utilized to incorporate the sequence encoding the tetra-cysteine motif (Cys-Cys-X-Y-Cys-Cys, X and Y are still the amino acids of the wild-type sequence) in the sequence of CaM gene from *Bos taurus* (Bovine). We designed a gene of CaM with the following mutations, E7C, E8C, A11C, and E12C. Two primers were used. An oligonucleotide of 57 nt as forward primer containing the sequence for the tetra-Cys motif as well as a few additional nucleotides at the 5'-end which serve as restriction site of NdeI. The NdeI restriction site is shown in red, the initiation codon ATG is also underlined, and the codons for Cys in green.

##### BtaCaMmut(4Cys)-6His\_FP



Accordingly, an oligonucleotide of 57 nt was used as reverse primer containing the complementary sequence of the 3'-end of the gene as well as the complementary of 6 triplets that code for histidines, and additional nucleotides at the 5'-end which serve as restriction site for XhoI. The His<sub>6</sub>-tag is shown in purple, the stop codon TAA in black and underlined, and the XhoI restriction site in orange. The final construct contains the His<sub>6</sub>-tag so that the mutant can be overexpressed and purified at a later step.

BtaCaMmut(4Cys)-6His RP



The wild-type sequence of CaM gene that was already cloned into pET11a was used as a template (courtesy by Prof. Dr. Arnd Baumann, ICS-4: Cellular Biophysics, Forschungszentrum Jülich). The PCR conditions described in Materials and Methods were utilized, and the PCR product was electrophorized in 1 % agarose gel (Fig 3.1-1). The band at ~450 bp was sliced from the gel and the DNA was extracted.

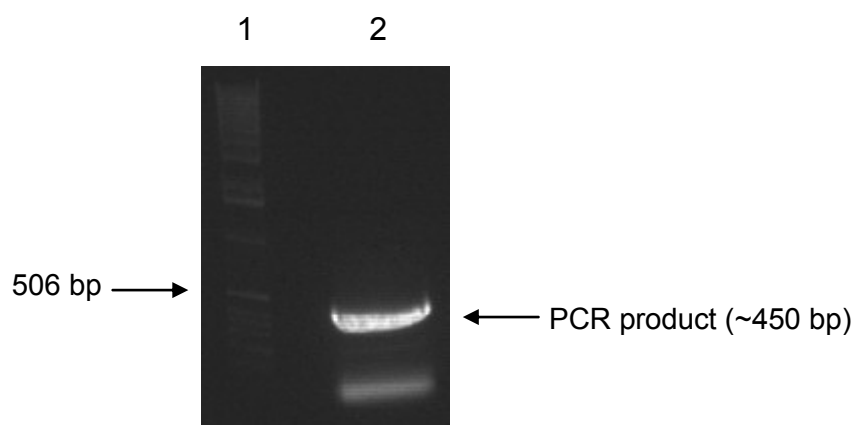


**Fig. 3.1-1.** PCR with the wild-type gene of CaM used as template to isolate the mutated gene of CaMmut(4Cys)-6His. The PCR product was analyzed by electrophoresis in 1 % agarose gel. Lane 1: size markers, Lane 2: PCR product.

3.1-2 Cloning of the gene of CaMmut(4Cys)-6His into pCR-Blunt, and subsequently into pET27b

The extracted PCR product was first ligated with pCR-Blunt vector using T4 DNA ligase. The pCR-Blunt ligated product can be easily checked by DNA sequencing. Afterwards, it can be digested and inserted in an expression vector. TOP10 *E. coli* cells were transformed with the ligation reaction, they were streaked on a kanamycin-selective agar plate, and incubated at 37 °C overnight. Then, plasmid isolation from minipreps, and screening by digestion with NdeI and XhoI followed. The next step was sequencing analysis that was utilized to check if the nucleotide sequence of the insert is the desired one. Once we had the correct clone, it was cloned into pET27b vector following in principle the same procedure. In the beginning, both pCR-BLUNT-insert and pET27b were digested with the same set of restriction endonucleases, NdeI and XhoI. They were electrophorized in 1 % agarose gel, and the bands corresponding to the insert and the linearized pET27b vector were sliced from the gel and DNA was extracted. The pET27b vector was also dephosphorylated. A mixture of insert and pET27b was heated up to 70 °C and cooled down, then fast ligation buffer of T4 DNA ligase and the enzyme itself were added, and incubation at room temperature for 10 min followed. TOP10 *E. coli* cells were transformed with the ligation reaction, they were streaked on a kanamycin-selective agar plate, and incubated at 37 °C overnight. Finally, plasmid isolation from minipreps, and screening by digestion with NdeI and XhoI followed. Henceforth, in any reference to preparation of new constructs and cloning in vectors, the above-mentioned protocol was followed.

3.1-3 Purification of CaMmut(4Cys)-6His by Ni-NTA column and size-exclusion chromatography

The first step to purify CaM with the four cysteines was to overexpress it in bacteria. Therefore, *E. coli* BL21 (DE3) cells were transformed with the pET27b vector containing the gene of the mutant, they were streaked on a

kanamycin-selective agar plate, and overnight incubation at 37 °C followed. Colonies from the agar plate were picked, and kanamycin-selective small cultures of 5 ml were inoculated with these colonies. Overnight incubation at 37 °C followed. A kanamycin-selective big culture of 200 ml was inoculated with cells from a small culture and incubation at 37 °C followed. When the OD<sub>600</sub> was equal to 0.5, IPTG was added to a final concentration 1 mM to induce the overexpression, and incubation at 37 °C for 45 min followed. Then, cells were harvested by centrifugation. To check if the protein was overexpressed, 1 ml of culture was kept before and after addition of IPTG. The cells of these 1 ml samples were centrifuged and the pellet was dissolved in buffer 20 mM Tris-HCl, 6 M urea, pH 7.5. The cells were disrupted by three freeze-thaw cycles and, then, centrifugation followed. Finally, the supernatant was electrophorized in a 15 % SDS-polyacrylamide gel (Fig. 3.1-3.1). Visualization of protein bands was realized by staining with Coommasie blue and destaining by washing the gel with 10 % acetic acid.

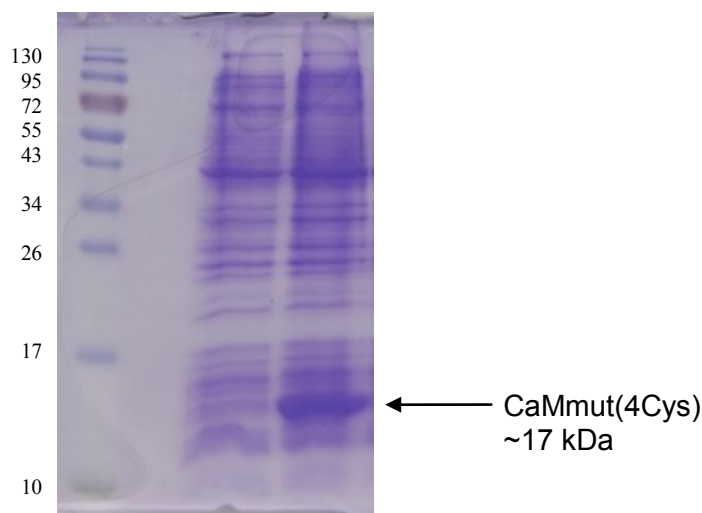


**Fig. 3.1-3.1.** Overexpression of CaMmut(4Cys)-6His in BL21 DE3 cells. IPTG was added when OD<sub>600</sub> was equal to 0.5.

The next step was to purify CaM utilizing a batch purification protocol as described in Section 2.3-1 in Materials and Methods. Then, the collected samples were electrophorized again in a 15 % SDS-polyacrylamide gel to visualize the proteins (Fig. 3.1-3.2).

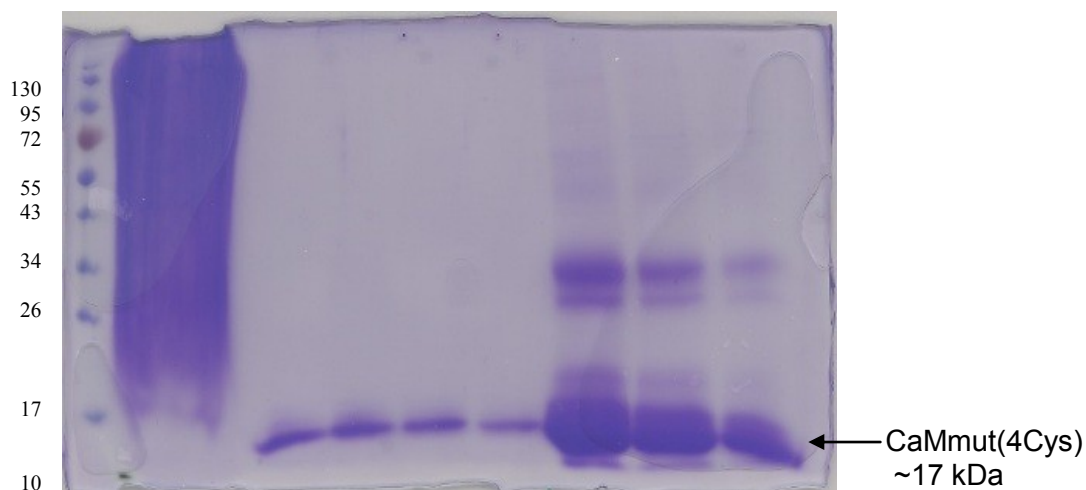


**Fig. 3.1-3.2.** Purification of CaMmut(4Cys)-6His by Ni-NTA column following a batch purification protocol. The three last lanes are the elutions. Perhaps the band at ~34 kDa is two monomers linked by a disulphide bond.

The collected elutions also contained imidazole, but since imidazole would disturb further experiments, it was removed by size-exclusion chromatography. A PD-10 column (Sepharose G-25) was utilized for this purpose. The protein was now dissolved in 10 mM MOPS, 500 mM NaCl, pH 7.4. The fractions were collected and the protein concentration was calculated by absorption measurements at 280 nm. Herein, it should be noted that the corrected molar absorption coefficient, which also takes into consideration the presence of cysteine residues, was used ( $\epsilon=3230 \text{ M}^{-1}\text{cm}^{-1}$ ).

The collected fractions were also electrophorized in a 15 % SDS-polyacrylamide gel to visualize the proteins (Fig. 3.1-3.3). Henceforward, in any reference to protein purification, the above-mentioned procedure was followed.

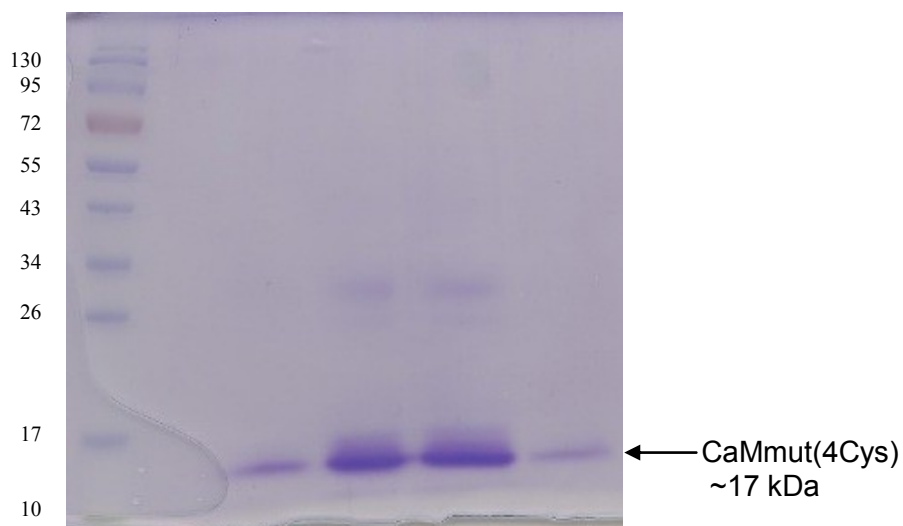


**Fig. 3.1-3.3.** Excess of imidazole was removed by size-exclusion chromatography.

## 3.2 Characterization of CaM with the tetra-Cys motif

Before starting the steady-state and time-resolved fluorescence measurements, it was necessary to perform experiments to check if the mutant can function, and if the secondary structure has been retained. It was also essential to check if labelling of the mutant with FIAsH is possible.

### 3.2-1 Functionality tests with Ca<sup>2+</sup>

It is known that CaM is a calcium-sensor. Its function is to bind calcium ions as one of the first steps of a biochemical path. To check if the mutated CaM is still able to function, some control experiments had to be performed. Some of them are costly, while other protocols cost nothing; the latter was our choice and this protocol is described in Section 2.4-4 in Materials and Methods. The procedure is simple. Both the mutant and the wild-type protein were diluted in an apo-buffer as well as in a Ca<sup>2+</sup>-saturated buffer to final concentration 6  $\mu$ M, and both were left at room temperature for 1 hour. Then, the excitation and the emission spectra of phenylalanines as well as the excitation and the emission spectra of tyrosines were measured (see figures in next pages).

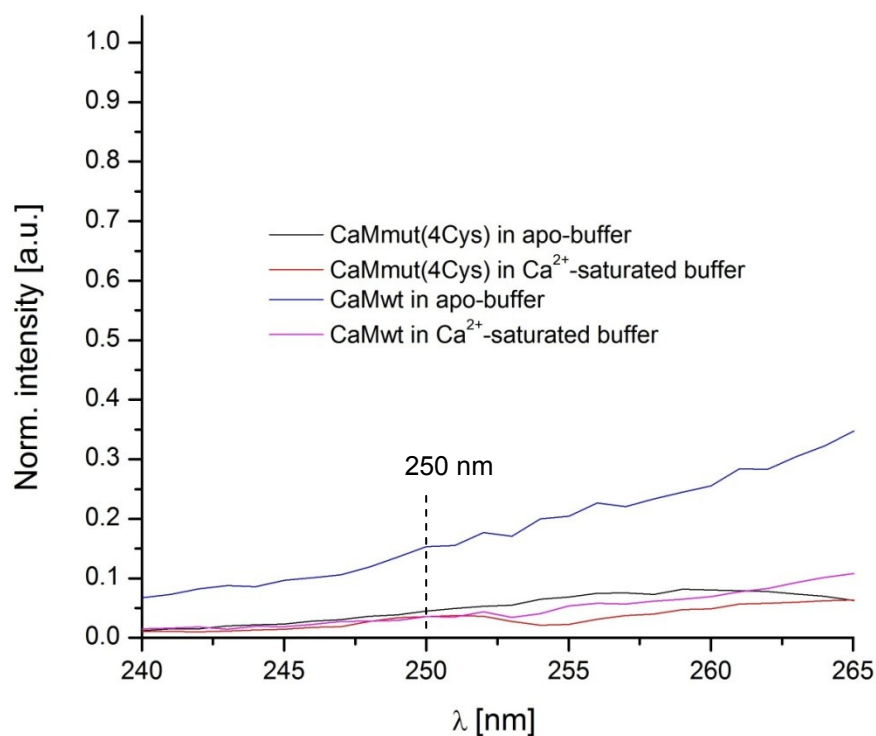


Fig. 3.2-1.1. Excitation spectra of phenylalanine, 240-265 : 280.

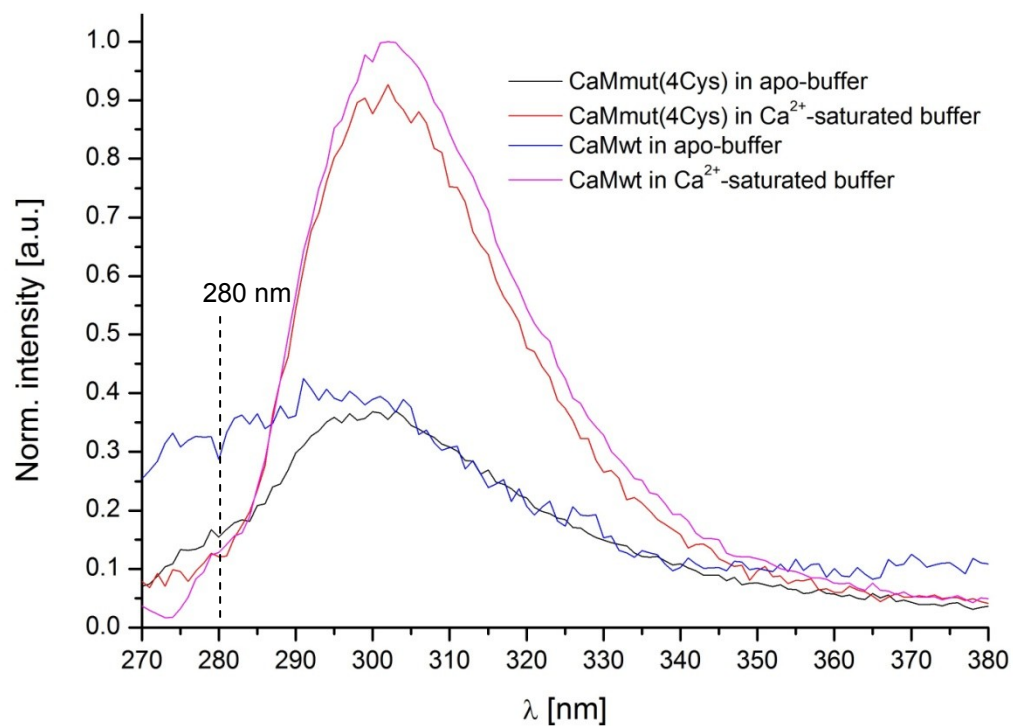
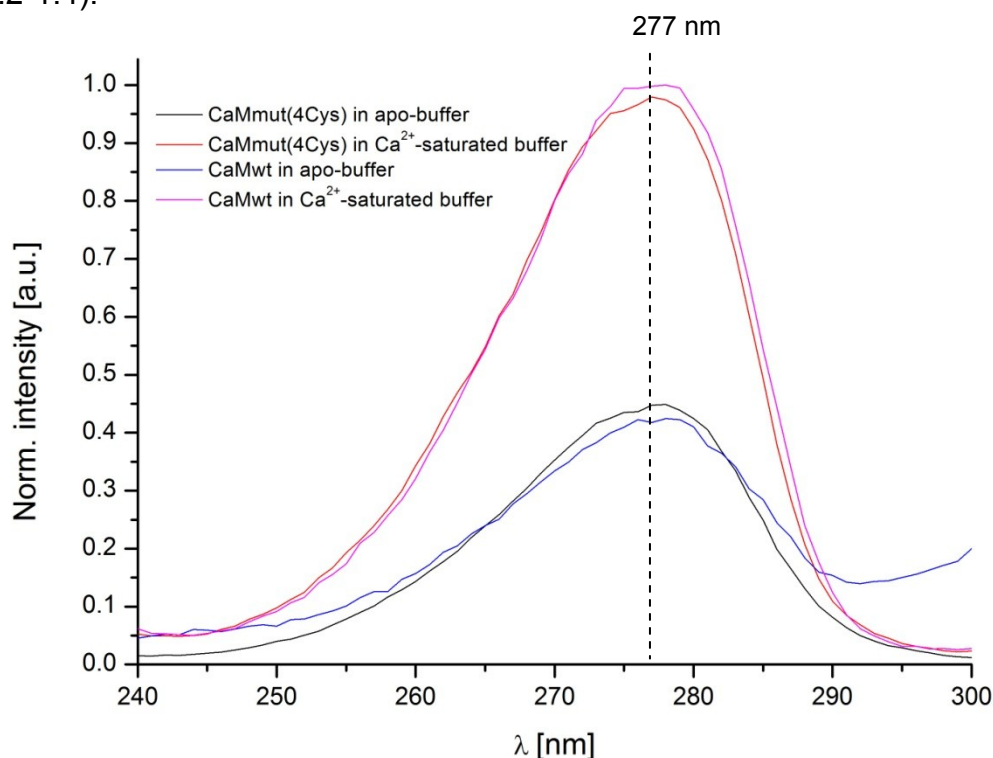
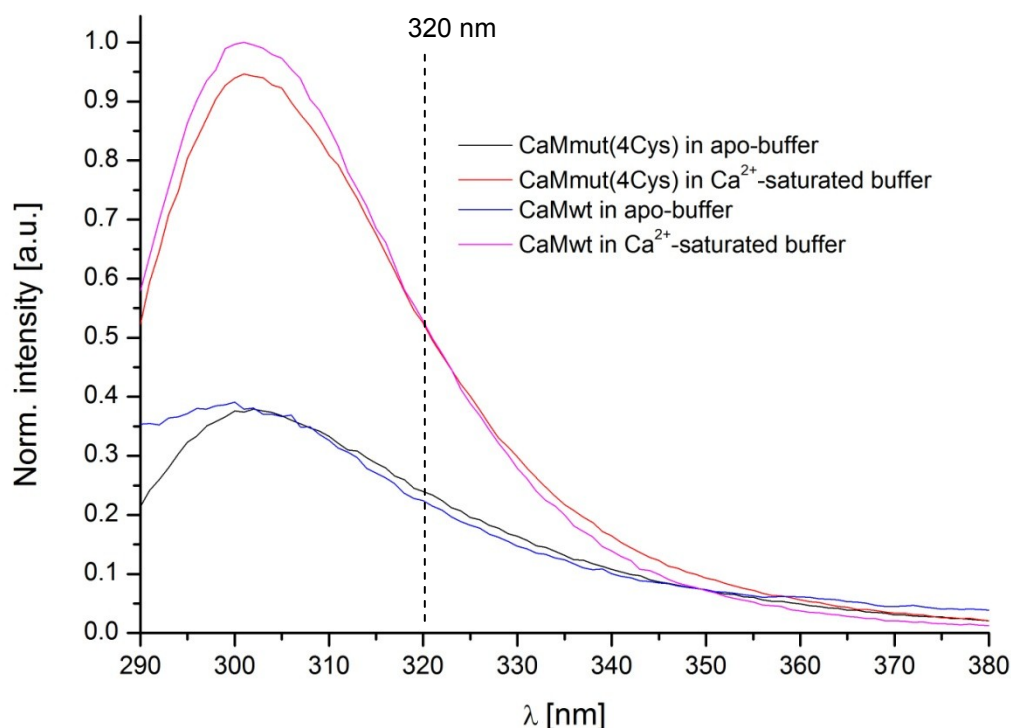


Fig. 3.2-1.2. Emission spectra of phenylalanine, 250 : 270-380.

It can be observed in the figures above (Fig. 3.2-1.1 and 3.2-1.2) that the N-terminal loops of the mutant cannot bind  $\text{Ca}^{2+}$ , while those of the wild-type can bind  $\text{Ca}^{2+}$ . This comes as no surprise since hydrophilic amino acids of the wild-type sequence near the N-terminus were mutated to cysteines whose side chains are hydrophobic (hydropathy index: +2.5). It is rather probable that the structure has also changed. An increase in the intensity at around 305 nm upon binding of  $\text{Ca}^{2+}$  can also be observed in the emission spectrum above (Fig. 3.2-1.2). This might be consistent with the point of view that upon  $\text{Ca}^{2+}$  binding to the C-terminal loops, a change in the tertiary structure is induced and phenylalanines in the C-terminal domains come closer to the C-terminal tyrosines and resonance energy transfer occurs [73]. Most remarkable is that an increase in the intensity is observed for both the mutant and the wild-type. This supports the idea that the C-terminal domains of the mutated CaM retained their wild-type secondary structure, while this is uncertain for the N-terminal ones. The fact that the emission spectrum of Phe is noisy could be attributed to the low molar absorption coefficient of Phe ( $\sim 4 \text{ M}^{-1}\text{cm}^{-1}$ ). The binding of  $\text{Ca}^{2+}$  to the C-terminal loops of both proteins can also be confirmed by observing the following spectra of tyrosine (Fig. 3.2-1.3 and 3.2-1.4).



**Fig. 3.2-1.2.** Excitation spectra of tyrosine, 240-300 : 320.



**Fig. 3.2-1.4.** Emission spectra of tyrosine, 277 : 290-380.

Indeed, an increase in the intensities of both the excitation and the emission spectra can be observed. This means that the C-terminal loops can bind  $\text{Ca}^{2+}$ , and presumably, the C-terminal domains of the mutant retained their wild-type secondary structure.

### 3.2-2 Circular dichroism (CD) measurements on CaMmut(4Cys) and CaMwt, both in apo-buffer and upon $\text{Ca}^{2+}$ binding

In order to prove that the secondary structure of CaM had not been significantly altered by the introduction of the cysteines, CD spectroscopy was employed. Both the mutant and the wild-type protein were diluted in either an apo-buffer, 10 mM MOPS, 500 mM NaCl, pH 7.4, or buffer containing  $\text{Ca}^{2+}$ , 10 mM MOPS, 500 mM NaCl, 15  $\mu\text{M}$   $\text{CaCl}_2$ , pH 7.4, and they were left at room temperature for 1 hour. Subsequently, a CD spectrum was acquired for each protein (Fig. 3.2-2).

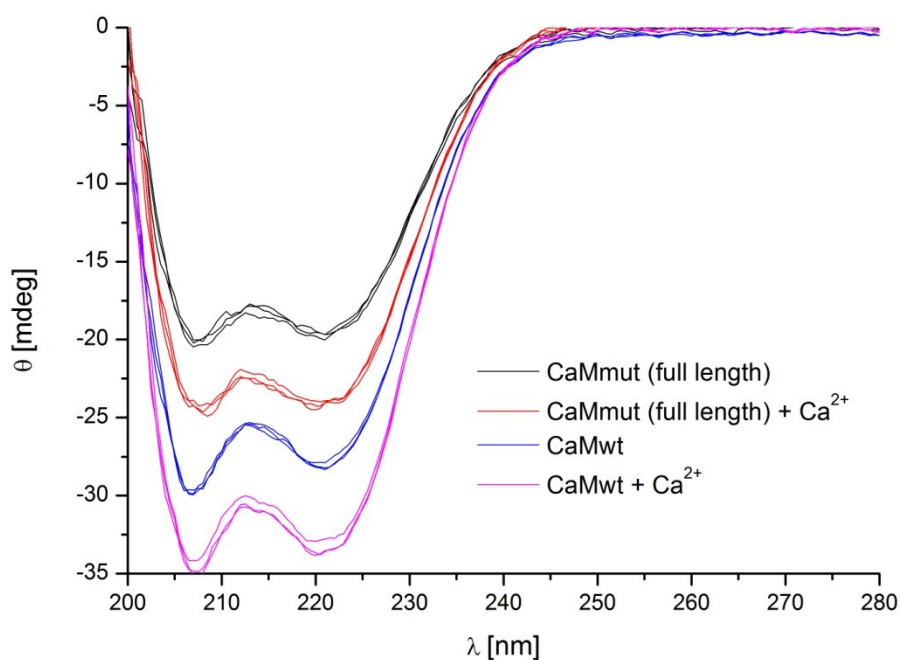


**Fig. 3.2-2.** CD spectra of CaMmut(4Cys) and CaMwt both in the absence and the presence of  $\text{Ca}^{2+}$ . The concentration of both proteins was 0.2 mg/ml.

It can be inferred from the CD spectra in Fig. 3.2-2 that the exchange of the four amino acids perturbs the secondary structure of CaM. Regarding the apo-proteins, an almost 30 % decrease in the ellipticity of the mutant is observed. As it can be observed in Fig. 3.2-2, three independent measurements were performed in each case and the error was very low, less than 5 %. Herein, it should be mentioned that whenever the mutant was purified and the ellipticities were measured, a 10-30 % decrease in the CD signal was observed. If the number of amino acids from a crystal structure of CaM (PDB: 1PRW) that comprise the  $\alpha$ -helices is calculated, then 30 % of them is almost 30 amino acids. Actually, four amino acids of the N-terminal sequence were mutated to cysteines, and the 30 % observed deviation ( $\sim 30$  amino acids) could be assigned to the first  $\alpha$ -helix. This does not necessarily mean that only the first  $\alpha$ -helix is not folded. The 30 % of the total  $\alpha$ -helical content is lost. This finding is also in agreement with the results from functionality tests with  $\text{Ca}^{2+}$ , as described earlier. Perhaps, there is a change

in the secondary structure of the N-terminal part of the mutant so that the N-terminal domains cannot bind  $\text{Ca}^{2+}$  any more. Upon addition of  $\text{Ca}^{2+}$ , a significant change is observed for both proteins. Both ellipticities are increased. This is consistent with what is published about how CaM behaves upon  $\text{Ca}^{2+}$  binding. The conformation of the protein becomes more ordered, with higher  $\alpha$ -helical content when  $\text{Ca}^{2+}$  is bound [77].

### 3.2-3 Labelling of CaMmut(4Cys) with FIAsh

First, the optimal conditions for labelling of CaM with the biarsenical ligand FIAsh had to be found. Several labelling reactions were performed, where the ratio between the concentrations of protein and dye was different as well as the temperature at which the labelling took place. CaM was dissolved in labelling buffer (10 mM MOPS, 500 mM NaCl, 1 mM TCEP, pH 7.4) to final concentrations of 20  $\mu\text{M}$  or of 4  $\mu\text{M}$ . Labelling reactions were performed both at room temperature (20 °C) and at 37 °C. The labelling mixtures were degassed for 30 min under vacuum 250 mbar, and were left at room temperature for 2.5 h, so that the disulphide bonds are reduced. Then, FIAsh was added to final concentration 4  $\mu\text{M}$  in the presence of nitrogen gas in all cases. The labelling reactions took place in complete darkness. There were two reactions with a molar ratio between protein and dye of 5:1, and another two of 1:1. Finally, the eppendorf tubes were stored at 4 °C, again in complete darkness, for 2 days. Potential excess of dye was removed by size-exclusion chromatography (Sephadex G-25). The concentration of FIAsh in the eluted fractions (1 ml) was acquired by measuring the absorbance at 508 nm ( $\epsilon_{\text{max, FIAsh}} \approx 74,000 \text{ M}^{-1} \text{ cm}^{-1}$ ). In the following table, we can observe the moles of FIAsh that we were contained in each fraction compared to the moles of FIAsh that was initially added to the labelling mixtures. In this way, the percentage of the dye molecules that were attached to the protein can be roughly calculated. But it should be noted that the label ratio is defined in a different way. It is the percentage of the labelled protein molecules.

| Temperature (°C) | Protein:dye ratio in the labelling reaction | FIAsH content in the fractions (pmoles) | Total number of moles of FIAsH (pmoles) | Dye attached to protein <sup>a</sup> |
|------------------|---|---|---|--------------------------------------|
| 37 °C            | 1:1   | <i>Fr. 8</i> : 200                      | 530                                     | ~ 30 %                               |
|                  |   | <i>Fr. 9</i> : 250                      |   |                                      |
|                  |   | <i>Fr. 10</i> : 80                      |   |                                      |
| R.T. (20 °C)     | 1:1   | <i>Fr. 8</i> : 190                      | 500                                     | ~ 25 %                               |
|                  |   | <i>Fr. 9</i> : 230                      |   |                                      |
|                  |   | <i>Fr. 10</i> : 80                      |   |                                      |
| 37 °C            | 5:1   | <i>Fr. 8</i> : 600                      | 1900                                    | ~ 95 %                               |
|                  |   | <i>Fr. 9</i> : 900                      |   |                                      |
|                  |   | <i>Fr. 10</i> : 400                     |   |                                      |
| R.T. (20 °C)     | 5:1   | <i>Fr. 8</i> : 520                      | 1440                                    | ~ 70 %                               |
|                  |   | <i>Fr. 9</i> : 670                      |   |                                      |
|                  |   | <i>Fr. 10</i> : 250                     |   |                                      |

**Table 3.2-3.** Labelling reactions of CaM with FIAsH at different conditions.

<sup>a</sup> All reactions contained 2000 pmoles of FIAsH.

As it can be inferred from the table above, the most dye molecules (90-100 %) were attached to the tetra-Cys motif when the ratio between protein and dye in the labelling reaction was 5:1, and when the reaction took place at 37 °C. However, the label ratio that could be achieved was low, around 20 %. It is speculated that the mechanism of the attachment of a dye with four cysteines is more complicated than it is with dyes that can be attached to cysteines through a single covalent bond [77]. Perhaps, this is the reason why low labelling efficiency was observed. Nevertheless, that would not cause any problem to the measurements because unlabelled CaM is not detected.

### 3.2-4 Characterization of the CaM-FIAsH complex

An argument that can be raised is that there could still be free diffusing dye in the collected fractions. Therefore, a calculation of a label ratio is not enough. More control experiments are needed to check if this argument is plausible. But there are some advantages with the dye that is utilized in this study. One of them is that the Stokes shift observed for free diffusing FIAsH-EDT<sub>2</sub> in solution is smaller compared to that of FIAsH attached to peptides containing the tetra-Cys motif. The Stokes shift of peptide-FIAsH is also given in the protocol of how one can produce biarsenical ligands like FIAsH-EDT<sub>2</sub>; the emission maximum of peptide-FIAsH is around 528 nm [78]. Absorption and fluorescence measurements were performed for both freely diffusing FIAsH and CaM-FIAsH complex, and the data were normalized to unity to compare the Stokes shift (Fig. 3.2-4.1). Indeed, the above-mentioned Stokes shift was also observed when FIAsH reacted with the protein of our interest.

Another advantage of FIAsH-EDT<sub>2</sub> is that it becomes highly fluorescent when it is bound to its target. The quantum yield of the FIAsH-peptide complex is 0.49, whereas FIAsH-EDT<sub>2</sub> is much less fluorescent. The small size of EDT (1,2-ethanedithiol) probably allows rotation of the aryl-arsenic bond and quenching of excited state is caused by vibrational deactivation or photoinduced electron transfer. On the contrary, the peptide-FIAsH complex may preclude quenching of the dye because its more rigid conformation can hinder conjugation of the arsenic lone pair electrons with the fluorescein orbitals [67]. Indeed, comparing the emission spectra of 2 μM freely diffusing FIAsH and 400 nM CaM-FIAsH, the fluorescence was much stronger and red shifted when the dye was attached (Fig. 3.2-4.2).

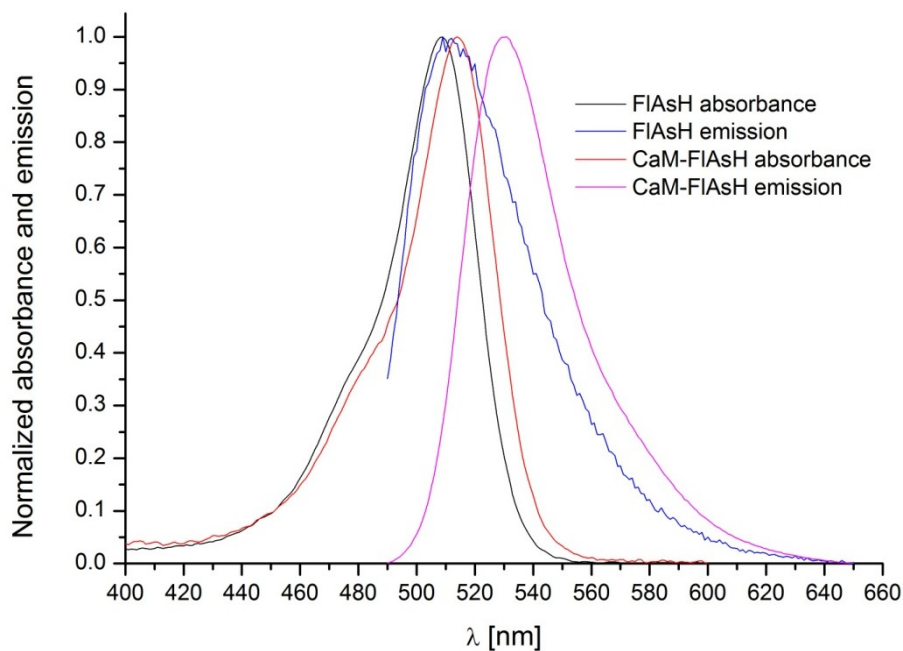


**Fig. 3.2-4.1.** Normalized absorbance and emission intensities of free FIAsH and CaM-FIAsH. A larger Stokes shift ( $\sim 17$  nm) is observed when FIAsH is bound to a tetra-Cys motif.

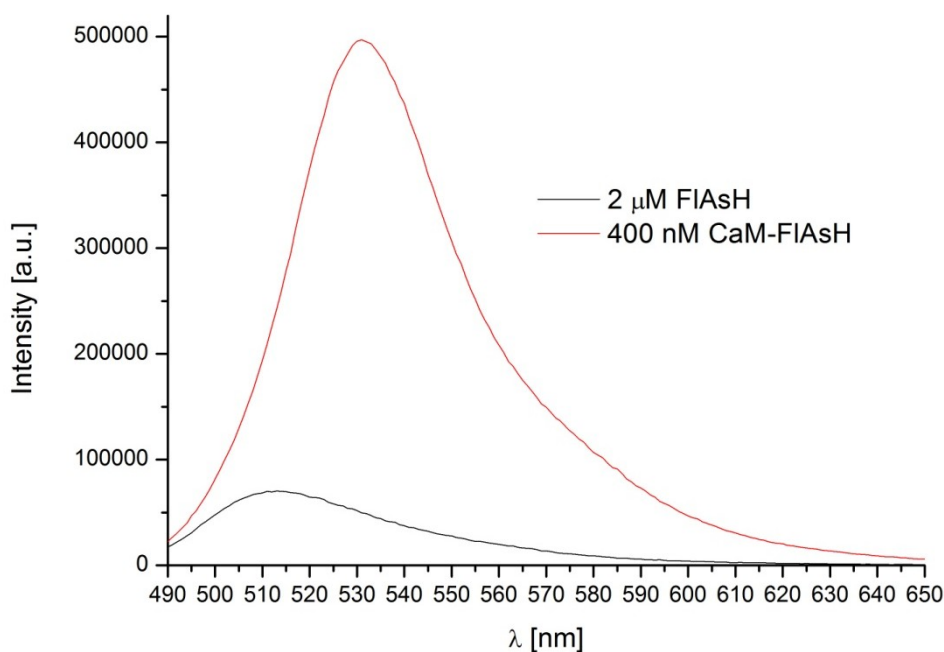


**Fig. 3.2-4.2.** Bound FIAsH vs. unbound. The fluorescence of CaM-FIAsH complex is much stronger and red-shifted.

As mentioned in Section 2.4-6 in Materials and Methods, steady-state anisotropy can still give evidence whether a fluorophore is able to change its orientation and to what extent. If a fluorophore is rigidly attached then this would have an impact on the anisotropy of the fluorescence, since the average angular displacement of a dye, which occurs between absorption and fluorescence emission, reflects the mobility of the fluorophore as well as that of the protein molecule. Four individual measurements,  $I_{HH}$ ,  $I_{HV}$ ,  $I_{VV}$  and  $I_{VH}$ , were performed (Fig. 3.2-4.3).

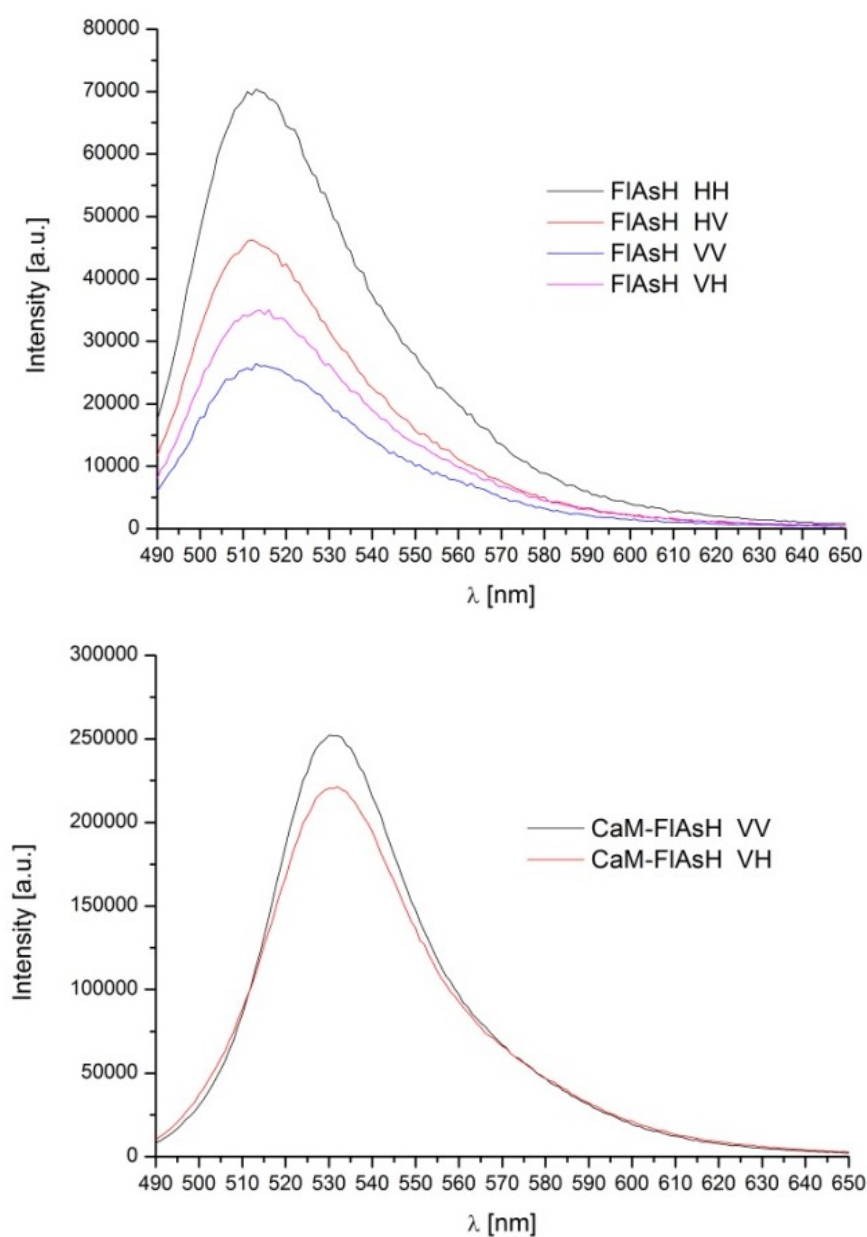


**Fig. 3.2-4.3.** Polarizations of fluorescence of free FIAsH (top) vs. bound (bottom).

It is also necessary to correct for different transmission efficiencies for different polarizations. The correction factor, G-factor, can be easily obtained by measuring the polarizations of free diffusing dye, according to the following formula:  $G = \frac{I_{HV}}{I_{HH}}$ . It should be noted that the G-factor is just a number, which represents a property of the detection system. Therefore, the G-factor was calculated taking into consideration the intensities of the peak of the emission, where better statistics is expected to acquire. The mean value was calculated to be  $0.64 \pm 0.01$ . This value was used for calculation of the steady-state anisotropy,  $r_{ss}$ . The steady-state anisotropy was obtained in a similar way. It was calculated using the following formula:  $r = \frac{I_{VV} - G I_{VH}}{I_{VV} + 2 G I_{VH}}$ . Then, the mean values were calculated, the steady-state anisotropy of free FIAsH was  $0.05 \pm 0.01$ , while the steady-state anisotropy of CaM-FIAsH complex was  $0.22 \pm 0.01$ , as it can be observed in Fig. 3.2-4.4. It seems obvious that when FIAsH is attached to CaM, it can change its orientation to less extent as compared to freely diffusing FIAsH.

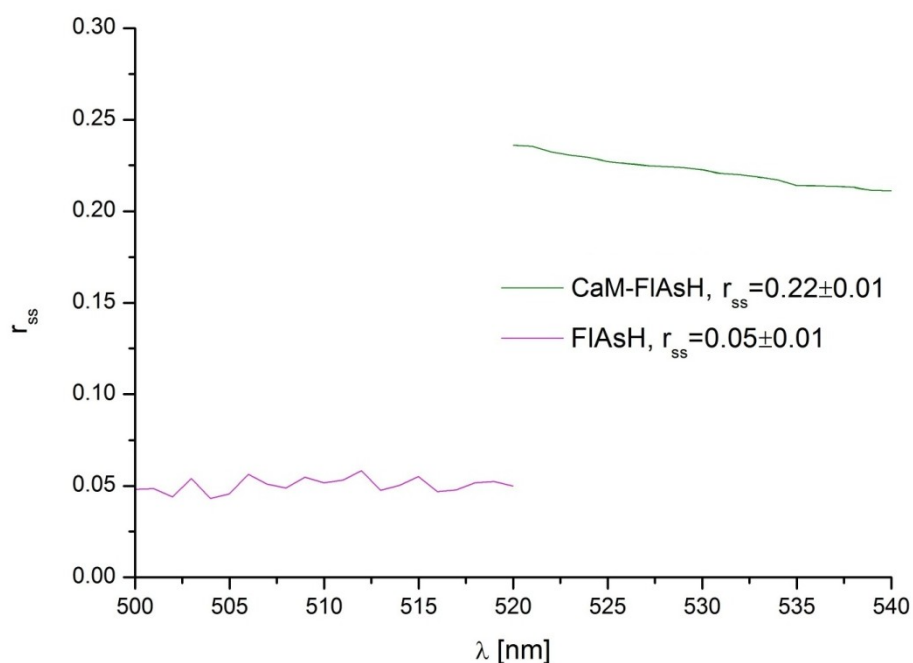


**Fig. 3.2-4.4.** Fluorescence anisotropy of bound FIAsH vs. unbound.

Another way to check whether there is freely diffusing dye in the protein solution is performing fluorescence correlation spectroscopy (FCS) as described in Section 2.4-5 in Materials and Methods. Free dye would diffuse fast through the focal volume, while the diffusion coefficient of bound dye would be that of the protein molecule. Three concentrations of CaM-FIAsH, 5 nM, 500 pM, and 50 pM were measured, to check whether reliable FCS data could be obtained. Herein, it should be noted that bigger dilutions cannot be made because the  $k_d$  of CaM-FIAsH complex is around 10 pM [66]. A further dilution can cause dissociation of FIAsH from CaM. It is known that CaM-FIAsH is quite a stable complex but there are some limitations. As mentioned in Section 2.4-5, the  $G(0)$  of an FCS curve is equal to the inverse of the average number,  $\langle N \rangle$ , of fluorophores that are present in the focal volume at any time. Therefore, by diluting the solution with the fluorophores ten times, a ten-times increase in the value of  $G(0)$  is expected. The next step was the calculation of the autocorrelation curves (Fig. 3.2-4.5).

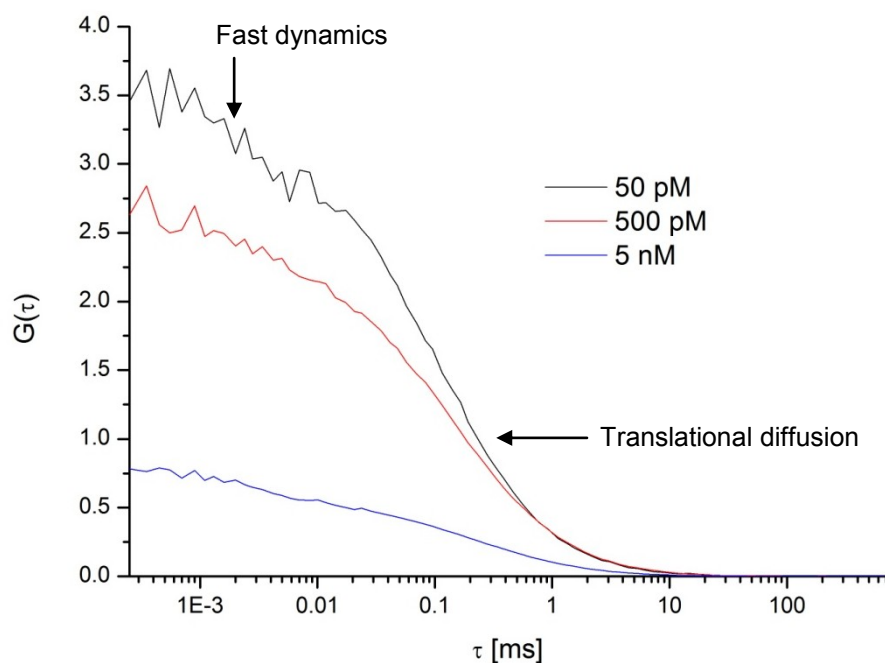


**Fig. 3.2-4.5.** FCS curves of three different dilutions of CaM-FIAsH (raw data) using Symphotime 5.2 from Picoquant.

First, it can be inferred from the figure above (Fig. 3.2-4.5) that our assumption cannot be confirmed. Second, the diffusion time was found to be equal to 0.3 ms which is smaller than the expected, 0.6 ms. This is not reasonable. It should be highlighted that FCS measurements do not always give clear answer what diffuses through the focal volume, especially when fluorophores are not so emissive. Such fluorophores are those that can be bleached easily or those that transit to triplet states after excitation. When a fluorophore is bleached while it diffuses through the focal volume, this will be recorded as fast diffusion. It seems that FIAsH does not emit a lot of photons, which are necessary for a high signal-to-noise ratio. Therefore, FCS data should always be critically analyzed. It can also be argued that there is free dye in the samples. However, probable presence of freely diffusing FIAsH would not cause a problem to anisotropy measurements because its fluorescence is very weak.

The drawback of this dye can be compensated by the fact that it is rigidly attached to its target, and for this reason, it provides information about the overall tumbling of a protein. All in all, we wanted to show in this section about the CaM-FIAsH complex, that the dye is specifically attached to the tetra-Cys motif. Solid evidence that there is specific attachment of FIAsH to CaM will be provided in the sections about fluorescence anisotropy of ribosome-nascent chain complexes, later on, using less sophisticated biochemistry techniques.

### 3.3 Time-resolved fluorescence anisotropy of free diffusing CaM-FIAsH complex in solution

As already mentioned, FIAsH can be rigidly attached to tetra-Cys motifs within a larger segment of a protein. The question was if time-resolved data can provide information about the overall rotation of CaM using FIAsH as a probe. This also includes whether it is possible to detect segmental motions in the nanosecond timescale. In principle, the idea was to find out how this dye can be used. An attempt was made to find out which is the rotational correlation time for overall rotation of CaM. First, this information about full

length CaM was needed to use it as a control to compare conformational changes of CaM when  $\text{Ca}^{2+}$  is bound. Second, it was valuable to know that it is possible to resolve dynamics of free CaM. Fluorescence anisotropy data might also reveal folding of more complex systems, such as ribosome-bound nascent chains, and folding of released polypeptides, as well.

As already discussed in Material and Methods, to analyze time-resolved fluorescence anisotropy data, fluorescence lifetime components have to be analyzed first. In all cases, iterative ‘reconvolution’ was performed to analyze the data. It is useful to explain shortly how a good fit is defined. In all cases, non-linear least-squares analysis was performed. A least-squares analysis starts with a model that is assumed to describe the data. The goal is to test whether the model is consistent with the data and to obtain the parameter values for the model that provide the best match between the measured data,  $N(t_k)$ , and the calculated data,  $N_c(t_k)$ , using assumed parameter values. This is accomplished by minimizing the goodness-of-fit parameter, which is given by

$$\chi^2 = \sum_{k=1}^n \frac{1}{\sigma_k^2} [N(t_k) - N_c(t_k)]^2 \quad \text{Eq. 3.3 - 1}$$

In TCSPC, it is straightforward to assign the standard deviations,  $\sigma_k$ . From Poisson statistics, it can be deduced that the standard deviation is equal to the square root of the number of photon counts:  $\sigma_k = \sqrt{N(t_k)}$ . Least-squares analysis was performed for one simple reason. The least-squares analysis has the drawback that it assumes the residuals follow a normal distribution centred around zero. Measurements on ensemble level were performed because good statistics were necessary to analyze anisotropy decays, on condition that pile-up effects do not occur. It is usually the case that the residuals are randomly distributed around zero when measurements on ensemble are performed. However, it is not convenient to interpret the values of  $\chi^2$  directly because it depends on the number of data points. Its value will be larger for data sets with more data points. For this reason, the value of reduced  $\chi^2$  was used:

$$\chi_R^2 = \frac{\chi^2}{n - p} = \frac{\chi^2}{\text{dof}} \quad \text{Eq. 3.3 - 2}$$

where  $n$  is the number of data points,  $p$  is the number of parameters, and  $\text{dof}=n-p$  are the degrees of freedom. So,  $\chi_R^2$  should also be minimized. If only random errors contribute to  $\chi_R^2$ , then this value is expected to be equal to 1-2. This is because the average  $\chi^2$  per data point should be about one, and typically the number of data points,  $n$ , is much larger than the number of the parameters,  $p$ . If the model does not fit,  $\chi_R^2$  is much larger than really expected [68]. There is another runs test of randomness that was taken into consideration to judge if the weighted residuals are randomly distributed. This is the  $h$  criterion; it performs a runs test on the sequence of observations in the vector  $x$ . This is a test of the null hypothesis that the values in  $x$  come in random order, against the alternative that they do not. The test is based on the number of runs of consecutive values above or below the mean of  $x$ . Too few runs indicate a tendency for high and low values to cluster. Too many runs indicate a tendency for high and low values to alternate. The test returns the logical value  $h=1$  if it rejects the null hypothesis at the 5 % significance level, and  $h=0$  if it cannot [79]

In the next sections, time-resolved fluorescence anisotropy analyses of apo-CaM and CaM-Ca<sup>2+</sup> will be presented. It is instructive to visualize CaM-FIAsH complex both in the apo-form and when Ca<sup>2+</sup> is bound. It is known that CaM adopts a 'semi-open' conformation in the absence of Ca<sup>2+</sup>. FIAsH is rigidly bound to a flexible segment that might be able to exhibit a rotary motion. So, except from the overall rotation of the protein, a segmental motion might also occur (Fig. 3.3 A). CaM adopts an 'open' conformation upon Ca<sup>2+</sup> binding. The structure of the protein also becomes more rigid (Fig. 3.3 B). VMD and PyMol software were used to visualize CaM-FIAsH complex (pdb files were created by Henning Höfig, master student at I. Physikalisches Institut (IA) in RWTH Aachen). The liquid NMR structure of apo-CaM (PDB: 1DMO) and the crystal structure of CaM-Ca<sup>2+</sup> (PDB: 1CLL) were used for visualizations.

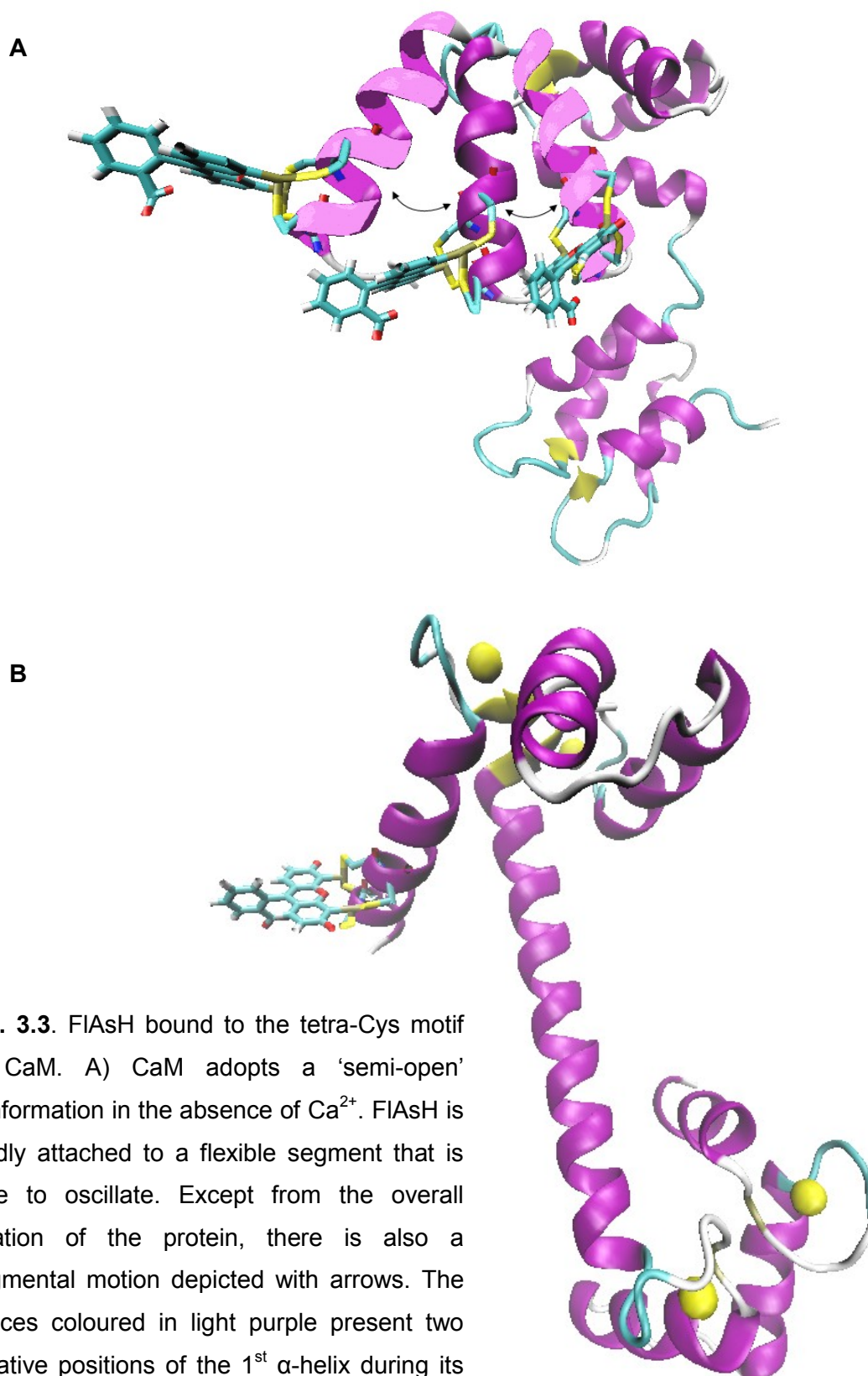


**Fig. 3.3.** FIAsH bound to the tetra-Cys motif of CaM. A) CaM adopts a 'semi-open' conformation in the absence of  $\text{Ca}^{2+}$ . FIAsH is rigidly attached to a flexible segment that is able to oscillate. Except from the overall rotation of the protein, there is also a segmental motion depicted with arrows. The helices coloured in light purple present two putative positions of the 1<sup>st</sup>  $\alpha$ -helix during its tumbling motion. B) CaM adopts an 'open' conformation upon  $\text{Ca}^{2+}$  binding. The structure of the protein also becomes more rigid.

## 3.3-1 Time-resolved fluorescence anisotropy of apo-CaM-FIAsH complex

The analyzed fluorescence intensity decay of CaM-FIAsH complex is shown in Fig. 3.3-1.1 along with the residuals weighted by the standard deviations,  $\sigma_k$ , of each data point. In all cases, the collected data were corrected first for the background. The raw data is the sum of emitted photons plus scattered photons. To acquire knowledge about the scattered light, the buffer of the protein was also measured under the same conditions, and it was subtracted from the raw data. It is important to define the fluorescence intensity decay as accurately as possible to analyze anisotropy decays. Therefore, three exponential components had to be used to fit the data (Fig. 3.3-1.1). The formula to fit the fluorescence intensity decays in all cases was the following:

$$I(t) = \sum_{i=1}^3 A_i e^{-\frac{t}{\tau_i}}$$

The accurateness of the fast component is probably ambiguous because this decay falls into the instrument response function (IRF). There are systematic errors introduced into the analysis like colour effects of the IRF as well as the detection system is not perfect, which are unavoidable. The fluorescence lifetime components are summarized in Table 3.3-1.1, the average lifetime,  $\bar{\tau}$ , applying Eq. 2.4-3.2, is also mentioned.

| apo-CaM-FIAsH, lifetime fit |               |          |               |          |               |                   |                       |
|-----------------------------|---------------|----------|---------------|----------|---------------|-------------------|-----------------------|
| $A_1$                       | $\tau_1$ [ns] | $A_2$    | $\tau_2$ [ns] | $A_3$    | $\tau_3$ [ns] | $\bar{\tau}$ [ns] |                       |
| 255.4±3.3                   | 0.4±0.1       | 91.1±2.1 | 1.9±0.1       | 42.4±2.5 | 5.2±0.1       | <b>3.1</b>        | $\chi_R^2=1.9$<br>h=0 |

**Table 3.3-1.1.** Fluorescence lifetime components of apo-CaM-FIAsH complex.

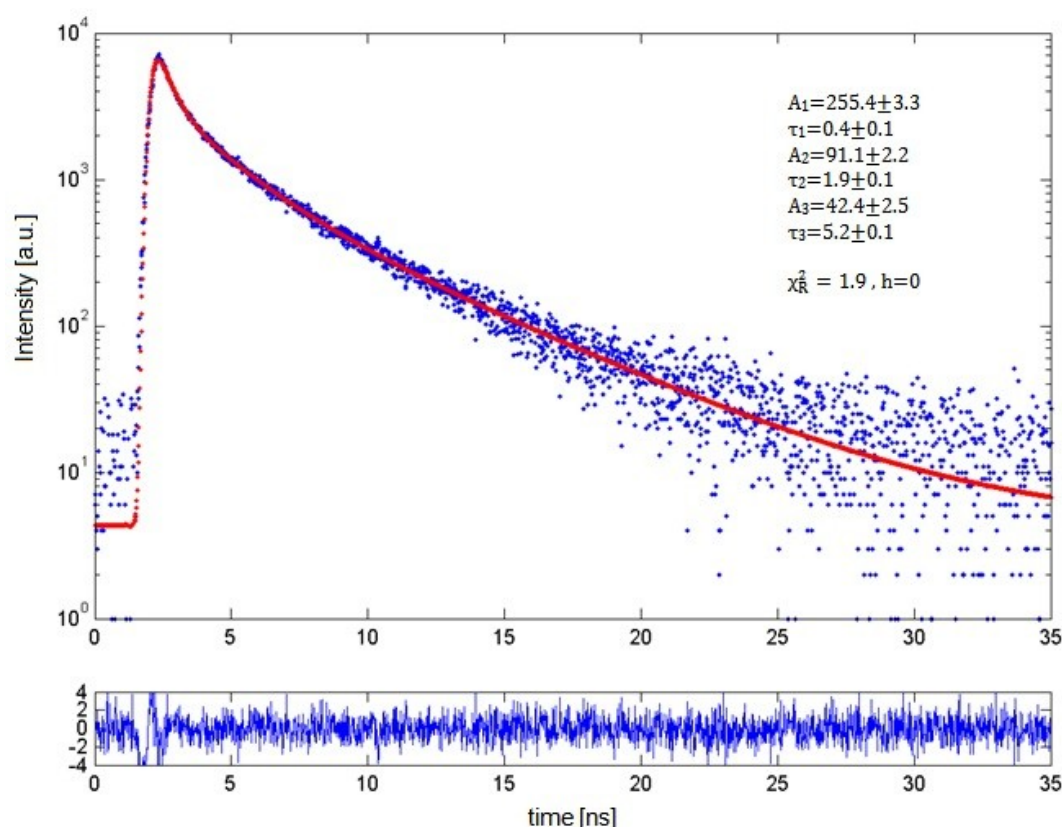


**Fig. 3.3-1.1.** Fluorescence intensity decay of apo-CaM-FIAsH complex. The fit is shown in red.

The next step was the analysis of the time-resolved fluorescence polarization data. Unfortunately, the fundamental anisotropy,  $r_0$ , of CaM-FIAsH is a priori not known, and procedures to measure this are not straightforward. Of course, the  $r_0$  could be another floating parameter in the fitting procedure, but it is recommended to fix as many parameters as possible. The reason is that when there are many floating parameters in a fitting procedure, they are not totally independent of each other, and parameters like the rotational correlation times would be biased by the value of  $r_0$ . So, we attempted to find the  $r_0$  in an indirect way. All available raw data, also those of ribosome nascent chain complexes were analyzed, and we tried to find a value of  $r_0$  so that a trend in the rotational correlation times could be observed. This means that the obtained rotational correlation times should reflect the size and the dynamics of the rotating unit. The calculated value of  $r_0$  was 0.31. Using this

approximation of  $r_0$ , it had to be specified which mathematical model best describes the raw data, and if that model offers a reasonable explanation of the structural properties of the polypeptide. There are three putative models, the single-exponential, the hindered rotor, and the wobbling-in-a-cone (see also Section 2.4-6.5). The result obtained by applying each of these models is described in the following pages. The plots of apo-CaM results will be presented in this section as an example. The plots and corresponding fits of all the other cases can be found in Appendix B. First, the result applying the single-exponential model is presented (Fig. 3.3-1.2, 3.3-1.3).

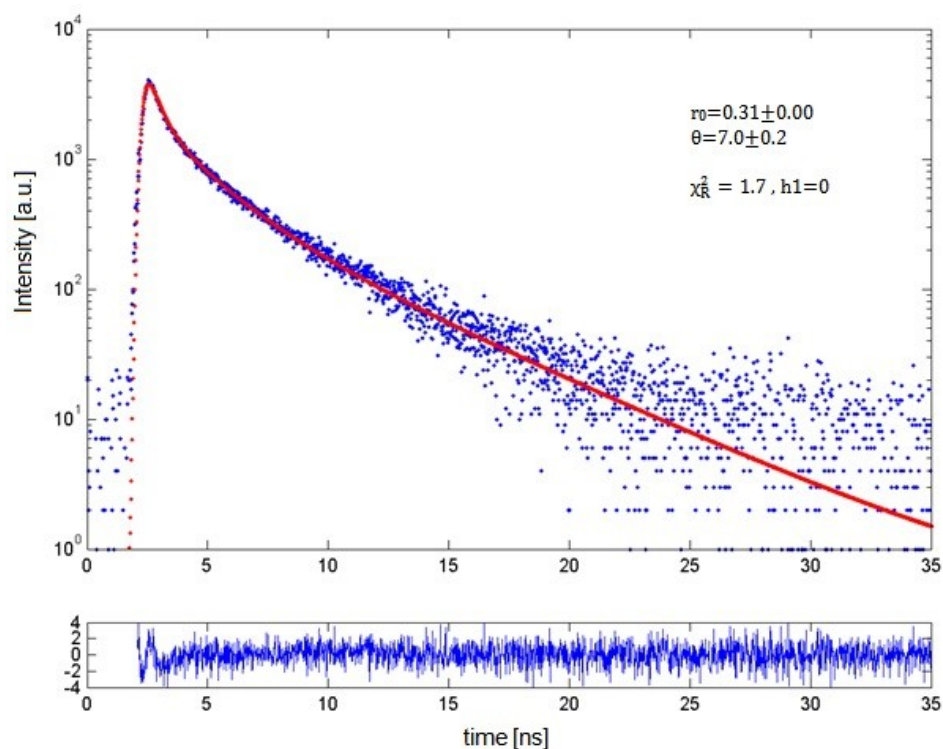


**Fig. 3.3-1.2.** Fluorescence intensity decay of parallel polarized component of apo-CaM-FIAsH complex. The fit using the single-exponential model is shown in red.

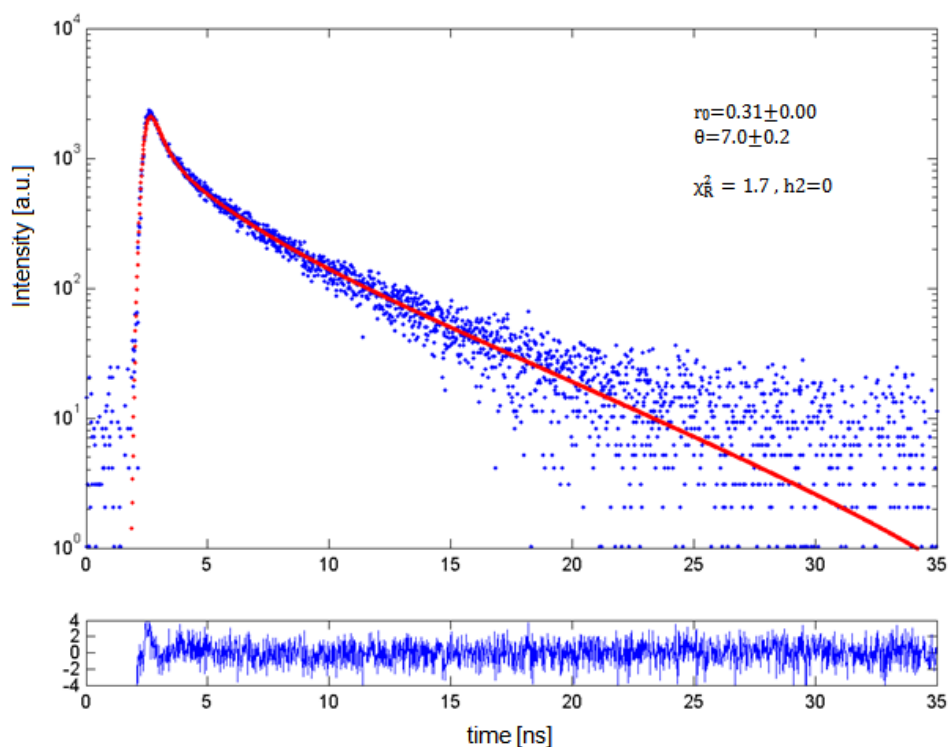


**Fig. 3.3-1.3.** Fluorescence intensity decay of perpendicular polarized component of apo-CaM-FIAsH complex. The fit using the single-exponential model is shown in red.

The result is summarized in Table 3.3-1.2, the steady-state anisotropy,  $r_{ss}$ , using Eq. 2.4-6.7, is also mentioned.

| apo-CaM-FIAsH, single-exponential |               |          |                            |
|-----------------------------------|---------------|----------|----------------------------|
| $r_0$                             | $\theta$ [ns] | $r_{ss}$ |                            |
| 0.31±0.00                         | 7.0±0.2       | 0.22     | $\chi_R^2=1.7, h1=0, h2=0$ |
| $r(t) = 0.31 e^{-\frac{t}{7.0}}$  |               |          |                            |

**Table 3.3-1.2.** Anisotropy decay of apo-CaM-FIAsH complex using the single-exponential model.

A rotational correlation time (see Section 2.4-6.4),  $\theta$ , equal to 7 ns was obtained. By applying the Perrin equation ( $\theta = \frac{\eta MW(\bar{v}+h)}{RT}$ ,  $MW_{CaM} \sim 17$  kDa), and assuming that CaM has a spherical shape, although it looks like a dumbbell, a value of  $\theta$  close to 7 ns can be obtained.

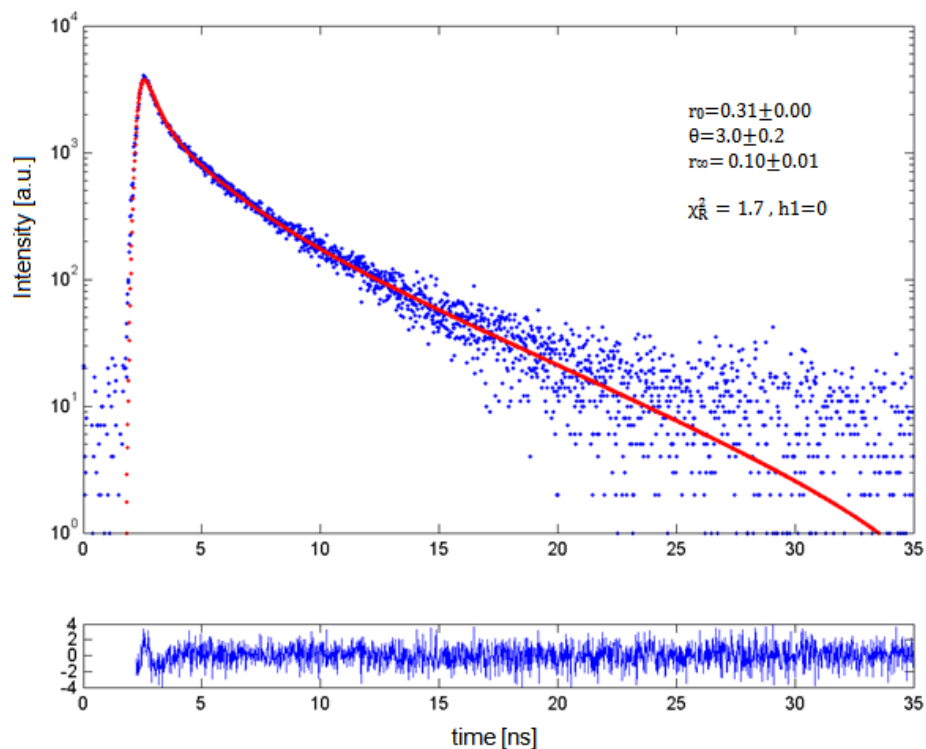


**Fig. 3.3-1.4.** Fluorescence intensity decay of parallel polarized component of apo-CaM-FIAsH complex. The fit using the hindered rotor model is shown in red.

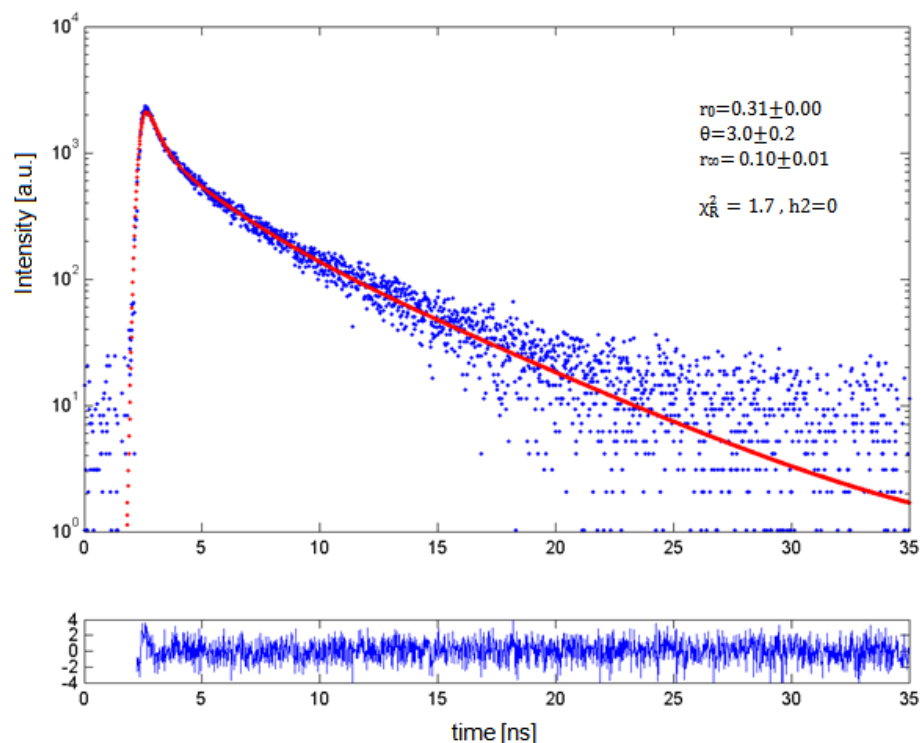


**Fig. 3.3-1.5.** Fluorescence intensity decay of perpendicular polarized component of apo-CaM-FIAsH complex. The fit using the hindered rotor model is shown in red.

The fits using the hindered rotor model are shown above (Fig. 3.3-1.4, 3.3-1.5). The result is summarized in Table 3.3-1.3, the semicone angle,  $\varphi_{\max}$ , using Eq. 2.4-6.21, is also mentioned.

| apo-CaM-FIAsH, hindered rotor                                       |            |               |          |                             |
|---|------------|---------------|----------|-----------------------------|
| $r_0$   | $r_\infty$ | $\theta$ [ns] | $r_{ss}$ |                             |
| 0.31±0.00   | 0.10±0.01  | 3.0±0.2       | 0.22     | $\chi_R^2=1.7$ , h1=0, h2=0 |
| $r(t) = 0.21 e^{-\frac{t}{3.0}} + 0.10$ , $\varphi_{\max}=46^\circ$ |            |               |          |                             |

**Table 3.3-1.3.** Anisotropy decay of apo-CaM-FIAsH complex using the hindered rotor model.

A  $\theta$  equal to 3 ns was observed. At first glance, this model should be rejected because the obtained correlation time is not reasonable with respect to the size of CaM. At second glance, it can be argued that when the data are fitted with the hindered rotor model, the motion of half length CaM is revealed. If the Perrin equation is applied to calculate the correlation time of half length CaM, the N-terminal globule, a value of  $\theta$  close to 4 ns can be obtained. Finally, the data were fitted with the wobbling-in-a-cone model (Fig. 3.3-1.6, 3.3-1.7). The result is summarized in Table 3.3-1.4, the semicone angle,  $\varphi_{\max}$ , is also mentioned.

| apo-CaM-FIAsH, wobbling-in-a-cone   |            |               |                 |          |                              |
|---|------------|---------------|-----------------|----------|------------------------------|
| $r_0$   | $A_\infty$ | $\theta$ [ns] | $\theta_G$ [ns] | $r_{ss}$ |                              |
| 0.31±0.00   | 0.75±0.01  | 1.1±0.1       | 12.2±0.5        | 0.22     | $\chi_R^2=1.7$<br>h1=0, h2=0 |
| $r(t) = 0.08 e^{-\frac{t}{1.1}} + 0.23 e^{-\frac{t}{12.2}}$ , $\varphi_{\max}=26^\circ$ |            |               |                 |          |                              |

**Table 3.3-1.4.** Anisotropy decay of apo-CaM-FIAsH complex using the wobbling-in-a-cone model.

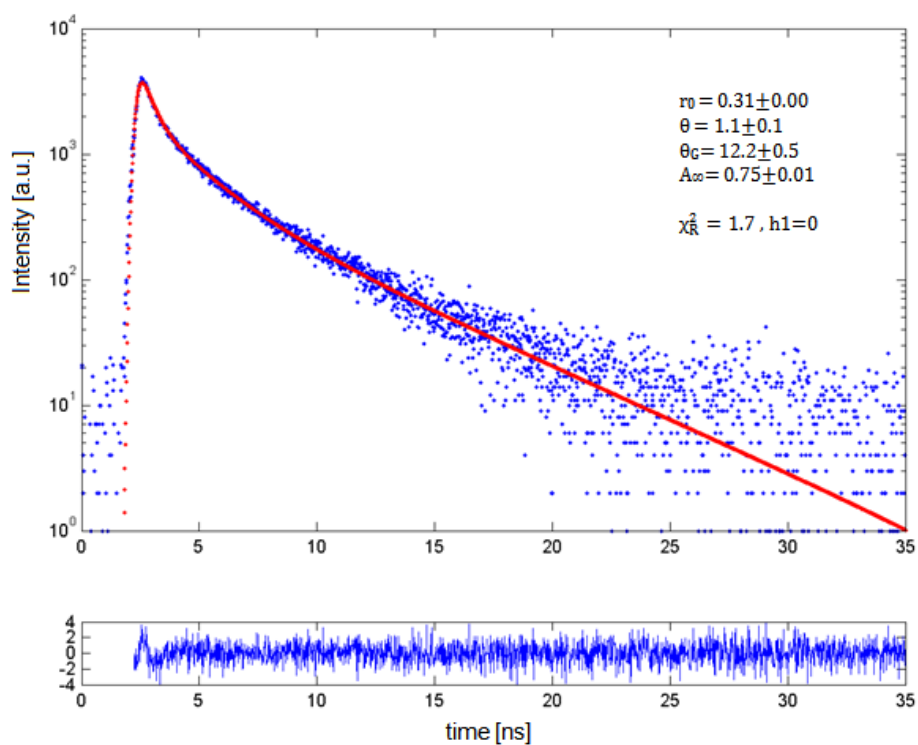


**Fig. 3.3-1.6.** Fluorescence intensity decay of parallel polarized component of apo-CaM-FIAsH complex. The fit using the wobbling-in-a-cone model is shown in red.

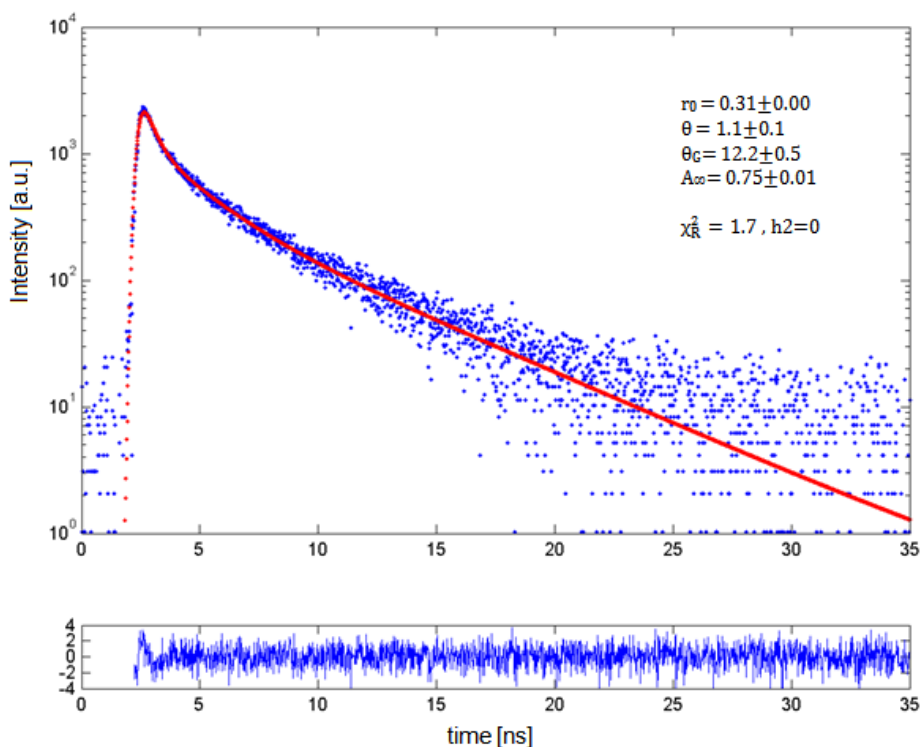


**Fig. 3.3-1.7.** Fluorescence intensity decay of perpendicular polarized component of apo-CaM-FIAsH complex. The fit using the wobbling-in-a-cone model is shown in red.

All results are summarized in the following table, where volumes of rotating units as well as hydrodynamic radii are also calculated using the Perrin equation to have an approximation of these parameters.

|                    | $r_0$       | $\theta$ [ns] | $\theta_G$ [ns] | $A_\infty$      | $\Phi_{\max}$ [deg] | Volume ( $\text{\AA}^3$ ) | $r_h$ ( $\text{\AA}$ ) |
|--------------------|-------------|---------------|-----------------|-----------------|---------------------|---------------------------|------------------------|
| single-exponential | <b>0.31</b> | ---           | $7.0 \pm 0.2$   | ---             | ---                 | 17053                     | 16                     |
| hindered rotor     | <b>0.31</b> | ---           | $3.0 \pm 0.2$   | $0.32 \pm 0.01$ | $46^\circ$          | 7308                      | 12                     |
| wobbling-in-a-cone | <b>0.31</b> | $1.1 \pm 0.1$ | $12.2 \pm 0.5$  | $0.75 \pm 0.01$ | $26^\circ$          | 29720                     | 19                     |

**Table 3.3-1.5.** Anisotropy decays of apo-CaM-FIAsH complex using different models.

Let us see now which model can be sustained. First, it is already mentioned that when CaM is in the apo-form, its conformation is less ordered. Thus, it is expected that segmental motions also occur. Second, CaM does not have a spherical shape, and thus, the rotational correlation time should be larger than that obtained by applying Perrin equation ( $\sim 7$  ns). Third, the calculated hydrodynamic radius of the protein, when the data are fitted with the wobbling-in-a-cone model, is closer to the experimentally found by dynamic light scattering measurements, which is  $23 \text{ \AA}$  [80]. Therefore, it could be accepted that the model which best describes the structural properties of CaM is the ‘wobbling-in-a-cone’. However, the residuals look similar as well as the value of the goodness-of-fit parameter,  $\chi_R^2$ , is the same in all cases, it is equal to 1.7. It is important to understand that if  $\chi_R^2$  is not decreasing when more fitting parameters are inserted, there is no justification to accept a more complicated model than the single-exponential.

### 3.3-2 Time-resolved fluorescence anisotropy of CaM-FIAsH complex in the presence of Ca<sup>2+</sup>

CaM-FIAsH complex was first diluted into a buffer containing Ca<sup>2+</sup> (10 mM MOPS, 500 mM NaCl, 15  $\mu$ M CaCl<sub>2</sub>, pH 7.4), and it was left at room temperature for 1 h. The fluorescence anisotropy data were fitted using the single-exponential model and the hindered rotor model (Table 3.3-2.1).

| CaM-FIAsH + Ca <sup>2+</sup> , single-exponential                   |                |          |                 |                                |
|---|----------------|----------|-----------------|--------------------------------|
| r <sub>0</sub>  | r <sub>∞</sub> | θ [ns]   | r <sub>ss</sub> |                                |
| 0.31±0.00   | ---            | 16.1±0.1 | 0.25            | $\chi_R^2=1.9$ ,<br>h1=0, h2=1 |
| $r(t) = 0.31 e^{-\frac{t}{16.1}}$                                   |                |          |                 |                                |
| CaM-FIAsH + Ca <sup>2+</sup> , hindered rotor                       |                |          |                 |                                |
| r <sub>0</sub>  | r <sub>∞</sub> | θ [ns]   | r <sub>ss</sub> |                                |
| 0.31±0.00   | 0.21±0.01      | 2.5±0.1  | 0.25            | $\chi_R^2=1.9$ ,<br>h1=0, h2=1 |
| $r(t) = 0.10 e^{-\frac{t}{2.5}} + 0.21$ , $\varphi_{\max}=29^\circ$ |                |          |                 |                                |

**Table 3.3-2.1.** Anisotropy decay of CaM-FIAsH complex in the presence of Ca<sup>2+</sup> using the single-exponential and the hindered rotor model.

The data were also fitted with the wobbling-in-a-cone model, but the result was not reasonable. First of all, the  $\chi_R^2$  is again not decreasing when more parameters are inserted. We should be hesitant to accept other models than the single-exponential. The obtained correlation time of CaM-Ca<sup>2+</sup> by using the single-exponential model is around 16 ns. This is larger than that of apo-CaM, around 7 ns, and in agreement with published data [77]. The result from time-resolved fluorescence anisotropy measurements is consistent with the result from CD measurements. It was observed that the ellipticity increased upon Ca<sup>2+</sup> binding, which shows that the  $\alpha$ -helical content of the protein has increased. It is known that upon Ca<sup>2+</sup> binding to CaM, its conformation becomes highly ordered. These findings are also in agreement with the crystal

structure of CaM-Ca<sup>2+</sup> (PDB: 1CLL) where it is shown that CaM is stretched and more rigid when Ca<sup>2+</sup> is bound. Second, the result applying the hindered rotor model also gives a hint that the segmental motion is highly restricted, the  $r_{\infty}$  was found to be quite large.

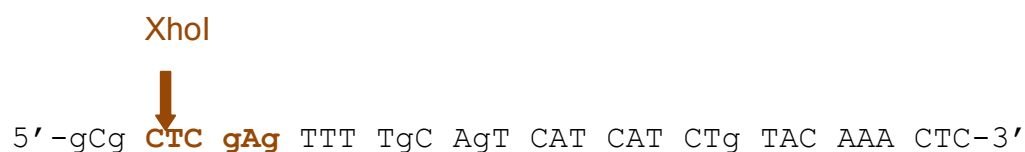
### 3.4 Preparation and characterization of ribosome-nascent chain complexes (RNCs)

Since it is now known that it is possible to detect conformational dynamics of free diffusing CaM-FIAsH complex, information about the behaviour of free diffusing ribosome-nascent chain complexes (RNCs) will be presented.

#### 3.4-1 Isolation of the mutated gene of CaM containing the tetra-Cys motif near the N-terminus, without stop codon

The sequence encoding the tetra-Cys motif was incorporated also by PCR. The difference is that the His<sub>6</sub>-tag and the stop codon are missing. The reason is that this construct would be subcloned into a vector that encoded for a linker rich in Ser and Gly, and the SecM arrest sequence downstream the insert (courtesy by Dr. Alexandros Katranidis, ICS-5: Molecular Biophysics, Forschungszentrum Jülich). The SecM arrest sequence is useful because it stalls the ribosome. The linker was also necessary because it is desirable for the polypeptide corresponding to the protein of interest to be protruding out of the ribosomal tunnel [81]. The length of the Ser/Gly linker together with the SecM arrest sequence is 43 amino acids, which are expected to span an 80-100 Å ribosomal tunnel. The oligonucleotide BtaCaMmut(4Cys)-6His\_FP was used as forward primer; its sequence was described in Section 3.1-1. A new reverse primer was designed, which is depicted below; the XhoI restriction site is shown in orange, the stop codon and the sequence encoding the His<sub>6</sub>-tag are missing.

BtaCaMmut(4Cys)-no\_STOP\_RP



The construct with the gene of CaMmut(4Cys)-6His cloned in pCR-Blunt was used as a template. The PCR conditions described in Materials and Methods were utilized, and the PCR product was electrophorized in 1 % agarose gel. The band at ~450 bp was sliced from the gel and the DNA was extracted. Cloning into pCR-Blunt and, subsequently, sequencing analysis followed.

3.4-2 Creating the construct of CaMmut(4Cys) fused with Ser/Gly linker and SecM without stop codon, and cloning in pRSET

A pCR-Blunt vector which already contained the gene of GFPem with tags upstream as well as the Ser/Gly linker and the SecM downstream, was utilized. The first step was to transfer the whole construct to pRSET vector by usage of NdeI and HindIII endonucleases; pRSET was needed because it does not contain the lacO operator, and thus, it is suitable for *in vitro* transcription-translation reactions. After that, the gene for GFPem with its tags were removed by digestion with NdeI and XhoI, and the gene of CaMmut(4Cys)-no\_STOP was inserted. In the end, a pRSET vector containing the mutated gene of CaM fused with the Ser/Gly linker and the SecM downstream was prepared (Fig. 3.4-2.1). The next step was to isolate a larger quantity of this plasmid; this was necessary because 5.5 nM of plasmid are needed in a 25 µl *in vitro* transcription-translation reaction. Thus, a midiprep protocol as described in the Materials and Methods was utilized.

Another construct was also designed, the gene of CaMmut(4Cys)-6His with stop codon is cloned into pRSET without the Ser/Gly linker and the SecM; this is the pRSET plasmid from Invitrogen. This construct was used as a control because it was not certain whether SecM is really capable of inhibiting the release of the polypeptide. Theoretically, the control polypeptide should be

released in an *in vitro* reaction, while SecM is expected to inhibit the release. For this purpose, the pRSET vector without the Ser/Gly linker and the SecM was used, and GFPem was exchanged with CaM (Fig. 3.4-2.2). A midiprep protocol has also been utilized to isolate a larger quantity of plasmid.

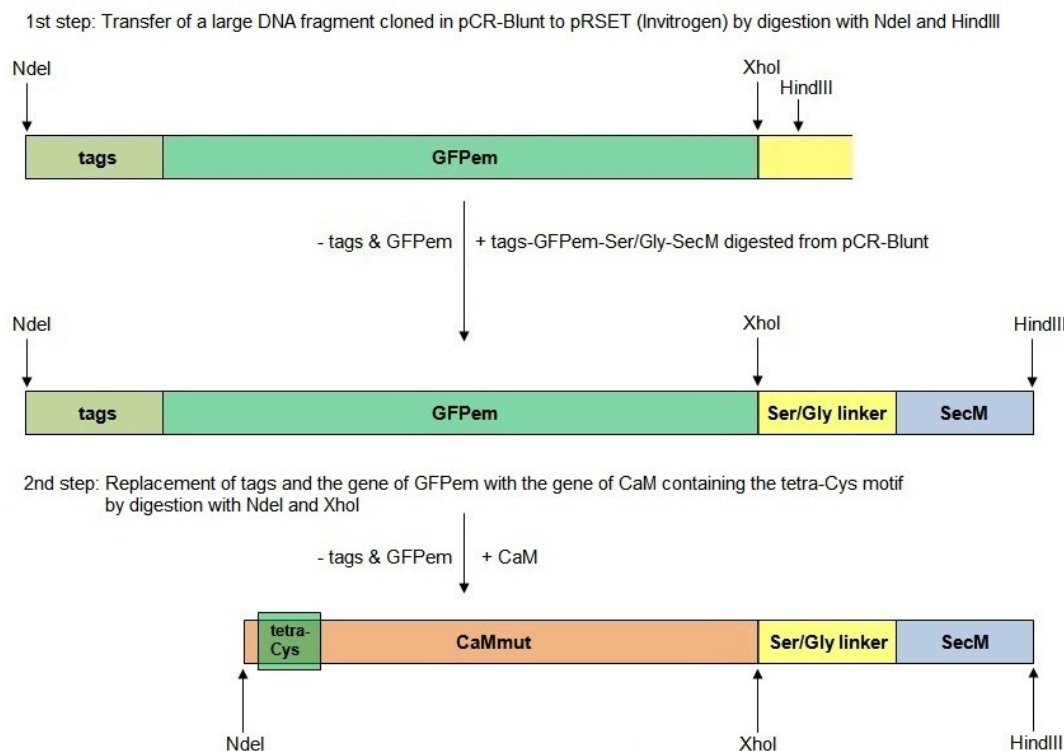


**Fig. 3.4-2.1.** Strategy to prepare the construct of mutated gene of CaM fused with the Ser/Gly linker and SecM arrest sequence.

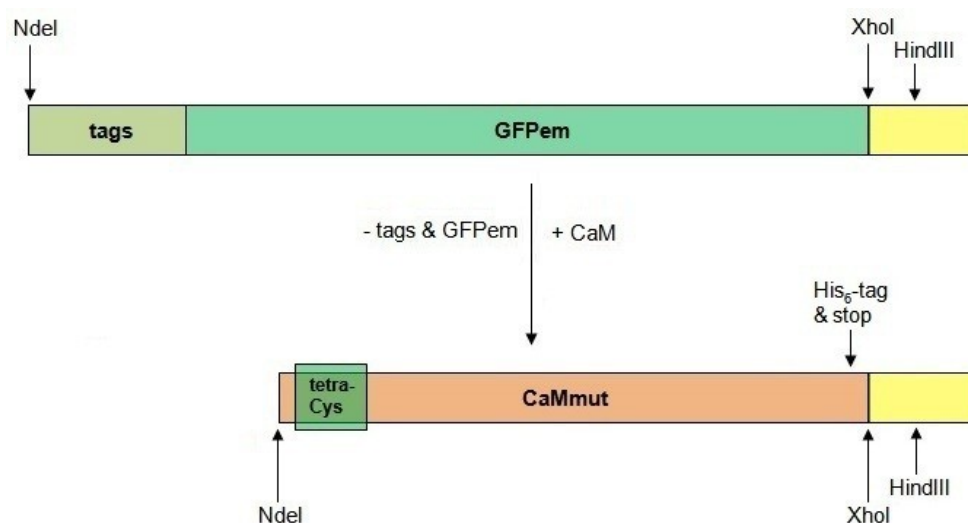
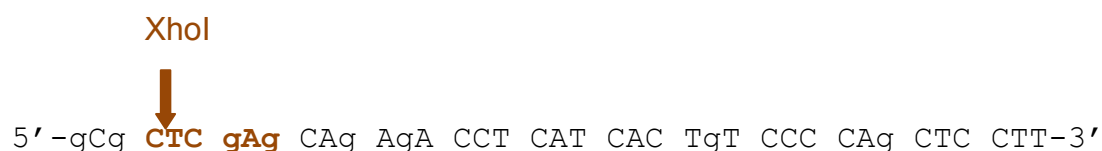


**Fig. 3.4-2.2.** Strategy to clone the mutated gene of CaM into pRSET.

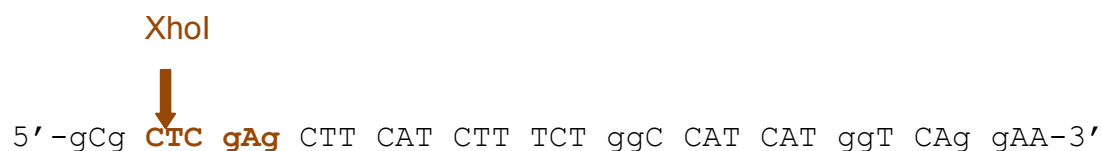
3.4-3 Isolation of the mutated gene of the 1<sup>st</sup> EF-hand of CaM and half CaM, and cloning in pRSET with Ser/Gly linker and SecM

The sequence encoding the tetra-Cys motif was incorporated by PCR; the His<sub>6</sub>-tag and the stop codon are also missing. The reason is that these truncated genes would also be subcloned into pRSET that encoded for Ser/Gly linker and the SecM arrest sequence downstream the insert. The oligonucleotide BtaCaMmut(4Cys)-6His\_FP was also used as forward primer. Two new reverse primers were designed, which are depicted below, one for each truncated gene; the XhoI restriction site is shown in orange, the stop codon and the sequence encoding the His<sub>6</sub>-tag are missing.

Bta 1st EF-hand (4Cys)-no STOP RP



Bta half-CaM N-term (4Cys)-no STOP RP



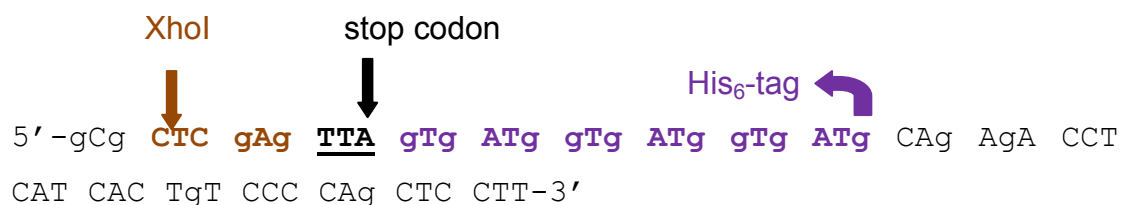
The construct with the gene of CaMmut(4Cys)-6His cloned in pCR-Blunt was used as a template in both cases. The PCR conditions described in Materials and Methods were utilized, and the PCR product was electrophorized in 1 % agarose gel. The bands at ~120 bp and ~230 bp were sliced from the gel and the DNA was extracted. Cloning into pCR-Blunt and, subsequently, sequencing analysis followed. The truncated genes were cloned into pRSET encoding for Ser/Gly linker and the SecM in a similar way the full length mutated CaM was cloned into this vector (see Section 3.4-2). The pRSET plasmid containing the gene of GFPem along with the Ser/Gly linker and the SecM was used in both cases; the tags and the gene of GFPem were replaced with the truncated genes. Finally, the 1<sup>st</sup> EF-hand(4Cys) and

half-CaM(4Cys) cloned in a vector encoding for Ser/Gly linker and SecM downstream was prepared. A midiprep protocol was also utilized to isolate a larger quantity of these plasmids.

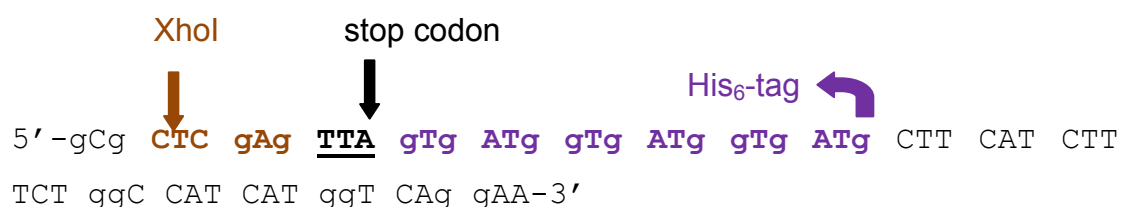
### 3.4-4 Isolation of the mutated gene of the 1<sup>st</sup> EF-hand of CaM and half CaM, and cloning in pET27b

The sequence encoding the tetra-Cys motif was incorporated by PCR. The truncated genes this time contain the His<sub>6</sub>-tag at the C-terminus because they would be cloned into pET27b vector, overexpressed in *E. coli* cells, and purified. The purpose was to obtain information about the folding of the truncated proteins by CD measurements. The oligonucleotide BtaCaMmut(4Cys)-6His\_FP was used again as forward primer. Two new reverse primers were designed, which are depicted below, one for each truncated gene; the His<sub>6</sub>-tag is shown in purple, the stop codon TAA in black and underlined, and the XhoI restriction site in orange.

#### Bta 1st EF-hand (4Cys)-6His RP



#### Bta half-CaM N-term (4Cys)-6His RP



The construct with the gene of CaMmut(4Cys)-6His cloned in pCR-Blunt was used again as a template in both cases. The PCR conditions described in Materials and Methods were utilized, and the PCR product was

electrophorized in 1 % agarose gel. The bands at ~120 bp and ~230 bp were sliced from the gel and the DNA was extracted. Cloning into pCR-Blunt and, subsequently, sequencing analysis followed. The correct clones were cloned in pET27b by usage of the same set of restriction endonucleases, NdeI and XhoI.

### 3.4-5 Purification of 1<sup>st</sup> EF-hand of CaM and half CaM by Ni-NTA column and size-exclusion chromatography

First, the proteins were overexpressed in *E. coli* BL21 (DE3) cells. The same protocol was followed as described in Section 3.1-3. The overexpression was induced by addition of IPTG when OD<sub>600</sub> was 0.5, and it was checked by electrophoresis in a 20 % SDS-polyacrylamide gel (Fig. 3.4-5.1).

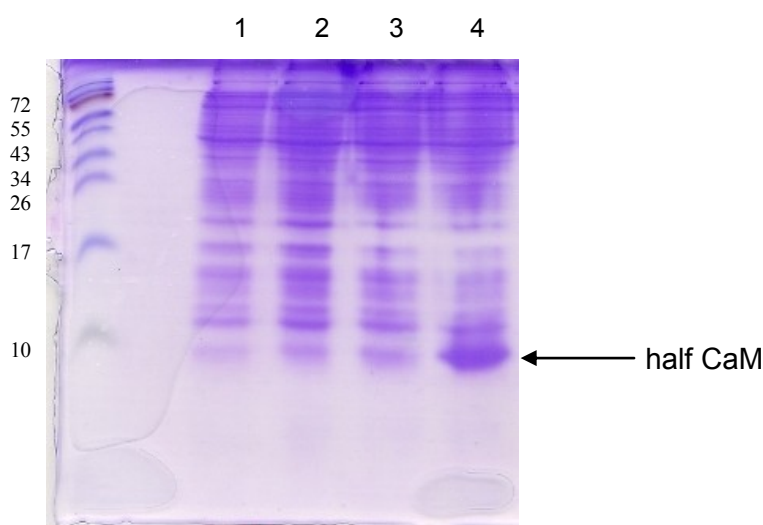


**Fig. 3.4-5.1.** Overexpression of truncated proteins. Lanes 1-2: 1<sup>st</sup> EF-hand (before and after induction). No band is visualized because the 1<sup>st</sup> EF-hand is ~4 kDa and its electrophoretic mobility is high. Lanes 3-4: half CaM, ~9 kDa (before and after induction).

The next step was purification using the same protocol as described in Section 2.3-1 in Materials and Methods. The eluted proteins were again visualized by electrophoresis in a 20 % SDS-polyacrylamide gel (Fig. 3.4-5.2). Again, no band was visible in the gel for the 1<sup>st</sup> EF-hand (~4 kDa) as its electrophoretic mobility in a gel is higher. Then, excess of imidazole was removed by size-exclusion chromatography. It should be noted that none of the two N-terminal domains contain tyrosines or tryptophans. Therefore, it is not possible to measure absorbance at 280 nm. Thus, the Bradford reagent was used to acquire the protein concentration by calculating a standard curve first, and then measuring the absorbance at 595 nm.

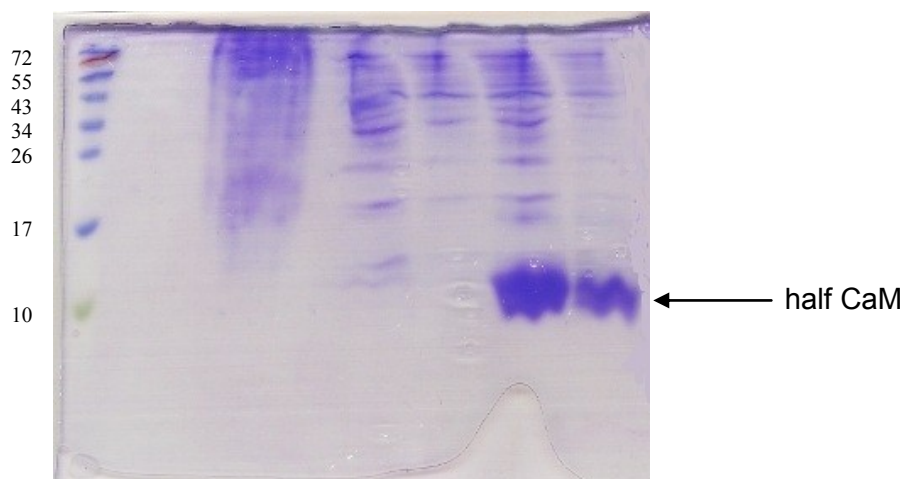


**Fig. 3.4-5.2.** Purification of truncated proteins by Ni-NTA column. The elutions are depicted in this gel. Last two lanes: half CaM, ~9 kDa.

#### 3.4-6 Circular dichroism (CD) measurements on truncated and full length CaM, both in apo-buffer and upon Ca<sup>2+</sup> binding

The truncated proteins were measured in the same way like full length mutant and the wild-type protein. The concentration of all proteins was adjusted to 0.18 mg/ml and the concentration of CaCl<sub>2</sub> to 15 μM. The samples were left at room temperature for 1 hour, and a CD spectrum was acquired for each protein. The truncated proteins were also measured in apo-buffer. In Fig. 3.4-6 the CD spectra of full length mutant and CaMwt are also depicted for comparison.

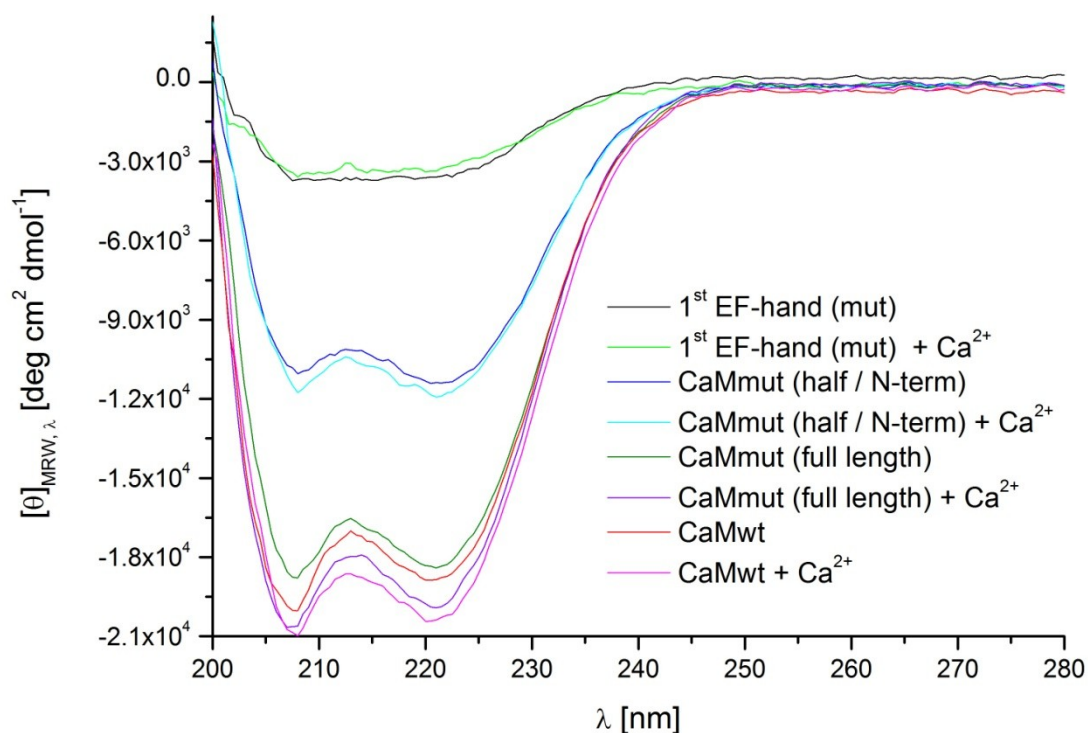


**Fig. 3.4-6.** CD spectra of truncated and full length CaM, both in the absence and the presence of  $\text{Ca}^{2+}$ .

First, it can be observed that upon addition of  $\text{Ca}^{2+}$  there is a considerable change in the ellipticities of the full length proteins only. On the contrary, those of the half length protein, that is the N-terminal domains, and the first EF-hand, remain, in principle, unaltered. Second, the mean residue ellipticity of the half length protein is almost the half of that of the full length protein and that of the first EF-hand around one fourth. Obviously, the relative  $\alpha$ -helix content for the half length CaM, and even more for the EF-hand, is drastically reduced as compared to the full length CaM. These findings are consistent with those from functionality tests with  $\text{Ca}^{2+}$  (see Section 3.2-1). CD measurements were performed to acquire knowledge about the folding of full length, half length protein as well as the 1<sup>st</sup> EF-hand. That was necessary to compare with the result from time-resolved fluorescence anisotropy measurements of RNCs. Taking everything into consideration, it seems that the N-terminal part of the protein is not folded correctly. This was somewhat expected because hydrophilic residues were replaced with hydrophobic ones.

Nevertheless, with regard to labelling with FIAsH, it is known that FIAsH can be attached more effectively to conformations that are not  $\alpha$ -helices [66][77].

3.4-7 *In vitro* transcription-translation reactions, labelling with FIAsH, and purification of ribosome-nascent chain complexes (RNCs)

The PURE *in vitro* transcription-translation system which contains ribosomes, purchased from New England Biolabs (NEB), was utilized to generate the ribosome-nascent chain complexes (RNCs). The ingredients of the *in vitro* reactions are shown in the following table.

| Ingredients         | Final concentration                       |
|---------------------|---|
| Solution A          | 10 $\mu$ l                                |
| Solution B          | 7.5 $\mu$ l                               |
| AS-tmRNA            | 2 $\mu$ l (final concentration 5 $\mu$ M) |
| plasmid             | x $\mu$ l (final concentration 5.5 nM)    |
| RNAase free water   | y $\mu$ l                                 |
| <b>Final volume</b> | 25 $\mu$ l                                |

**Table 3.4-7.** *In vitro* transcription-translation reactions with PURE system. The reaction mixture contains around 2  $\mu$ M ribosomes. The plasmid concentration in the reactions was adjusted to 5.5 nM in all cases. (Solution A and Solution B are contained in the kit of PURE system. Information about concentrations of translation factors is not provided by NEB. Solution B contains the ribosomes.)

The antisense-tmRNA (AS-tmRNA) was necessary to prevent the release of nascent chains, though it is alleged in the manuscript of NEB that there is not tmRNA in the reaction mixture. The tmRNA is an RNA molecule that releases the nascent chain from the ribosome when for some reason the ribosome has

stalled and it cannot resume the protein synthesis. It resembles a tRNA molecule, which enters the P-site so that the ribosome can resume the synthesis. There is also a stop codon in tmRNA that can be recognized by release factors so that the polypeptide chain can be released when that stop codon occurs in P-site.

The *in vitro* transcription-translation reactions took place at 37 °C for 30 min in low-adhesion tubes. Then, TCEP was added to a final concentration of 1 mM, the mixture was degassed for 30 min under 250 mbar vacuum, and it was left at room temperature for 2.5 h, so that the disulphide bonds are reduced. Afterwards, FIAsh was added to a final concentration of 400 nM, so that the ratio between assumed nascent chains and dye is 5:1, in the presence of nitrogen gas. The labelling reactions took place at room temperature for 3 h in complete darkness. Finally, the eppendorf tubes were stored at 4 °C, again in complete darkness, for 2 days.

To isolate the labelled RNCs and to remove the excess of dye, size-exclusion chromatography was utilized. The Sephadex G-75 material was used for separation because the cutoff is around 55000 Da, therefore, it is expected that it can separate the large RNCs from small proteins and released polypeptide chains. The column with the material was equilibrated first with Tico buffer (20 mM Hepes-KOH, 6 mM (CH<sub>3</sub>COO)<sub>2</sub>Mg, 30 mM CH<sub>3</sub>COONH<sub>4</sub>, pH 7.6). Then, the labelling reaction was added on top of the material and it passed through the column. The fluorescence spectra of fractions collected after purification of labelled with FIAsh ribosome-(1<sup>st</sup> EF-hand), ribosome-(half CaM/ N-term.), and ribosome-(CaM full length) can be seen in the following figures. A buffer scan was subtracted from each spectrum. There was also a control reaction where the protein is supposed to be released from the ribosome (see Section 3.4-2). The labelling and purification were performed in the same way. Afterwards, the steady-state anisotropy,  $r_{ss}$ , of some of the fractions was measured as well as that of free diffusing CaM-FIAsh and free diffusing FIAsh. The steady-state anisotropy was measured as it is described in Section 3.2-4. To calculate the anisotropies, the intensity peaks were taken into consideration, where it is expected that we have better statistics. The G-factor was also obtained by measuring free diffusing dye as described in Section 2.4-6.3, and it was equal

to  $0.65 \pm 0.01$ . The steady-state anisotropy measurements were found to be an easy way to distinguish which fractions contained the RNCs, since steady-state anisotropy can provide information whether a fluorophore can change its orientation integrated over all time scales accessible by the respective fluorescence lifetime. Labelled RNCs are expected to present higher fluorescence anisotropy because they are larger particles.

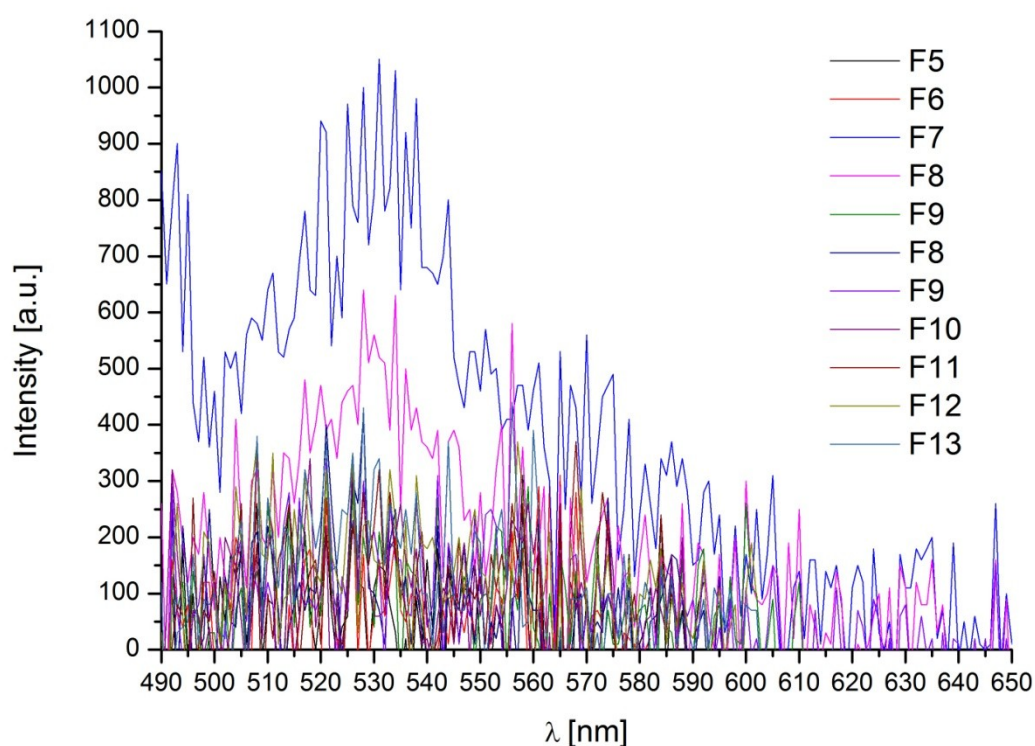


**Fig. 3.4-7.1.** Fluorescence spectra of elutions after purification of ribosome- (1<sup>st</sup> EF-hand) by size-exclusion chromatography (Sephadex G-75),  $\lambda_{\text{exc.}}=470$  nm.

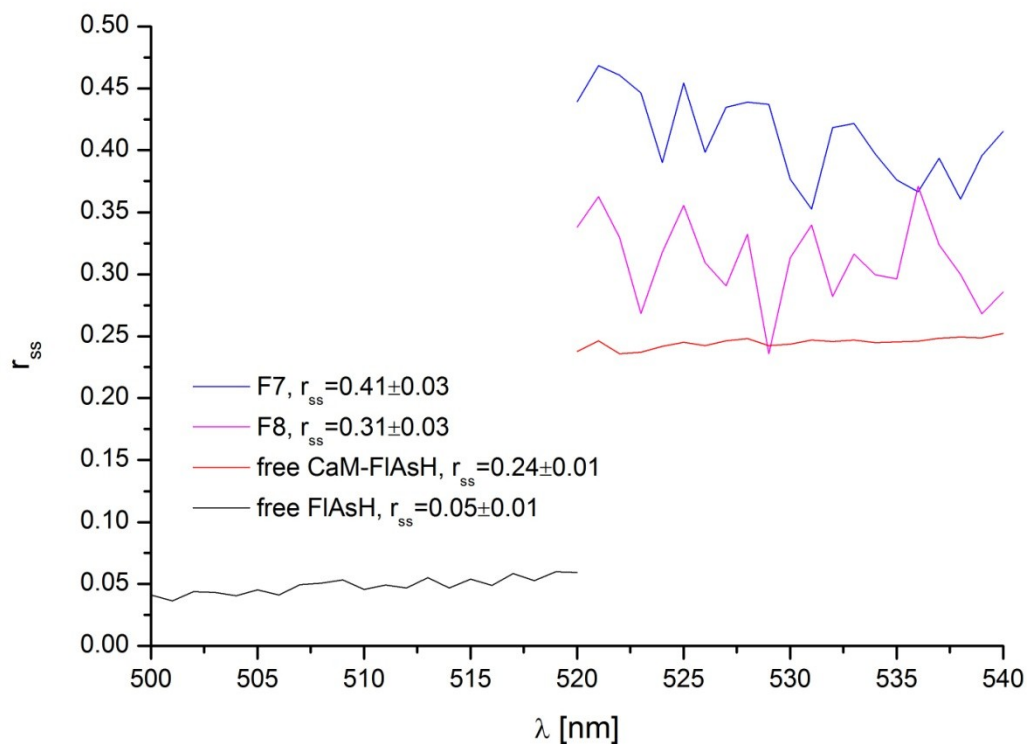


**Fig. 3.4-7.2.** Ribosome-(1<sup>st</sup> EF-hand) : steady-state anisotropy of fractions F7 and F8, free CaM-FIAsH, and free FIAsH.

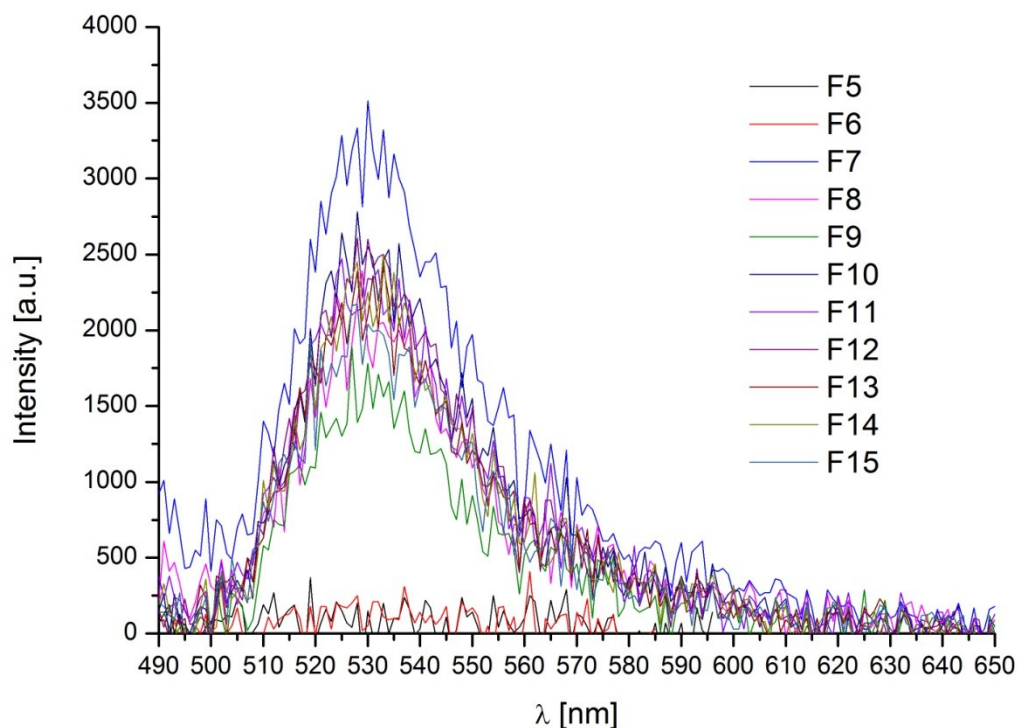


**Fig. 3.4-7.3.** Fluorescence spectra of elutions after purification of ribosome-(half CaM/ N-term.) by size-exclusion chromatography (Sephadex G-75),  $\lambda_{exc.} = 470$  nm.

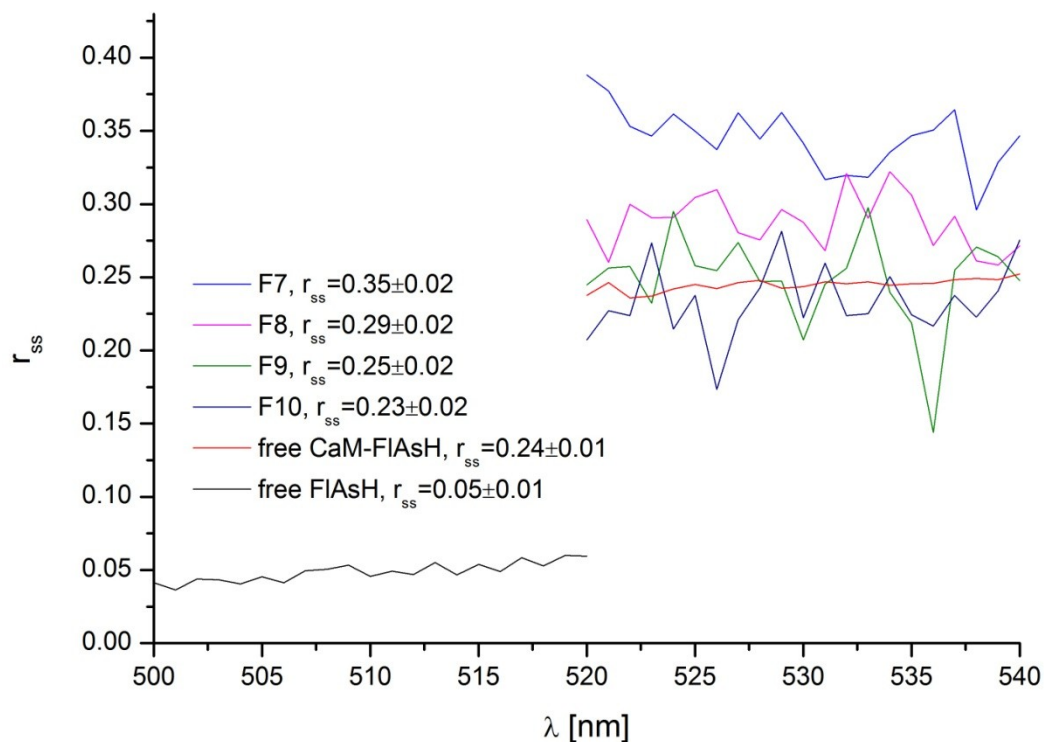


**Fig. 3.4-7.4.** Ribosome-(half CaM/ N-term.) : steady-state anisotropy of fractions F7, F8, F9, F10, free CaM-FIAsH, and free FIAsH.

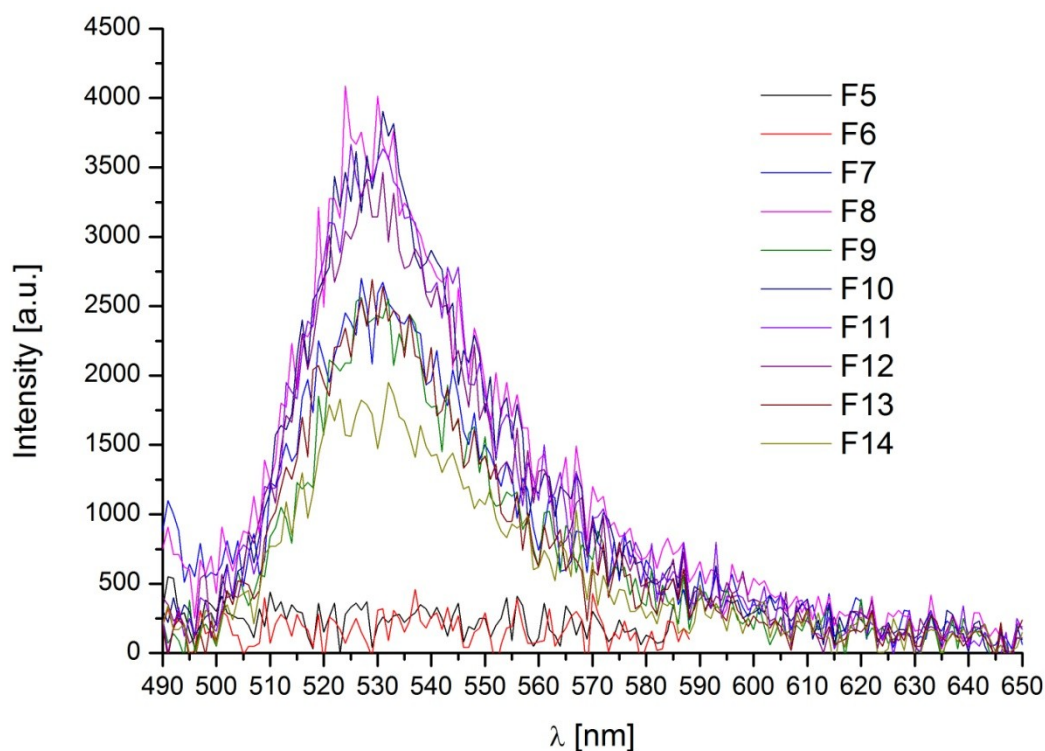


**Fig. 3.4-7.5.** Fluorescence spectra of elutions after purification of ribosome-(CaM full length) by size-exclusion chromatography (Sephadex G-75),  $\lambda_{exc.} = 470$  nm.

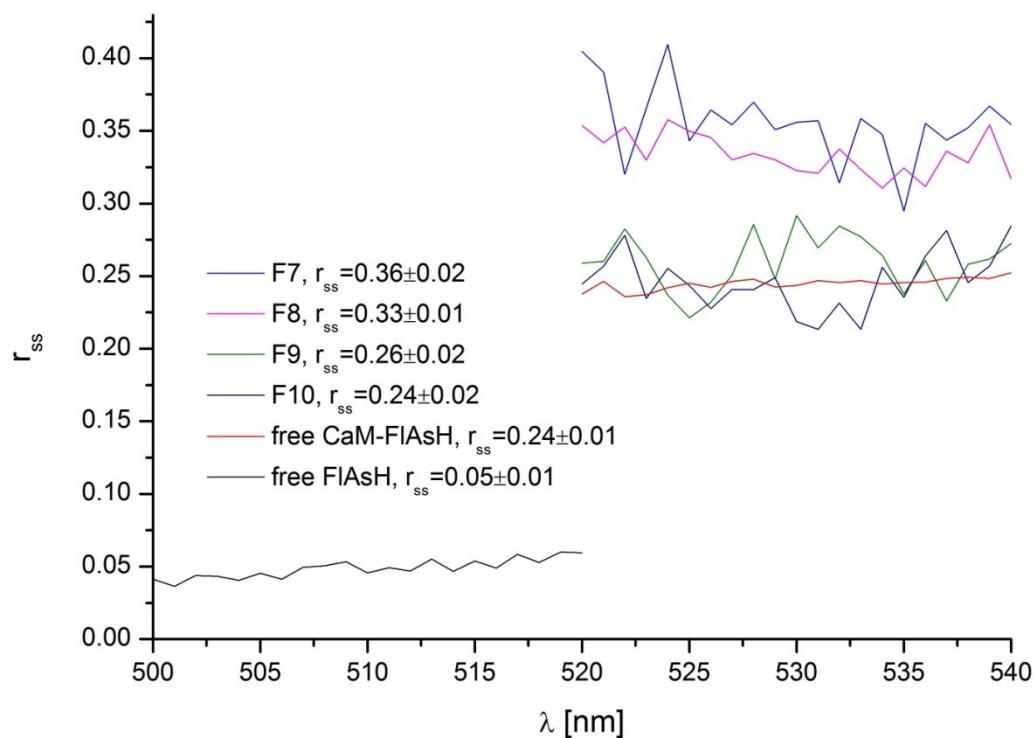


**Fig. 3.4-7.6.** Ribosome-(CaM full length) : steady-state anisotropy of fractions F7, F8, F9, F10, free CaM-FIAsH, and free FIAsH.

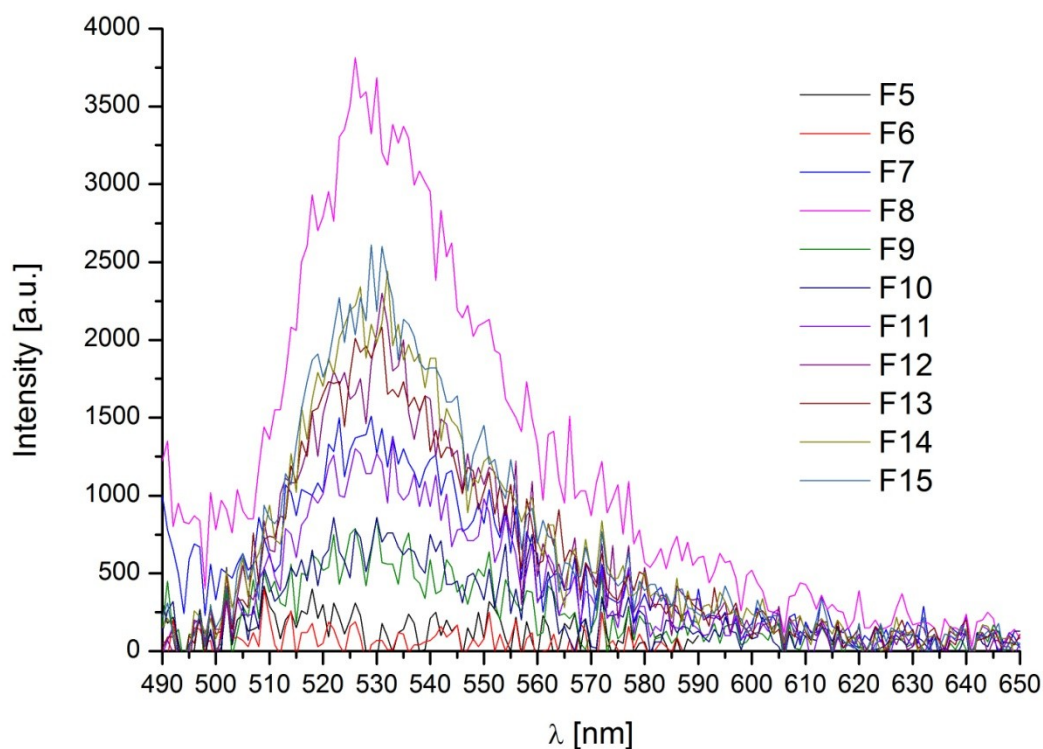


**Fig. 3.4-7.7.** Fluorescence spectra of elutions after purification of control, ribosomes + CaM full length, by size-exclusion chromatography (Sephadex G-75),  $\lambda_{exc.} = 470$  nm.

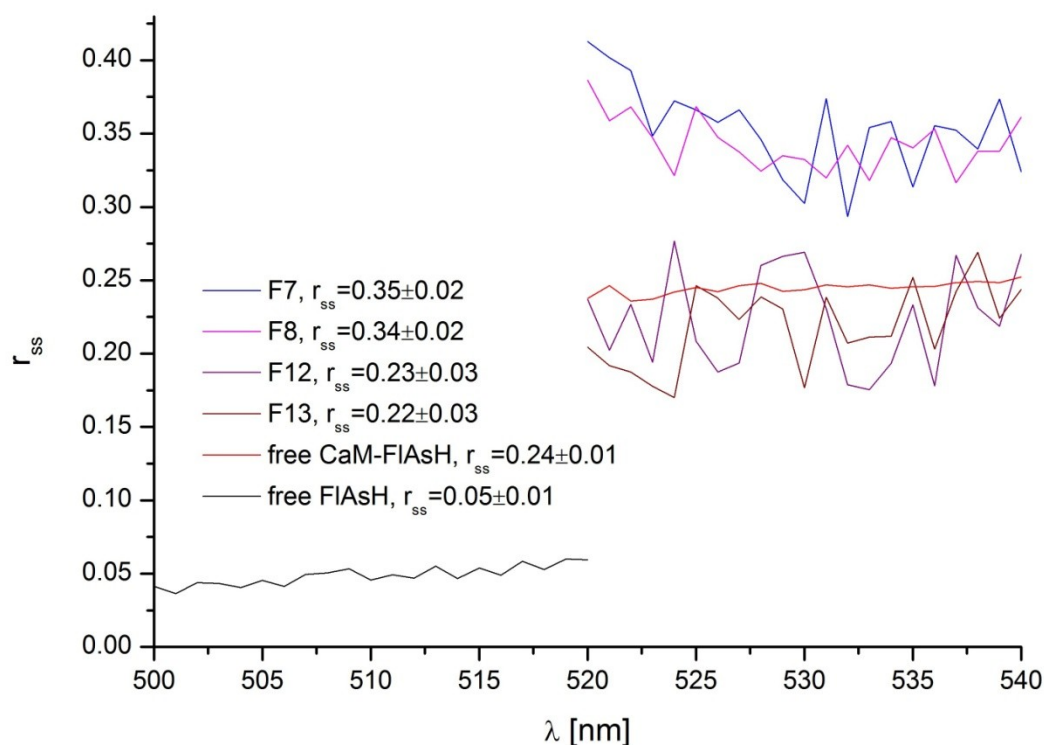


**Fig. 3.4-7.8.** Control : steady-state anisotropy of fractions F7, F8, F12, F13, free CaM-FIAsH, and free FIAsH.

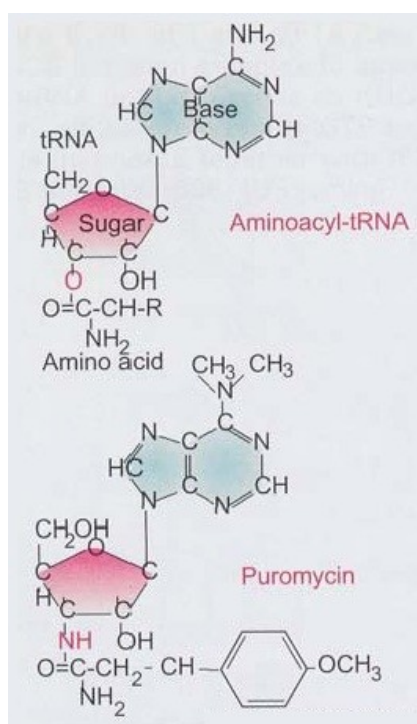
First, in all fluorescence spectra, emission peaks at around 530 nm are observed, which is the same red shift (Stokes shift) that was observed when FIAsH reacted with free diffusing CaMmut(4Cys). Hereafter, CaMmut(4Cys) will be denoted as CaM. Fig. 3.4-7.1 about 1<sup>st</sup> EF-hand might give valuable information. First, there are fluorescence peaks at around 530 nm only in two fractions, F7 and F8, where RNCs are expected to be eluted. Second, in the other fractions there is only noise. This does not prove that there are not released polypeptides. It implies that there are also released polypeptides in later fractions, but not all the cysteines of the tetra-Cys motif were accessible to FIAsH, so, the released polypeptides are not labelled (see also Fig. 2.3-2). It is known that ribosomes have exposed cysteines and many cavities. If the dye is not attached unspecifically to the released nascent chains, it might also not be attached unspecifically to the ribosomes. Solid proof will be provided in the next section.

In the figures with the fluorescence spectra of half CaM, CaM full length, and control (Fig. 3.4-7.3, 3.4-7.5, 3.4-7.7), fluorescence is observed in all fractions after F7 which means that the separation is not good enough. This is the reason the steady-state anisotropies were measured, i.e. to find which fractions contain the RNCs. Henceforth, steady-state fluorescence anisotropies will be abbreviated to “ $r_{ss}$ ”. In Fig. 3.4-7.2 about 1<sup>st</sup> EF-hand only fraction F7 presents the highest  $r_{ss}$ ,  $0.40 \pm 0.03$ , while F8 might also contain released polypeptides because the  $r_{ss}$  is closer to that of free CaM-FIAsH. The same is more or less observed in figures with the  $r_{ss}$  of half CaM, CaM full length, and the control. In Fig. 3.4-7.8 about the  $r_{ss}$  of the control, something unexpected is observed. It is expected that when a stop codon occurs in mRNA, the nascent polypeptide chain will be released. Therefore, an  $r_{ss}$  which is much the same with that of free CaM-FIAsH would be expected. On the contrary, there are fractions, F7 and F8, with high  $r_{ss}$ , around 0.35. This possibly means that some of the nascent polypeptides were not released and they are protruding out of the ribosomal tunnel. Another explanation could be that the polypeptides were released, but they are non-specifically attached to the ribosomes. This would make things more complicated because all so-called RNCs could be ribosomes with released polypeptides non-specifically attached to them. Fortunately, the latter is not the case. Solid proof that FIAsH binds specifically to the tetra-Cys will be provided in the following section about control experiments where RNCs were isolated by ultracentrifugation. Fluorescence of fractions F9 and F10 does not provide good statistics, so it would be meaningless to measure their  $r_{ss}$  because it would be very noisy.

Regarding 1<sup>st</sup> EF-hand, fraction F7 was chosen for time-resolved anisotropy measurements because the steady-state anisotropy is higher. Fractions F7 of half length CaM and full length CaM were chosen, because higher steady-state fluorescence anisotropies were obtained, while fraction F8 of the control was selected because better statistics were obtained.

### 3.4-8 Isolation of ribosome-nascent chain complexes (RNCs) by ultracentrifugation: control experiments

To prove that polypeptides do not attach non-specifically to ribosomes, some control experiments were performed. It is known that puromycin (Puro) can release the nascent chain from the ribosome. Puro is an aminonucleoside antibiotic that resembles an amino acid attached to the terminal adenosine of tRNA.



antibiotic that resembles an amino acid attached to the terminal adenosine of tRNA. The figure on the left shows Puro; an N atom instead of O atom joins an amino acid to tRNA. The antibiotic is treated by the ribosome as though it was an incoming aminoacyl-tRNA. Then the polypeptide attached to peptidyl-tRNA is transferred to the  $\text{NH}_2$  group of the puromycin. Because the Puro moiety is not anchored to the A-site of the ribosome, the polypeptidyl-Puro adduct is released from the ribosome in the form of polypeptidyl-Puro. This premature termination of protein synthesis is responsible for the

lethal action of the antibiotic [25]. This action of Puro was implemented to release nascent chains that emerge from the ribosomal tunnel. The idea is simple. If a nascent chain is already released, and it is non-specifically attached to the ribosome, addition of Puro would not have an effect on the complex. Thus, it would be possible to detect the fluorescence of a labelled polypeptide after ultracentrifugation through a 20 % sucrose cushion.

The pRSET vector carrying the gene for CaM full length together with the sequence for the linker and the SecM was used for these experiments. The pRSET vector carrying the gene for CaM full length with stop codon but without the linker and the SecM was also used as control. *In vitro* transcription-translation reactions and, subsequently, labelling with FIAsh were performed, as described in the previous section. Then, the labelling reactions were split to two tubes; each one of them contained half of the labelling reaction. Therefore, there were four tubes in total, two containing the

ribosomes-(CaM full length) complex, and two containing the control reaction. Puro was added to one of the tubes of each case to a final concentration of 1.3 mM and it reacted with the RNCs for 10 min at 37 °C [82]. Afterwards, all reactions with and without Puro were centrifuged at 10000 x g for 10 min, so that dust and aggregates are spun down; the pellet is not visible. The supernatants were carefully removed and they were loaded onto tubes containing 20 % sucrose dissolved in Tico buffer. Then, ultracentrifugation at 160000 x g for 100 min followed. Only big particles like ribosomes, and maybe 50S subunits, can pass through a 20 % sucrose cushion. After ultracentrifugation, the supernatant was discarded, the tubes were left to dry, and the spot of the tube where ribosomes are expected to precipitate was washed with Tico buffer; the pellet is not visible. Fluorescence of all pellets was measured as well as steady-state anisotropies,  $r_{ss}$ , of the samples without addition of Puro, as it can be seen in Fig. 3.4-8.1, 3.4-8.2, and 3.4-8.3. If Puro had an effect on RNCs, it will not be possible to detect their fluorescence after ultracentrifugation because small polypeptides cannot pass through the 20 % sucrose cushion. The  $r_{ss}$  was measured to confirm that RNCs were really isolated.

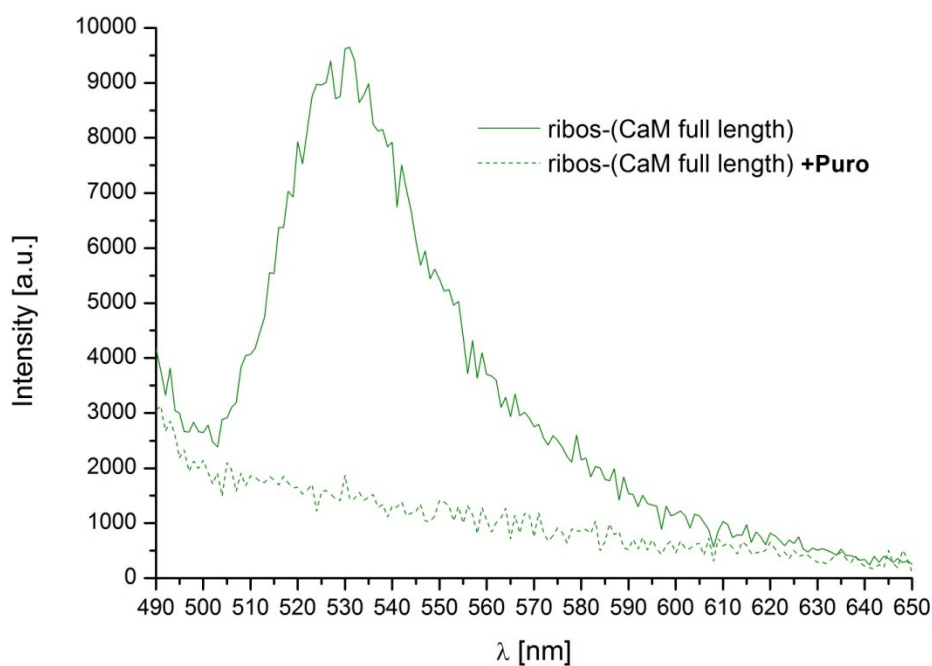


**Fig. 3.4-8.1.** Emission spectra of ribosomes-(CaM full length), after ultracentrifugation through a 20 % sucrose cushion,  $\lambda_{exc}=470$ nm.

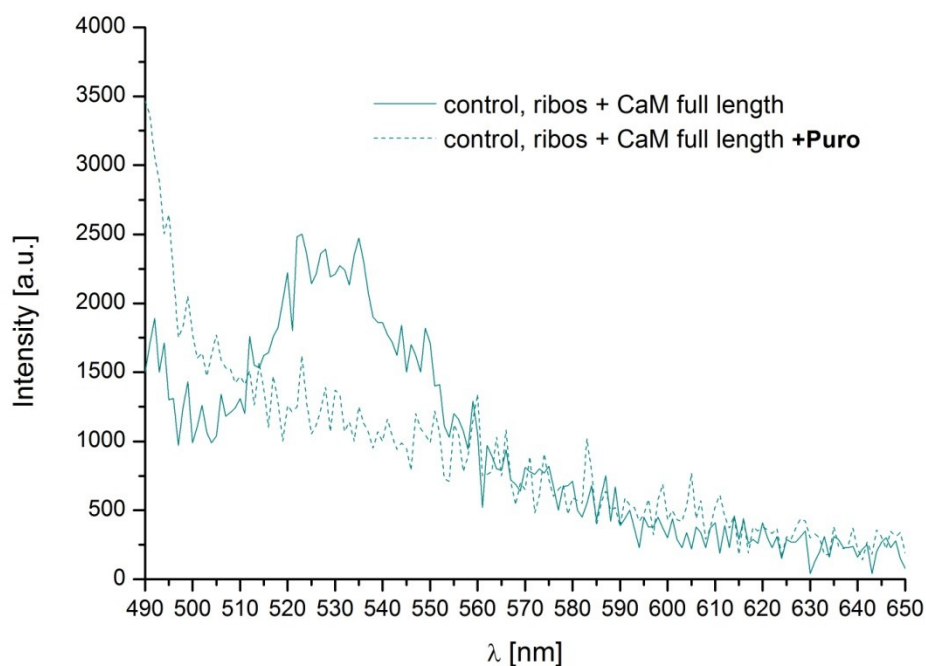


**Fig. 3.4-8.2.** Emission spectra of control, ribosomes + CaM full length, after ultracentrifugation through a 20 % sucrose cushion,  $\lambda_{exc}=470nm$ .

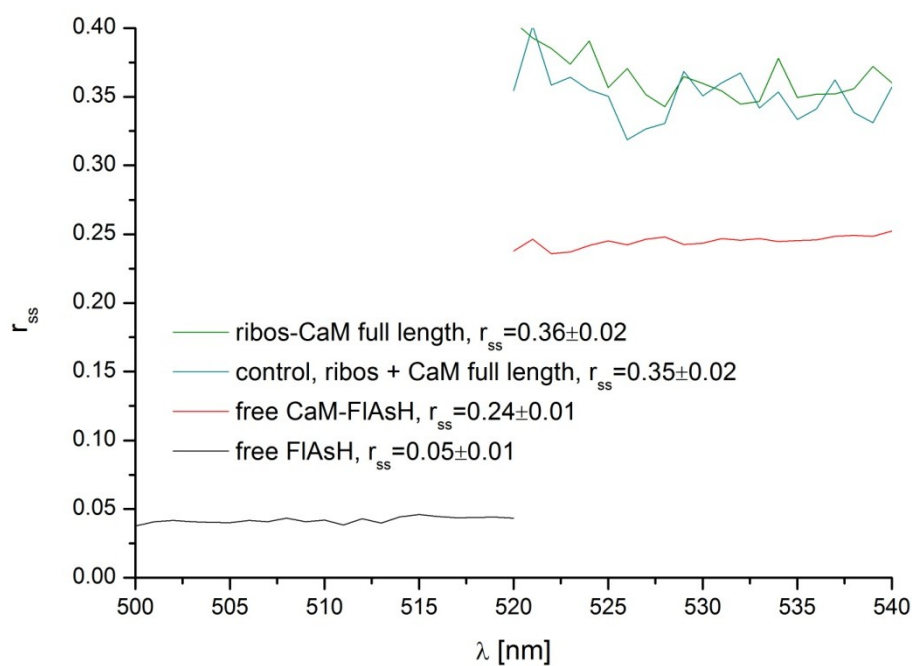


**Fig. 3.4-8.3.** Steady-state fluorescence anisotropies of ribosome-nascent chain complexes (RNCs) without addition of Puro, after ultracentrifugation through a 20 % sucrose cushion.

Indeed, no fluorescence was observed in the samples incubated with Puro. On the contrary, fluorescence at around 530 nm was observed in the sample where presence of the SecM, theoretically, stalls the ribosome, which was actually expected. Additionally, the result of the control reaction as described in the previous section could be observed again with another method of purification of RNCs. Fluorescence at around 530 nm, with the same red shift (Stokes shift), was observed in samples where Puro was not added. This means that nascent chains are really protruding out of the ribosomal tunnel, otherwise addition of Puro would have no effect. In addition, some more important information came out. Taking into consideration that ribosomes have a few exposed cysteines, at least, the fact that fluorescence was not detected in any of the samples that were incubated with Puro proves that FIAsh is attached specifically to the tetra-Cys motif of the nascent chain. This is relieving because it proves that FIAsh is also specifically attached to free diffusing CaM. The fact that RNCs were isolated can also be proved by measuring the  $r_{ss}$  (Fig. 3.4-8.3). It can be observed that the  $r_{ss}$  of RNCs is higher than that of free CaM-FIAsh and free FIAsh. This is reasonable since by measuring the steady-state anisotropy, an average value is obtained, and the rotation of a very big particle, the ribosome itself, contributes to the averaging process.

### 3.5 Time-resolved fluorescence anisotropy of free diffusing ribosome-nascent chain complexes (RNCs) and released polypeptides in solution

In the next few sections, we will present that it was possible to detect motions of ribosome-bound nascent chains and released polypeptides after addition of puromycin (Puro) in the nanosecond timescale as well as the degree of confinement. The nascent chains were polypeptide sequences corresponding to the first EF-hand (CaM<sub>1-40</sub>), half length CaM (the two N-terminal domains, CaM<sub>1-78</sub>), and full length CaM (CaM<sub>1-149</sub>). Of course, all of them contained the tetra-Cys motif (Fig. 3.5.1). The expected rotational

correlation times and hydrodynamic radii applying the Perrin equation are shown in Table 3.5.1. The question was whether dynamics of those nascent polypeptides of different lengths, using FIAsh as a probe, can be resolved. Additionally, a control measurement was made, where full length polypeptide chain is presumed to be released. The aim of this was to confirm the result from steady-state measurements in a time-resolved manner.

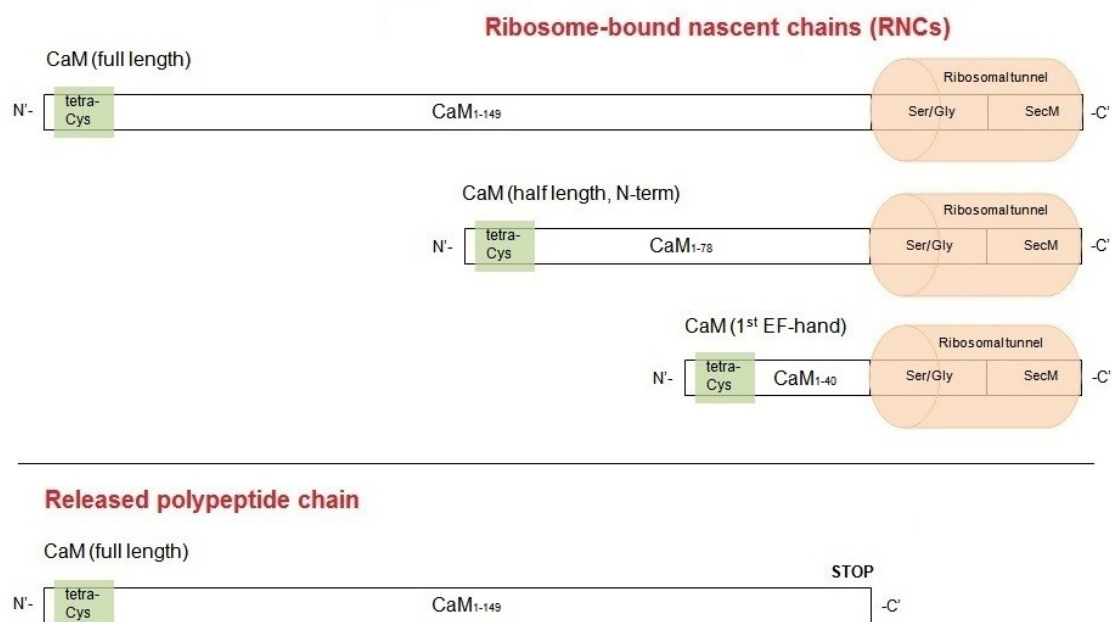


**Fig. 3.5.1.** Schematic representation of ribosome-nascent chain complexes (RNCs) and control. The linker consists of 26 aa and the SecM arrest consists of 17 aa.

|                                     | $\theta_{\text{Perrin}}$ [ns] | $r_h$ [Å] |
|-------------------------------------|-------------------------------|-----------|
| 1 <sup>st</sup> EF-hand             | 2                             | 10        |
| 1 <sup>st</sup> EF-hand+linker+SecM | 3.3                           | 12        |
| Half length CaM                     | 4                             | 13        |
| Half length CaM+linker+SecM         | 5                             | 14        |
| Full length CaM                     | 7                             | 16        |
| Full length CaM+linker+SecM         | 8.5                           | 17        |

**Table 3.5.1.** Rotational correlation times of full length CaM and truncated proteins, and hydrodynamic radii, applying the Perrin equation.

Before starting with the description of the results, the raw fluorescence anisotropy decays will be presented (Fig. 3.5.2). This was necessary to have an idea about the size of the polypeptides and their freedom of movement before and after release. As it can be observed in Fig. 3.5.2, the anisotropy of the fluorescence of labelled EF-hand decays faster than that of half CaM. The anisotropy of the fluorescence of labelled half CaM also decays faster than that of full length CaM. That means that the size of EF-hand is smaller than that of half CaM, and half CaM is smaller than full length construct, which are expected. By comparison between the anisotropy decays of polypeptides before and after release, it can be observed that those of after release decay faster than those before release. This is expected because while the nascent chains protrude out of the ribosomal tunnel, their rotation is hindered by structural elements near the tunnel exit.

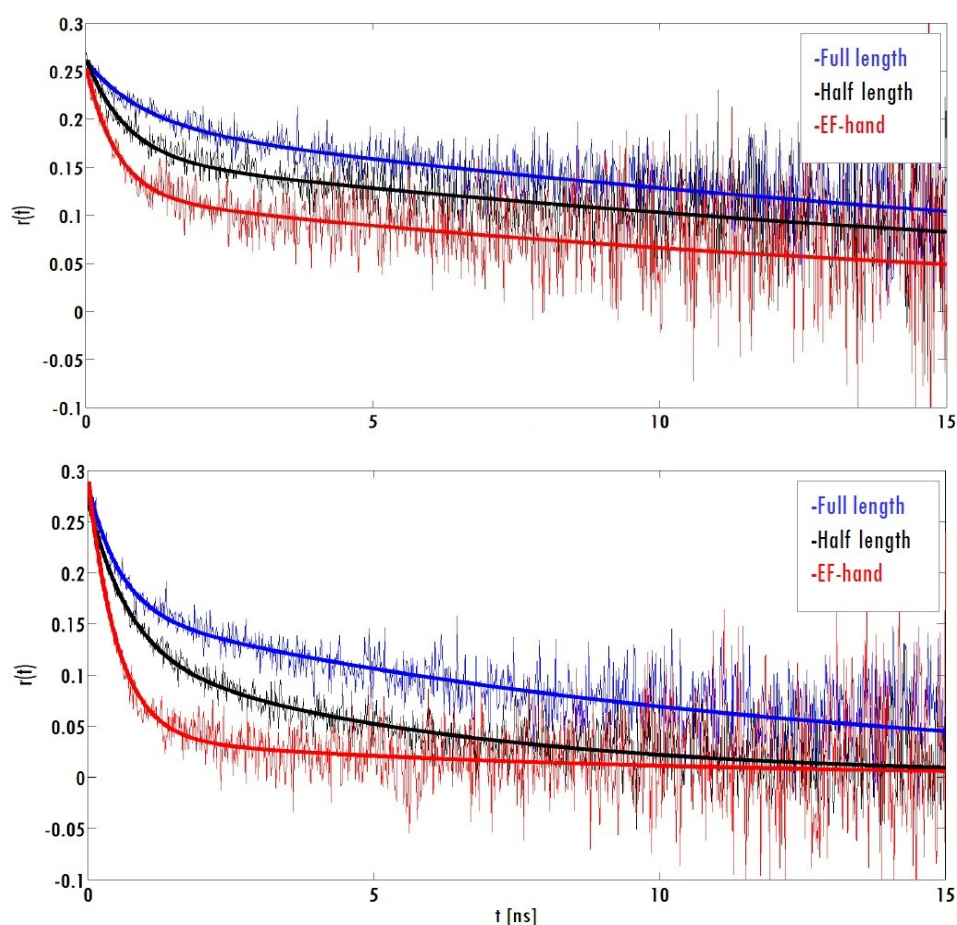


**Fig. 3.5.2.** (Top) Anisotropy decays of nascent chains before release. (Bottom) Anisotropy decays of nascent chains after release by addition of Puro.

### 3.5-1 Time-resolved fluorescence anisotropy of Ribos-(1<sup>st</sup> EF-hand) and released EF-hand

It should be highlighted that in this case RNCs are measured, which are big particles. The correlation time, around 900 ns, that can be attributed to the overall rotation of a ribosome is not resolvable because it is much higher than the fluorescence time window. For that reason, the correlation time of ribosomes was not taken into account in the data analysis. The nascent chain is expected to tumble, therefore, the hindered rotor model was used (Table 3.5-1.1).

| Ribos-(1 <sup>st</sup> EF-hand), hindered rotor                     |            |               |          |                                    |
|---|------------|---------------|----------|------------------------------------|
| $r_0$   | $r_\infty$ | $\theta$ [ns] | $r_{ss}$ |                                    |
| 0.21±0.01   | 0.12±0.01  | 2.3±0.4       | 0.16     | $\chi_R^2=1.7$ , $h_1=0$ , $h_2=1$ |
| $r(t) = 0.09 e^{-\frac{t}{2.3}} + 0.12$ , $\varphi_{\max}=35^\circ$ |            |               |          |                                    |

**Table 3.5-1.1.** Anisotropy decay of Ribos-(1<sup>st</sup> EF-hand).

First, it was not possible to fit the data with  $r_0$  equal to 0.31. By CD measurements, it was observed that the EF-hand has very small  $\alpha$ -helical content (see Section 3.4-6). Therefore, fast segmental motions possibly also occur, and the motion responsible for this loss of anisotropy occurs on a timescale faster than the resolution of the instrument (FWHM: 400 ps). If the correlation time is too short, it cannot be detected and the obtained time-zero anisotropy is smaller than the actual value [68]. Second, it can be observed that the measured correlation time agrees with the expected one, around 2 ns.

The result after release of nascent chains by addition of Puro will now be presented. The anisotropy data were fitted with both the single-exponential and the hindered rotor model (Table 3.5-1.2). We should recall that both the Ser/Gly linker and the SecM are present. Therefore, the rotating unit is expected to be larger.

| Ribos + 1 <sup>st</sup> EF-hand after addition of Puro , single-exponential |            |               |          |                               |
|---|------------|---------------|----------|-------------------------------|
| $r_0$   | $r_\infty$ | $\theta$ [ns] | $r_{ss}$ |                               |
| 0.23±0.01   | ---        | 1.8±0.1       | 0.11     | $\chi_R^2=1.8,$<br>h1=0, h2=0 |
| $r(t) = 0.23 e^{-\frac{t}{1.8}}$  |            |               |          |                               |
| Ribos + 1 <sup>st</sup> EF-hand after addition of Puro , hindered rotor     |            |               |          |                               |
| $r_0$   | $r_\infty$ | $\theta$ [ns] | $r_{ss}$ |                               |
| 0.25±0.01   | 0.03±0.01  | 1.2±0.1       | 0.11     | $\chi_R^2=1.7,$<br>h1=0, h2=0 |
| $r(t) = 0.22 e^{-\frac{t}{1.2}} + 0.03$ , $\varphi_{\max}=62^\circ$         |            |               |          |                               |

**Table 3.5-1.2.** Anisotropy decay of Ribos + 1<sup>st</sup> EF-hand after addition of Puro using the hindered rotor model.

An attempt to fit the data with the wobbling-in-a-cone model was made, but fitting was not possible. There is no considerable decrease in the  $\chi_R^2$ , so, the single-exponential model should be accepted. By CD measurements, it was observed that the EF-hand has low  $\alpha$ -helical content. A smaller correlation time than expected (around 3 ns) was obtained which indicates that fast motions of segments depolarize the emission quickly. Therefore, it can be inferred that when only the first EF-hand protrudes out of the ribosomal tunnel it is almost a random coil.

### 3.5-2 Time-resolved fluorescence anisotropy of Ribos-(half CaM / N-term.) and released polypeptide

The next step was to measure fluorescence anisotropy of half length CaM. The nascent chain is expected to tumble. It is expected that except from the overall rotation, segmental motions also occur. Therefore, the best model would be the cone-in-a-cone model (Eq. 2.4-6.23). But, it was not possible to fit the data with that model. So, the next plausible model is the hindered rotor.

| Ribos-(half CaM / N-term.) , hindered rotor                         |            |               |          |                            |
|---|------------|---------------|----------|----------------------------|
| $r_0$   | $r_\infty$ | $\theta$ [ns] | $r_{ss}$ |                            |
| 0.31±0.00   | 0.15±0.01  | 3.2±0.1       | 0.24     | $\chi_R^2=1.6, h1=0, h2=0$ |
| $r(t) = 0.16 e^{-\frac{t}{3.2}} + 0.15$ , $\varphi_{\max}=38^\circ$ |            |               |          |                            |

**Table 3.5-2.1.** Anisotropy decay of Ribos-(half CaM / N-term.).

First, the  $r_\infty$  is high which shows that the rotation of the polypeptide is hindered. There is a speculation that the folding of a nascent polypeptide chain takes place into a cavity that is near the tunnel exit [83]. The fact that a high  $r_\infty$  was obtained indicates that the nascent chain is inside such a cavity. Second, the obtained rotational correlation time is close to the expected one, around 4 ns.

The result obtained after release of the nascent chain will be presented. The data were fitted with both the single exponential and the hindered rotor model (Table 3.5-2.2). An attempt to fit the data with the ‘wobbling-in-a-cone’ model was made, but the result was not reasonable.

| Ribos + (half CaM / N-term.) after addition of Puro , single-exponential |            |               |          |                            |
|--|------------|---------------|----------|----------------------------|
| $r_0$  | $r_\infty$ | $\theta$ [ns] | $r_{ss}$ |                            |
| 0.31±0.00  | ---        | 3.2±0.1       | 0.16     | $\chi_R^2=1.9, h1=1, h2=1$ |
| $r(t) = 0.31 e^{-\frac{t}{3.2}}$   |            |               |          |                            |
| Ribos + (half CaM / N-term.) after addition of Puro , hindered rotor     |            |               |          |                            |
| $r_0$  | $r_\infty$ | $\theta$ [ns] | $r_{ss}$ |                            |
| 0.31±0.00  | 0.03±0.01  | 2.6±0.1       | 0.16     | $\chi_R^2=1.9, h1=1, h2=0$ |
| $r(t) = 0.28 e^{-\frac{t}{2.6}} + 0.03$ , $\varphi_{\max}=64^\circ$      |            |               |          |                            |

**Table 3.5-2.2.** Anisotropy decay of Ribos + (half CaM / N-term.) after addition of Puro.

First, again there is no considerable decrease in the  $\chi_R^2$ , so, the single-exponential model should be accepted. Second, we should recall that when the polypeptide is released, a C-terminal tail comprising the Ser/Gly linker and the SecM is also present. By applying the Perrin equation, the expected  $\theta$  is close to 5 ns. The fact that a smaller correlation time was obtained indicates that there are fast motions that depolarize the emission quickly. Comparison with the result from CD measurements is not really possible because we do not know how the secondary structure of the rest of the polypeptide is affected by the C-terminal tail. However, by CD measurements it was observed that half length CaM has less relative  $\alpha$ -helical content than the full length (around 60 %). This shows that when half length CaM protrudes out of the ribosomal tunnel, it has not adopted its native structure.

### 3.5-3 Time-resolved fluorescence anisotropy of Ribos-(CaM full length) and released CaM

An attempt to fit the anisotropy data with the cone-in-a-cone model was made, but fitting was not possible. Thus, the data were fitted with the hindered rotor model (Table 3.5-3.1).

| Ribos-(CaM full length) , hindered rotor                         |            |               |          |                            |
|--|------------|---------------|----------|----------------------------|
| $r_0$  | $r_\infty$ | $\theta$ [ns] | $r_{ss}$ |                            |
| 0.31±0.00  | 0.12±0.01  | 10.4±0.6      | 0.26     | $\chi_R^2=1.7, h1=0, h2=1$ |
| $r(t) = 0.19 e^{-\frac{t}{10.4}} + 0.12$ , $\phi_{max}=44^\circ$ |            |               |          |                            |

**Table 3.5-3.1.** Anisotropy decay of Ribos-(CaM full length).

First, it can be observed the rotational correlation time is larger than that of half length CaM (~ 3 ns). The obtained correlation time is also close to that of apo-CaM, around 12 ns. Second, the large  $r_\infty$  indicates that the overall tumbling motion of the protein is restricted by structural elements near the

tunnel exit, which is expected. The result obtained after release of the nascent chain is presented in Table 3.5-3.2. The data were fitted with each model.

| Ribos + CaM full length after addition of Puro , single-exponential                 |               |               |                 |                            |                                |
|---|---------------|---------------|-----------------|----------------------------|--------------------------------|
| $r_0$   | $r_\infty$    | $\theta$ [ns] | $r_{ss}$        |                            |                                |
| 0.31±0.00   | ---           | 7.5±0.1       | 0.21            | $\chi_R^2=2.2, h1=1, h2=1$ |                                |
| $r(t) = 0.31 e^{-\frac{t}{7.5}}$  |               |               |                 |                            |                                |
| Ribos + CaM full length after addition of Puro , hindered rotor                     |               |               |                 |                            |                                |
| $r_0$   | $r_\infty$    | $\theta$ [ns] | $r_{ss}$        |                            |                                |
| 0.31±0.00   | 0.10±0.01     | 4.2±0.1       | 0.22            | $\chi_R^2=2.1, h1=0, h2=1$ |                                |
| $r(t) = 0.21 e^{-\frac{t}{4.2}} + 0.10, \varphi_{max}=47^\circ$                     |               |               |                 |                            |                                |
| Ribos + CaM full length after addition of Puro , wobbling-in-a-cone                 |               |               |                 |                            |                                |
| $r_0$   | $\theta$ [ns] | $A_\infty$    | $\theta_G$ [ns] | $r_{ss}$                   |                                |
| 0.31±0.00   | 2.8±0.2       | 0.48±0.04     | 26.0±5.0        | 0.21                       | $\chi_R^2=2.0$<br>$h1=0, h2=1$ |
| $r(t) = 0.16 e^{-\frac{t}{2.8}} + 0.15 e^{-\frac{t}{26.0}}, \varphi_{max}=39^\circ$ |               |               |                 |                            |                                |

**Table 3.5-3.2.** Anisotropy decay of Ribos + CaM full length after addition of Puro.

First, there is no considerable decrease in the  $\chi_R^2$  also in this case, so, it seems that the single-exponential model should be accepted. But, the weighted residuals when the data were fitted with a single-exponential look worse than those obtained with other models (see Appendix B.7). Second, by applying the Perrin equation, the expected  $\theta$  for full length CaM with the C-terminal tail of Ser/Gly linker and the SecM is close to 8.5 ns assuming that the nascent chain has a spherical shape. But, the tail comprising the Ser/Gly linker and the SecM is expected to be a random coil. Therefore, we cannot allege that the whole polypeptide has a spherical shape. For that reason, the wobbling-in-a-cone model should be accepted as the most plausible. Also in this case, we cannot really compare the result of the released nascent chain

with that from CD measurements because it is not known how that large C-terminal tail affects the secondary structure of the rest of the polypeptide.

#### 3.5-4 Time-resolved fluorescence anisotropy of Ribos-(CaM full length) and released CaM using the control construct with STOP codon

The data were fitted with the hindered rotor model (Table 3.5-4.1).

| Ribos-(CaM full length), control construct , hindered rotor        |            |               |          |                            |
|--|------------|---------------|----------|----------------------------|
| $r_0$  | $r_\infty$ | $\theta$ [ns] | $r_{ss}$ |                            |
| 0.31±0.00  | 0.13±0.01  | 3.0±0.1       | 0.23     | $\chi_R^2=1.6, h1=0, h2=0$ |
| $r(t) = 0.18 e^{-\frac{t}{3.0}} + 0.13$ , $\varphi_{max}=42^\circ$ |            |               |          |                            |

**Table 3.5-4.1.** Anisotropy decay of Ribos-(CaM full length), control construct.

First, the rotational correlation time is equal to 3 ns. This is smaller than the observed one for full length CaM, around 10 ns. We should recall that the DNA construct used in this case did not contain sequences encoding for Ser/Gly linker and SecM arrest. Thus, an explanation is that almost half CaM is still buried into the ribosomal tunnel since around 40 amino acids are expected to span the tunnel. Therefore, the N-terminal half CaM is protruding out. Second, a large  $r_\infty$  can be observed in Table 3.5-4.1. This indicates that the polypeptide chain still protrudes out of the ribosomal tunnel. It also demonstrates that the result from steady-state anisotropy measurements can be confirmed (see also Fig. 3.4-7.8).

Ribosome-bound nascent chains were also incubated with Puro, and the data were fitted with each model (Table 3.5-4.2). First, the correlation time obtained using the single-exponential model is not reasonable with respect to the size of CaM. For that reason, the wobbling-in-a-cone model can be accepted though the  $\chi_R^2$  is not decreased when more fitting parameters are used. Second, when the data were fitted with the hindered rotor model, it was observed that the  $r_\infty$  is smaller than that before addition of Puro. This implies

that almost half length CaM was really protruding out of the ribosomal tunnel. It is remarkable that it was possible to detect a change in the rotational freedom of the nascent chain after addition of Puro. We were able to observe the release of entire CaM by time-resolved anisotropy measurements.

| Ribos + CaM full length, control construct, after addition of Puro ,<br>single-exponential |               |               |                 |                            |                                |
|--|---------------|---------------|-----------------|----------------------------|--------------------------------|
| $r_0$  | $r_\infty$    | $\theta$ [ns] | $r_{ss}$        |                            |                                |
| 0.31±0.00  | ---           | 4.4±0.1       | 0.18            | $\chi_R^2=1.6, h1=0, h2=0$ |                                |
| $r(t) = 0.31 e^{-\frac{t}{4.4}}$   |               |               |                 |                            |                                |
| Ribos + CaM full length, control construct, after addition of Puro ,<br>hindered rotor     |               |               |                 |                            |                                |
| $r_0$  | $r_\infty$    | $\theta$ [ns] | $r_{ss}$        |                            |                                |
| 0.31±0.00  | 0.05±0.01     | 3.2±0.1       | 0.18            | $\chi_R^2=1.6, h1=0, h2=0$ |                                |
| $r(t) = 0.26 e^{-\frac{t}{3.2}} + 0.05, \varphi_{max}=58^\circ$                            |               |               |                 |                            |                                |
| Ribos + CaM full length, control construct, after addition of Puro ,<br>wobbling-in-a-cone |               |               |                 |                            |                                |
| $r_0$  | $\theta$ [ns] | $A_\infty$    | $\theta_G$ [ns] | $r_{ss}$                   |                                |
| 0.31±0.00  | 2.6±0.2       | 0.32±0.05     | 13.5±3.5        | 0.17                       | $\chi_R^2=1.6$<br>$h1=0, h2=0$ |
| $r(t) = 0.21 e^{-\frac{t}{2.6}} + 0.10 e^{-\frac{t}{13.5}}, \varphi_{max}=48^\circ$        |               |               |                 |                            |                                |

**Table 3.5-4.2.** Anisotropy decay of Ribos + CaM full length, control construct, after addition of Puro.

## 4. Discussion and Conclusion

Our aim was to study the folding of apo-CaM, CaM-Ca<sup>2+</sup> as well as structural properties of nascent chains that emerge from the ribosomal tunnel. Fluorescence anisotropy analysis mainly gives information about the size of a rotating unit. Therefore, CD measurements were performed to obtain information about the secondary structure of CaM and truncated proteins. First, the result from CD measurements will be discussed, and the result from fluorescence anisotropy analysis will follow. The result from CD measurements combined with the result from time-resolved fluorescence anisotropy analysis provides information about the folding of CaM and nascent chains.

### CD measurements and functionality tests with calcium

It was observed that the mutation of four amino acids to cysteines perturbs the  $\alpha$ -helical structure of CaM. By comparison between the CD spectrum of the mutant and that of wild-type, a 10-30 % reduction in the ellipticity of the mutant was observed. Actually, the 10-30 % of the  $\alpha$ -helical content of CaM can be assigned to the first  $\alpha$ -helix. But, this does not mean that only the first  $\alpha$ -helix is not folded; the 10-30 % of the total  $\alpha$ -helical content is lost. This is not surprising because hydrophilic side chains were mutated to hydrophobic ones. Upon addition of Ca<sup>2+</sup>, a significant change was observed, both ellipticities are increased. This is consistent with what is known from the literature about CaM and how it behaves upon Ca<sup>2+</sup> binding. The conformation of a protein becomes more ordered, with higher helical content when Ca<sup>2+</sup> is bound [77][84][85][86]. In addition, CD spectra of truncated proteins carrying the tetra-Cys motif were also acquired. The  $\alpha$ -helical content of half length CaM was almost 60 % of full length CaM, and that of the 1<sup>st</sup> EF-hand, around 22 % of full length CaM. This means that the N-terminal part of the mutant has few secondary structure elements. If a part of the protein is missing or not synthesized, we should not expect that the rest of the

polypeptide will adopt its native structure. This possibly occurs because native-like interactions between segments of the protein are missing. It also indicates that CaM adopts a native-like structure only when the full length polypeptide protrudes out of the ribosomal tunnel. The fact that the tertiary structure of the mutant has been changed was also proved by functionality tests with  $\text{Ca}^{2+}$ . It was observed that the N-terminal loops of the mutant cannot bind  $\text{Ca}^{2+}$ , while the C-terminal ones can bind  $\text{Ca}^{2+}$ . It seems that the C-terminal domains of the mutant retained their tertiary structure, while this is uncertain for the N-terminal ones. Therefore, another reason why folding of the N-terminal part of CaM was observed to be incorrect is the presence of the hydrophobic side chains of cysteines.

### Time-resolved fluorescence anisotropy analysis

Our intention was to investigate the possibility to use a dye probe (FIAsH) which binds rigidly to an amino acid sequence within a macromolecule (CaM) to obtain information about the folding of a protein. It is expected that when a dye (FIAsH) is rigidly attached to a protein, the dye motion will follow the movement of the segment to which the dye is attached, at least. But there were some impediments. First, it was not possible to measure the time-zero anisotropy directly. Rotational correlation times cannot be compared if at the same time the time-zero anisotropy also changes. So, we tried to get an approximation of the  $r_0$  indirectly. All available raw data were analyzed, also those of ribosome-nascent chain complexes, and we tried to find a value of  $r_0$  in order to observe a trend in the rotational correlation times. This value of  $r_0$  was 0.31, which is close to a previously reported, 0.30 [87]. Different values for time-zero anisotropy were published by other groups [66][88][89]. Second, the weighted residuals look rather similar between different models for each case (apo-CaM, CaM- $\text{Ca}^{2+}$ , nascent chains, released polypeptides). Third, the values of the goodness-of-fit parameter,  $\chi_R^2$ , also do not differ so much between different models. These were the tools we had in our hands, and we tried to get some answers.

### **Time-resolved fluorescence anisotropy of apo-CaM and CaM-Ca<sup>2+</sup>**

Regarding apo-CaM, the correlation time obtained by fitting with the single-exponential model was around 7 ns, while by fitting with the wobbling-in-a-cone model, it was around 12 ns. It was hypothesized that the rotational correlation time for overall rotation of apo-CaM is around 12 ns mainly because the shape of CaM is not spherical; rather it looks like a dumbbell. When Ca<sup>2+</sup> was bound to CaM, the correlation time increased to around 16 ns. However, it was also observed for both apo-CaM and CaM-Ca<sup>2+</sup> that the  $\chi_R^2$  did not decrease when more fitting parameters were used to fit the fluorescence polarization data. Therefore, it can be argued that we should not accept more complicated models than the single-exponential. It seems that time-resolved anisotropy measurements do not give a clear answer which model best describes the structural properties of CaM. This observation is in contrast to what is claimed by other research groups [77][87][90]. In both cases, the measured concentration of CaM was 1 nM. We could also argue that we need high signal-to-noise ratio to give an answer which is the best model. But when a higher concentration of CaM was measured (around 3 nM), fitting was not possible with any model. The  $\chi_R^2$  was between 3 and 4, and the weighted residuals were not randomly distributed around zero. Nevertheless, whether the correlation time of apo-CaM is equal to 7 ns or 12 ns, it becomes 16 ns upon Ca<sup>2+</sup> binding. This means that when Ca<sup>2+</sup> was bound, the size of the molecule was changed. It became more stretched, and this is the important result. It was possible to detect the change of the tertiary structure of CaM on Ca<sup>2+</sup> binding by time-resolved fluorescence anisotropy. These findings are also in agreement with the result from CD measurements. It was observed that when Ca<sup>2+</sup> was bound, the  $\alpha$ -helical content increased, and thus, a change in the tertiary structure is expected to have occurred. They are also consistent with what is published for CaM, and with the crystal structure of CaM-Ca<sup>2+</sup> (PDB: 1CLL). These results also demonstrate the advantage of the rigid linkage between the dye and the protein to obtain information about the rotational freedom of a macromolecule. If the dye was linked by a single-covalent bond, the result would be biased by the free

rotation of the dye-protein bond, with a correlation time of around 400 ps, and data analysis would not be straightforward. An attempt was also made to study unfolded CaM, but unreliable data could only be obtained. We decided not to study unfolded CaM with more effort because other experiments were of bigger interest.

### **Time-resolved fluorescence anisotropy of nascent and released polypeptide chains**

We studied two cases, ribosome-bound and released nascent chains of different lengths of CaM. The fluorescence anisotropy decays of ribosome-bound nascent chains (RNCs) revealed some important features of the nascent chains. The anisotropy of the 1<sup>st</sup> EF-hand decays faster than that of half length CaM. The anisotropy of half length CaM also decays faster than that of full length CaM. The rotational correlation times,  $\theta$ , of EF-hand, half length and full length CaM were around 2, 3 and 10 ns, respectively. They are also close to the expected correlation times by applying Perrin equation. Thus, the obtained  $\theta$  values are reasonable with respect to the size of the nascent chain. These show that the 1<sup>st</sup> EF-hand is smaller than half length CaM, and half length CaM is smaller than full length CaM. We were able to detect the difference in the size of nascent chains that correspond to segments of CaM by time-resolved fluorescence anisotropy measurements. It was necessary to check with an independent method (CD) the folding state before interpreting anisotropy data.

CD measurements were performed to acquire knowledge about the  $\alpha$ -helical content of each nascent chain. We did not measure the CD signal of RNCs because ribosomal proteins would also absorb in the far UV. Thus, data analysis would not be straightforward. For that reason, we preferred to produce these polypeptides that correspond to segments of CaM in *E. coli* and purify them. The 1<sup>st</sup> EF-hand had very low relative  $\alpha$ -helical content, around 22 % of the full length, while more secondary structure elements appeared as the size of the polypeptide chain became larger. These indicate that only when the full length nascent chain protrudes out of the ribosomal tunnel, it starts adopting a native-like conformation with its full content of

secondary structure elements. Other groups also suggest that there should be a minimal length of nascent chain that must emerge from the ribosomal tunnel before the formation of any persistent secondary or tertiary structure occurs [91][92][93][94]. Therefore, another probable reason that the anisotropy of the smaller polypeptides decays fast is the occurrence of fast segmental motions. The correlation time of ribosome-bound CaM was around 10 ns while that of apo-CaM expressed *in vivo* was around 7 ns. This shows that nascent full length CaM is more stretched than apo-CaM indicating that some native-like interactions between segments of the protein do not occur. In this study, a commercially available *in vitro* transcription-translation system (PURE system) that does not contain chaperones was used. Several studies showed that concurrently with protein synthesis by the ribosome, nascent chains are subject to chaperone-assisted folding [95][96][97]. An *in vitro* system that contains chaperones can also be used to check which are the differences in folding of nascent chains.

The second important feature is that the anisotropy of all constructs before release does not decay to zero. It is also confirmed by the obtained high  $r_{\infty}$  in all cases. In our opinion, the anisotropy is not influenced by the slow rotation of the ribosome. In addition, its correlation time, around 900 ns, is much larger than the fluorescence time window, therefore, it cannot be detected. The nascent chains are tethered to the ribosome through a linker. Effectively, this linker is a polypeptide chain which contains single-covalent bonds, thereby providing a large rotational freedom. On this account, it is expected that the nascent chains are able to make an overall rotation on one axis, at least, while they protrude out of the ribosomal tunnel. The most reasonable explanation why the anisotropy does not decay to zero is that the rotation of the nascent chains is retarded. It is probable that this retardation is caused by strong interactions between the nascent chain and the surface of the ribosome, e.g. collisions.

Fluorescence anisotropy decays of nascent chains after addition of puromycin (Puro) were also acquired. We were also able in this case to characterize the three different lengths of polypeptide chains. The anisotropy of a smaller in size polypeptide decays faster than that of a larger one. The obtained correlation times were also reasonable with respect to the size of the

polypeptide chain. Moreover, there is a significant difference in the anisotropy decays as compared to those before addition of Puro. The anisotropy of all polypeptides decays to zero. This shows that there is no strong interaction between the nascent chains and the surface of the ribosome which means that the nascent chains were released from the ribosome as expected. It was possible to detect this release by time-resolved anisotropy measurements. Other groups also propose the usage of Puro or hydroxylamine (NH<sub>2</sub>OH) to release nascent chains [98][99][100]. We should also recall that when the nascent chain is released, there is also a large C-terminal tail comprising the Ser/Gly linker and the SecM arrest sequence. We do not know how these influence the secondary structure of the rest of the polypeptide. However, the obtained correlation times of the 1<sup>st</sup> EF-hand and half length CaM give a hint about the folding of these polypeptide chains. The size of the rotating unit is increased because of the presence of the large C-terminal tail. Thus, it is expected that the correlation time is larger. We observed smaller correlation times than the expected by applying Perrin equation. This indicates that these are correlation times of segmental motions. If the polypeptide is almost a random coil, there will be a large freedom of segmental movement. Therefore, this motion will depolarize the emission quickly, and thus, the correlation time will be small. We can conclude that the 1<sup>st</sup> EF-hand and half length CaM have few secondary structure elements. This is also confirmed by CD measurements of segments of CaM. These findings also indicate that chaperones might be really necessary for correct folding.

Studies on ribosome-bound and released nascent chains gave very promising results. Time-resolved fluorescence anisotropy measurements combined with CD measurements can give information about structural properties of nascent chains. Unfortunately, we cannot provide a clear answer about correlation times of segmental motions of ribosome-bound nascent chains and released polypeptides. Other groups claim that they were able to detect segmental motions of polypeptide chains [77][88][89][90][98][99]. It is rather probable that these groups did not characterize fully their constructs. We characterized mutated CaM and CaM-FIAsH complex, and we had to avoid overinterpretation of our data. A roundup of the most important information can be found in Table 4.1.

|                                     |                    | $r_0$           | $\theta$ [ns] | $\theta_G$ [ns] | $A_\infty$      | $\varphi_{\max}$ [deg] | Volume ( $\text{\AA}^3$ ) | $r_h$ ( $\text{\AA}$ ) |
|-------------------------------------|--------------------|-----------------|---------------|-----------------|-----------------|------------------------|---------------------------|------------------------|
| <b>apo-CaM</b>                      | single-exp         | <b>0.31</b>     | ---           | $7.0 \pm 0.2$   | ---             | ---                    | 17053                     | 16                     |
|                                     | wobbling-in-a-cone | <b>0.31</b>     | $1.1 \pm 0.1$ | $12.2 \pm 0.5$  | $0.75 \pm 0.01$ | $26^\circ$             | 29720                     | 19                     |
| <b>CaM-Ca<sup>2+</sup></b>          |                    | <b>0.31</b>     | ---           | $16.1 \pm 0.1$  | ---             | ---                    | 39221                     | 21                     |
| Ribos-<br>(1 <sup>st</sup> EF-hand) |                    | $0.21 \pm 0.01$ | ---           | $2.3 \pm 0.4$   | $0.57 \pm 0.01$ | $35^\circ$             | 5603                      | 11                     |
|                                     | <b>+ Puro</b>      | $0.23 \pm 0.01$ | ---           | $1.8 \pm 0.1$   | ---             | ---                    | 4385                      | 10                     |
| Ribos-<br>(half CaM /<br>N-term.)   |                    | <b>0.31</b>     | ---           | $3.2 \pm 0.1$   | $0.48 \pm 0.01$ | $38^\circ$             | 7795                      | 12                     |
|                                     | <b>+ Puro</b>      | <b>0.31</b>     | ---           | $3.2 \pm 0.1$   | ---             | ---                    | 7795                      | 12                     |
| Ribos-CaM<br>(full length)          |                    | <b>0.31</b>     | ---           | $10.4 \pm 0.6$  | $0.39 \pm 0.01$ | $44^\circ$             | 25335                     | 18                     |
|                                     | <b>+ Puro</b>      | <b>0.31</b>     | $2.8 \pm 0.2$ | $26.0 \pm 5.0$  | $0.48 \pm 0.04$ | $39^\circ$             | 63338                     | 25                     |

**Table 4.1.** Roundup of most important information obtained by analysis of time-resolved fluorescence polarization data.

## Outlook

It is challenging to study co-translational protein folding. Several groups have proposed the production of ribosome-bound nascent chains to study co-translational protein folding [98][101][102][103][104][105][106].

Our data were not adequate to distinguish which model best describes the structural properties of CaM and nascent chains. The main reason is that data with not good statistics were obtained. It is clear that the signal-to-noise ratio should be increased. Attempts were made to increase the signal-to-noise ratio by increasing the concentration of the measured protein but without success. A promising alternative is to increase the observation time of the molecules.

In addition, we observed that the introduction of the tetra-Cys motif perturbed the structure of the protein. It caused partial unfolding of the protein. As a next step, different positions of the tetra-Cys motif should be tested in order to make sure that the bound dye also reports for overall rotation of the protein and not only for local flexibility. CD measurements should every time be performed to check that the wild-type secondary structure is retained.

Chaperones are usually needed for correct folding of nascent chains. We observed that shorter polypeptides of CaM had low  $\alpha$ -helical content when produced in *E. coli*. CaM is a eukaryotic protein and eukaryotic chaperones might assist better its folding. Thus, these proteins could be produced in yeast cells, and checked for their  $\alpha$ -helical content. Additionally, we can check which are the differences when *in vitro* systems that contain chaperones are used. A eukaryotic *in vitro* system can also be used for comparison. Alternatively, the samples can be incubated with chaperones.

Other dyes that can be rigidly attached to a target introduced into a protein can also be used. For instance, we can use bifunctionalized rhodamine since rhodamine is known to be emissive.

We studied CaM on ensemble level. The drawback with ensemble measurements is that heterogeneous populations of unfolding/refolding transitions of a protein are observed. Such events are not synchronized in our measurements. These obstacles can be overcome if we analyze one single molecule at a time. There are two possibilities to measure on the single-

molecule level by fluorescence spectroscopy techniques. The first is to measure very low concentrations (50 pM or even less), so that only one molecule diffuses through the focal volume each time. The observation time of one single molecule is limited by the diffusion time through the focal volume which is in the order of a few milliseconds. In our case, the signal-to-noise ratio will be very low, and as already mentioned, a high signal-to-noise ratio is required. A very promising alternative is to tether single molecules to a PEG-blocked glass surface. In this way, the observation time of a single molecule can be increased. By increasing the observation time, we have the chance to detect more photons that are necessary for a high signal to noise ratio [107][108]. Observation of single molecules can be applied to monitor the folding of a protein while it is synthesized by a tethered ribosome.

## Summary

In the presented work, we developed a fluorescence spectroscopy method to study folding of ribosome-bound nascent polypeptide chains. We have chosen Calmodulin (CaM) as a protein model because it is a small protein comprising  $\alpha$ -helical structure. To follow the folding, we used a biarsenical ligand (Fluorescein Arsenical Helix Binder or FIAsH), which binds rigidly to a tetra-Cys motif. Such a motif was introduced into the N-terminal sequence of CaM. If a dye (FIAsH) is rigidly bound to its target, this will influence the anisotropy of the fluorescence, as the average angular displacement of a fluorophore, which occurs between absorption and fluorescence emission, reflects the mobility of the molecule. The idea is that if we have a dye probe that can be rigidly attached to a protein, its rotational freedom will report for local dynamics and overall tumbling motion of the protein, as well. Measurements on apo-CaM and CaM-Ca<sup>2+</sup> were performed. A considerable increase in the rotational correlation time of CaM upon Ca<sup>2+</sup> binding was observed. This shows that when Ca<sup>2+</sup> is bound to the molecule, the tertiary structure changes and it becomes more stretched. In a next step, ribosome-nascent chain complexes (RNCs) with the first EF-hand, the half and the full length CaM protruding out of the ribosomal tunnel were studied. The obtained result showed a tendency in the correlation times that were consistent with respect to the size of nascent chains. Another remarkable observation is that it was possible to detect the release of the protein from the ribosome after treatment with puromycin (Puro). Further analysis by circular dichroism measurements showed that CaM started adopting native-like conformation only when the full length nascent chain was emerging from the ribosome. Finally, we got evidence that rigid binding of a dye to a protein provides an advantage over the single covalent bond attachment. Taking everything into consideration, we made some first steps in understanding the co-translational folding process by time-resolved fluorescence anisotropy measurements.

## Zusammenfassung

In der vorliegenden Arbeit haben wir versucht eine fluoreszenzspektroskopische Methode zur Untersuchung der Faltung von Ribosom-gebundenen naszierenden Polypeptidketten zu entwickeln. Wir wählten Calmodulin (CaM) als Modellprotein, da es ein kleines, aus alpha-Helices bestehendes Protein ist. Um den Faltungsweg zu studieren, entschieden wir einen bi-arsenischen Liganden (Fluorescein Arsenical Helix Binder oder FIAsH) zu benutzen, der rigide an ein tetra-Cystein Motiv bindet. Solch ein Motiv wurde in die N-terminale Sequenz des CaM integriert. Die starre Bindung eines Farbstoffs (FIAsH) an ein Zielmolekül beeinflusst seine Fluoreszenzanisotropie, da der durchschnittliche Winkelversatz des Fluorophores zwischen Absorption und Fluoreszenzemission nicht mehr seine eigene, sondern die Rotationsmobilität des Zielmoleküls widerspiegelt. Die Idee dabei ist, dass der Grad an Rotationsfreiheit des rigide gebundenen Farbstoffs Aufschluss geben kann über die lokale Dynamik sowie die Gesamtrotation des Proteins. Zuerst führten wir Messungen des gereinigten Apo-CaM durch. Diese ergaben die Existenz einer Rotationbewegung, deren Rotationskorrelationszeit nah am Erwartungswert lag. Anschließend untersuchten wir CaM-Ca<sup>2+</sup> und ermittelten eine größere Rotationskorrelationszeit. Dieses Ergebnis entsprach unserer Annahme, denn CaM adaptiert eine geordnetere und ausgedehntere Konformation unter Bindung von Ca<sup>2+</sup>. Unser nächster Schritt waren Messungen von Komplexen aus Ribosomen und gelabelten naszierenden Ketten (RNCs) unterschiedlicher Länge, nämlich der ersten EF-Hand und der Polypeptidketten von halber und ganzer Länge. Die ermittelten Resultate zeigten die erwartete Tendenz in den Korrelationszeiten: je länger die naszierende Kette desto größer die Rotationskorrelationszeit. Eine andere bemerkenswerte Beobachtung war, dass wir nach Zugabe von Puromycin die Freisetzung des Proteins vom Ribosom beobachten konnten. Weitere Analysen indizierten, dass CaM anfängt nur dann seine native Konformation zu adaptieren, wenn die Polypeptidkette der vollen Länge aus dem Ribosom heraustritt. Abschließend erhielten wir den Beweis, dass die rigide kovalente

Befestigung eines Fluorophores an ein Protein Vorteile bietet im Vergleich zu flexibleren kovalenten Einfachbindungen. In Anbetracht all dessen haben wir mittels zeitaufgelöster Fluoreszenz-Anisotropie Messungen einige erste Erkenntnisse bezüglich der Konformationsdynamik eines Proteins sowie co-translationaler Faltungsprozesse erhalten.

## Bibliography

1. C.M. Dobson (2003). Protein folding and misfolding. *Nature* **426**: 884-890.
2. F.U. Hartl, M. Hayer-Hartl (2009). Converging concepts of protein folding *in vitro* and *in vivo*. *Nature Structural and Molecular Biology* **16**: 574-579.
3. S.A. Weinreis, J.P. Ellis, S. Cavagnero (2010). Dynamic fluorescence depolarization: A powerful tool to explore protein folding on the ribosome. *Methods* **52**: 57-73.
4. S. Lee, L. Antony, R. Hartmann, *et al* (2010). Conformational diversity in prion protein variants influences intermolecular  $\beta$ -sheet formation. *EMBO Journal* **29**: 251-262.
5. P.J. Thomas, B. Qu, P.L. Pedersen (1995). Defective protein folding as a basis of human disease. *TIBS* **20**: 458-459.
6. J.C. Young, V.R. Agashe, F.U. Hartl (2004). Pathways of chaperone-mediated protein folding in the cytosol. *Nature reviews* **5**: 781-791.
7. C.M. Dobson, M. Karplus (1999). The fundamentals of protein folding: bringing together theory and experiment. *Current Opinion in Structural Biology* **9**: 92-101.
8. C.B. Anfinsen (1973). Principles that govern the folding of protein chains. *Science* **181**: 223-230.
9. C. Levinthal (1968). Are there pathways for protein folding? *Extrait du Journal de Chimie Physique* **65**: 44-45.
10. J.B. Udgaonkar (2008). Multiple routes and structural heterogeneity in protein folding. *Annu. Rev. Biophys.* **37**: 489-510.
11. W.J. Wedemeyer, H.A. Scheraga (2001). Protein folding: overview of pathways. *Encyclopedia of Life Sciences*: 1-9.
12. D.V. Fedyukina, S. Cavagnero (2011): Protein folding at the exit tunnel. *Annu. Rev. Biophys.* **40**: 337-359.
13. A.R. Ferhst (2008). From the first protein structures to our current knowledge of protein folding: delights and skepticisms. *Nature reviews* **9**: 650-654.

14. K. Sridevi, J.B. Udgaokar (2002). Unfolding rates of Barstar determined in native and low denaturant conditions indicate the presence of intermediates. *Biochemistry* **41**: 1568-1578.
15. K.A. Dill, H.S. Chan (1997). From Levinthal to pathways to funnels. *Nature Structural Biology* **4**: 10-19.
16. P.G. Wolynes, J.N. Onuchic, D. Thirumalai (1995). Navigating the folding routes. *Science* **267**: 1619-1620.
17. A.R. Dinner, A. Sali, L.J. Smith, *et al* (2000). Understanding protein folding via free-energy surfaces from theory and experiment. *TIBS* **25**: 331-339.
18. W.A. Eaton, V. Munoz, P.A. Thompson, *et al* (1998). Kinetics and dynamics of loops,  $\alpha$ -helices,  $\beta$ -hairpins, and fast-folding proteins. *Acc. Chem. Res.* **31**: 745-753.
19. K.W. Plaxco, K.T. Simons, D. Baker (1998). Contact order, transition state placement and the refolding rates of single domain proteins. *J. Mol. Biol.* **277**: 985-994.
20. U. Mayor, N.R. Guydosh, C.M. Johnson, *et al* (2003). The complete folding pathway of a protein from nanoseconds to microseconds. *Nature* **421**: 863-867.
21. M. Vendruscolo, E. Paci, C.M. Dobson (2003). Structures and relative free energies of partially folded states of proteins. *PNAS* **100**: 14917-14821.
22. C.J. Wilson, P. Wittung-Stafshede (2005). Role of structural determinants in folding of the sandwich-like protein *Pseudomonas aeruginosa* azurin. *PNAS* **102**: 3984-3987.
23. V. Ramakrishnan, P.B. Moore (2001). Atomic structures at last: the ribosome in 2000. *Curr. Opin. Struct. Biol.* **11**: 144-154.
24. K.S. Wilson, H.F. Noller (1998). Molecular movement inside the translational engine. *Cell* **92**: 337-349.
25. Genes VIII, B. Lewin, 8<sup>th</sup> edition, Pearson Education Inc., 2004.
26. J. Harms, F. Schluenzen, R. Zarivach, *et al* (2001). High resolution structure of the large ribosomal subunit from a mesophilic eubacterium. *Cell* **107**: 679-88.

27. F. Schluenzen, A. Tocilj, R. Zarivach, *et al* (2000). Structure of functionally activated small ribosomal subunit at 3.3 Å resolution. *Cell* **102**: 615-623.
28. B.T. Wimberly, D.E. Brodersen, W.M. Clemons, *et al* (2000). Structure of the 30S ribosomal subunit. *Nature* **407**: 327-339.
29. P. Nissen, J.A. Ippolito, N. Ban, *et al* (2001). RNA tertiary interactions in the large ribosomal subunit: the A-minor motif. *Proc. Natl. Acad. Sci. U.S.A* **98**: 4899-4903.
30. H.J. Rheinberger, H. Sternbach, K.H. Nierhaus (1981). Three tRNA binding sites on *Escherichia coli* ribosomes. *Proc. Natl. Acad. Sci.* **78**: 5310-5314.
31. J. Shine, L. Dalgarno (1974). The 3'-terminal sequence of *Escherichia coli* 16S ribosomal RNA: complementarity to nonsense triplets and ribosome binding sites. *Proc. Natl. Acad. Sci.* **71**: 1342-1346.
32. B.S. Laursen, H.P. Sorensen, K.K. Mortensen, *et al* (2005). Initiation of protein synthesis in bacteria. *Microbiol. Mol. Biol. Rev.* **69**: 101-123.
33. K.D. Dahlquist, J.D. Puglisi (2000). Interaction of translation initiation factor IF1 with the *E. coli* ribosomal A-site. *J. Mol. Biol.* **299**: 1-15.
34. M. Grunberg-Manago, P. Dessen, D. Pantaloni, *et al* (1975). Light-scattering studies showing the effect of initiation factors on the reversible dissociation of *Escherichia coli* ribosomes. *J. Mol. Biol.* **94**: 461-478.
35. C. Gualerzi, G. Risuleo, C.L. Pon (1977). Initial rate kinetic analysis of the mechanism of initiation complex formation and the role of initiation factor IF3. *Biochemistry* **16**: 1684-1689.
36. J. Tomsic, L. Vitali, T. Daviter, *et al* (2000). Late events of translation initiation in bacteria: a kinetic analysis. *EMBO Journal* **19**: 2127-2136.
37. M.V. Rodnina, T. Pape, R. Fricke, *et al* (1996). Initial binding of the elongation factor Tu.GTP.aminoacyl-tRNA complex preceding codon recognition on the ribosome. *J. Biol. Chem.* **271**: 646-652.
38. S. Uemura, M. Dorywalska, T.H. Lee, *et al* (2007). Peptide bond formation destabilizes Shine-Dalgarno interaction on the ribosome. *Nature* **446**: 454-457.

39. D. Beyer, E. Skripkin, K.H. Nierhaus (1994). How the ribosome moves along the mRNA during protein synthesis. *J. Biol. Chem.* **269**: 30713-30717.
40. K.H. Nierhaus (1990) The allosteric three-site model for the ribosomal elongation cycle: features and future. *Biochemistry* **29**: 4997-5008.
41. N. Burkhardt, C.M. Spahn, K.H. Nierhaus (1998). Ribosomal tRNA binding sites: three-site models of translation. *Crit. Rev. Biochem. Mol. Biol.* **33**: 95-149.
42. U. Geigenmuller, K.H. Nierhaus (1990). Significance of the third tRNA binding site, the E site, on E. coli ribosomes for the accuracy of translation: an occupied E site prevents the binding of non-cognate aminoacyl-tRNA to the A-site. *EMBO Journal* **9**: 4527-4533.
43. D.V. Freistroffer, M.Y. Pavlov, J. MacDougall, *et al* (1997). Release factor RF3 in E.coli accelerates the dissociation of release factors RF1 and RF2 from the ribosome in a GTP-dependent manner. *EMBO Journal* **16**: 4126-4133.
44. A. Hirashima, A. Kaji (1972). Factor-dependent release of ribosomes from messenger RNA. Requirement for two heat-stable factors. *J. Mol. Biol.* **65**: 43-58.
45. M. Selmer, S. Al-Karadaghi, G. Hirokawa, *et al* (1999). Crystal structure of *Thermotoga maritima* ribosome recycling factor: a tRNA mimic. *Science* **286**: 2349-2352.
46. G. Hirokawa, M.C. Kiel, A. Muto, *et al* (2002). Post-termination complex disassembly by ribosome recycling factor, a functional tRNA mimic. *EMBO Journal* **21**: 2272-2281.
47. F.U. Hartl, M. Hayer-Hartl (2002). Molecular chaperones in the cytosol: from nascent chain to folded protein. *Science* **295**: 1852-1858.
48. B. Bukau, A. Horwich (1998). The Hsp70 and Hsp60 chaperone machines. *Cell* **92**: 351-356.
49. T. Maier, L. Ferbitz, E. Deuerling, *et al* (2005). A cradle for new proteins: trigger factor at the ribosome. *Current Opinion in Structural Biology* **15**: 204-212.

50. F. Merz, D. Boehringer, C. Schaffitzel, *et al* (2008). Molecular mechanism and structure of trigger factor to the translating ribosome. *EMBO Journal* **27**: 1622-1632.
51. S.A. Teter, W.A. Houry, D. Ang, *et al* (1999). Polypeptide flux through bacterial Hsp70: DnaK cooperates with trigger factor in chaperoning nascent chains. *Cell* **97**: 755-765.
52. T. Kiefhaber, R. Rudolph, H. Kohler, *et al* (1991). Protein aggregation *in vitro* and *in vivo*: a quantitative model of the kinetic competition between folding and aggregation. *Biotechnology* **9**: 825-829.
53. W.J. Netzer, F.U. Hartl (1997). Recombination of protein domains facilitated by co-translational folding in eukaryotes. *Nature* **388**: 343-349.
54. C.H. Makhoul, E.N. Trifonov (2002). Distribution of rare triplets along mRNA and their relation to protein folding. *Journal of Biomolecular Structure & Dynamics* **20**: 413-420.
55. M. Oresic, D. Shalloway (1998). Specific correlations between relative synonymous codon usage and protein secondary structure. *J. Mol. Biol.* **281**: 31-48.
56. C.F. Wright, S.A. Teichmann, C.M. Dobson (2005). The importance of sequence diversity in the aggregation and evolution of proteins. *Nature* **438**: 878-881.
57. S. Batey, A. Nickson, J. Clarke (2008). Studying the folding of multidomain proteins. *HFSP Journal* **2**: 365-377.
58. J. Han, S. Batey, A. Nickson, *et al* (2007). The folding and evolution of multidomain proteins. *Nature reviews* **8**: 319-330.
59. D. Schmid, A. Baici, H. Gehring, *et al* (1994). Kinetics of molecular chaperone action. *Science* **263**: 971-973.
60. W.Y. Cheung (1980). Calmodulin plays a pivotal role in cellular regulation. *Science* **207**: 19-26.
61. T. Yang, B.W. Poovaiah (2003). Calcium/Calmodulin-mediated signal network in plants. *Trends in Plant Sciences* **8**: 505-512.
62. D. Chin, A.R. Means (2000). Calmodulin: a prototypical calcium sensor. *Trends in Cell Biology* **10**: 322-327.

63. J.R. Geiser, D. Tuinen, S.E. Brockerhoff, *et al* (1991). Can Calmodulin function without binding calcium? *Cell* **65**: 949-959.
64. Principles of Gene Manipulation, S.B. Primrose, R.M. Twyman, and R.W. Old, 6<sup>th</sup> edition, Blackwell Science
65. R. Zahn, C. Schroetter, K. Wüthrich (1997). Human prion proteins expressed in *Escherichia coli* and purifies by high-affinity column refolding. *FEBS Letters* **417**: 400-404.
66. S.R. Adams, R.E. Campbell, L.A. Gross, *et al* (2002). New biarsenical ligands and tetracysteine motifs for protein labelling *in vitro* and *in vivo*: Synthesis and biological applications. *J. Am. Chem. Soc.* **124**: 6063-6076.
67. B.A. Griffin, S.R. Adams, R.Y. Tsien (1998). Specific covalent labelling of recombinant protein molecules inside live cells. *Science* **281**: 269-272.
68. J.R. Lacowicz, Principles of fluorescence spectroscopy, 3<sup>rd</sup> edition, Springer science, 2006
69. S.M. Kelly, T.J. Jess, N.C. Price (2005). How to study proteins by circular dichroism. *Biochimica et Biophysica Acta* **1751**: 119-139.
70. G.D. Fasman, *et al*, Circular dichroism and the conformational analysis of biomolecules, 1996
71. B. Herman, J.R. Lacowicz, D.B. Murphy, *et al*. <http://www.olympusconfocal.com/theory/fluoroexciteemit.html>, 2011
72. A. Miyawaki, J. Liopis, R. Heim, *et al* (1997). Fluorescent indicators for Ca<sup>2+</sup> based on green fluorescent proteins and Calmodulin. *Nature* **388**: 882-887.
73. W.S. VanScyoc, B.R. Sorensen, E. Rusinova, *et al* (2002). Calcium binding to Calmodulin mutants monitored by domain-specific intrinsic phenylalanine and tyrosine fluorescence. *Biophysical Journal* **83**: 2767-2780.
74. M. Wahl. Time-Tagged Time-Resolved fluorescence data correlation, Technical note, Picoquant GmbH, 2004
75. M. Kashioka, K. Sasaki, H. Masuhara (1995). Time-dependent fluorescence depolarization analysis in three-dimensional microspectroscopy. *Applied Spectroscopy* **45**: 224-228.

76. G.F. Schröder, U. Alexiev, H. Grubmüller (2005). Simulation of fluorescence anisotropy experiments: Probing protein dynamics. *Biophysical Journal* **89**: 3757-3770.
77. B. Chen, M.U. Mayer, L.M. Markillie, et al (2005). Dynamic motion of helix A in the amino-terminal domain of Calmodulin is stabilized upon calcium activation. *Biochemistry* **44**: 905-914.
78. S.R. Adams, R.Y. Tsien (2008). Preparation of the membrane-permeant biarsenicals, FIAsh-EDT<sub>2</sub> and ReAsH-EDT<sub>2</sub> for fluorescent labeling of tetracysteine-tagged proteins. *Nat. Protoc.* **3**: 1527-1534.
79. Manual of Matlab R2007b, runstest (h criterion)
80. A.L. Papish, L.W. Tari, H.J. Vogel (2002). Dynamic light scattering study of Calmodulin-target peptide complexes. *Biophysical Journal* **83**: 1455-1464.
81. A. Rutkowska, M. Beerhaum, N. Rajagopalan, et al (2009). Large-scale purification of ribosome-nascent chain complexes for biochemical and structural studies. *FEBS Letters* **583**: 2407-2413.
82. M. Behrmann, H. Koch, T. Hengelage, et al (1998). Requirements for the translocation of elongation-arrested, ribosome-associated OmpA across the plasma membrane of *Escherichia coli*. *Journal of Biophysical Chemistry* **273**: 13898-13904.
83. G. Kramer, V. Ramachandiran, B. Hardesty (2001). Co-translational folding – omnia mea mecum porto? *International Journal of Biochemistry & Cell Biology* **33**: 541-553.
84. B.D. Slaughter, J.R. Unruh, M.W. Allen, et al (2005). Conformational substates of Calmodulin revealed by single-pair fluorescence resonance energy transfer: Influence of solution conditions and oxidative modification. *Biochemistry* **44**: 3694-3707.
85. C.A. Wang (1989). pH-dependent conformational changes of wheat germ Calmodulin. *Biochemistry* **28**: 4816-4820.
86. A. Kumari, T. Rosenkranz, J. Fitter (2010). The effect of calcium binding on the unfolding barrier: A kinetic study on homologous  $\alpha$ -amylases. *Biophysical Chemistry* **151**: 54-60.

87. X. Tan, D. Hu, P. Lu (2004). Probing nanosecond protein motions of Calmodulin by single-molecule fluorescence anisotropy. *Applied Physics Letters* **85**: 2420-2422.
88. M. Sun, J.L. Oakes, S.K. Ananthanarayanan, *et al* (2006). Dynamics of the upper 50-KDa domain of Myosin-V examined with fluorescence resonance energy transfer. *Journal of Biological Chemistry* **281**: 5711-5717.
89. J. Spille, A. Zürn, C. Hoffman, *et al* (2011). Rotational dynamics of the  $\alpha_{2a}$  adrenergic receptor revealed by FIAsh labelling in living cells. *Biophysical Journal* **100**: 1139-1148.
90. B. Chen, M.U. Mayer, T. Squier (2005). Structural uncoupling between opposing domains of oxidized Calmodulin underlies the enhanced binding affinity and inhibition of the plasma membrane  $\text{Ca}^{2+}$ -ATPase. *Biochemistry* **44**: 4737-4747.
91. M.S. Evans, K.G. Ugrinov, P.L. Clark (2005). Homogeneous stalled ribosome nascent chain complexes produced *in vivo* and *in vitro*. *Nature Methods* **2**: 757-762.
92. J. Stigler, F. Ziegler, A. Gieseke, *et al* (2011). The complex folding network of single Calmodulin molecules. *Science* **334**: 512-516.
93. S.D. Hsu, P. Fucini, L.D. Cabrita, *et al* (2007). Structure and dynamics of a ribosome-bound nascent chain by NMR spectroscopy. *PNAS* **104**: 16516-16521.
94. L.D. Cabrita, S.D. Hsu, H. Launay, *et al* (2009). Probing ribosome-nascent chain complexes produced *in vivo* by NMR spectroscopy. *PNAS* **106**: 22239-22244.
95. G. Kramer, D. Bochringer, B. Bekau (2009). The ribosome as a platform for co-translational processing, folding and targeting of newly synthesized proteins. *Nature Structural & Molecular Biology* **16**: 589-595.
96. T.M. Schmeing, V. Ramakrishnan (2009). What recent ribosome structures have revealed about the mechanism of translation. *Nature* **461**: 1234-1242.
97. E. Haas (2005). The study of protein folding and dynamics by determination of intramolecular distance distributions and their

- fluctuations using ensemble and single-molecule FRET measurements. *ChemPhysChem* **6**: 858-870.
98. J.P. Ellis, C.K. Bakke, R.N. Kirchdoerfer, *et al* (2008). Chain dynamics of nascent polypeptides emerging from the ribosome. *ACS Chemical Biology* **3**: 555-566.
99. J.P. Ellis, P.H. Culviner, S. Cavagnero (2009). Confined dynamics of a ribosome-bound nascent globin: Cone angle analysis of fluorescence depolarization decays in the presence of two local motions. *Protein Science* **18**: 2003-2015.
100. D.R. Ziehr, J.P. Ellis, S. Cavagnero (2010). Production of ribosome-released nascent proteins with optimal physical properties. *Anal. Chem.* **82**: 4637-464.
101. S. Uemura, R. Iizuka, T. Ueno, *et al* (2008). Single-molecule imaging of full protein synthesis by immobilized ribosomes. *Nucleic Acids Research* **36**: 1-6.
102. V. Kolb, E. Makeyev, A. Spirin (1994). Folding of firefly luciferase during translation in cell-free system. *EMBO Journal* **13**: 3631-3637.
103. A. Katranidis, D. Atta, R. Schlesinger, *et al* (2009). Fast biosynthesis of GFP molecules: A single-molecule fluorescence study. *Angew. Chem. Int. Ed.* **48**: 1758-1761.
104. A. Katranidis, W. Grange, R. Schlesinger, *et al* (2011). Force measurements of the disruption of the nascent polypeptide chain from the ribosome by optical tweezers. *FEBS Letters* **585**: 1859-1863.
105. A.E. Johnson (2005). The co-translational folding and interactions of nascent protein chains: a new approach using fluorescence resonance energy transfer. *FEBS Letters* **579**: 916-920.
106. S.C. Blanchard (2009). Single-molecule observations of ribosome function. *Current Opinion in Structural Biology* **19**: 103-109.
107. D. Hu, P. Lu (2003). Single-molecule nanosecond anisotropy dynamics of tethered protein motions. *J. Phys. Chem. B* **107**: 618-626.
108. R. Liu, D. Hu, P. Lu (2006). Revealing two-state protein-protein interactions of Calmodulin by single-molecule spectroscopy. *J. Am. Chem. Soc.* **128**: 10034-10042.

## Erklärung

Ich erkläre, dass ich die vorliegende Arbeit selbständig und ohne unerlaubte Hilfe verfasst habe. Die vorliegende Arbeit wurde weder in der jetzigen oder in ähnlicher Form bei einer anderen Institution eingereicht. Es wurden zuvor keinerlei Promotionsversuche unternommen.

Jülich, 26. Juni 2013

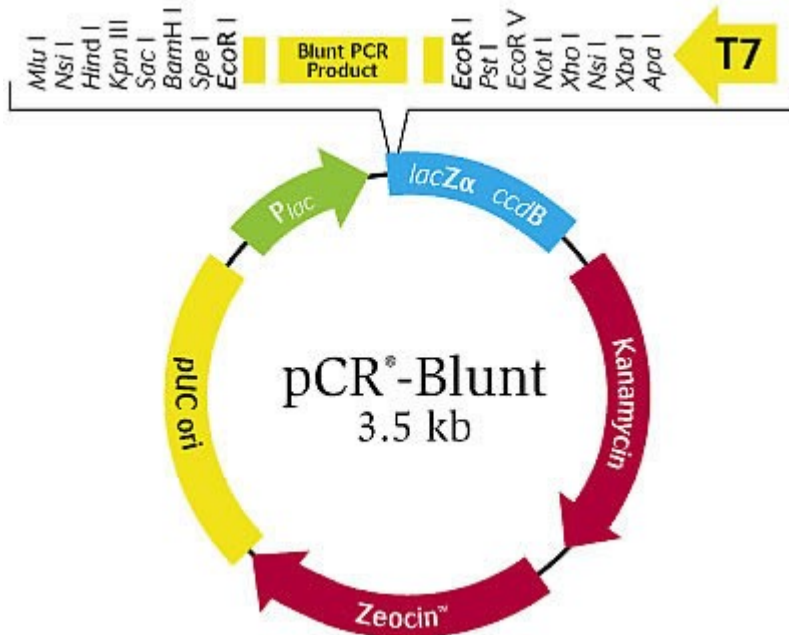
.....

Paraskevas Lamprou

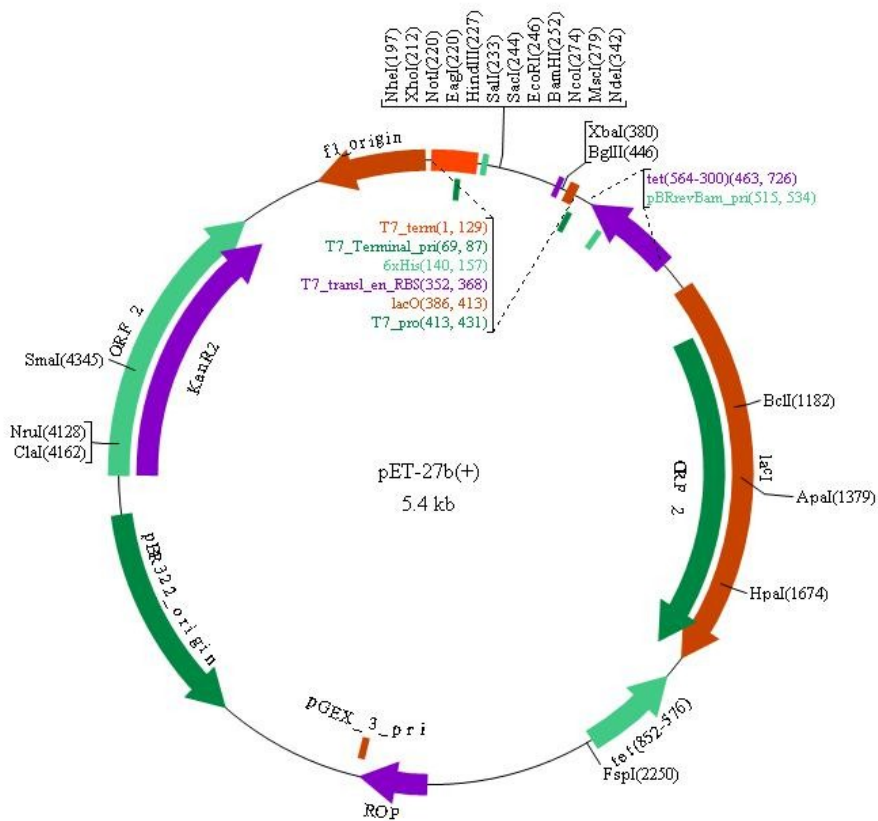
P. Lamprou, D. Kempe, A. Katranidis, G. Büldt, J. Fitter. Nanosecond dynamics of Calmodulin and ribosome-bound nascent chains studied by time-resolved fluorescence anisotropy. [to be submitted]

## Appendix A

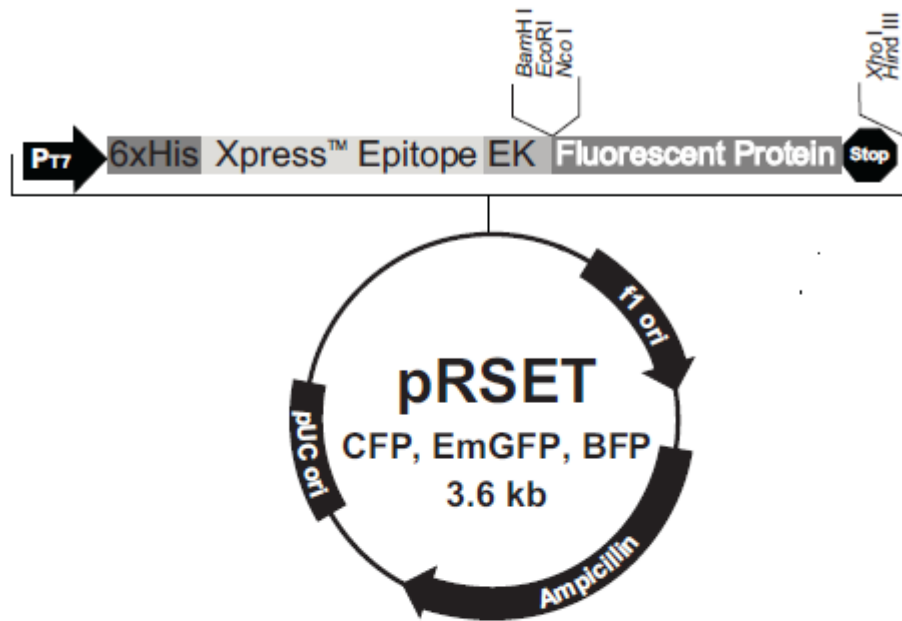
pBLUNT plasmid map



pET27b plasmid map



pRSET plasmid map



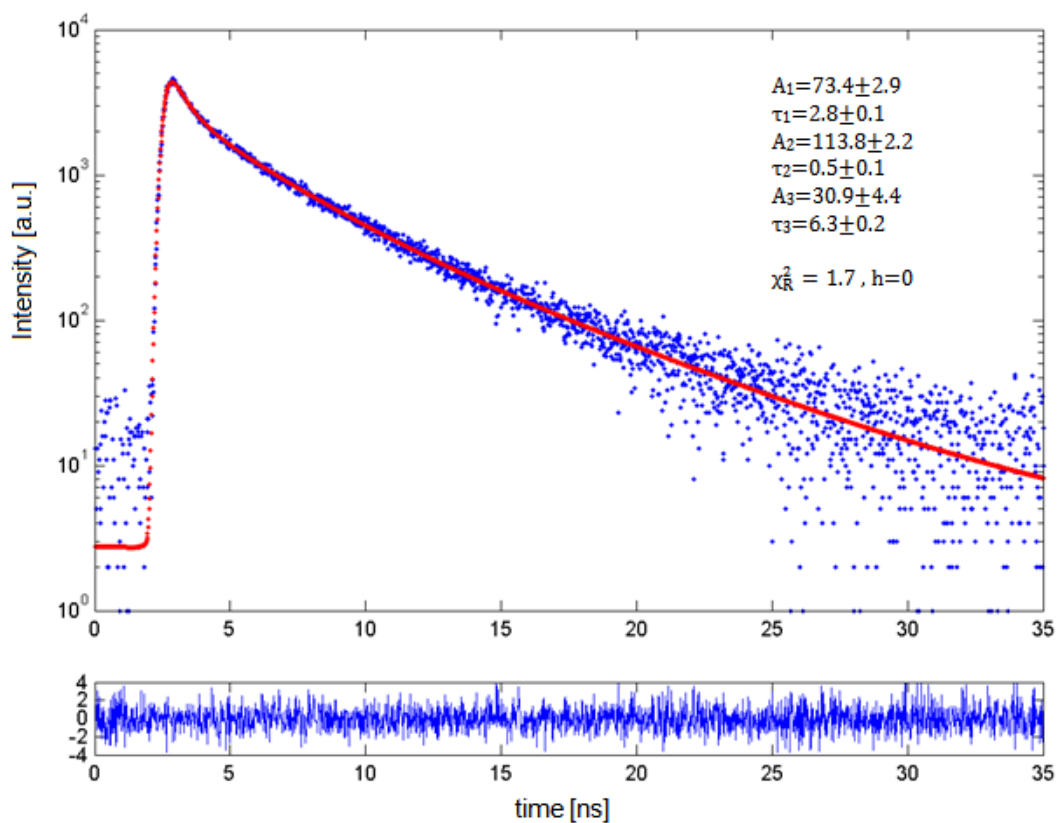
Comments for pRSET/CFP, EmGFP and BFP  
3600 nucleotides

- T7 promoter/priming site: bases 9-28
- 6xHis tag: bases 101-118
- T7 gene 10 leader: bases 122-154
- Xpress™ epitope: bases 158-181
- EK cleavage site: bases 167-181
- Fluorescent Protein (CFP, EmGFP, BFP): bases 209-928
- T7 reverse priming site: bases 987-1006
- T7 transcription terminator: bases 948-1084
- f1 origin: bases 1148-1603
- bla promoter: bases 1635-1739
- Ampicillin (bla) resistance gene: bases 1734-2594
- pUC origin: bases 2739-3412

## Appendix B

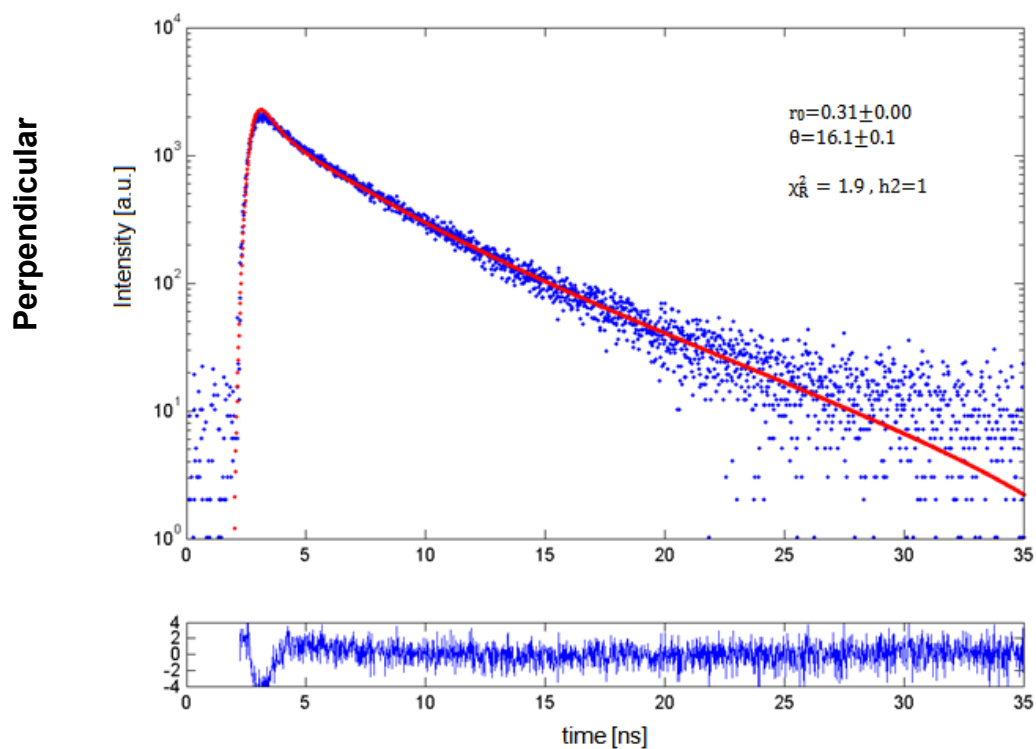
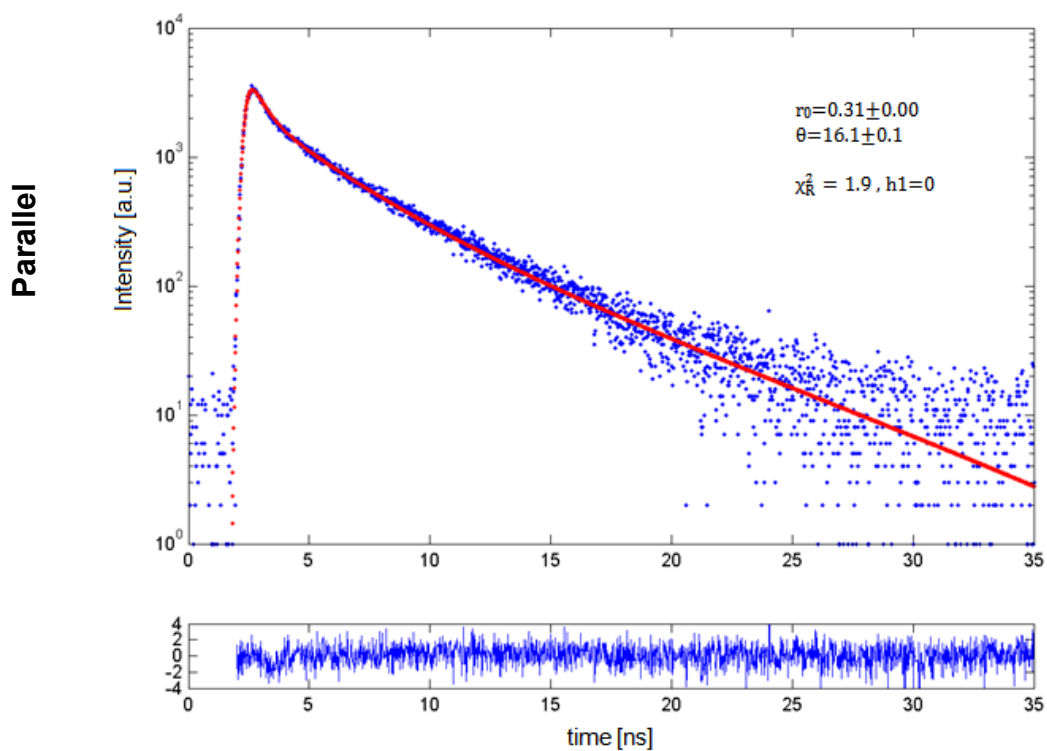
- Time-resolved fluorescence anisotropy of CaM-FIAsH complex when  $\text{Ca}^{2+}$  is bound

### a. Fluorescence lifetime components

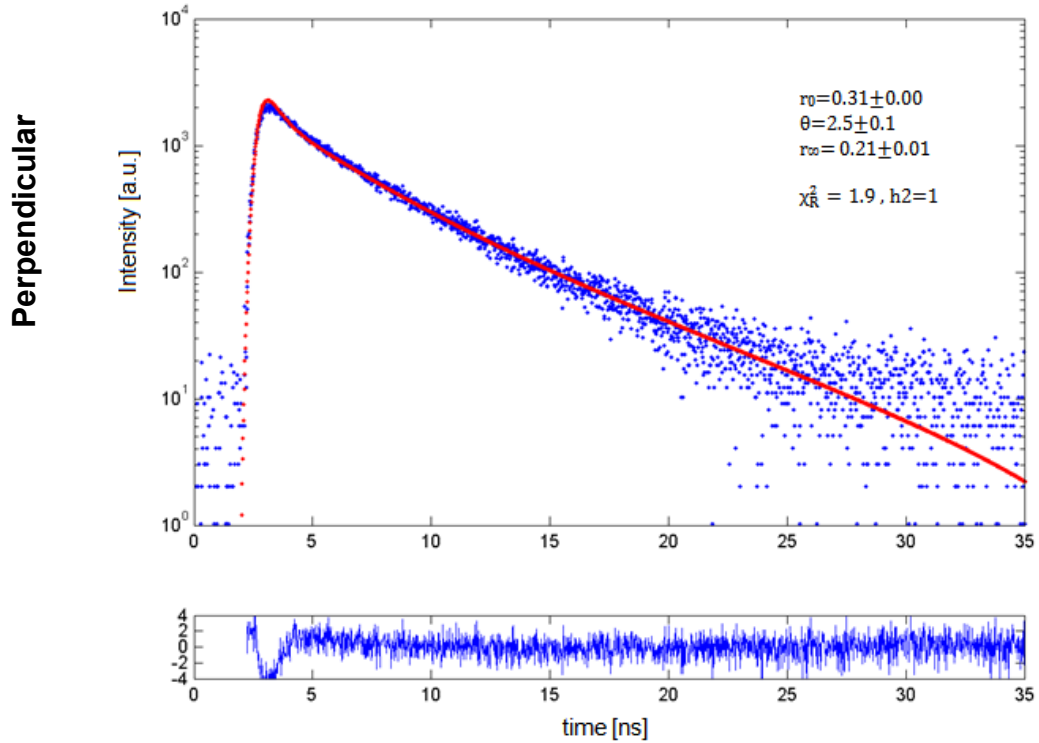
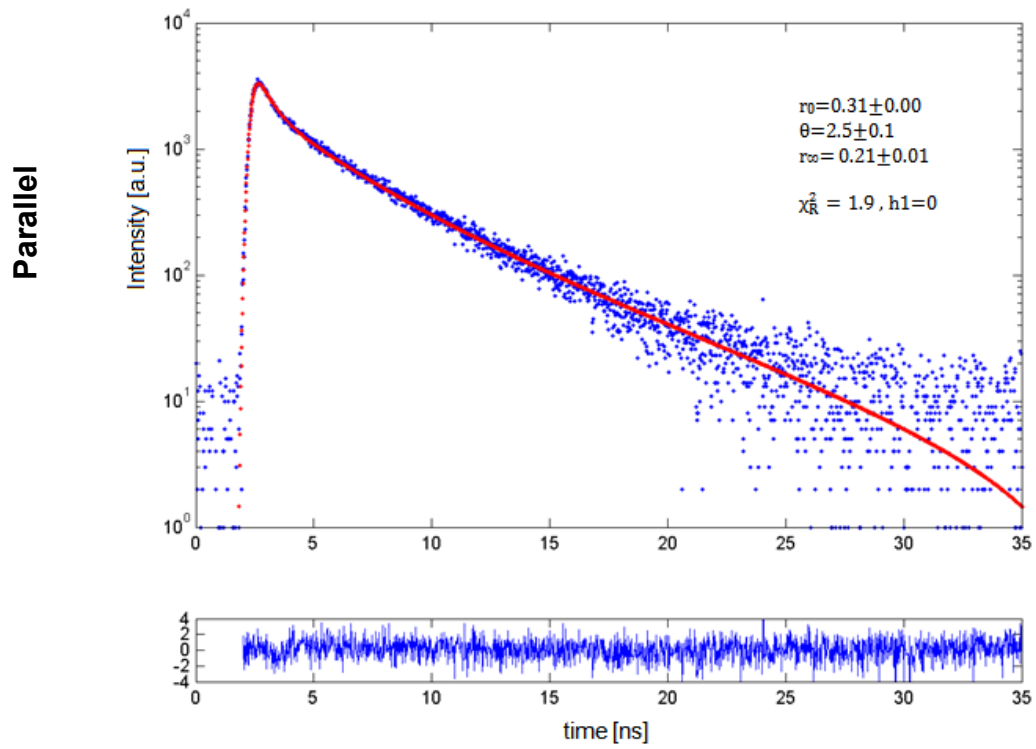


| CaM-FIAsH + $\text{Ca}^{2+}$ , lifetime fit |               |           |               |          |               |                   |                       |
|---|---------------|-----------|---------------|----------|---------------|-------------------|-----------------------|
| $A_1$                                       | $\tau_1$ [ns] | $A_2$     | $\tau_2$ [ns] | $A_3$    | $\tau_3$ [ns] | $\bar{\tau}$ [ns] |                       |
| 73.4±2.9                                    | 2.8±0.1       | 113.8±2.2 | 0.5±0.1       | 30.9±4.4 | 6.3±0.2       | <b>4.0</b>        | $\chi_R^2=1.7$<br>h=0 |

## b. Fluorescence polarized components – single-exponential model

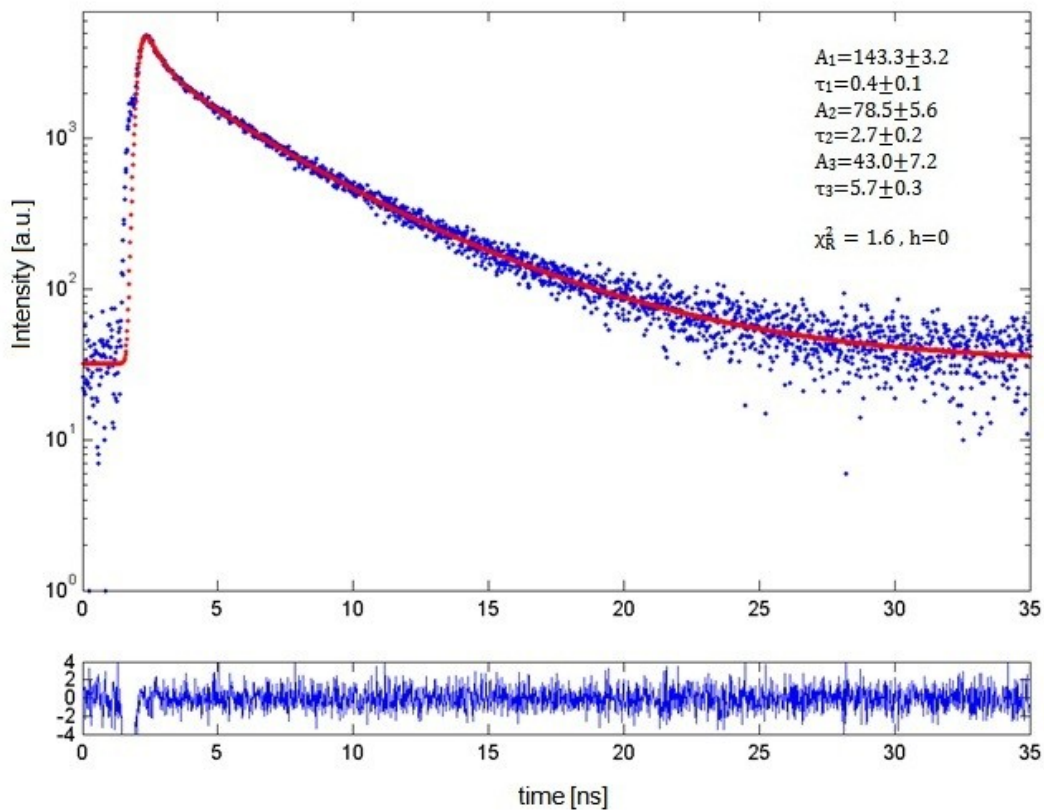


## c. Hindered rotor model



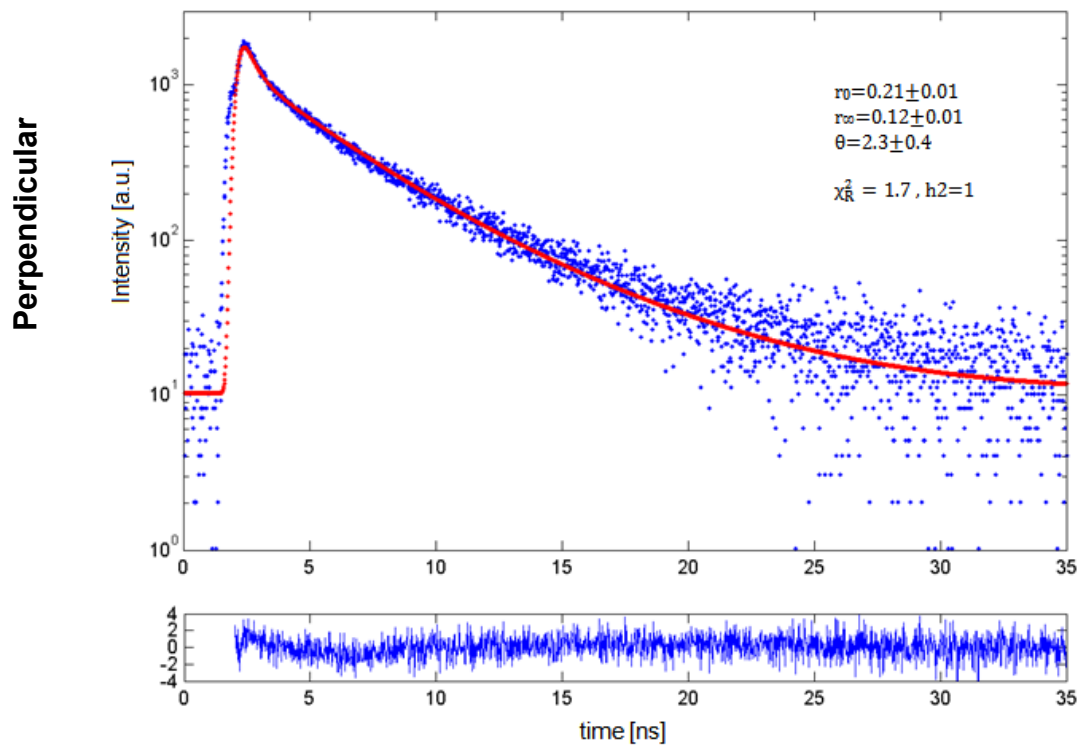
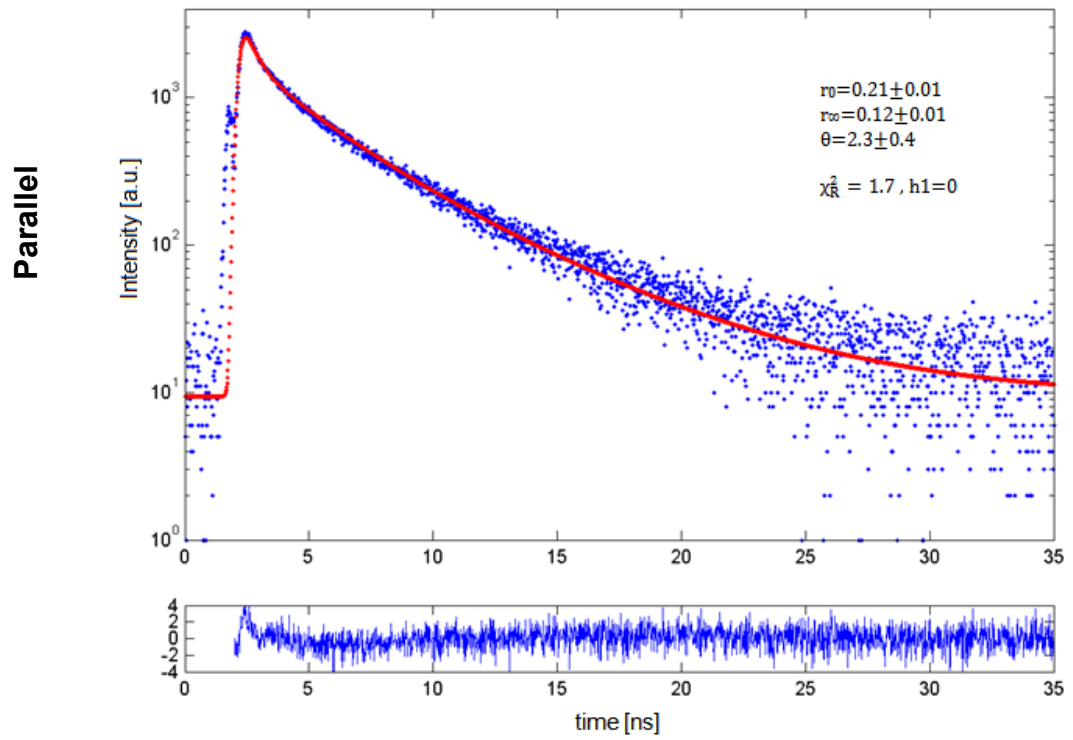
2. Time-resolved fluorescence anisotropy of Ribos-(1<sup>st</sup> EF-hand)

## a. Fluorescence lifetime components



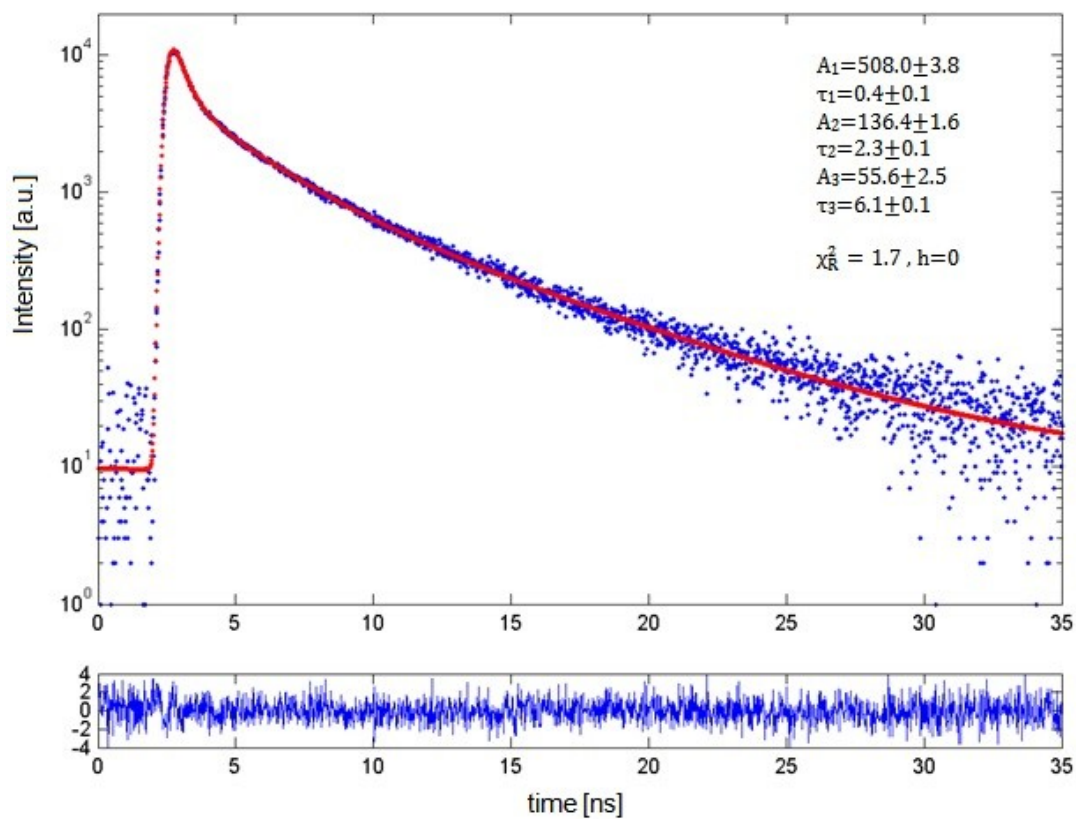
| Ribos-(1 <sup>st</sup> EF-hand), lifetime fit |               |          |               |          |               |                   |                       |
|---|---------------|----------|---------------|----------|---------------|-------------------|-----------------------|
| $A_1$   | $\tau_1$ [ns] | $A_2$    | $\tau_2$ [ns] | $A_3$    | $\tau_3$ [ns] | $\bar{\tau}$ [ns] |                       |
| 143.3±3.2                                     | 0.4±0.1       | 78.5±5.6 | 2.7±0.2       | 43.0±7.2 | 5.7±0.3       | <b>3.8</b>        | $\chi^2_R=1.6$<br>h=0 |

## b. Fluorescence polarized components – hindered rotor model



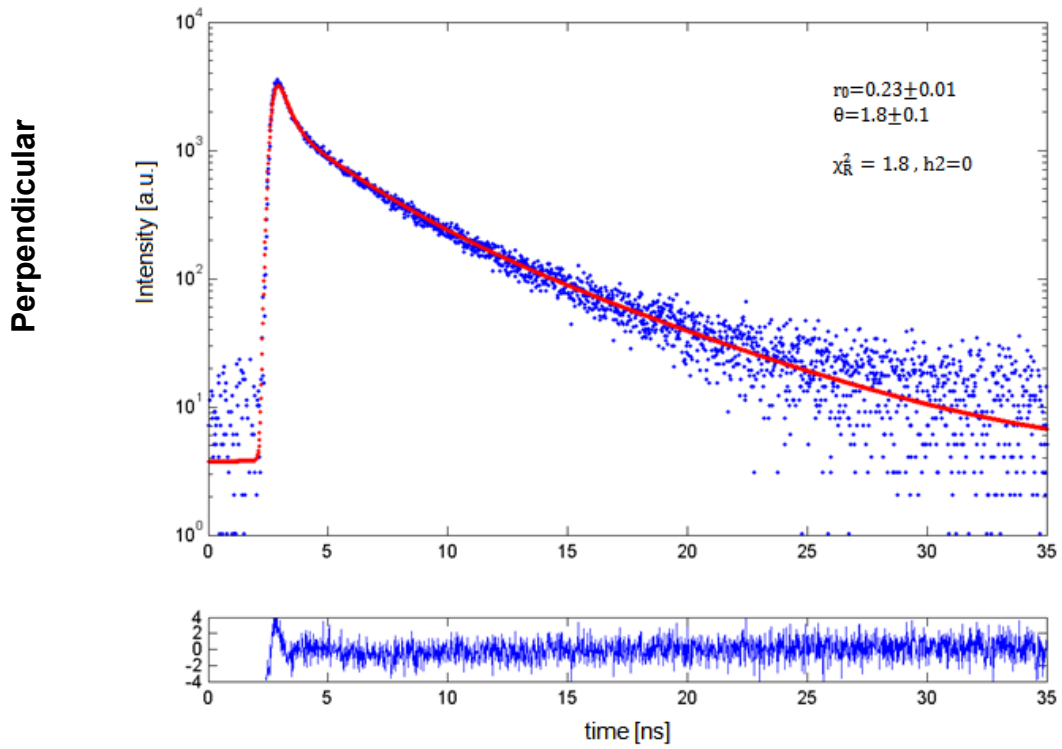
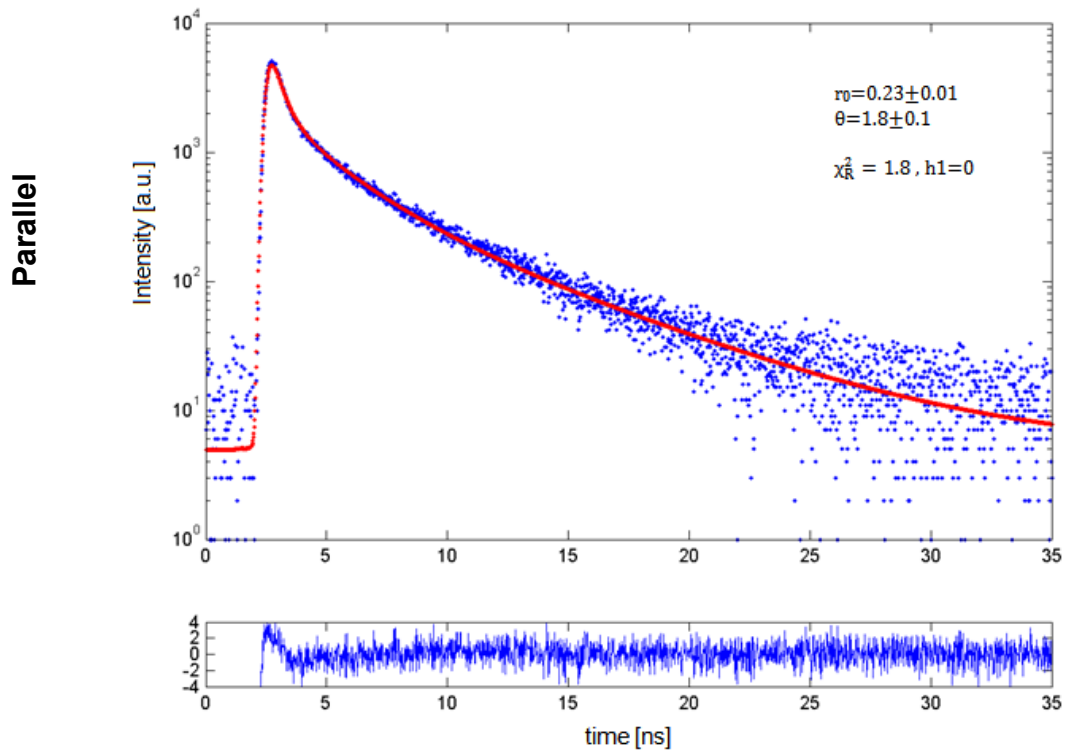
### 3. Time-resolved fluorescence anisotropy of Ribos+(1<sup>st</sup> EF-hand) after addition of Puro

#### a. Fluorescence lifetime components

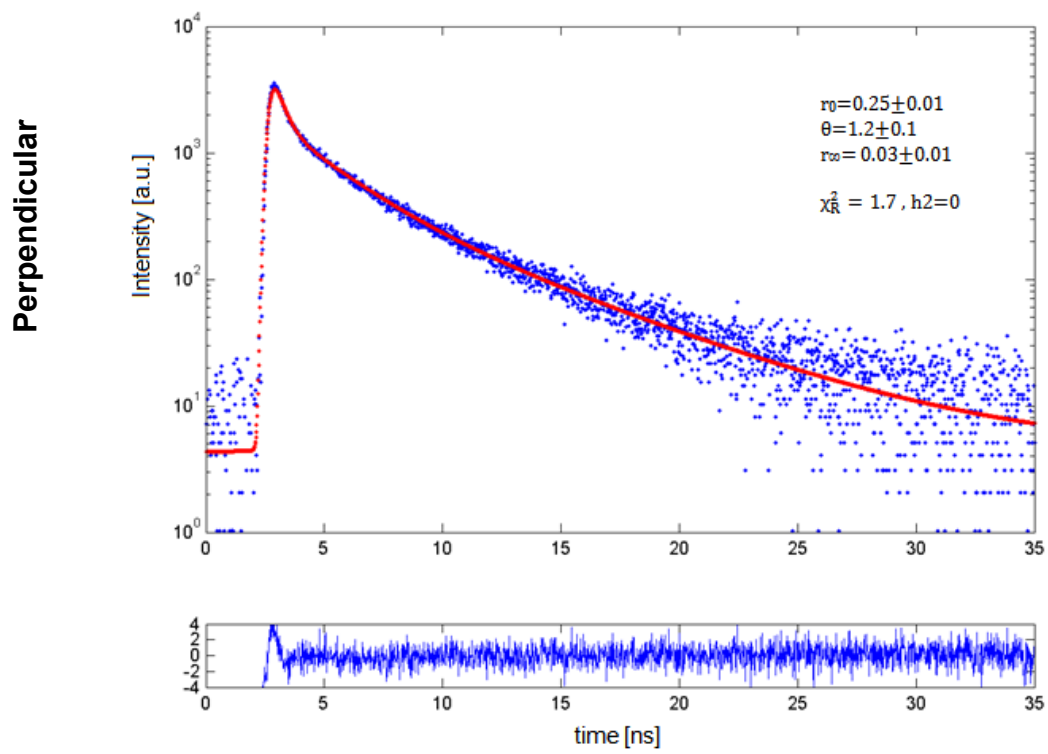
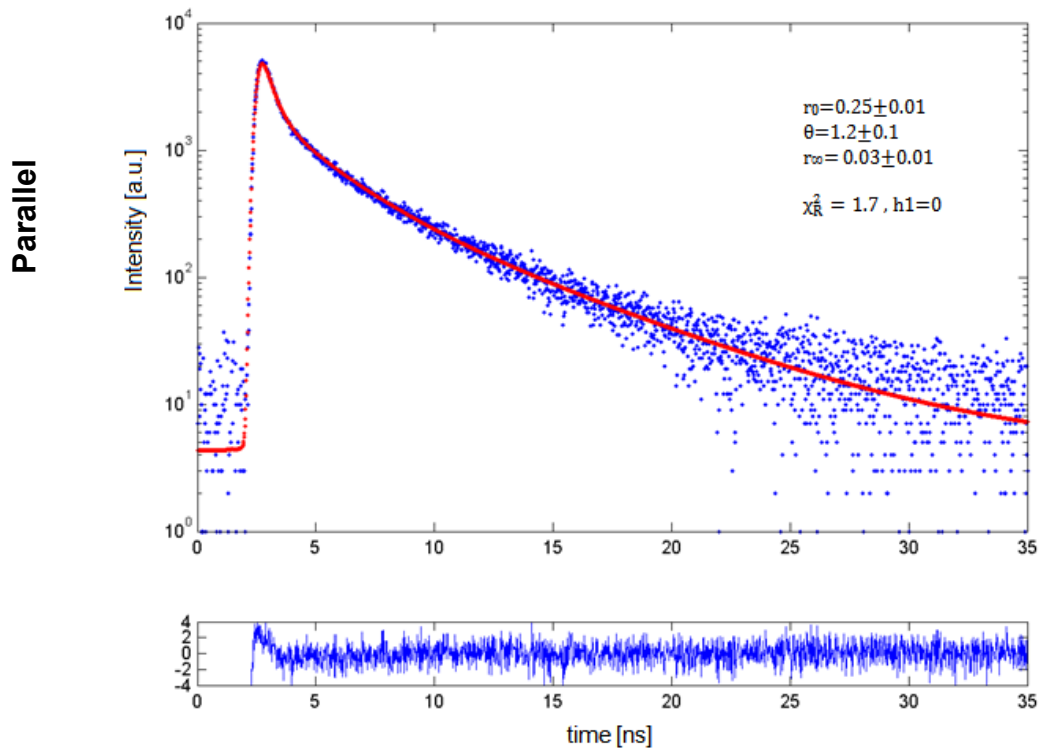


| Ribos + 1 <sup>st</sup> EF-hand after addition of Puro, lifetime fit |               |           |               |          |               |                   |                       |
|--|---------------|-----------|---------------|----------|---------------|-------------------|-----------------------|
| $A_1$  | $\tau_1$ [ns] | $A_2$     | $\tau_2$ [ns] | $A_3$    | $\tau_3$ [ns] | $\bar{\tau}$ [ns] |                       |
| 508.0±3.8  | 0.4±0.1       | 136.4±1.6 | 2.3±0.1       | 55.6±2.5 | 6.1±0.1       | <b>3.4</b>        | $\chi_R^2=1.7$<br>h=0 |

## b. Fluorescence polarized components – single-exponential model

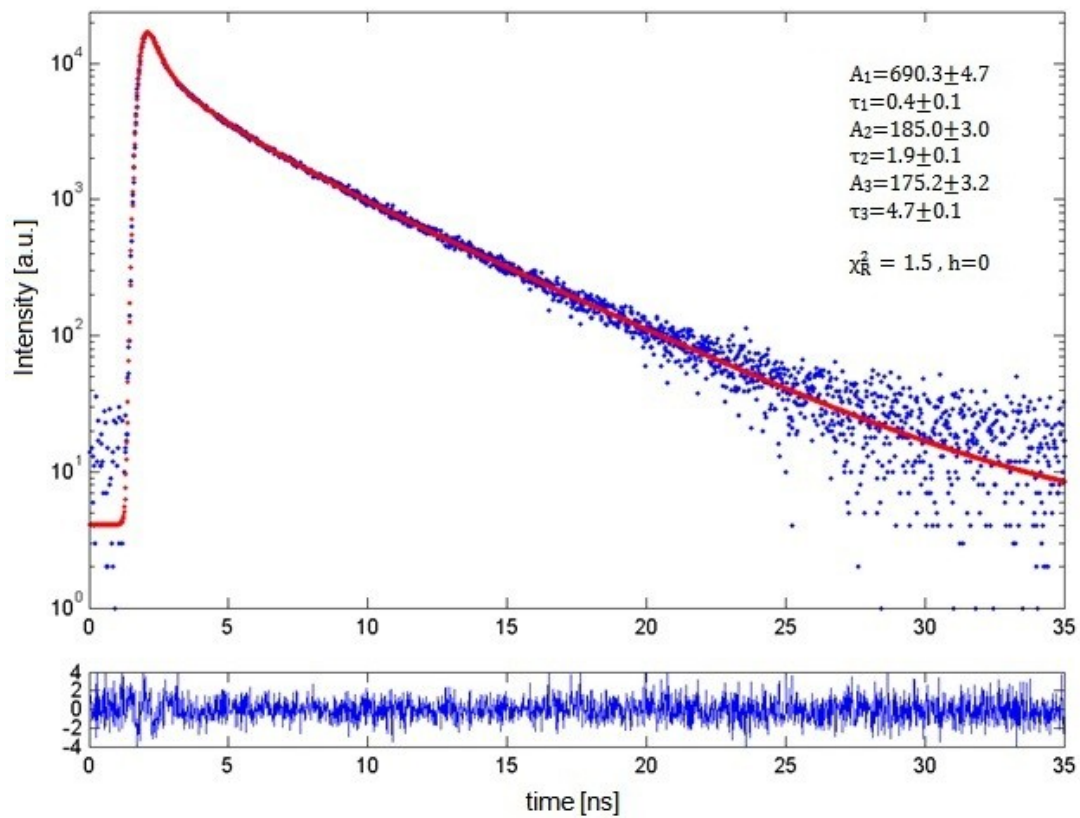


## c. Hindered rotor model



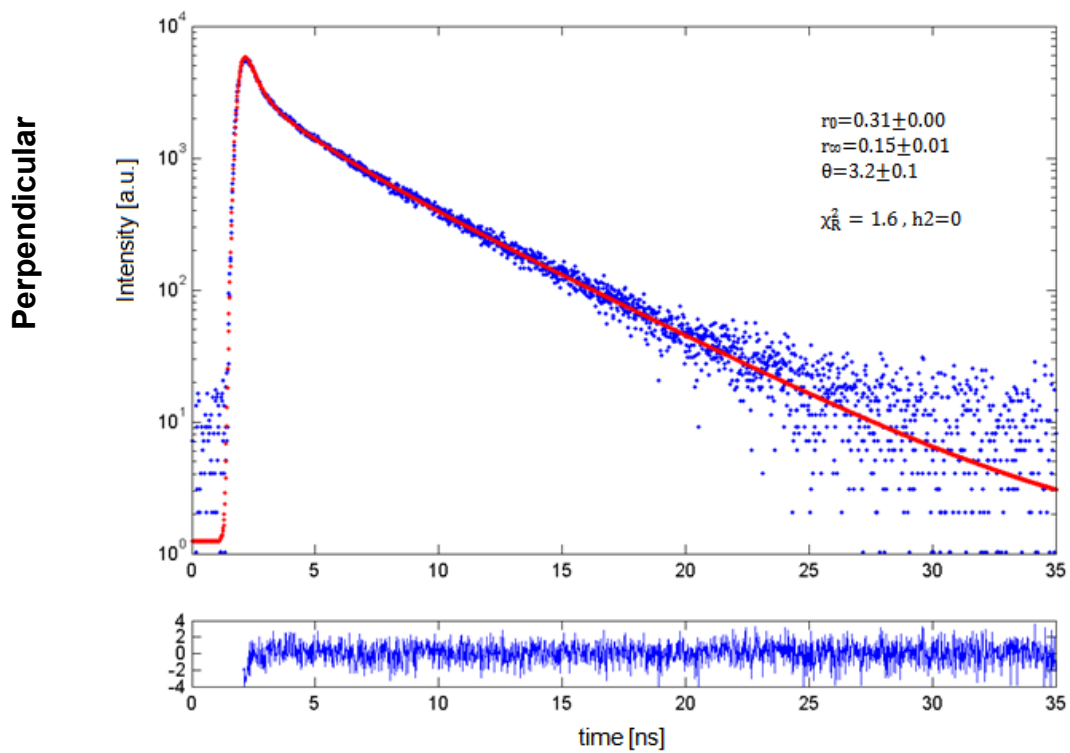
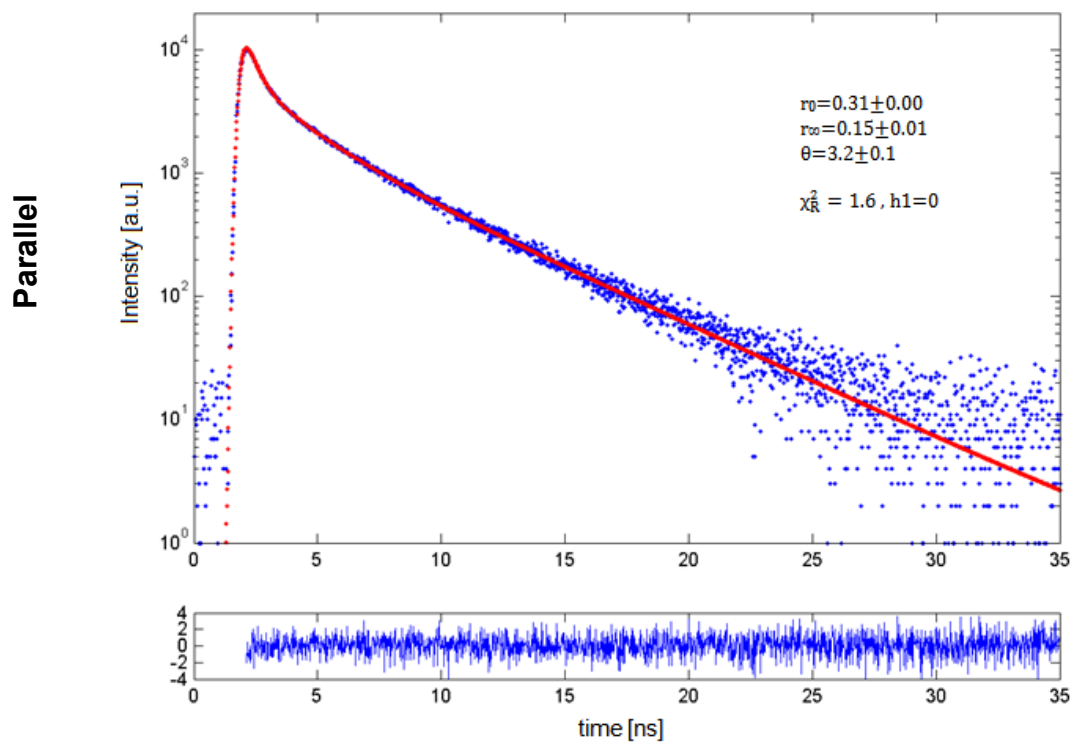
## 4. Time-resolved fluorescence anisotropy of Ribos-(half CaM / N-term.)

## a. Fluorescence lifetime components



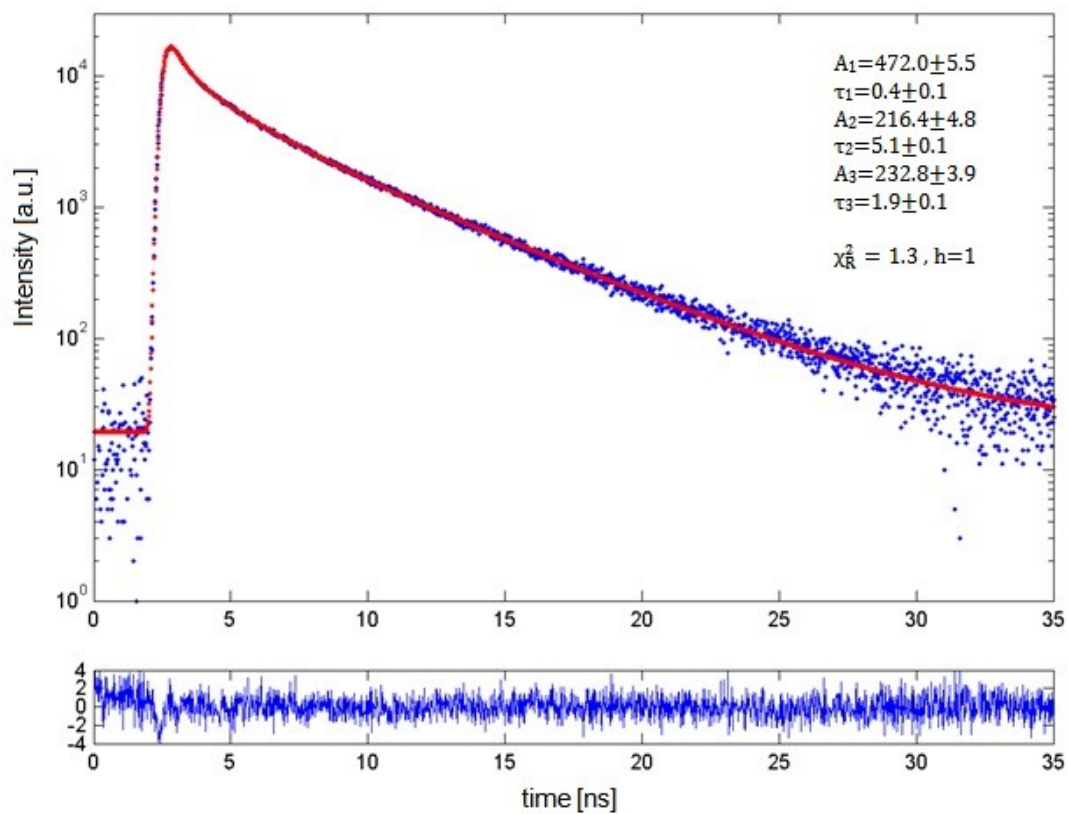
| Ribos-(half CaM / N-term.), lifetime fit |               |           |               |           |               |                   |                       |
|--|---------------|-----------|---------------|-----------|---------------|-------------------|-----------------------|
| $A_1$                                    | $\tau_1$ [ns] | $A_2$     | $\tau_2$ [ns] | $A_3$     | $\tau_3$ [ns] | $\bar{\tau}$ [ns] |                       |
| 690.3±4.7                                | 0.4±0.1       | 185.0±3.0 | 1.9±0.1       | 175.2±3.2 | 4.7±0.1       | <b>3.2</b>        | $\chi_R^2=1.5$<br>h=0 |

## b. Fluorescence polarized components – hindered rotor model



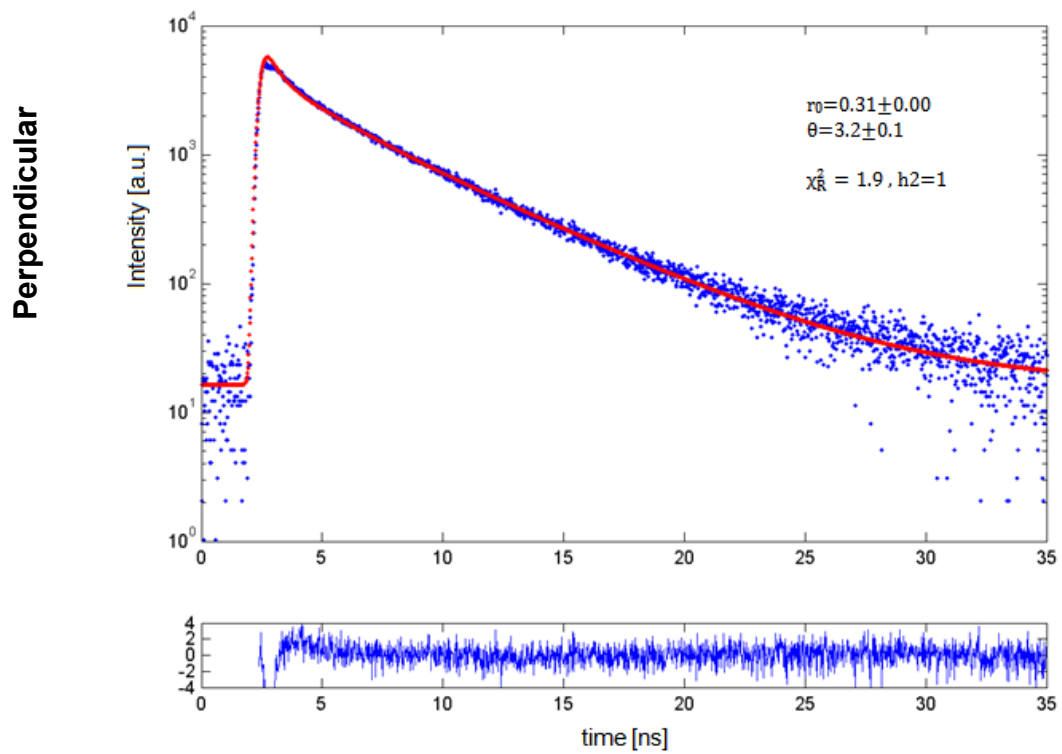
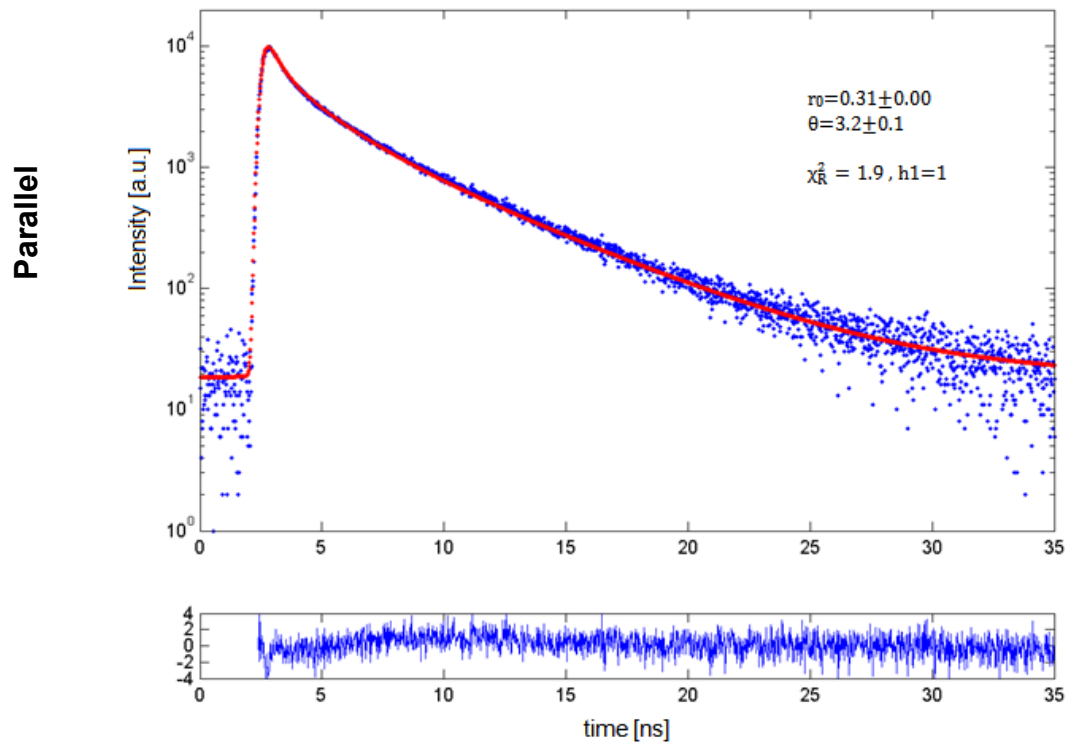
5. Time-resolved fluorescence anisotropy of Ribos + (half CaM / N-term.)  
after addition of Puro

a. Fluorescence lifetime components

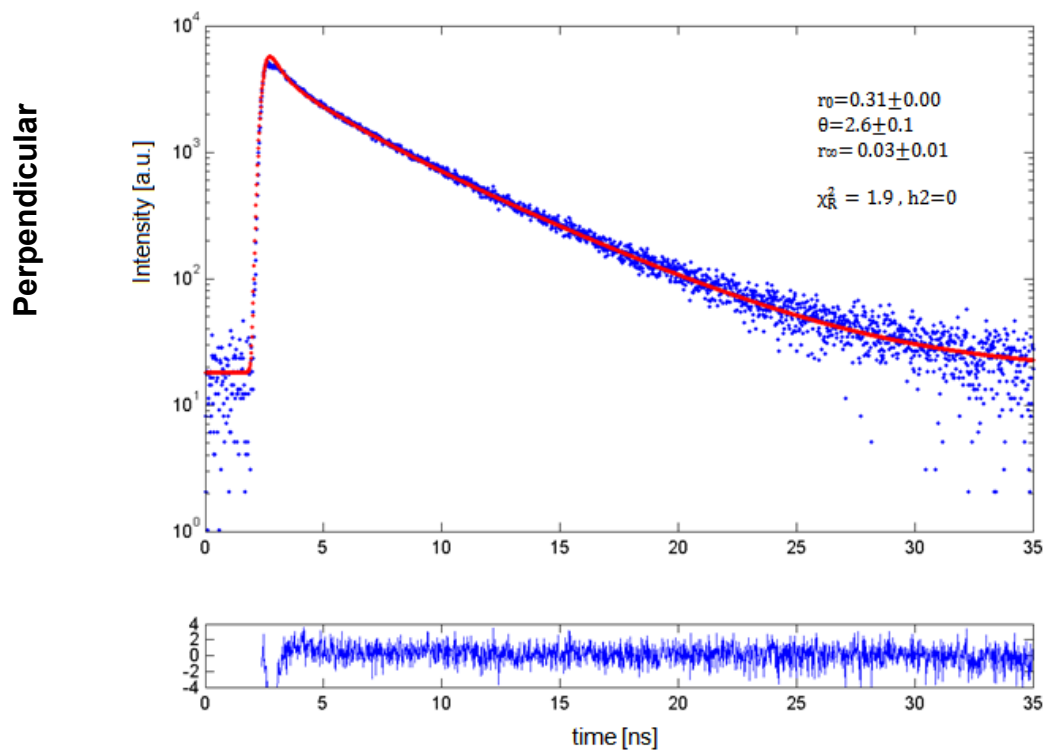
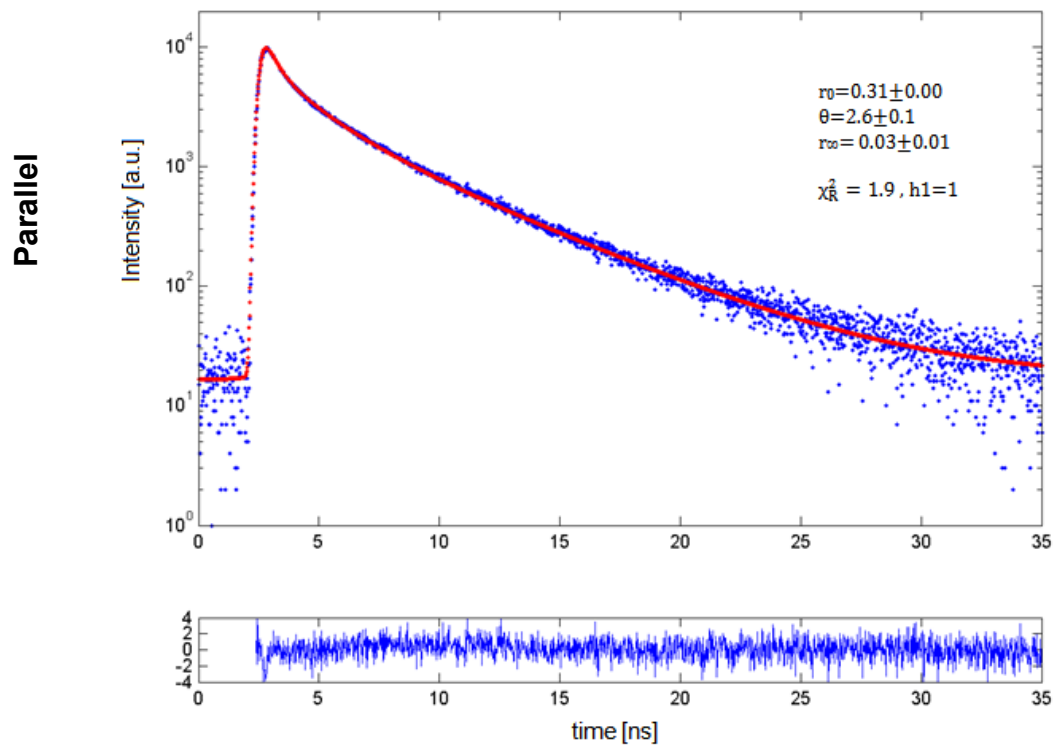


| Ribos + (half CaM / N-term.) after addition of Puro , lifetime fit |               |           |               |           |               |                   |                       |
|--|---------------|-----------|---------------|-----------|---------------|-------------------|-----------------------|
| $A_1$  | $\tau_1$ [ns] | $A_2$     | $\tau_2$ [ns] | $A_3$     | $\tau_3$ [ns] | $\bar{\tau}$ [ns] |                       |
| 472.0±5.5  | 0.4±0.1       | 216.4±4.8 | 5.1±0.1       | 232.8±3.9 | 1.9±0.1       | <b>3.7</b>        | $\chi_R^2=1.3$<br>h=1 |

## b. Fluorescence polarized components – single-exponential model

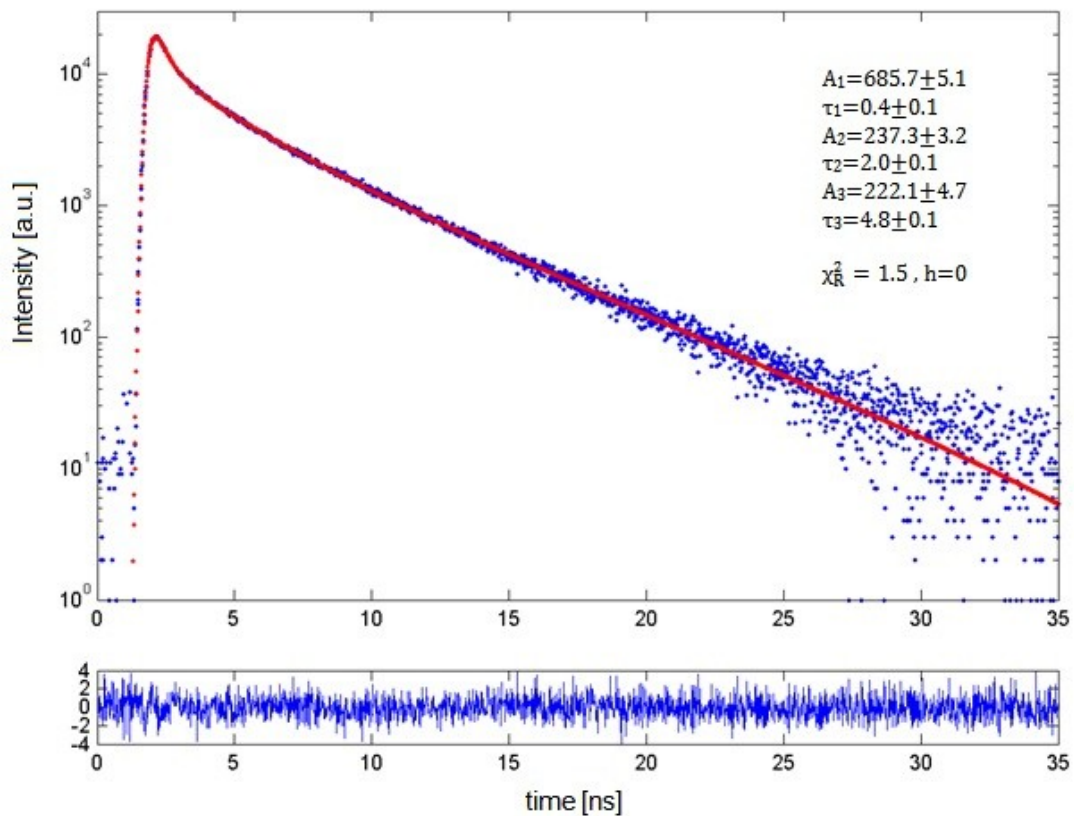


## c. Hindered rotor model



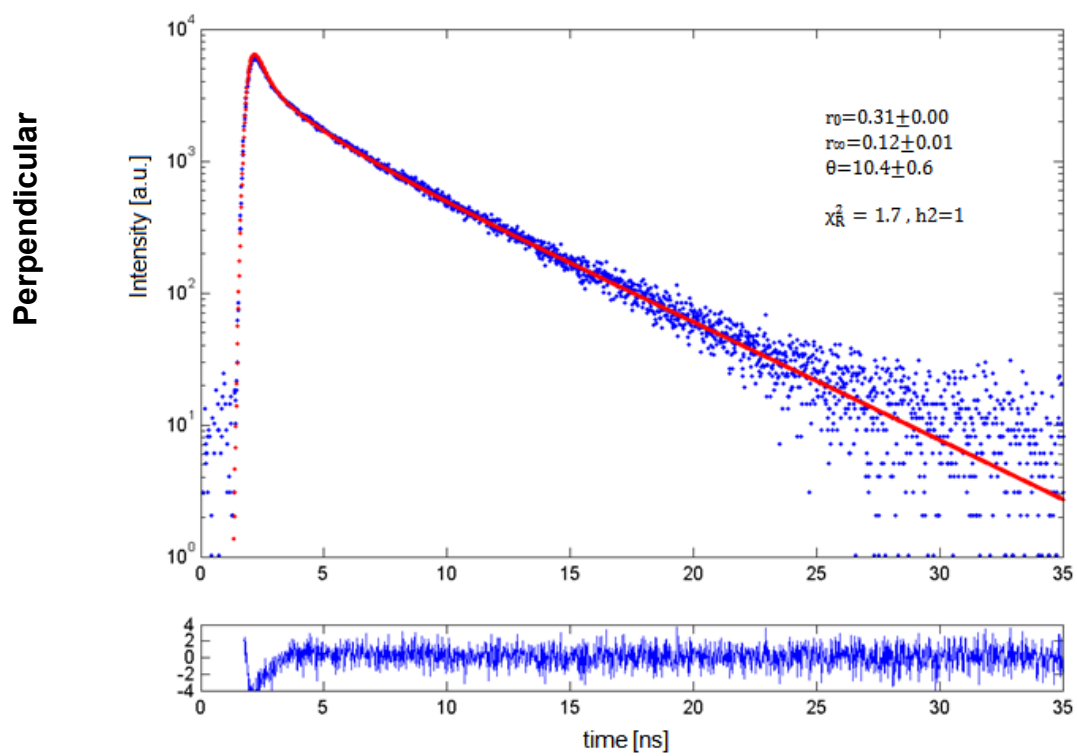
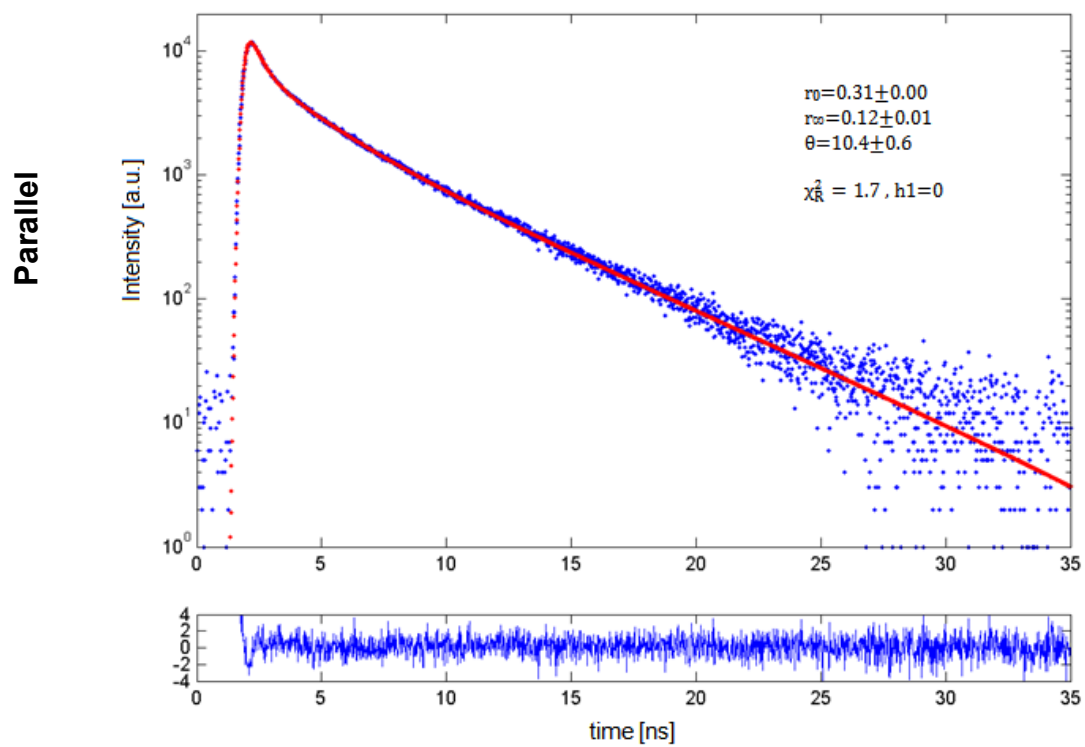
## 6. Time-resolved fluorescence anisotropy of Ribos-(CaM full length)

## a. Fluorescence lifetime components



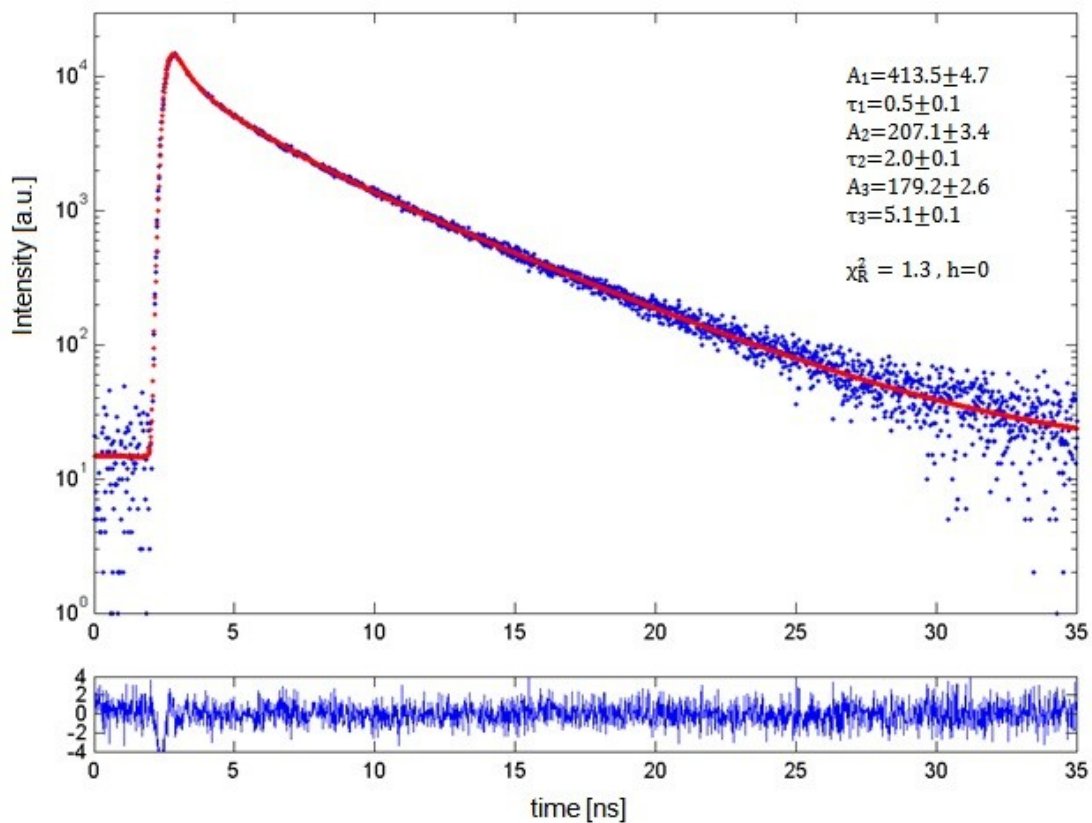
| Ribos-(CaM full length), lifetime fit |               |           |               |           |               |                   |                       |
|---------------------------------------|---------------|-----------|---------------|-----------|---------------|-------------------|-----------------------|
| $A_1$                                 | $\tau_1$ [ns] | $A_2$     | $\tau_2$ [ns] | $A_3$     | $\tau_3$ [ns] | $\bar{\tau}$ [ns] |                       |
| 685.7±5.1                             | 0.4±0.1       | 237.3±3.2 | 2.0±0.1       | 222.1±4.7 | 4.8±0.1       | <b>3.4</b>        | $\chi_R^2=1.5$<br>h=0 |

## b. Fluorescence polarized components – hindered rotor model



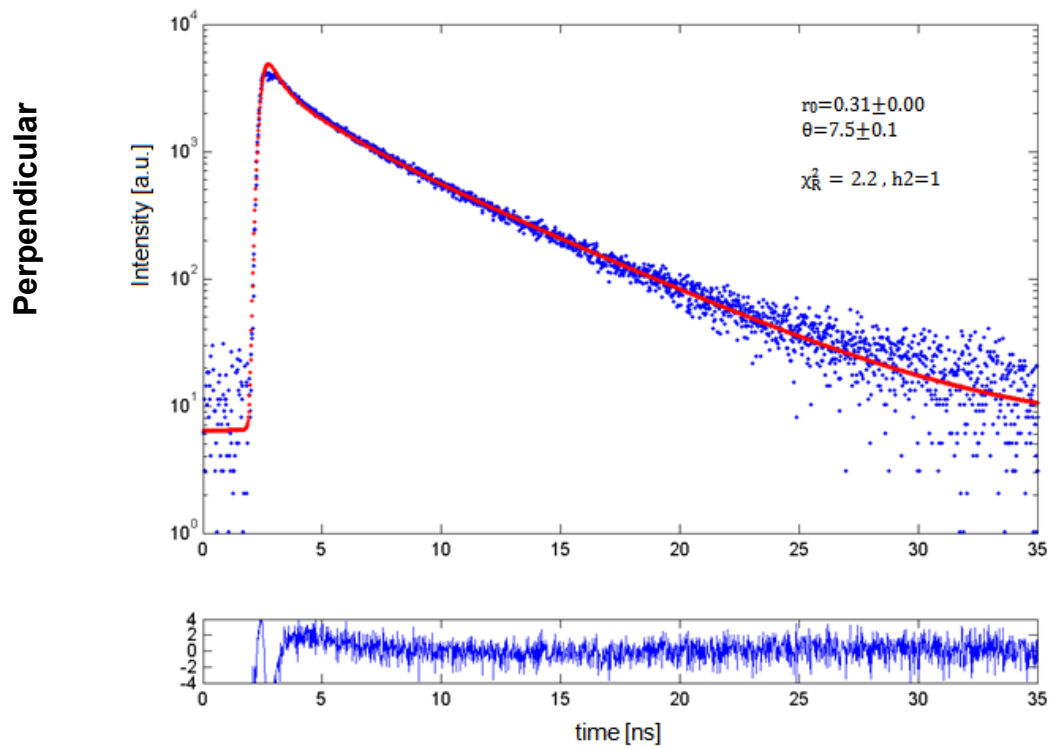
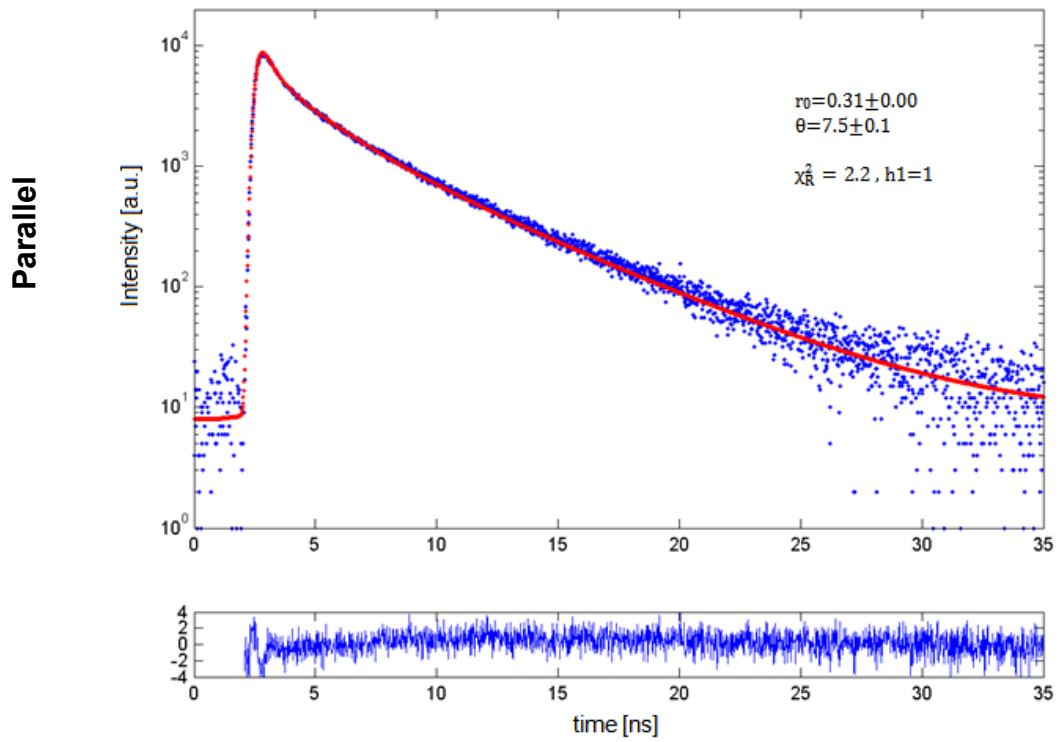
7. Time-resolved fluorescence anisotropy of Ribos+(CaM full length) after addition of Puro

a. Fluorescence lifetime components

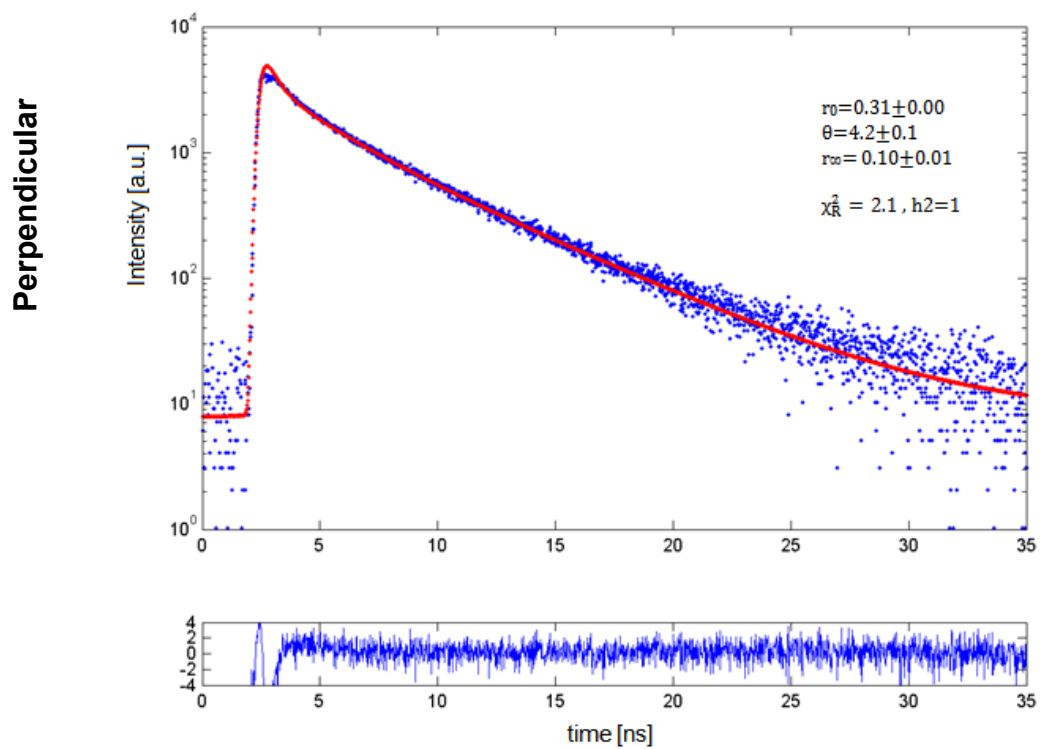
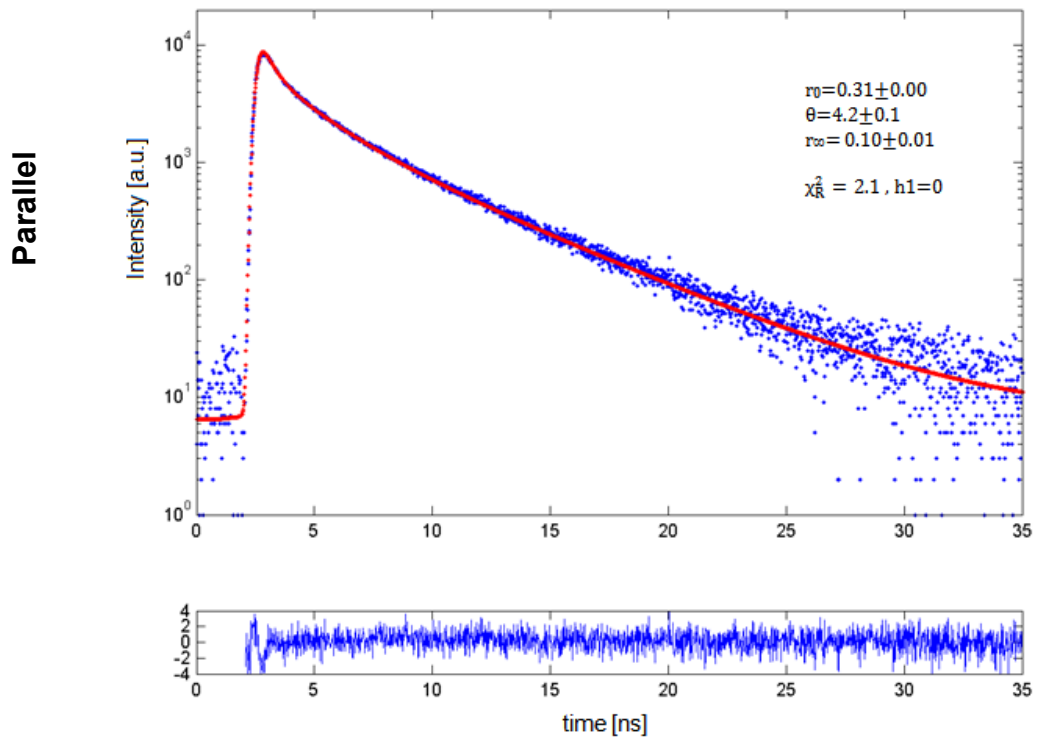


| Ribos + CaM full length after addition of Puro, lifetime fit |               |           |               |           |               |                   |                       |
|--|---------------|-----------|---------------|-----------|---------------|-------------------|-----------------------|
| $A_1$  | $\tau_1$ [ns] | $A_2$     | $\tau_2$ [ns] | $A_3$     | $\tau_3$ [ns] | $\bar{\tau}$ [ns] |                       |
| 413.5±4.7  | 0.5±0.1       | 207.1±3.4 | 2.0±0.1       | 179.2±2.6 | 5.1±0.1       | <b>3.7</b>        | $\chi_R^2=1.3$<br>h=0 |

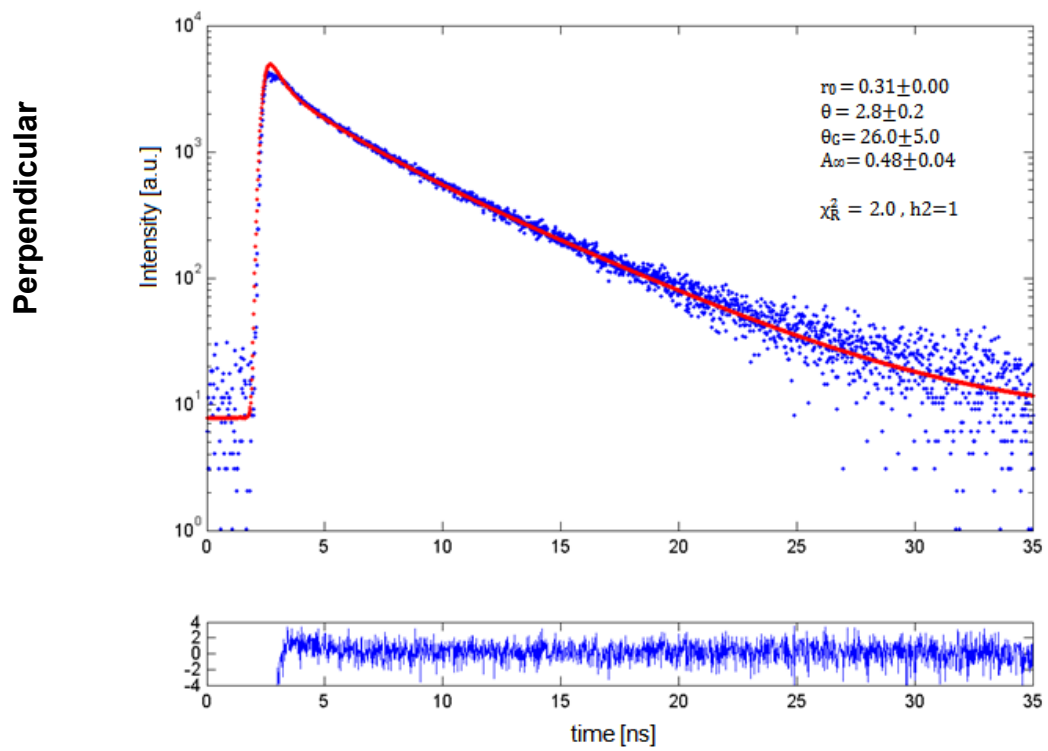
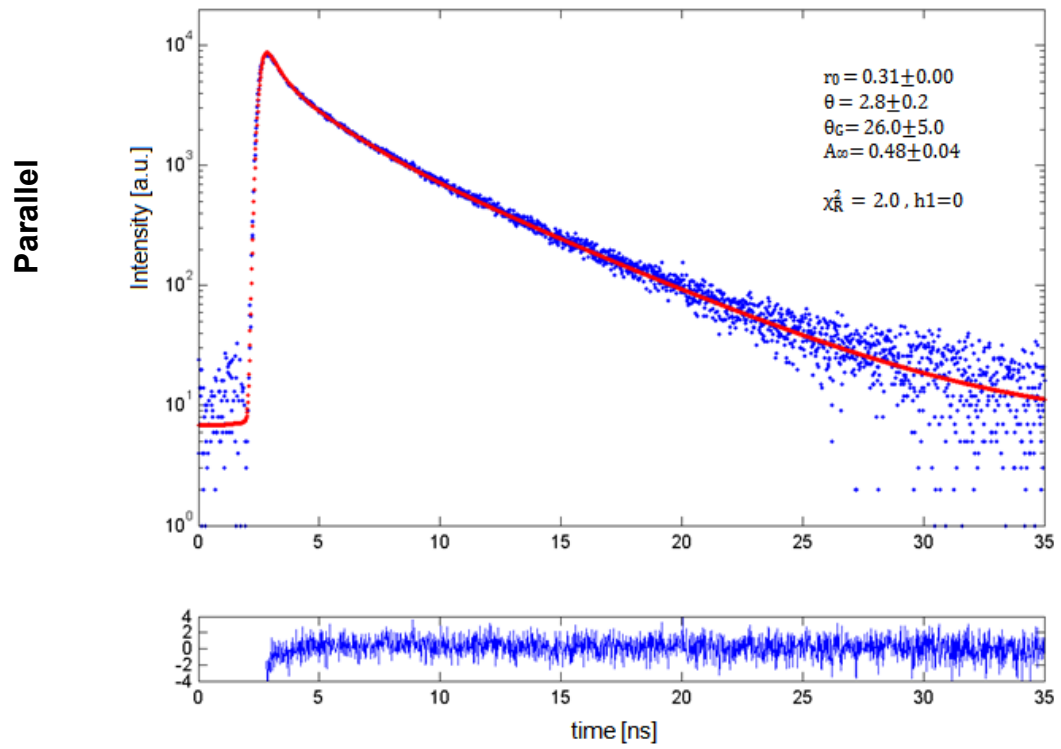
## b. Fluorescence polarized components – single-exponential model



## c. Hindered rotor model

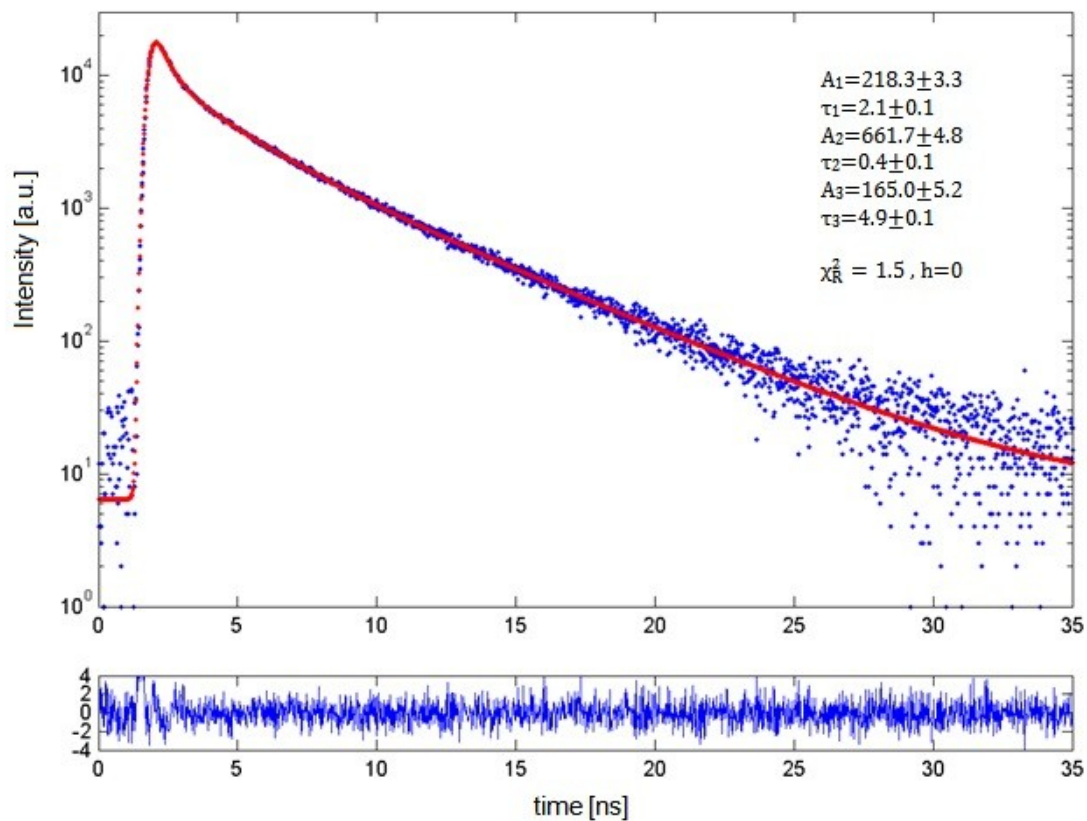


## d. Wobbling-in-a-cone model



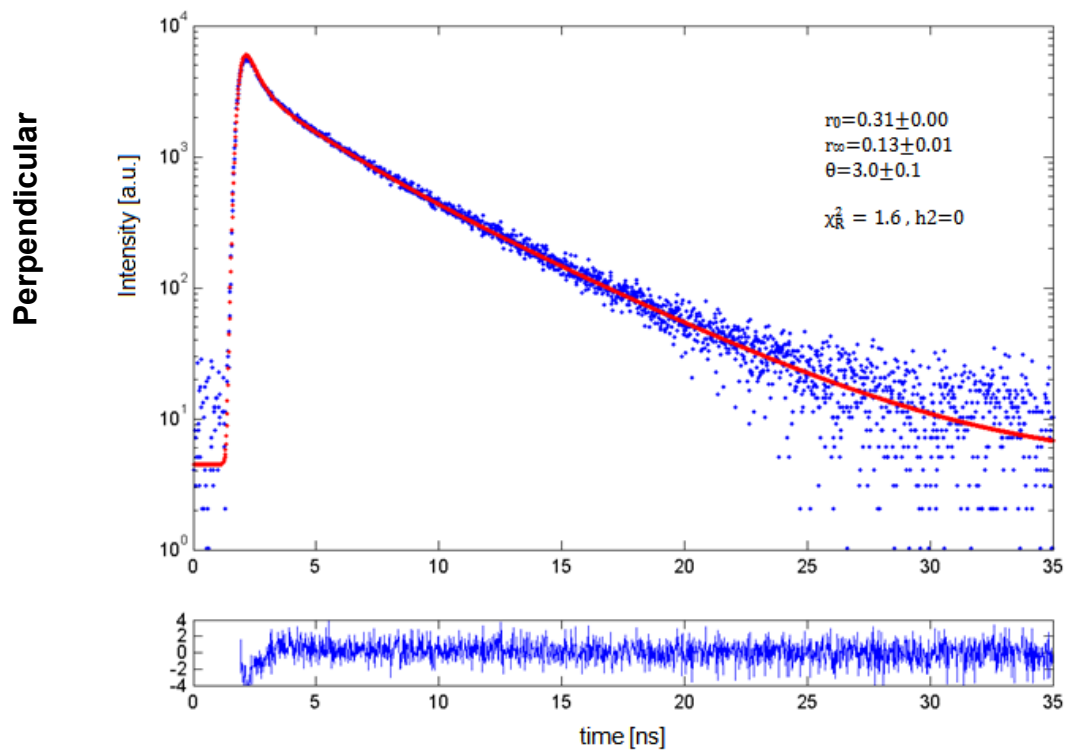
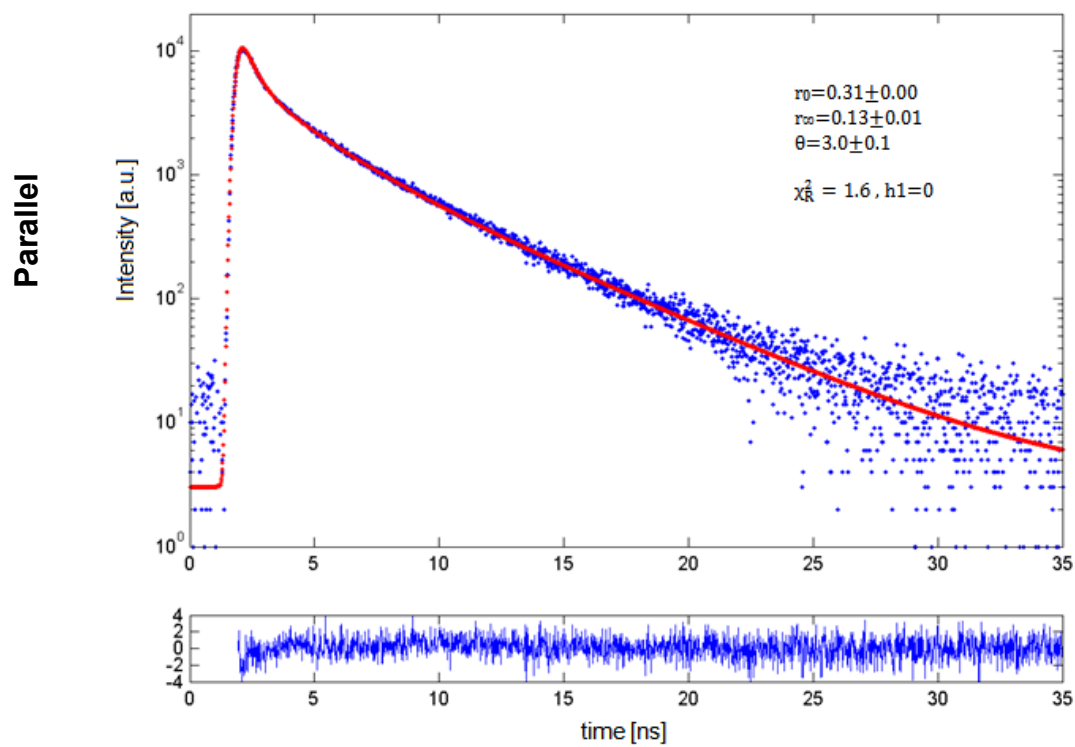
## 8. Time-resolved fluorescence anisotropy of Ribos-(CaM full length, control construct)

## a. Fluorescence lifetime components



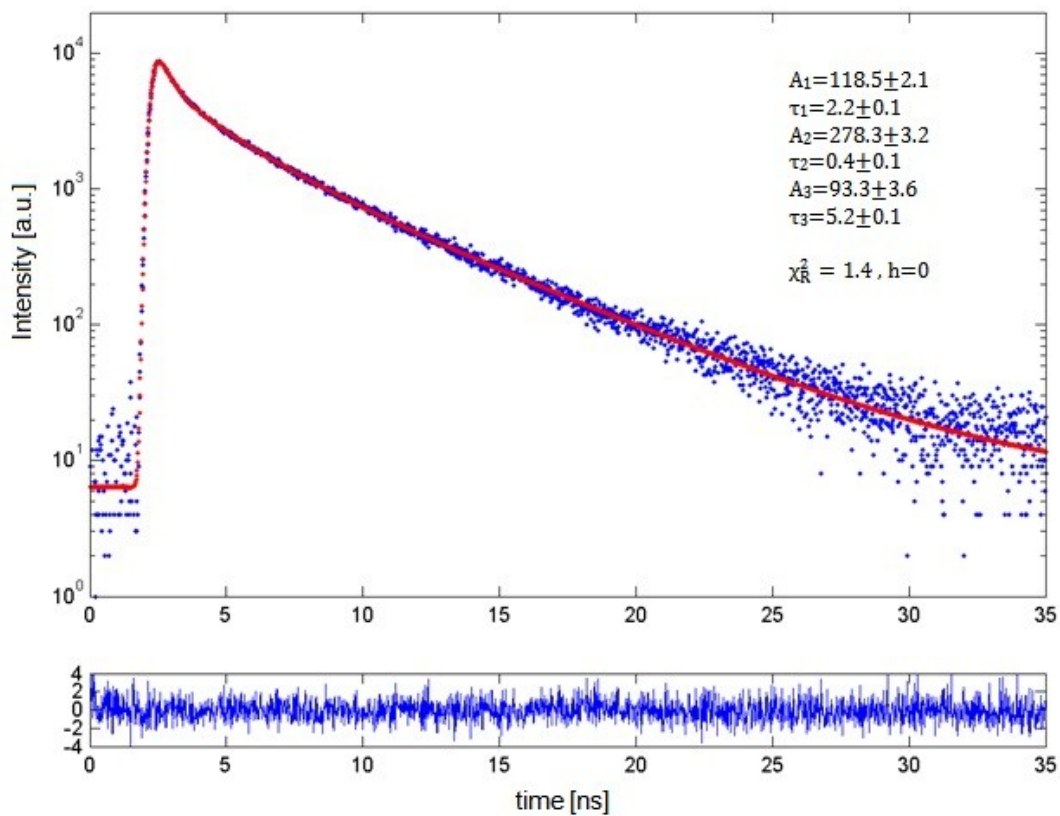
| Ribos-(CaM full length), control construct, lifetime fit |               |           |               |           |               |                   |                       |
|--|---------------|-----------|---------------|-----------|---------------|-------------------|-----------------------|
| $A_1$  | $\tau_1$ [ns] | $A_2$     | $\tau_2$ [ns] | $A_3$     | $\tau_3$ [ns] | $\bar{\tau}$ [ns] |                       |
| 218.3±3.3  | 2.1±0.1       | 661.7±4.8 | 0.4±0.1       | 165.0±5.2 | 4.9±0.1       | <b>3.3</b>        | $\chi_R^2=1.5$<br>h=0 |

## b. Fluorescence polarized components – hindered rotor model



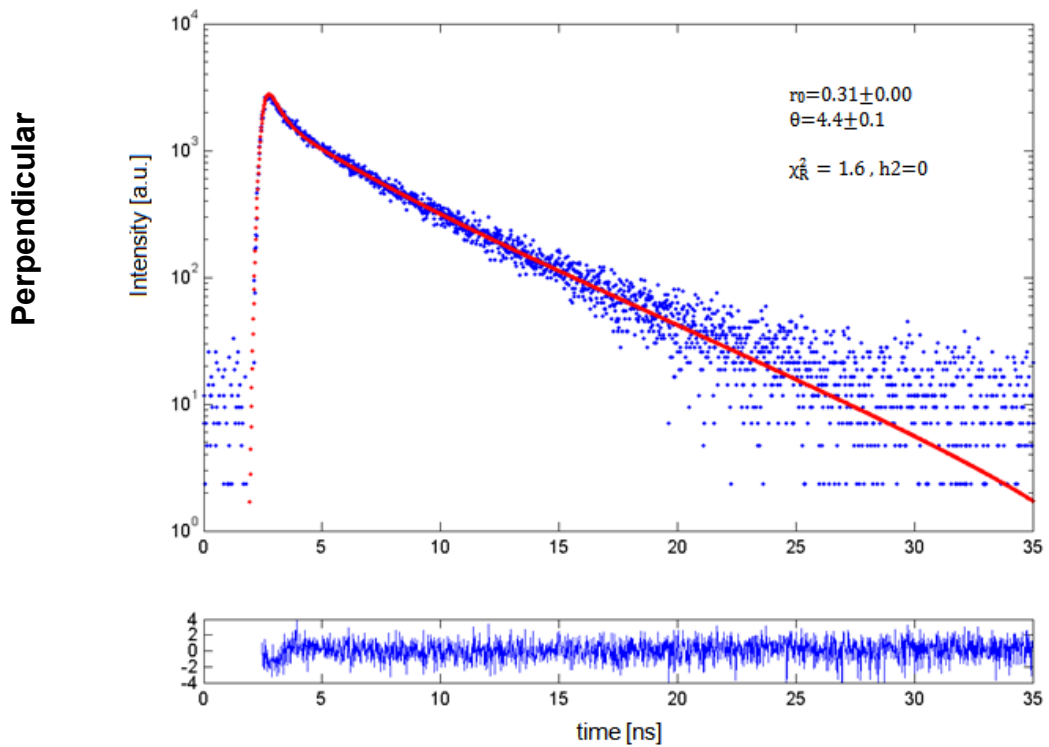
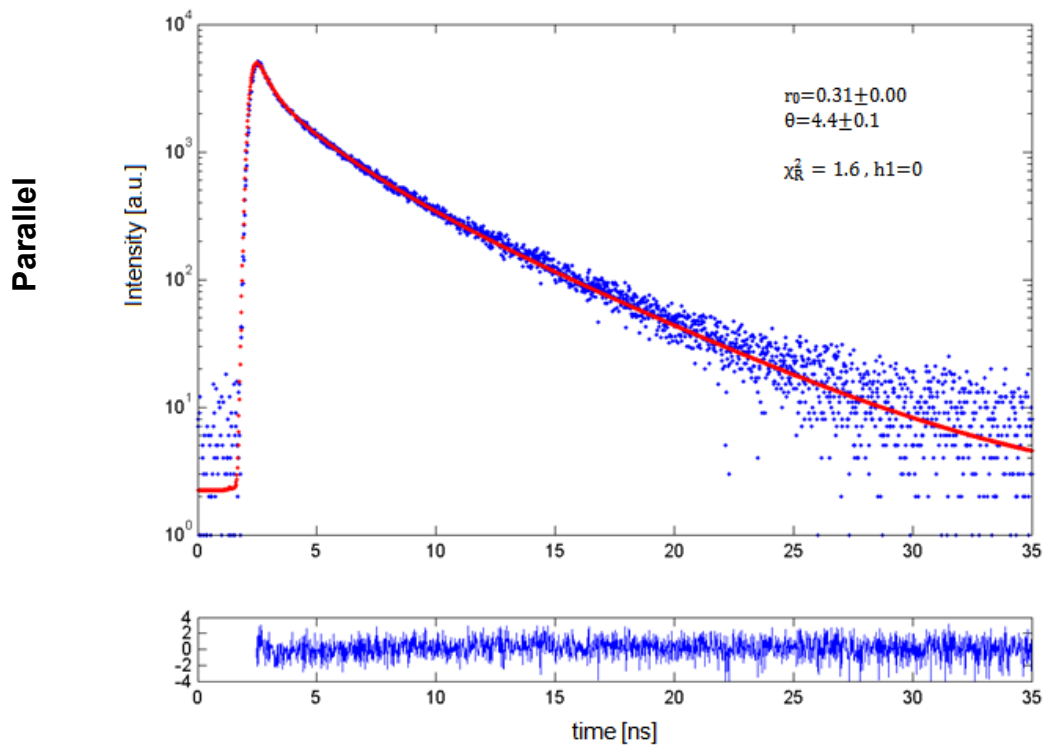
9. Time-resolved fluorescence anisotropy of Ribos+(CaM full length, control construct) after addition of Puro

a. Fluorescence lifetime components

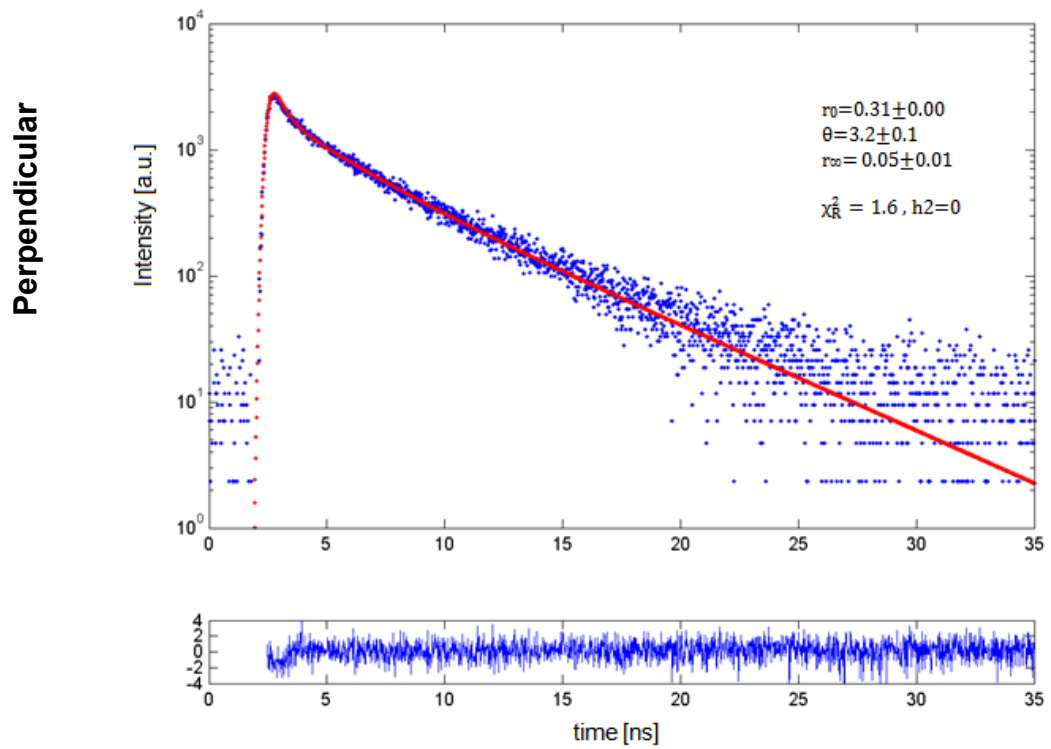
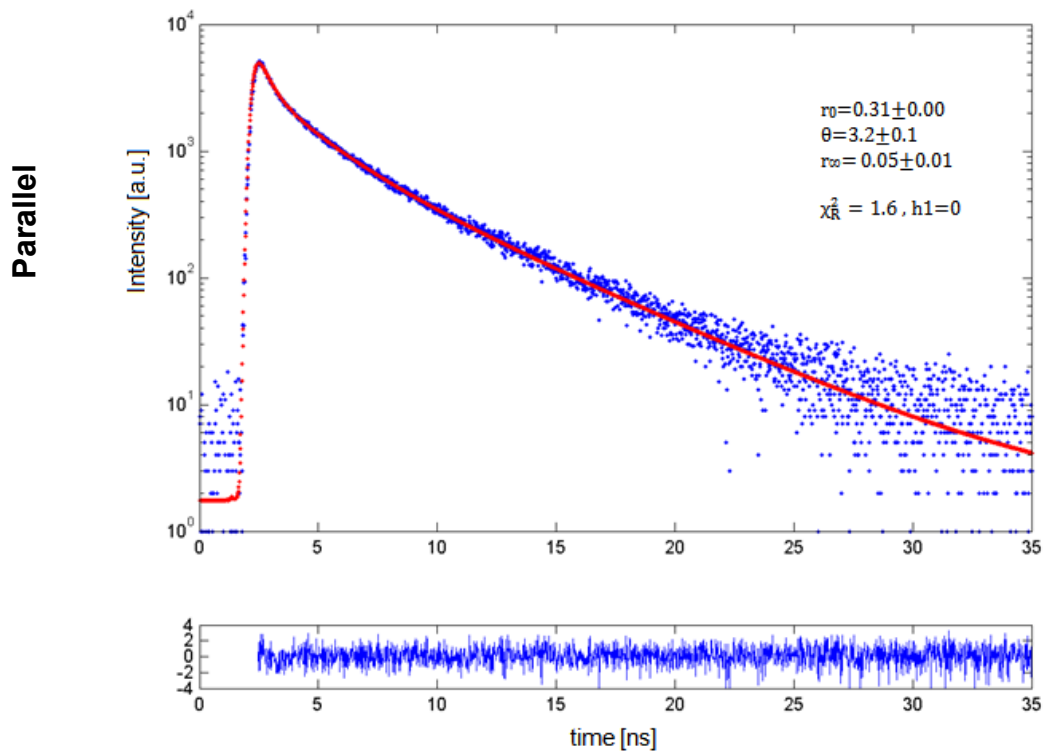


| Ribos + CaM full length, control construct, after addition of Puro , lifetime fit |               |           |               |          |               |                   |                       |
|---|---------------|-----------|---------------|----------|---------------|-------------------|-----------------------|
| $A_1$   | $\tau_1$ [ns] | $A_2$     | $\tau_2$ [ns] | $A_3$    | $\tau_3$ [ns] | $\bar{\tau}$ [ns] |                       |
| 118.5±2.1   | 2.2±0.1       | 278.3±3.2 | 0.4±0.1       | 93.3±3.6 | 5.2±0.1       | <b>3.6</b>        | $\chi_R^2=1.4$<br>h=0 |

## b. Fluorescence polarized components – single-exponential model



## c. Hindered rotor model



## d. Wobbling-in-a-cone model

